

Alma Mater Studiorum – Università di Bologna

DOTTORATO DI RICERCA IN  
Scienze della Terra, della Vita e dell' Ambiente

Ciclo XXX

Settore Concorsuale di afferenza: 04/A2

Settore Scientifico disciplinare: GEO/02

**Thermochronometric evidence of far-field stress transfer  
in continental collisions**

**Presentata da: Dott. Silvia Cattò**

**Coordinatore Dottorato:**

**Prof. Giulio Viola**

**Supervisore:**

**Prof. William Cavazza**

**Co-supervisore:**

**Prof. Massimiliano Zattin  
(Università di Padova)**

**Esame finale anno 2018**



## LIST OF CONTENTS

LIST OF FIGURES	v
LIST OF TABLES	vi
ABSTRACT	vii
RIASSUNTO	xi
PART ONE	
Chapter One – INTRODUCTION AND GOALS	1
1.1. Goals of the study	6
Chapter Two – GEOLOGICAL OVERVIEW	7
2.1. The Pontides	8
2.2. The North Anatolian Fault	12
2.2. The Anatolide-Tauride terrane	14
2.3. The Lesser Caucasus	25
Chapter Three – METHODS	33
3.1. Thermochronometry: the theory	34
3.2. Fission-track thermochronology	36
3.3. AFT data analysis	40
3.4. (U-Th)/He thermochronology	41
3.5. $\alpha$ -ejection correction	42
3.6. (U-Th)/He data analysis	43
3.7. T-t modelling	44
REFERENCES – PART ONE	47

## PART TWO

Chapter Four – MANUSCRIPT SUMMARY	57
4.1. Manuscript 1	59
4.2. Manuscript 2	60
4.3. Manuscript 3	62
Chapter Five – MANUSCRIPTS	63
5.1. Manuscript 1 – <i>The Miocene Arabia-Eurasia collision zone of southeastern Turkey</i>	65
5.2. Manuscript 2 – <i>On the Mesozoic-Cenozoic thermochronological evolution of the Lesser Caucasus</i>	107
5.3. Manuscript 3 – <i>No significant Alpine tectonic overprint on the Cimmerian Strandja Massif (SE Bulgaria and NW Turkey)</i>	143
Chapter Six – CONCLUSIONS	163
REFERENCES – PART TWO	169
APPENDIX A – THERMOCHRONOLOGICAL EVOLUTION OF NORTHWESTERN IRAN	171

## LIST OF FIGURES\*

\*Manuscript figures (Chapter Five) are not listed.

### Chapter One

- 1.1 Conceptual model illustrating intraplate back-arc extension and compression
- 1.2 Tectonic model illustrating development of tensional intra-plate discontinuities

### Chapter Two

- 2.1 Tectonic map of the eastern Mediterranean and Middle East
- 2.2 Tectonic map of Asia Minor and the surrounding regions
- 2.3 Stratigraphic sections of the İstanbul, Strandja and Sakarya terranes
- 2.4 Neotectonic map of the Middle East
- 2.5 The Lake Van Dome showing topography, drainage and crustal thickness
- 2.6 Simplified geological map and tectonic units of the Eastern Anatolian Plateau
- 2.7 Schematic cross-sectional tectonic evolution of the East Anatolian Plateau
- 2.8 Tectonic evolution of the Anatolia-Aegean region after to the formation of the NAF
- 2.9 Progressive evolution of the mantle lithosphere delamination for eastern Anatolia
- 2.10 Moho depth in Anatolian Plateau-Caucasus-Caspian region
- 2.11 Tectonic sketch map of the Caucasus
- 2.12 Simplified stratigraphic columns for the Rioni and Kura basins
- 2.13 Geodynamic model of the evolution of the Lesser Caucasus

### Chapter Three

- 3.1 Nominal closure temperatures of various geochronometers
- 3.2 Partial Retention Zones for He and FT thermochronometers
- 3.3 Effective closure temperature as a function of cooling rate
- 3.4 The “Ion Explosion Spike” model for FT formation
- 3.5 Schematic procedure for FT analysis with the EDM method
- 3.6 Relationship between track length distribution and thermal history
- 3.7 The effects of long  $\alpha$ -stopping distances on He retention

## **Appendix**

- A.1 Tectonic sketch map of the Middle East
- A.2 Geological sketch map of the study area
- A.3 Radial plots of single-grain apatite fission-track ages
- A.4 Radial plots of single-grain apatite fission-track ages
- A.5 Summary of analytical results, radial plots, T-t inverse modelings and histograms
- A.6 Summary of analytical results, radial plots, T-t inverse modelings and histograms
- A.7 Summary of analytical results, radial plots, T-t inverse modelings and histograms
- A.8 Summary of analytical results, radial plots, T-t inverse modelings and histograms
- A.9 Summary of analytical results, radial plots, T-t inverse modelings and histograms
- A.10 Summary of analytical results, radial plots, T-t inverse modelings and histograms

## **LIST OF TABLES**

### **Appendix**

- A.1 Apatite fission-tracks analytical data

## ABSTRACT

In this dissertation, two low-temperature thermochronometers [fission-track analysis on apatite and (U-Th)/He analyses on zircons] are applied on various tectonostratigraphic units from three collisional settings: (i) the Bitlis-Pütürge Massif (SE Turkey), (ii) the Lesser Caucasus (Georgia, Armenia, Azerbaijan), and (iii) the Strandja Massif (SE Bulgaria and NW Turkey). The aim of the study is to better understand the syn- and post-collisional thermochronological evolution of collisional orogens, thus elucidating the dynamics of stress partitioning and transmission during continental collisions. Another focal point of this study is to constrain better the timing of the Arabia-Eurasia collision in the area of its maximum indentation and clarify the overall evolution of the area.

The first locality is the Bitlis-Pütürge Massif, a collisional orogen which developed along the >2,400 km-long Bitlis-Zagros suture between the Eurasian (to the north) and the Arabian (to the south) plates. Data from (U-Th)/He analyses on zircons and fission-track analyses on apatites, were integrated with pre-existing U-Pb and Ar-Ar age determinations. Such integrated dataset provides for the first time an overall picture of the thermochronometric evolution of the orogen. Thermochronological ages can be grouped in three discrete, coherent clusters: (i) higher-temperature thermochronometers point to a latest Cretaceous ages episode of metamorphism not only along the suture zone but across the entire width of the Anatolia-Tauride block north of the suture; lower temperature thermochronometers indicate (ii) an Early - Middle Paleogene cooling episode coeval with the late stage of development of the İzmir-Ankara-Erzincan suture, and (iii) an additional mid-Miocene cooling/exhumation episode along the central metamorphic core of the orogenic wedge. The entire Oligocene is characterized by a rather flat thermochronometric evolution, contrary to the widely held belief that this epoch marked the inception of the Arabia-Eurasia collision and was characterized by widespread deformation.

The second locality is the Lesser Caucasus (Georgia, Armenia, Azerbaijan). In this region, the Sevan-Akera suture constitutes the main tectonic structure, demarcating the boundary between the Arabian and Eurasian plates. As seen previously for the Bitlis- Pütürge

Massif and in general for the hinterland of the Africa-Eurasia collision, the AFT ages cluster in two groups, some of them retaining Late Cretaceous ages, while others display very coherent Middle Miocene ages. This suggests efficient stress transfer in this area as well, with reactivation and exhumation of segments of rheological discontinuities conveniently oriented within the stress field.

From a more general viewpoint, low-temperature thermochronological data and field evidence for the Eurasian foreland north of the Bitlis-Pütürge suture zone suggest that the tectonic stresses related to the Arabian collision during mid-Miocene time were transmitted efficiently over large distances, focusing preferentially at rheological discontinuities located as far as the Lesser Caucasus and the Eastern Pontides. Since the late Middle Miocene a new tectonic regime is active as the westward translation of Anatolia is accommodating most of the Arabia-Eurasia convergence, thus decoupling the foreland from the orogenic wedge and precluding efficient northward stress transfer.

The third locality is the Strandja Massif, a poly-deformed, deeply-eroded orogenic belt (NW Turkey and SE Bulgaria) affected by the Variscan, Cimmerian and Alpine orogenies. The first comprehensive picture of the thermochronometric evolution of the Strandja Massif shows that the bulk of the massif has escaped significant Alpine-age deformation. Following Late Jurassic heating, the central part of the massif underwent a Kimmeridgian-Berriasian phase of relatively rapid cooling followed by very slow cooling in Cretaceous-to-Early Eocene times. These results are consistent with a Late Jurassic–Early Cretaceous Neocimmerian (palaeo-Alpine) phase of north-verging thrust imbrication and regional metamorphism, followed by slow cooling/exhumation driven by erosion. From a thermochronometric viewpoint, the bulk of the Cimmerian Strandja orogen was largely unaffected by the compressional stress related to the closure of the Vardar–İzmir–Ankara oceanic domain(s) to the south, contrary to the adjacent Rhodopes. Evidence of Alpine-age deformation is recorded only in the northern sector of the Strandja massif, where both basement and sedimentary cover underwent cooling/exhumation associated with an important phase of shortening of the East Balkan fold-and-thrust belt starting in the Middle–Late Eocene. Such shortening focused in the former Srednogorie rift zone, an area which had been rheologically weakened by Late Cretaceous extension.



The burial/exhumation histories inferred for the Bitlis and Strandja orogens show two very different mechanisms of collisional stress transmission. In the Bitlis orogen the stress focused on both the orogenic prism and the foreland, where it reactivated conveniently oriented older structures. Conversely, in the Strandja orogen the stress mostly bypassed the orogenic prism and focused on the Srednogie rift basin to the north, rheologically weakened by previous Late Cretaceous back-arc extension.



## RIASSUNTO

Due termocronometri di bassa temperatura [analisi delle tracce di fissione su apatite e analisi (U-Th)/He su zirconio] sono stati applicati a campioni provenienti da varie unità tettonostratigrafiche di tre orogeni collisionali, (i) il massiccio di Bitlis-Pütürge (Turchia sud-orientale), (ii) il Caucaso Minore (Georgia-Armenia-Azerbaijan), e (iii) il massiccio di Strandja (Bulgaria sud-orientale e Turchia nord-occidentale). Il fine ultimo di questa tesi di dottorato è quello di comparare l'evoluzione termocronologica di orogeni collisionali, con particolare attenzione alle dinamiche di ripartizione degli stress tettonici tra prisma orogenico e hinterland. Questo studio punta inoltre a vincolare le tempistiche della collisione Arabia-Eurasia nell'area di massima indentazione fra le due placche, definendo meglio l'evoluzione generale dell'intera zona.

La prima località indagata è il massiccio di Bitlis-Pütürge, un orogene collisionale che si sviluppa lungo la zona di sutura di Bitlis-Zagros, lunga più di 2400 km, fra la placca eurasiatica (a nord) e quella araba (a sud). Il dataset derivante dall'analisi (U-Th)/He su zirconi e delle tracce di fissione su apatiti è stato opportunamente integrato con età radiometriche U-Pb e Ar-Ar preesistenti e fornisce per la prima volta una panoramica completa dell'evoluzione termocronometrica dell'orogene. Le età termocronologiche possono essere raggruppate in tre gruppi distinti e internamente coerenti: i termocronometri di alta temperatura registrano (i) un episodio di metamorfismo tardo-cretaceo, non solo lungo la zona di sutura ma in tutto l'intero Blocco Anatolide-Tauride a nord della sutura; i termocronometri di bassa temperatura indicano (ii) un episodio di raffreddamento nel Paleogene medio coevo con gli stadi finali di sviluppo della zona di sutura di İzmir-Ankara-Erzincan, e (iii) un episodio medio-miocenico di raffreddamento/esumazione nel nucleo metamorfico al centro del cuneo orogenico. Contrariamente a quanto affermato in numerosi studi che collocano l'inizio della collisione fra Arabia ed Eurasia nell'Oligocene e affermano che quest'epoca sia caratterizzata da un'importante e diffusa fase di deformazione, il nostro dataset indica che l'intero Oligocene è caratterizzato da un'evoluzione termica sostanzialmente piatta.

La seconda località è il Caucaso Minore (Georgia, Armenia, Azerbaijan). In questa regione la sutura di Sevan-Akera costituisce la struttura tettonica principale, separando la placca araba da quella eurasiatica. Come visto precedentemente per il massiccio di Bitlis-Pütürge e in generale per l'avampaese della collisione fra Africa ed Eurasia, le età AFT formano due gruppi: alcune di esse mantengono un'età tardo-cretacea mentre altre mostrano età medio-mioceniche coerenti. Questa distribuzione di età suggerisce che anche in quest'area lo stress collisionale sia stato trasmesso efficacemente, con la riattivazione e conseguente esumazione lungo alcuni segmenti opportunamente orientati di discontinuità reologiche preesistenti.

In un quadro più ampio, i dati della termocronometria di bassa temperatura e le evidenze di terreno relativi all'avampaese eurasiatico a nord della zona di sutura di Bitlis-Pütürge suggeriscono che lo stress tettonico generato dalla collisione della placca araba durante il Miocene Medio è stato trasmesso efficacemente su lunghe distanze e si è focalizzato prevalentemente lungo discontinuità reologiche molto distanti dal fronte di collisione, come il Caucaso Minore e le Pontidi Orientali. Dal Miocene Medio è subentrato un nuovo regime tettonico che vede la maggior parte dello stress legato alla convergenza fra Arabia ed Eurasia accomodato dall'estrusione verso ovest dell'Anatolia, con il conseguente disaccoppiamento meccanico dell'avampaese dal fronte orogenico. Un simile contesto preclude un efficiente trasferimento dello stress verso nord.

La terza ed ultima località investigata è il Massiccio di Strandja, un orogene situato al confine fra la Turchia nord-occidentale e la Bulgaria sud-orientale, polideformato e profondamente eroso dalle orogenesi varisca, cimmeride ed alpina. I dati raccolti forniscono per la prima volta una ricostruzione completa dell'evoluzione termocronometrica del massiccio, evidenziando che la maggior parte dell'orogene non è stato interessato da deformazione di età alpina. Dopo una fase tardo-giurassica di riscaldamento, la parte centrale del massiccio ha subito un episodio di raffreddamento relativamente rapido nel Kimmeridgiano-Berriasiano, seguito da un periodo di raffreddamento estremamente lento durante tutto il Cretaceo fino al primo Eocene. Questi risultati sono coerenti con una fase neocimmeride (paleo-alpina) di embriciatura nord-vergente di falde tettoniche e metamorfismo regionale avvenuta nel tardo

Giurassico superiore – Cretaceo inferiore, seguita da un lento raffreddamento/esumazione controllato dall'erosione. Da un punto di vista termocronometrico, la maggior parte dell'orogene cimmeride di Strandja non è stato influenzato dallo stress compressivo associato alla chiusura del domino oceanico di Vardar–İzmir–Ankara a sud, contrariamente ai Monti Rodopi a sud-ovest del massiccio di Strandja. La deformazione di età alpina è stata registrati solamente nella parte settentrionale del massiccio, dove il basamento cristallino e le coperture sedimentarie sono stati interessati da raffreddamento/esumazione associato ad un'importante fase di raccorciamento dei Balcani orientali a partire dall'Eocene medio-superiore. Il raccorciamento di età alpina si è invece focalizzato lungo la Zona di Srednogorie, un'antica zona di rift reologicamente indebolita da estensione tardo-cretacea.

Le storie di seppellimento ed esumazione ricavate per gli orogeni di Bitlis e di Strandja e gli avampaesi ad essi associati evidenziano una diversa ripartizione dello stress derivante da una collisione continentale. Nell'orogene di Bitlis lo stress ha agito sia sul prisma orogenico che sull'avampaese, dove ha riattivato strutture preesistenti, se opportunamente orientate. Al contrario, nel Massiccio di Strandja il prisma orogenico cimmeride è stato in gran parte bypassato dallo stress collisionale di età alpina, che si è invece focalizzato più a nord nel bacino di Srednogorie, un rift di retro-arco del Cretaceo superiore indebolito reologicamente e pertanto facilmente deformabile.



PART ONE

Chapter One

**INTRODUCTION AND GOALS**

The dynamics and mechanisms of stress generation, transmission and partitioning have attracted much attention since the validation of the plate tectonic theory in the 20<sup>th</sup> century, as the structural framework and evolution of orogenic systems are ultimately determined by how strain is accommodated within the Earth's crust. According to classic plate tectonics collision-related deformation and mountain building exclusively occur along plate boundaries. However, a mounting body of evidence [e.g. Zoback, 1992; Ziegler et al., 1995, 1998, 2002; Cloetingh et al., 2005] suggests that horizontal compressional stress can travel far from the collision front inducing an array of compressional features such as lithosphere folding, basement upthrusting and basin inversion. Stress transmission and related intraplate compressional and transpressional structures thus become major elements in the structural setting of broad areas of continental interiors. Recent models [e.g. Cloetingh et al., 1982, 1989; Jolivet et al., 1989; Ziegler, 1993, 1995; Faccenna et al., 2009] point out that collision-related stress can occasionally bypass large portions of crust and focus along rheological discontinuities, on distances of over 1700 km from the plate margin [Ziegler et al., 2002]. This behaviour is observed in both continent-ocean and continent-continent collisions, with the difference that in the former intraplate structures develop exclusively in the correspondent hinterland (Fig. 1.1B) whereas in the latter both the foreland and the hinterland are affected by deformation (Fig. 1.1C) In fact, oceanic lithosphere is much more homogeneous and generally stronger than the rheologically complex continental lithosphere and it is more prone to stress transmission rather than deformation. Many works have investigated how the dynamics of stress transmission and partitioning can be influenced by a wide range of factors, including, as mentioned before, the nature of the plate interface [e.g., Faccenna et al., 2008; Sokoutis and Willingshofer, 2011], the extent of coupling between the plates [e.g., Ziegler et al., 1999; Faccenna et al., 2009; Sokoutis and Willingshofer, 2011] and the presence of pre-existing crustal structures [e.g. Cloetingh et al., 1982, 1989; Jolivet et al., 1989; Ziegler, 1993, 1995; Ziegler et al., 2002].

A strong mechanical coupling between the orogenic wedge and its foreland/hinterland is crucial for strain localisation and mountain building. Notably, back-arc rift inversions often correlate with phases of increased mechanical coupling between colliding plates and the acceleration in their convergence rates [Cloetingh et al., 1982, 1989; Jolivet et al., 1989;



Ziegler, 1993]. Mechanical coupling and decoupling result from a complex interaction between the geometry of the collisional zone, convergence features (i.e. rate, direction), and the rheology and structural framework of the plates. Although mechanical coupling is essential for the development of intraplate compressional structures, decoupling is required to compensate the crustal shortening associated with basin inversion and basement upthrusting [Ziegler et al., 1995]. Faccenna et al., [2009] recognize two different geodynamic regimes for continental collisions depending on the degree of rheological coupling: coupled active collision zones, characterized by a thick crustal wedge and compressional stresses (i.e. Himalaya and Western Alps) and decoupled collision zones characterized by a thin crustal wedge compression in the foreland, and extension in the inner part of the orogen (i.e. Northern Apennines). Transition from coupled to decoupled regimes occurs at the early stages of continental collision after the end of the oceanic subduction, suggesting that the insertion of a weak, wet and thick upper crustal layer into the subduction channel plays a major role in triggering plates decoupling.

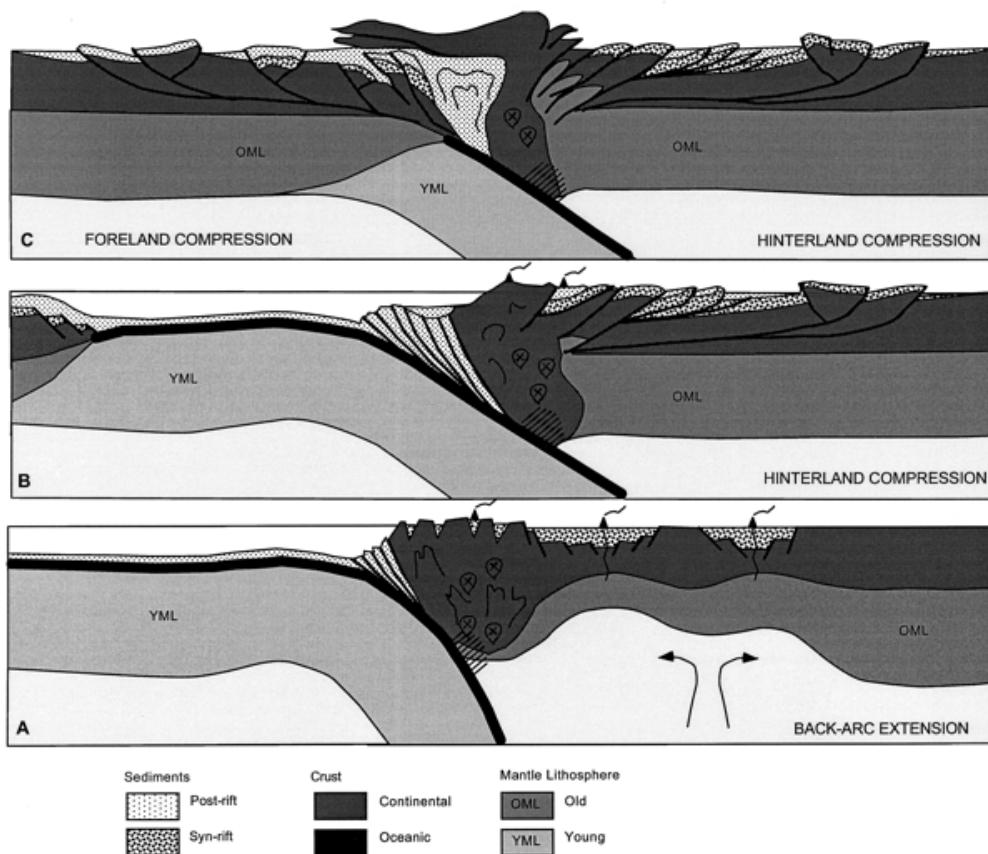


**Fig. 1.1.** Conceptual model illustrating intraplate (A) back-arc extension, (B) back-arc (hinterland) compression and, (C) collisional foreland and hinterland compression (not to scale) [Ziegler et al., 1998].

The pre-existing structural framework heavily influences the later stages of orogenic growth, crustal discontinuities acting as preferential loci of deformation due to their weakened rheological status. Generally, the stretched, thermally destabilized, poly-faulted crust which characterize rift and post-rift zones constitutes the weakest part of the foreland and usually deform first, provided that the orientation of the structure within the stress regime is convenient (Fig. 1.2). Major deep-rooted strike-slip faults are easily reactivated as well, under the same assumption, while thrust fronts and ancient suture zones are less susceptible to reactivation [Ziegler et al., 1998]. The reactivation of pre-existing structures is always preferred over the creation of new ones as long as their orientation is favourable, namely when the angle between

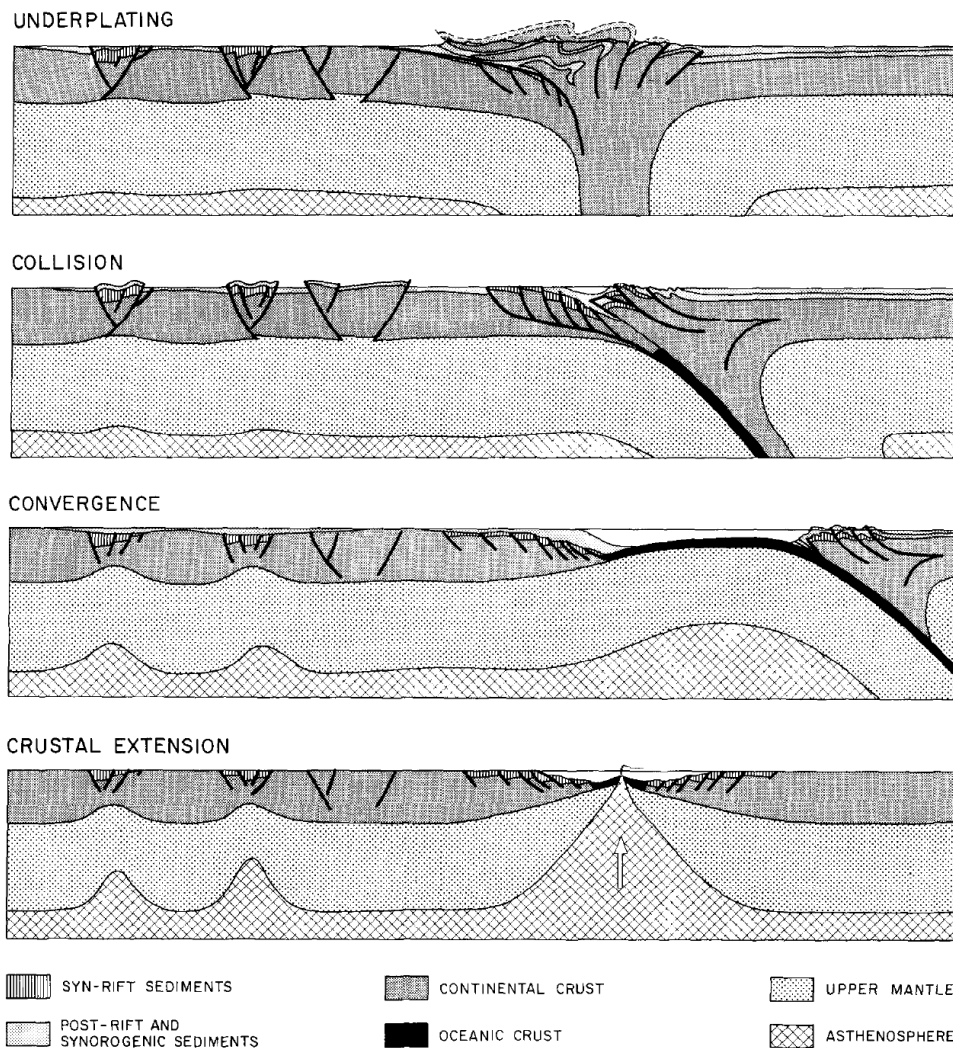


**Fig. 1.2. Tectonic model illustrating development of tensional intra-plate discontinuities and their compressional deformation during a collisional event (not to scale) [Ziegler et al., 1998].**

their strike and the direction of the major stress axis in less than 45° [Nalpas et al., 1995; Brun & Nalpas, 1996]. Compressional stress transfer between plates and deformation/exhumation of both the orogenic wedge and the foreland/hinterland is essentially synchronous and in the stratigraphic record it is usually marked by coeval coarse-grained syntectonic clastic wedges in pro-wedge foreland basin along the collision front and far into the hinterland near the reactivated structure [Ziegler et al., 2002].

In this dissertation, we will present thermochronometric evidence of far-field stress transfer in three case studies, (i) the Bitlis-Pütürge Massif (SE Turkey), (ii) the Lesser Caucasus (Georgia, Armenia, Azerbaijan), and (iii) the Strandja Massif (SE Bulgaria and NW Turkey). These areas are located within the western Tethyan realm, in a palinspastic structural background that can be seen as the “hinge” of the seafloor spreading and consumption of the Paleotethys and later of the Neotethys. Many small terranes gradually rifted from the Gondwana supercontinent (in the south) and moved northward to be accreted along the southern margin of Laurasia (in the north). Therefore, the investigated areas were affected through time by several different tectonic regimes and/or orogenies and subjected to multiple deformation phases. The exact determination of the thermal histories in these regions is crucial not only for understanding the evolution of the orogens *per se*, but also for elucidating the causative mechanism from a supra-regional point of view. This is achieved through the application of low-temperature thermochronometry, integrated with observations on the structural setting and with geophysical data available in the literature. Mountain building is an inherently destructive process and the geological record related to the early stages of an orogeny is often incomplete. In this sense, thermochronology provides a powerful instrument to elucidate the processes taking place during these early phases.

In the initial chapters, an introduction to the geology of the study region is provided, the applied analytical methodologies are illustrated, the scientific questions are detailed, and the main structure of the thesis is briefly outlined. Then, three manuscripts, already accepted or submitted, are presented. In the final chapter, the main conclusions of this dissertation are expounded.

## 1.1 Goals of the study

This study focuses on the issue of stress partitioning in the hinterland of continental collision zones. Low-temperature thermochronology was applied on three collisional orogens and the adjacent forelands in order to model their syn- and post-collisional thermal histories, thus reconstructing their relative movements with respect to the surface. The deformation (and thus the burial-exhumation evolution) of these orogens can be seen as a far-field tectonic effect of the collision, contrary to the widely held belief that the deformation focuses only in close proximity to the plate boundaries. Another aim of this study is to further constrain the timing of the Arabia-Eurasia collision in the area of its maximum indentation and clarify the overall evolution of the region. Despite the importance of the event, the areal extent, dynamics and timing of the Arabia-Eurasia collision is still poorly understood, with estimates (generally based on the stratigraphy) ranging from Late Cretaceous [Hall, 1976; Alavi, 1994], to Late Eocene-Oligocene [35-25 Ma; Jolivet & Faccenna, 2000; Agard et al., 2005; Allen & Armstrong, 2008], to Miocene [Şengör et al., 1985; Dewey et al., 1986; Yılmaz, 1993; Robertson et al., 2007].

Chapter Two

**GEOLOGICAL OVERVIEW**

The tectonic framework of the Middle East region is characterized by a number of continental fragments squeezed in between the Eurasian Plate in the north and the Arabian Plate in the south (Fig. 2.1). The area represents the western part of the Tethyan domain and through time was affected by many complex geodynamic processes, such as the rifting and following subduction of the Paleotethys and the Neotethys oceans. During Palaeozoic, Mesozoic and Cenozoic times these terranes rifted from the African plate (e.g. due to back-arc extension) and were eventually accreted against the opposite, European continental margin [e.g. Stampfli and Hochard, 2009]. This chapter provides a synthetic overview of the main lithospheric fragments and structures, whilst a more detailed description of the particular geological background is provided within each manuscript.

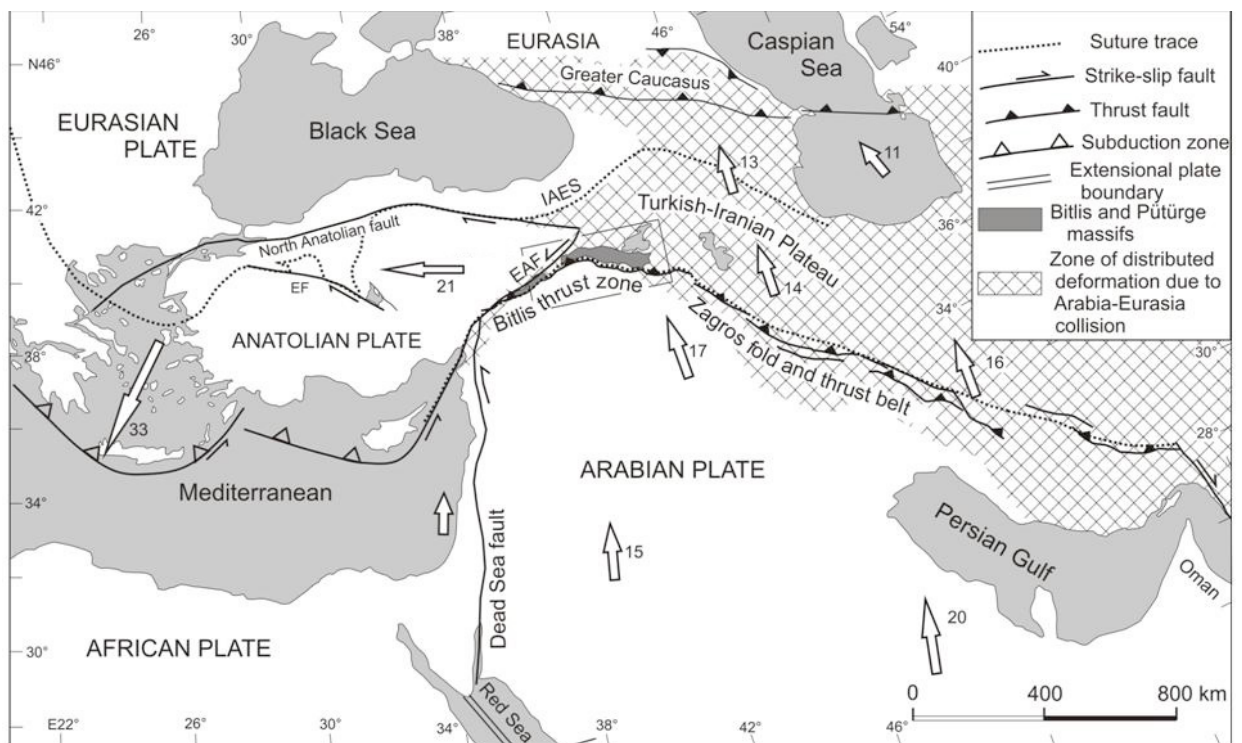


**Fig.2.1. Tectonic map of the eastern Mediterranean and Middle East (Okay et al.,2010). Arrows and numbers indicate global positioning system (GPS)-derived velocities with respect to Eurasia (modified from Reilinger et al.2006; Copley & Jackson, 2006). EAFS: East Anatolian Fault; EF: Ekişehir fault; İAES: İzmir-Ankara-Erzincan suture.**

### 2.1. The Pontides

The Pontides are an east-west trending orogenic belt stretching some 1,200 km from Bulgaria to the Lesser Caucasus, and consisting of three different tectono-stratigraphic terranes,

characterized by different geological features and evolutions: the Strandja Massif, the İstanbul terrane and the Sakarya terrane (Fig. 2.2). These terranes share a common Laurussian affinity and a complex structural history including Variscan (Carboniferous), Cimmeride (Late Triassic – Early Cretaceous), and Alpide (Late Cretaceous - Paleogene) deformation [Yılmaz et al., 1997]. The Strandja Massif belongs to the southern Balkan metamorphic province, also comprising the Serbo-Macedonian and the Rhodope massifs. It consists of a Variscan crystalline basement overlain by a Triassic–Jurassic continental to shallow-marine sedimentary sequence. The basement is made predominantly of quartzo-feldspathic gneisses intruded by late Carboniferous and Early Permian (ca. 257 Ma) granitoids [Okay et al., 2001; Sunal et al., 2006; Fig. 2.3.] and it forms a belt about 20 km wide extending from Bulgaria to Çatalca near İstanbul.

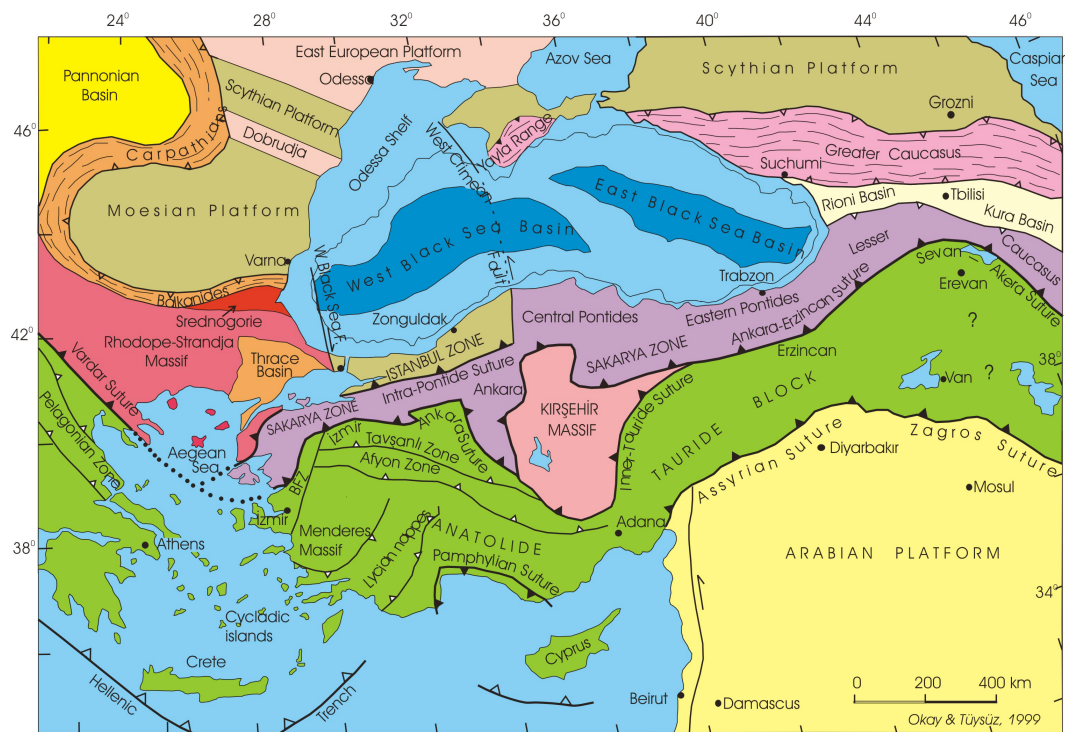


**Fig.2.2. Tectonic map of Asia Minor and the surrounding regions (Okay & Tüysüz,1999).**

The İstanbul Terrane is a continental fragment stretching along the southwestern margin of the Black Sea. It has a late Precambrian crystalline basement characterized by gneiss, amphibolite, metavolcanic rocks, metaophiolite and voluminous Late Precambrian granitoids [Chen et al., 2002; Yiğitbaş et al., 2004; Ustaömer et al., 2005; Fig. 2.3.]. The İstanbul and Sakarya terranes are separated by the Intra-Pontide suture, relict of the early

Carboniferous Intra-Pontide ocean that closed in the mid-Carboniferous due to the collision of the terranes [Okay, 2008]. It is noted by Okay [2008] and Cavazza et al. [2012] that the different Mesozoic stratigraphy between the two units suggests a reopening of the ocean in the Triassic and a new phase of subduction and collision in pre-Cenozoic times (arguably in the Late Cretaceous).

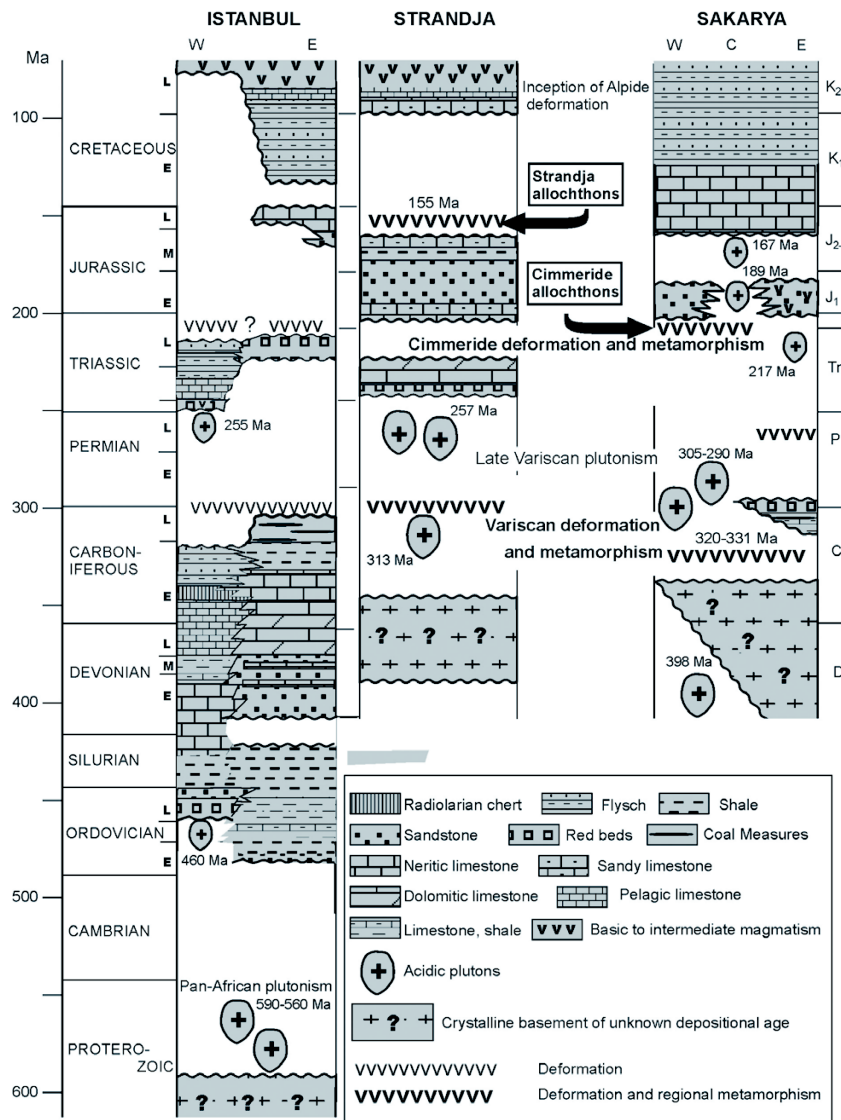


Fig. 2.3. Synthetic stratigraphic sections of the İstanbul, Strandja and Sakarya terranes [Okay et al., 2008].

The Sakarya terrane forms an elongate crustal ribbon extending from the Aegean in the west to the Eastern Pontides in the east. The Sakarya terrane, which includes the Eastern Pontides, is characterized by a general absence of in situ Paleozoic sedimentary rocks, by the



presence of Paleo-Tethyan Permo-Triassic accretion/subduction complexes (the Karakaya Complex) and by a ubiquitous Liassic transgression [Okay et al., 1996; Federici et al., 2010]. In contrast, the Taurides to the south show a well-developed Palaeozoic sedimentary succession and do not comprise Paleo-Tethyan accretion-subduction complexes.

The Sakarya and Tauride terranes and paleo geographic realms are separated by the Izmir-Ankara-Erzincan suture zone, which is marked by large bodies of peridotite and ophiolitic mélange. The three Pontic terranes were amalgamated in the Mesozoic following the closure of the Intra-Pontide suture and the opening of the western Black Sea. Isotopic data from eclogites and blueschists in the Central Pontides indicate that the NeoTethys was already subducting under the Pontides in the Early Cretaceous [ca. 105 Ma, Okay et al., 2006]. However, the corresponding magmatic arc started to develop only in the Late Cretaceous [ca. 90 Ma, Robinson et al., 1995; Okay & Sahinturk, 1997]. The Upper Cretaceous magmatic arc can be traced along the Black Sea coast from the Lesser Caucasus to Sredna Gora in Bulgaria. The magmatic arc switched off in the Maastrichtian, although the collision between Pontides and the Anatolide-Tauride was delayed until the Late Palaeocene–Early Eocene [Okay, 2008]. The collision was followed by uplift and extensive erosion. A new cycle of deposition and volcanism started in the Middle Eocene, probably related to extension associated with opening of the eastern Black Sea [e.g., Okay, 1994, 2008]. The sea finally left the Pontides by the end of the Eocene and the region has been subaerially exposed since the Oligocene.

The Eastern Pontides form a mountain chain 500 km long and 100 km wide along the southeastern coast of the Black Sea. Geographically, Eastern Pontides is a term used for the region skirting the eastern Black Sea coast of Turkey. Its western boundary is taken arbitrarily either as the Yeşilirmak or Kızılırmak rivers near Samsun. Geologically, the Eastern Pontides are well known as one of the best preserved examples of paleo-island arc, which was formed above the northward-subducting Tethyan ocean floor during the Senonian [Şengör & Yılmaz, 1981; Akinci, 1984; Okay & Şahintürk 1997]. The Eastern Pontides are bounded to the south by the Ankara-Erzincan Neo-Tethyan suture and to the north by the eastern Black Sea basin. Eastward they extend without a break into the Lesser Caucasus of Georgia (Adjara, Trialeti and Artvin, Bolnisi tectonic zones) [e.g., Khain, 1975; Yılmaz et al., 1999]. Their western

geological boundary with the Central Pontides is stratigraphic and corresponds to a facies change in the Cretaceous sequence.

## *2.2. The North Anatolian Fault*

The North Anatolian Fault (NAF) has been subject of numerous geological, geomorphological and seismological studies since its recognition as a major strike-slip fault in 1948 by Ketin [Şengör et al., 2005]. Ketin noted that during all major earthquakes in northern Turkey since 1939, the surface break always had the character of a generally east-west-striking, right-lateral fault. Ketin further pointed out that because the Anatolian interior south of the fault was largely aseismic, a whole Anatolian block had to be moving westward with respect to the Black Sea along the NAF. Ketin also argued that to accommodate such movement another left-lateral fault had to exist to the south of the Anatolian block; his prediction was confirmed a quarter of a century later when the East Anatolian Fault (EAF) was identified [Seymen & Aydin, 1972].

After the large earthquakes of 1999 [e.g., Barka et al., 2000a, 2002] the NAF has received renewed attention with many new studies from various Earth sciences disciplines, but the age and the current understanding of the origin and displacement history remains somewhat limited and controversial [Bozkurt, 2001].

The NAF is located almost entirely within Anatolia, only its westernmost extremity is located in the Marmara Sea, in the Gallipoli peninsula, and in the northern Aegean Sea [Şengör et al., 2005; Fig. 2.1, 2.2]. The Marmara Sea consists essentially of depressions and ridges aligned along the E-W trend of the NAF [Zattin et al., 2010; Fig. 2.1, 2.2]. In this region, the NAF widens into a complex fault zone stretching some 100 km in a N-S direction, from Ganos Mt. in southern Thrace [Okay et al., 2004] to Kazdağ in the southern Biga peninsula [Cavazza et al., 2008]. Such configuration translates into a high degree of structural complexity, with coexisting deep basins, push-up structures, and block rotations [Zattin et al., 2010]. The most important basins related to the activity of the NAF are well described in Şengör et al. (2005). Based on paleontological data these basins are Middle-Upper Miocene and Pliocene to Quaternary in age [Şengör et al., 2005].

There is an ongoing debate about whether the NAF was initiated in the Late Miocene, Early Pliocene [Barka, 2000; Bozkurt, 2001] or in the Middle Miocene [McKenzie, 1972; Şengör et al., 2005]. In recent times, a mounting body of evidence is suggesting that NAF follows the course of a pre-existing structural discontinuity. For the Ganos segment of the NAF in the Gallipoli peninsula Zattin et al. [2005, 2010] suggested, based on thermochronological evidence, the existence of a pre-existing discontinuity with a significant component of dip slip at least of Late Oligocene age and possibly older. This conclusion is also supported by Usyal et al. [2006] who studied a ca. 500 km long segment of the NAF east of the Marmara Sea by radiometric dating of fault gouges. They found that an early event of significant strike-slip was initiated at about 57 Ma, but further intensified at ca. 26 Ma and later at ca. 8 Ma. Kaymankci et al. [2007], on the basis of paleomagnetic data, proposed that the Ganos fault and other ENE, trending faults experienced dextral strike-slip activity before the Late Pliocene arrival of the NAF in the Marmara region. Another Oligocene major strike-slip shear zone in western Anatolia, with a right-lateral offset of ca. 100 km, was described by Okay et al. [2008] in the Uludağ area, near the city of Bursa. All these papers support the idea that pre-existing mechanical weakness zones such as faults and shear zones greatly influenced the locus of subsequent tectonic activity [Holdsworth et al., 1997; Zattin et al., 2010].

According to the common interpretation, the NAF and EAF nucleated in eastern Anatolia following Arabia-Eurasia collision and the southward roll-back of the Hellenic trench. Today the NAF and EAF accommodate most of the convergence between Arabia and Eurasia plate and the lateral transport westward of the Anatolian Plate [Reilinger et al., 2006]. The question if the nucleation of the NAF and EAF is related to (i) the collision between Arabia and Eurasia, (ii) roll-back of the Hellenic trench, or -perhaps more likely- (iii) a combination of both mechanisms, is still debated. Several data derived from GPS-velocity and seismicity [Reilinger et al., 2006], proprietary seismic stratigraphic data (i.e. Middle to Late Miocene clastic wedges generically prograding northwestward across the eastern Black Sea), Middle Miocene ages derived from apatite fission, track for Bitlif Massif along the collision zone [Okay et al., 2010], and other stratigraphic evidence (i.e. Middle Miocene unconformity between Late

Oligocene/Early Miocene and Late Miocene volcanic deposits) indicate that a major change in stress regime from contraction to extension or strike-slip occurred in the Middle Miocene.

### 2.3. The Anatolide-Tauride terrane

The hinterland of the Arabia collision zone is a high-standing plateau (the Turkish-Iranian plateau, Fig.2.1) with an average elevation of ca. 2 km above sea level. A large portion of the plateau is covered by Late Miocene-Quaternary calc-alkaline to alkaline volcanic rocks [Yılmaz et al., 1987; Pearce et al., 1990; Yılmaz, 1990]. The plateau displays structural evidence for active diffuse north-south shortening and broad east-west extension thru a conjugate system of strike-slip faults (Şengör et al., 2008; Fig. 2.4) displacing crustal fragments toward Iran and the Caspian Sea [Jackson & McKenzie, 1988; Dilek, 2006].

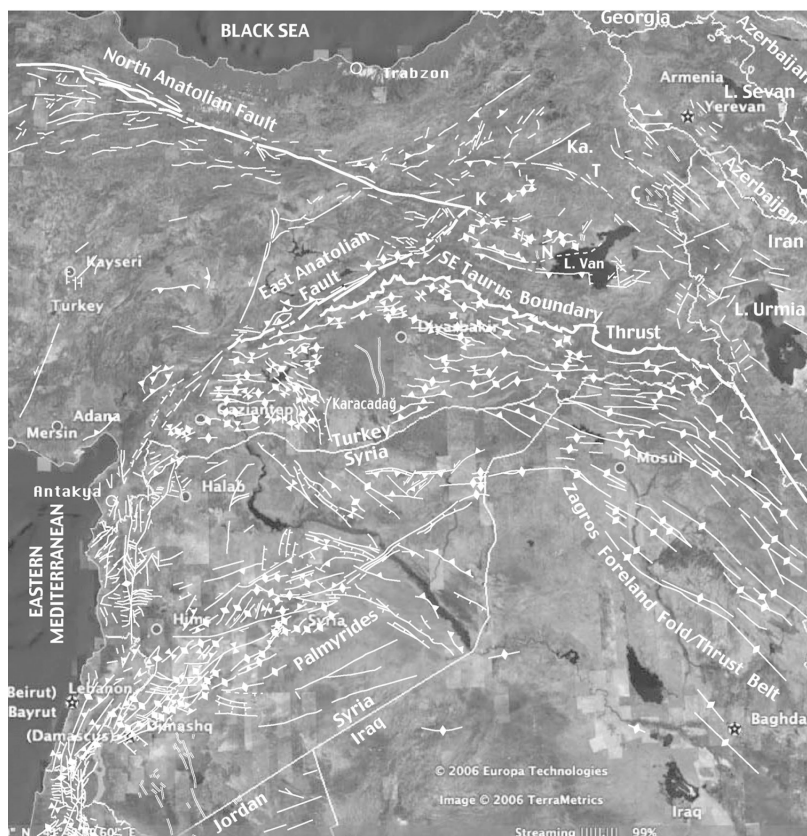


**Fig. 2.4 Neotectonic map of the Middle East showing the tectonic environment of the East Anatolian Plateau [Şengör et al., 2008].**

The plateau is divided into two high depressions surrounded by mountains. The bottom of each depression is commonly at elevations > 1,500 m. To the north, the triangular Erzurum-Kars plateau is separated from the larger and more trapezoidal Murat region in the

south by the Central Range, where elevations of the crests are consistently above 3,000 m above sea level. The city of Erzurum itself has an elevation of 1,950 m whereas the Araxes river flows in a valley that descends from 1,670 m just northeast of Erzurum to < 1,000 m in the Yerevan Plain, close to the Turkish-Armenian border [Şengör & Yılmaz, 2003].

The Murat region is entirely surrounded by higher mountains and is an endorheic area centred around Lake Van. Lake Van lies mainly in a major contractional structure, a sort of “ramp valley” [Şengör et al., 1985]. However, the rise of the topography is not due to the ramping, as it also rises where the ramp faults do not exist, especially to the east [Şengör & Yılmaz, 2003]. This is a common situation across eastern Anatolia, where the plateau seems to have attained its characteristic elevation by wholesale uplift rather than by cumulative structural relief along discrete structures.

The Lake Van region coincides with the thinnest crust in eastern Turkey at the acme of an asthenospheric dome. As seen in Fig. 2.5 such dome contains three of the five sub-active volcanic centres in eastern Turkey [Şengör et al., 2008]. With the exception of the Mt. Süphan volcano (Fig. 2.5), the Th/Ta ratios indicate that the volcanoes within the dome have been fed by an enriched asthenosphere. Güle. et al. [2002] found in the water samples from the Nemrut

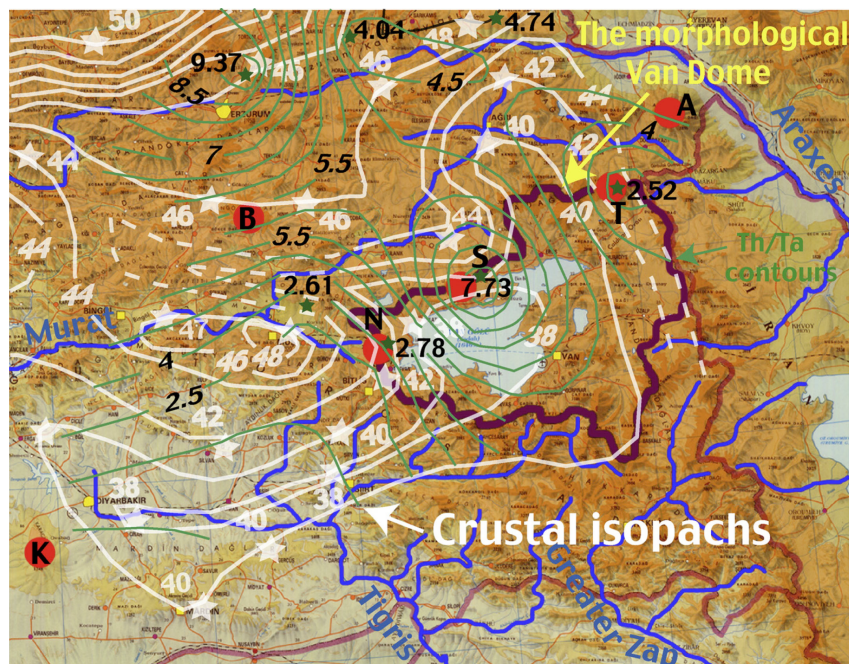


Fig. 2.5 The Lake Van Dome showing topography, drainage and crustal thickness [Şengör et al., 2008].

caldera lake and Lake Van, the highest R/RA values ( $R = \text{sample } ^3\text{He}/^4\text{He}$  and  $RA = \text{air } ^3\text{He}/^4\text{He}$ ) in Turkey (6.15 - 7.54), clearly indicating more than 75% mantle He. All of this would have been expected in an extensional region, but Lake Van lies mainly in a major shortening structure [Şengör et al., 1985, 2008], with significant strike-slip faulting along its northern and southern sides and some as yet unspecified amount of east-west extension.

The Arabia-Eurasia collision induced deformation in the Erzurum-Kars plateau and the Caucasian region. Such deformation is taken up by both strike-slip and thrust faulting [Dilek, 2006]. Lateral eastward displacements of crustal material along some major strike-slip fault systems (e.g., Pompak-Sevan fault and Van-Tebriz fault zone) have resulted in east-directed shortening, roughly perpendicular to the northwest-southeast regional strike of the fold-and-thrust belt in this region and show that the collision-induced strain is partitioned across a nearly 1,000-km-wide-zone encompassing eastern Anatolia, northern Iran, and the Caucasus [Dilek, 2006]. Large scale plate deformation in the region is dominated by plate convergence with shortening and contraction, but normal fault-controlled extensional basins such as the Kagizman-Tuzluca, Hınıs, Karlıova, and Muş basin are well documented within the plateau [Göğüş & Pysklywec, 2008]. Global Positioning System measurement slightly to the west of this region also indicate local extension, but directed N-NW [Reilinger et al., 2006].

Overall, GPS measurements indicate coherent W-ward motion vectors in the western Anatolian Plateau and NE- and E-ward vectors in its eastern portion. North-south shortening on thrust faults clearly also contributes to the motion of the points as represented by the relative velocity vectors. The velocities do not abruptly diminish but gradually decrease so that the southern parts of the Murat region move almost as fast as Arabia, whereas its northernmost part move almost slowly as the Erzurum-Kars plateau [Şengör et al., 2008].

Like the Lesser Caucasus, the East Anatolian Plateau is also characterized and shaped by three major groups of structures: (i) dextral to sinistral strike-slip faults, (ii) strike-slip basins, and (iii) N-S trending fissures and lines of Plio-Quaternary volcanoes. Again, these structures cut across and displace fold axes, reverse faults, dykes and sills of Late Miocene age and hence are younger than Late Miocene [Koçyiğit et al., 2001]. The total offset measured on drainage systems, formation boundaries, and fold axes cut and displaced by

strike-slip faults range from a minimum of 100 m to a maximum of 7 km. In more detail, two systems of strike-slip faults occur in the East Anatolian Plateau: (a) NW-SE trending dextral strike slip faults parallel to the North Anatolian Fault, (b) NE-SW trending sinistral strike-slip fault parallel to the East Anatolian Fault [Koçyiğit et al., 2001]. The two fault systems have mostly the same Pliocene age, and are generically connected with a stress field linked to the N-S directed intracontinental convergence between the Eurasian and the Arabian plates.

The geology of the East Anatolian Plateau is best described in terms of its neotectonic and paleotectonic rock packages and structures (Fig. 2.6). According to Şengör & Yılmaz [2003], the paleotectonic structures of the plateau occur in three major tectonic units described below from north to south:

- the East Rhodope-Pontide arc was an ensialic, south-facing magmatic arc of Albian to Oligocene age, as previously discussed. It formed by north-dipping subduction beneath the Eurasian continental margin [Yılmaz, 1993]. An extensive zone of backthrusting brings ophiolitic mélangé nappes of Cretaceous age onto its southern margin. These are the innermost parts of the East Anatolian Accretionary Complex [Şengör & Yılmaz, 1981];
- the East Anatolian Accretionary Complex basement consists of Late Cretaceous ophiolitic mélangé and Paleocene-to-Late Oligocene flysch sequences. The mélangé occurs in imbricate, mainly north-dipping, slices commonly incorporating younger flysch [e.g., Şengör & Yılmaz, 1981]. The flysch becomes younger from north to south and it represents progressively shallower environments from the Cretaceous to the Oligocene [Şengör & Yılmaz, 1981];
- the Bitlis-Pütürge Massif is a highly deformed metamorphic massif formed by the collision between the eastern end of the Menderes-Taurus block [Anatolide-Tauride Block of Okay & Tüysüz, 1999] and the northern margin of the Arabian Platform [Yılmaz, 1993].

In the Anatolian Plateau folding is widely distributed north and northwest of Lake Van, whereas thrusting is more confined to the Muş-Van depression, along the northern and the southern sections of the mountainous frame of the Murat region [Şengör et al., 2008]. This is

in agreement with a generic decrease in the amount of shortening from the Bitlis orogen towards the north into the foreland. There are exceptions to this general rule like, for example, in the area west of Yerevan in Armenia, where some thrusting is evident.

Except for the north-south striking Nemrut fissure [Şengör et al., 1985; Dewey et al., 1986] there are no notable north-south trending extensional features, although small-scale ones have been mapped following earthquakes [Koçyiğit, 2001; Şengör et al., 1985] and seismic reflection profiling has discovered a number of north-south trending normal faults in Lake Van [Şengör et al., 1985].

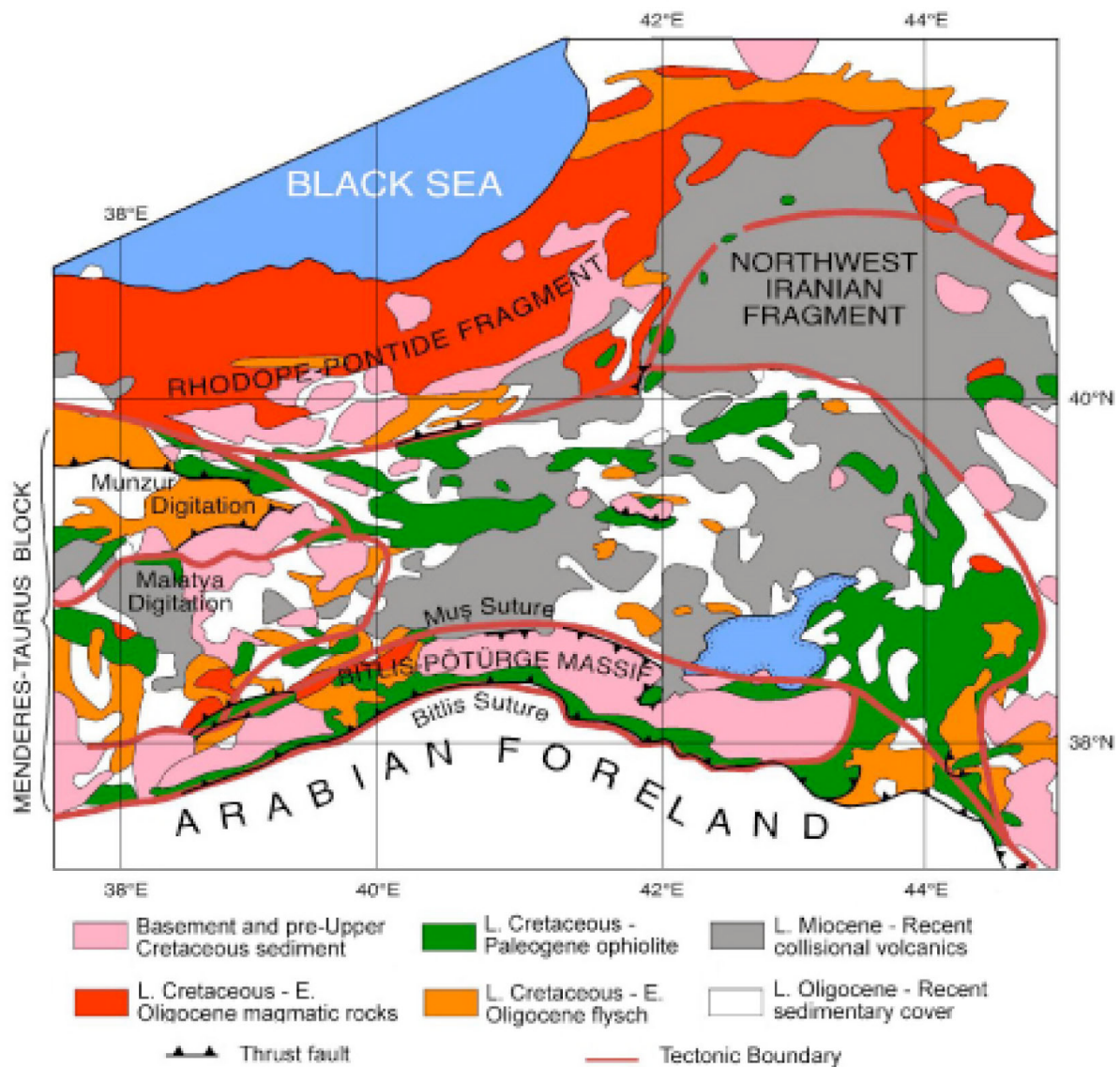


Fig. 2.6 Simplified geological map and tectonic units of the Eastern Anatolian Plateau [Şengör et al., 2003].



As previously pointed out, the eastern Anatolian Plateau is dominated by strike-slip fault that form two main sets: a sinistral northeast-southwest striking set and a dextral northwest-southeast striking set [Şengör et al., 1985; Bozkurt, 2001; Koçyiğit et al., 2001; Philip et al., 2001]. The first set is more dominant in the Erzurum-Kars plateau, whereas the latter set predominates to the south. GPS velocities corroborate the observation that in the Murat region the northwest-southwest striking right-lateral strike-slip fault set must be dominant, as the points in this region move NNW-ward with respect to Eurasia [Şengör et al., 2008]. The velocity field indicate that north-south-directed shortening on thrusts and folds continues to provide a significant contribution to overall shortening in the region [Şengör et al., 2008].

Four successions overlie the tectonic edifice of the east Anatolian Plateau. One of them is sedimentary, the remaining three are volcano-sedimentary successions separated from each other by angular unconformities [Koçyiğit et al., 2001]. The oldest succession consists of shallow-marine-to-continental conglomerate, siltstone, shale, gypsum, reefal limestone, and evaporite of Oligocene - Early Miocene age [Koçyiğit et al., 2001]. This sedimentary succession -ca. 1,500 m thick- is unconformably overlain by a 2,400 m thick succession consisting of coal-bearing fluvio-lacustrine deposits and andesitic to basaltic rocks alternation of late Miocene - early Pliocene age [Koçyiğit et al., 2001]. The transition from the shallow marine and transitional deposits of the first succession to the continental deposits of the second succession marks the acme of Arabia-Eurasia collision and the definitive closure of the Mediterranean-Indian Ocean seaway. The second succession is overlain with angular unconformity by a 2,000 m thick continental volcano-sedimentary succession dominated by Plio-Quaternary volcanics. These first three successions of East Anatolian Plateau are somewhat folded and reverse faulted, whereas the last Plio-Quaternary volcano-sedimentary succession is undeformed, confirming the transition from an earlier compressional-contractional paleotectonic regime to a strike-slip extensional neotectonic regime [Koçyiğit et al., 2001].

According to Zor et al. [2003], the crust beneath the plateau is 38-50 km thick, hence it has been suggested that the high topography is not isostatically supported by a thick crustal

root [Şengör & Yılmaz, 2003; Keskin, 2003]. Furthermore, seismic data for eastern Anatolia are interpreted as evidence for the complete absence of mantle lithosphere beneath the Plateau [Dilek, 2006; Gok et al., 2007] and are consistent with high heat flow and volcanic activity [e.g., Nemrut, Suphan, and Agri-Arat volcanoes) across eastern Anatolia.

Several interpretations have been proposed for the genesis of the East Anatolian Plateau. The evolutionary model by Şengör & Yılmaz [2003] (Fig. 2.7), explains well the geochemical characteristics and temporal-evolution of the widespread volcanics of the East Anatolian Plateau. Nevertheless, it must be pointed out that the model of Şengör & Yılmaz [2003] does not envision the presence of any continental block between the Pontide arc to the north and the Arabian platform to the south. In other words, the model implies that the Anatolide-Tauride terrane of western and central Turkey does not continue into eastern Anatolia. According to these authors, in the Early Eocene the Rhodope-Pontide arc was still active and associated with a large subduction-accretion complex. By Late Eocene time, the toe of this accretionary complex may, in some points, have touched the northern margin of the

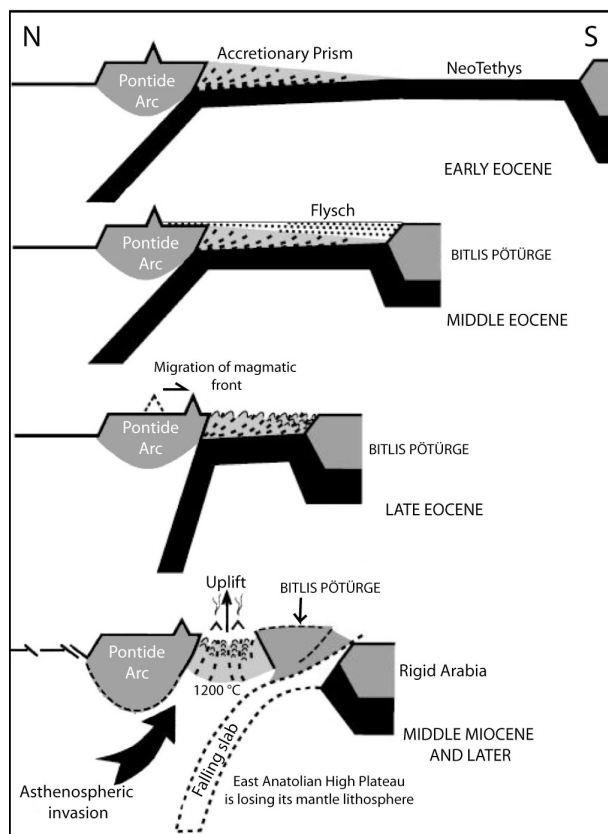


**Fig. 2.7 Schematic cross-sectional tectonic evolution of the East Anatolian Plateau from early Eocene to present days [Şengör & Yılmaz, 2003].**

Bitlis-Pötürge Massif. Throughout the Oligocene, the East Anatolian Accretionary Complex was shortened and thickened above an oceanic lithosphere sliding beneath it [Şengör & Yılmaz, 2003]. This “hidden subduction” [Şengör et al., 1984] may have created the last, Oligocene intrusions in the Rhodope-Pontide arc and extrusives to its immediate south [38.5 Ma; Keskin et al., 1998]. After the East Anatolian Accretionary Complex thickened to normal continental crustal thickness, subduction was arrested and Arabia-

Eurasia convergence began to be accommodated by intracontinental convergence and crustal shortening from the Greater Caucasus to northern Arabian Plate at the beginning of the Miocene (ca. 24 Ma ago).

Şengör & Yılmaz [2003] proposed that slab break-off commenced at 11 Ma, when the first collisional-related magmatism began about 200 km north of the present-day suture line and when the plateau surface entirely cleared out of water [Keskin et al., 1998]. By 8 Ma ago slab break-off was probably complete and post collisional volcanism became plateau wide by spreading mainly southward. The falling off of the slab exposed the underbelly of the East Anatolia Accretionary Complex to at least asthenospheric temperatures, which resulted in its widespread partial melting, [Şengör et al., 2003]. The volcanism of Eastern Turkey, exhibiting a complex composition and geochemistry ranging from andesitic-rhyolitic melts to alkali olivine basalts, probably reflects the rise of the asthenosphere, its adiabatic melting and heating of the overlying crust [Keskin, 2003]. It should be noted that according to Şengör & Yılmaz [2003] the scattered outcrops of metamorphic rocks locally cropping out in the volcanic and volcano-sedimentary series of the East Anatolian Plateau are the result of the progressive incorporation and metamorphism of older sediments in a large south-verging accretionary complex underlying much of eastern Anatolia. From this viewpoint, no Anatolide-Tauride terrane can be traced to the east of the eastern Taurus Mountains, in disagreement with much of the pre-existing literature. Keskin [2003] proposed that break-off of the northward-subducting oceanic Arabian plate in the past 7-8 my has caused domal uplift and volcanic activity in the eastern Anatolia through rising mantle. In this model is implicitly assumed a delamination-style separation of the mantle lithosphere from crust prior to its detachment. Alternatively, Ershov & Nikishin [2004], proposed a mantle plume scenario for eastern Anatolia. However, petrological and geophysical evidence, the migration of volcanism from north to south, its geochemical variation from change calc-alkaline to alkaline [Keskin, 2003], and seismic tomographic interpretations of the detached slab beneath the plateau [Lei & Zao, 2007], do not favor the plume model. Anderson [2005, 2007] suggested that topographic uplift with widespread volcanism in eastern Anatolia may be related to lithospheric delamination in the manner defined by Bird [1979]: mantle lithosphere is removed as a coherent slice by

peeling away along the crust, mantle boundary or at the upper margin of anomalously dense lower crust [Anderson, 2007]. Faccenna et al. [2006] proposed a model (Fig. 2.8) to explain the possibility that the formation of North Anatolian Fault (NAF) was accompanied by (i) uplift

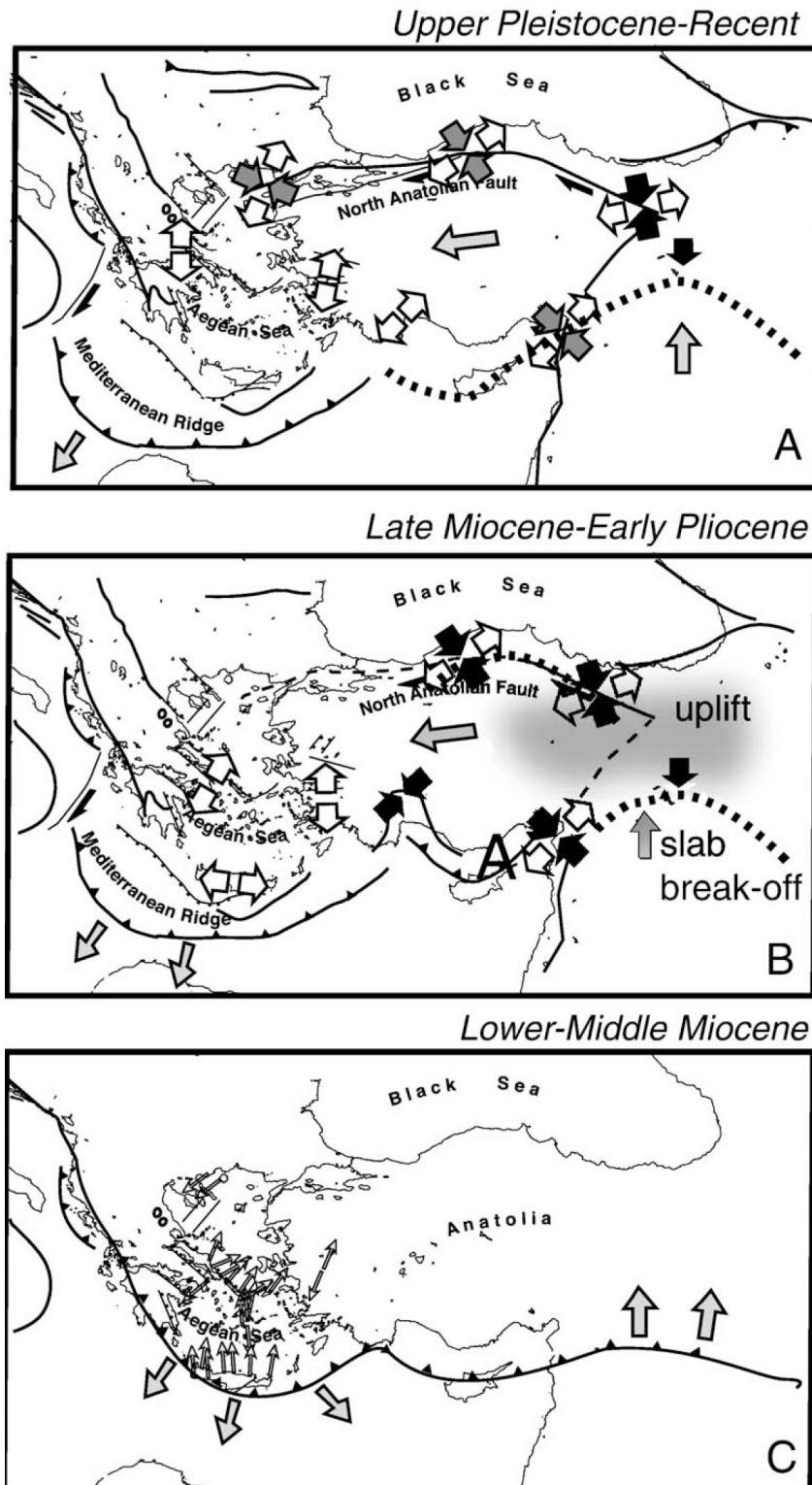


Fig. 2.8 Tectonic evolution of the Anatolia-Aegean region after to the formation of the NAF. Shadow area represents the uplifted region of the Anatolian Plateau. Dashed line indicates the broken slab [Faccenna et al., 2006].

of the Turkish-Iranian Plateau, (ii) a surge of volcanism in the eastern Anatolian collisional area, and (iii) acceleration of the Aegean trench retreat. In this model, uplift of Anatolian Plateau is interpreted as a surface manifestation of the slab rupture in the Middle-Late Miocene.

The result of recent seismic experiments across the eastern Anatolia plateau and the northernmost Arabian plate, combined with tomographic models of regional seismic velocity and attenuation, have definitively shown that most of the plateau is lacking mantle lithosphere and that it is supported by hot asthenospheric mantle [Dilek, 2006]. According to Dilek [2006], the absence of lithospheric mantle is interpreted to have resulted from break-off of northward, subducted slab beneath the east Anatolian accretionary prism. The extensive Pliocene-Quaternary volcanism in the region may be a consequence of melting of the lower crust above hot asthenosphere. Göğüş & Pysklywec [2008], using a computational geodynamic model, tested whether the geological and geophysical data are consistent with delamination of the mantle lithosphere. They proposed that all the primary tectonic anomalies for eastern Anatolian plateau uplift and heating, but also the presence of synconvergent crustal extension, may be interpreted as the coupled response of the crust to active underlying mantle dynamics during plate collision. They conducted a series of experiments with variable rates of imposed convergence of delaminated slab and with a higher yield strength of the mantle lithosphere. Fig. 2.9 shows the evolution of this model. The model shows that first the mantle lithosphere is delaminating from the crust, exposing a Moho width of 300 km ca. The detachment and/or break-off of this mantle lithosphere slab follows. In the latest stage the Eurasian mantle lithosphere undergoes a much more subducted delamination as it is eroded by the mantle flow. This geodynamic experiment demonstrates that the delamination causes surface uplift as a result of the isostatic and dynamic effects of lithospheric removal and possibly reconciles the high heat flow and volcanism that occur across eastern Anatolia.

The exact dynamics of uplift in the eastern Anatolian plateau are still debated, but it is fairly obviously that both crustal evolution and mantle dynamics played a significant role in the eastern Mediterranean region during the Late Tertiary [Dilek & Whitney, 2000]. It is commonly accepted that the plateau that the plateau was formed some time in the Middle Miocene,

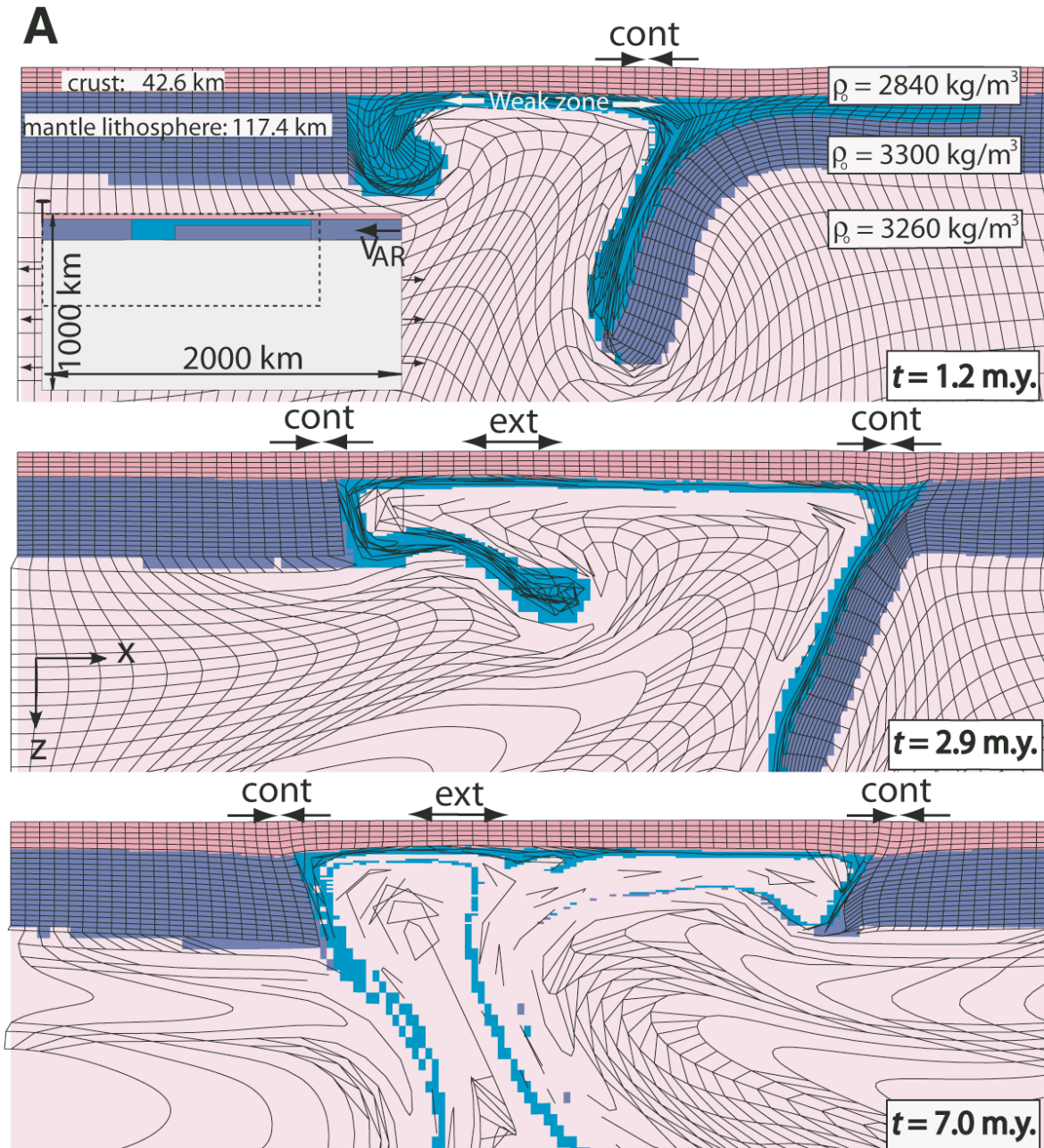


Fig. 2.9 Progressive evolution of the mantle lithosphere delamination for eastern Anatolia [Göğüş & Pysklywec, 2008].

following the terminal collision between Arabia-Eurasia and slab break-off. Subsequent removal of the lithospheric mantle (lithospheric delamination) beneath eastern Anatolia caused asthenospheric upwelling and extensive melting, leading to regional uplift and the ensuing high mean elevation of the Turkish-Iranian plateau.

A Miocene uplift for the plateau is also supported by Cosentino et al. [2012]. This work-based on nannofossil, ostracod, and planktic foraminifera biostratigraphy of the Başyayla section within the Mut and Köşelerli Formations in the central Anatolian Plateau, indicates a

Tortonian age for marine sediments unconformably capping basement rocks at ca. 2 km elevation.

The Anatolian Plateau-Caucasus-Caspian region is an area of complex structure accompanied by large variations in seismic wave velocities [Gök et al., 2009]. Such region shows considerable spatial variability in travel times and phase propagation. Regional phase variations have been documented by a number of a studies [e.g., Kadinsky-Cade et al., 1981; Rodgers et al., 1997; Gök et al., 2003] showing that Lg waves is blocked by both the Black Sea and south Caspian basins, and Sn does propagate through the cold and stable lithosphere of the south Caspian and Black Sea basins [Rodgers et al., 1997, Sandvol et al., 2001, Gök et al., 2003]. Recently Gök et al. [2009], to better constrain shear wave velocity model for the region, conducted a study based on the combination surface waves (SW) with receiver functions (RF).

The most important result of this study can be summarized as follows: the Moho map (Fig. 2.10) shows that the Moho is deepest in the Lesser Caucasus region and shallowest in the Arabian Plate. The resulting crustal thickness is at odds with several simplistic renditions. Average crustal thickness in the Anatolian Plateau is 42 km. The Lesser Caucasus in the border region between Turkey, Georgia and Armenia has the thickest crust in the region (ca. 52 km). Crustal thickness of the Arabian plate is around 35 km and the Greater Caucasus is similar to the Anatolian Plateau (ca. 42 km).

#### *2.4. The Lesser Caucasus*

The structure and geological evolution of the Caucasian segment of the Black Sea-Caspian region (Fig. 2.4) are largely determined by its position between the still converging Eurasia and Africa-Arabia lithosphere plates within a wide zone of continent-continent collision [e.g., Adamia et al., 1987]. According to some authors [Adamia et al., 1981, 2008; Zakariadze et al., 2007], the region in the Late Proterozoic, Palaeozoic, and Mesozoic until the Early Cretaceous belonged to the now-vanished branches of the Tethys Ocean and to its Eurasian and Gondwanan/Africa-Arabian margins. Within this ocean-continent convergence zone, there existed a system of island arcs, intra-arc rifts, and back-arc basins characteristic of the early

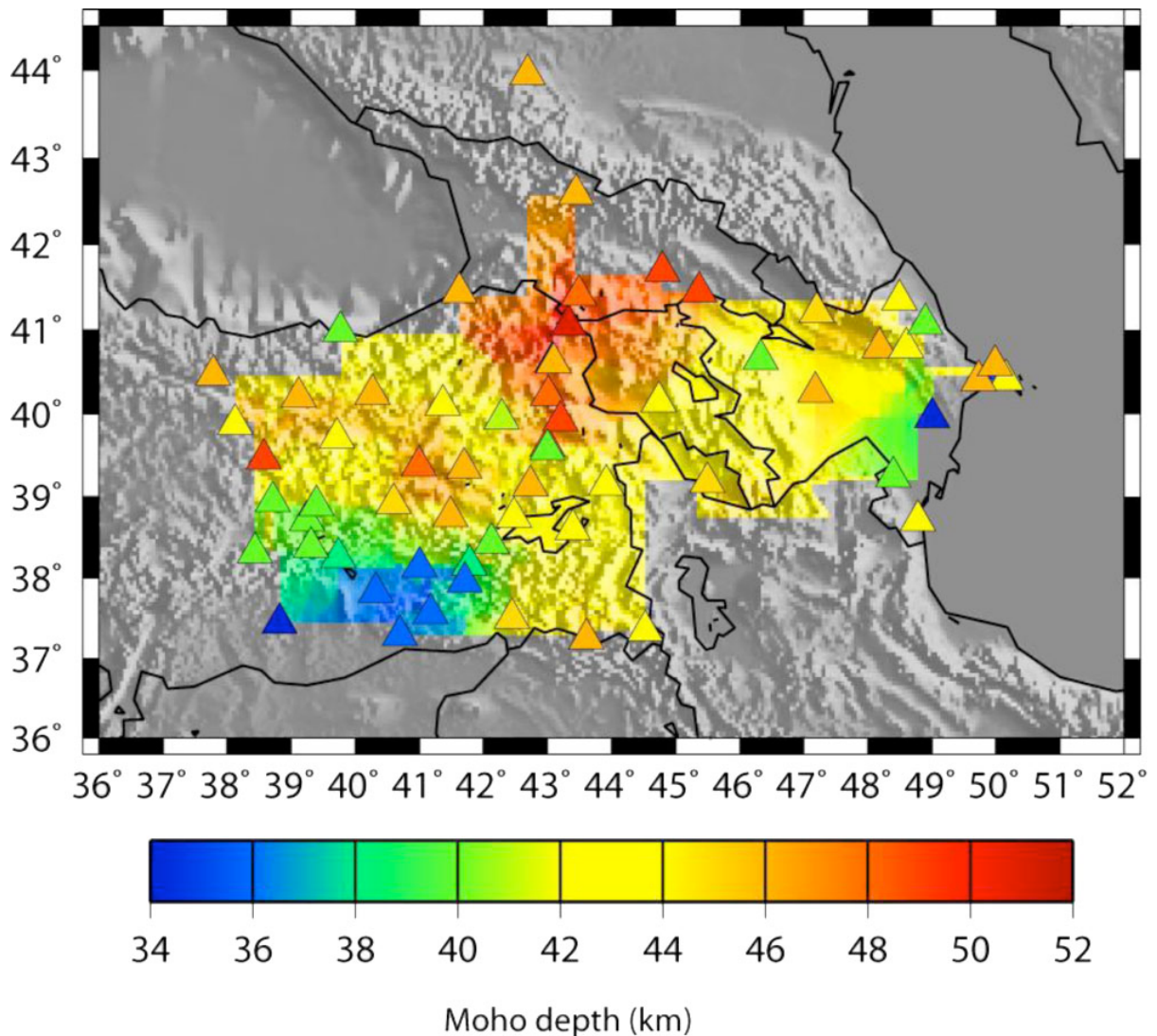


Fig. 2.10 Moho depth in Anatolian Plateau-Caucasus-Caspian region [Gök et al., 2009].

Cenozoic pre-collisional stage of evolution of the region. During the syn-collisional (Oligocene-Middle Miocene) and post collisional (Late Miocene–Quaternary) stages of the convergence between Africa-Arabia and Eurasia, back-arc basins were inverted to form fold-thrust belts in the Greater and Lesser Caucasus and, in between, the Transcaucasian intermontane depressions (Rioni and Kura basins; Fig. 2.11).

The Caucasus is located at the junction of the Turkish and Iranian segments of the Alpine-Himalayan fold-and-thrust belt. It is bordered by the Scythian Platform to the north and the southern Armenian-Nakhichevan sub-platform to the south. The Scythian Platform consists of an Hercynian basement overlain by late Hercynian molasse and calc-alkaline volcanic rocks,



in turn overlain by Mesozoic-Cenozoic epicontinental, marine, lagoonal and, continental deposits [Adamia et al., 2010, 2011]. The southern Armenian-Nakhichevan sub-platform is similar to the Taurus-south Anatolian zone, and characterized by a pre-Campanian basement complex overlain nonconformably by monotonous shelf carbonates of Palaeozoic-Triassic age.

The Caucasus is divided into several main tectonic units or terranes [Fig. 2.11]. From north to south these are (i) the Scythian (Pre-Caucasus) platform; (ii) the fold-and-thrust mountain belt of the Greater Caucasus, comprising the so-called Fore-Range, Main Range, and Southern Slope zones; (iii) the Transcaucasian intermontane depression superimposed mainly on a rigid platform zone (Georgian Massif); (iv) the Adjara-Trialeti (Georgia) and the

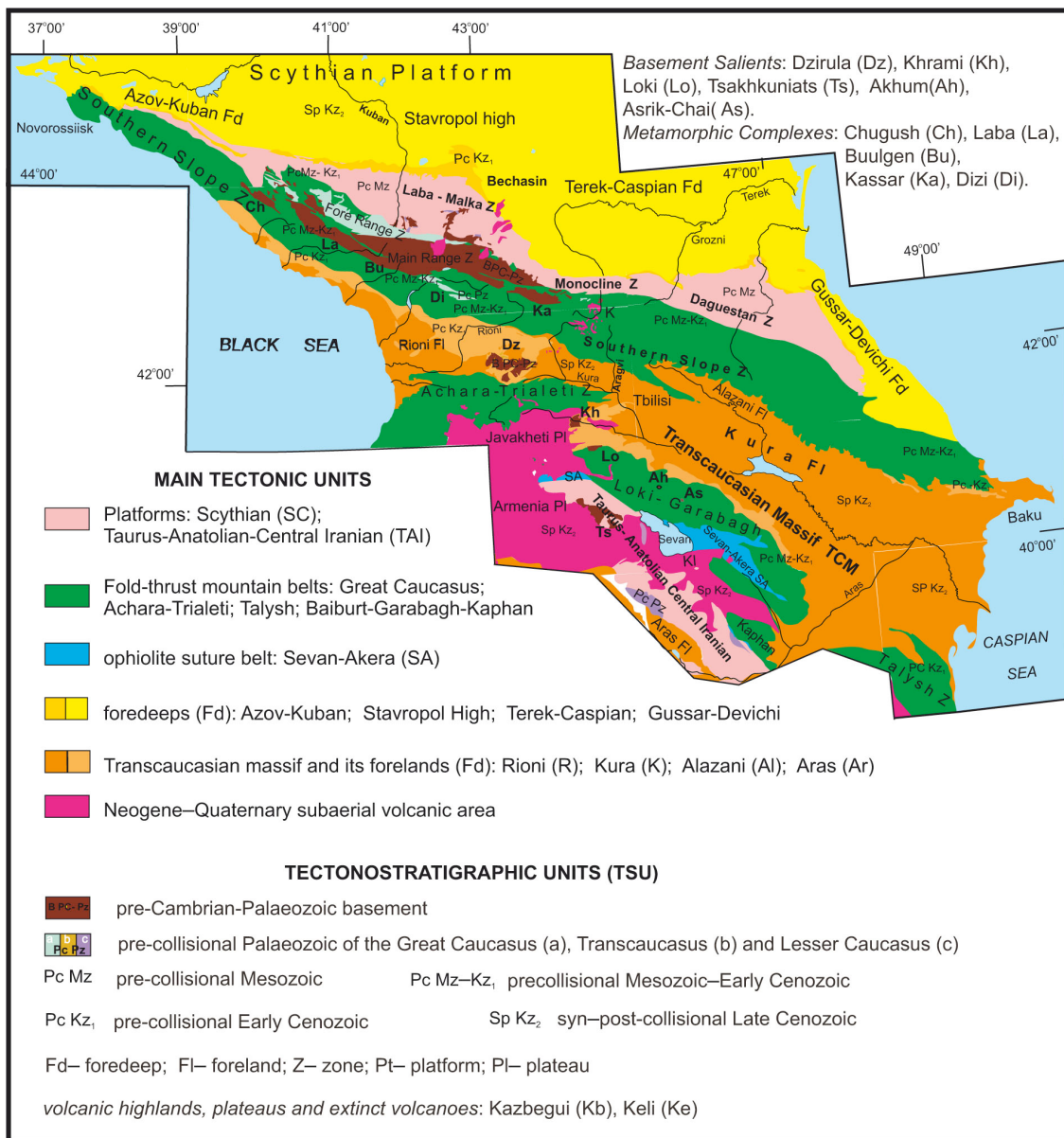


Fig. 2.11 Tectonic sketch map of the Caucasus [Adamia et al., 2010].

Talysh (Azerbaijan) fold-thrust mountains belts; (v) the Artvin-Bolnisi rigid massif; (vi) the Loki-Bayburt-Karabagh-Kaphan fold-thrust mountain belt; (vii) the Sevan-Akera ophiolitic suture; (viii) the Lesser Caucasian part of the Taurus-Anatolian-Central Iran platform; (viii) the Aras intermontane depression [Koçyiğit et al., 2001; Adamia et al., 2010, 2011]. The youngest tectonostratigraphic unit is composed of Neogene-Quaternary continental volcanic formations of the Armenian and Javakheti plateau and extinct volcanoes of the Greater Caucasus-Elbrus, Cheghem, Keli and Kazbegi. Existing data allow the division of the Caucasian region *sensu lato* into two large-scale geological provinces: southern Tethyan and northern Tethyan, respectively located to the south and to the north of the Lesser Caucasian ophiolite suture. The southern and northern provinces differ one from the other throughout the Mesozoic and Early Cenozoic. The boundary between them runs along the complex North Anatolian (İzmir-Ankara-Erzincan) – Lesser Caucasian (Sevan-Akera) – Iranian Karadagh ophiolitic suture belt.

The Lesser Caucasus, including Armenia, is an area of common ophiolite occurrences. Small ophiolite bodies include the Aparan-Arzacan Massif of late Precambrian age and Upper Jurassic-Lower Cretaceous outcrops in the Terter river basin (Rolland et al., 2009). The largest outcrops of ophiolitic rocks are invariably dated to the Jurassic.

From S to N across Armenia ophiolites are present in the following areas: (i) the Vedi ophiolite area, within the Armenian (Haikakan) Par Range, the Ararat Valley and the basins of the Azat, Vedi, Kuyusuz and Nakhichevan rivers, (ii) the Zangezur areas, within the Shirak and Bargushat ranges, (iii) the Amasia-Sevan-Akera area within the Shirak and Bargushat ranges (the basins of the Dzoraget, Akhurian and Akera rivers and Lake Sevan). The rocks cropping out in the areas listed above include a full ophiolite belt which can be considered as the easternmost part of the İzmir-Ankara-Erzincan ophiolite suture belt, interpreted by many authors as the main suture of the NeoTethys [e.g., Adamia et al. 1981, 1987, 2011].

The stratigraphy of the Lesser Caucasus is similar to the classic sections of other areas of the Mediterranean region (southern Europe, Balkan peninsula, Asia Minor and the Middle East). Rocks range in age from Precambrian to Pleistocene and volcanogenic rocks alternating with normal sedimentary deposits are widespread throughout the stratigraphic sequence [e.g., Aslanian, 1977, 1982]. Volcanogenic deposits are predominantly andesite-basalt and andesite

in composition. Along the Turkish-Georgian border area three volcano-sedimentary sequences occur (Fig. 2.12B). The oldest of these is 5.5 km thick and coal-bearing volcano-sedimentary sequence of Late Eocene - early Miocene age [Koçyiğit et al., 2001]. This sequence consists of andesitic-basaltic volcanic rocks, shallow-marine sedimentary clastic and fluvio-lacustrine magmatic rocks.

This first sequence is overlain with angular unconformity by a second volcano-sedimentary sequence consisting of various volcanic rocks alternating with fluvio-lacustrine deposits of Late Miocene-Early Pliocene age. The mid-Miocene angular unconformity described above is typical of the region and marks a rather fast episode of deformation, uplift and erosion. Such tectonic event is marked not only by the unconformity but also by clastic wedges prograding in the eastern Black Sea and by a distinctive cooling/exhumation episode documented by the thermochronologic data presented in this dissertation. The second sequence is > 500 m thick and overlain with angular unconformity by the third volcano-sedimentary sequence of Late Pliocene-Quaternary age. The first two sequences are folded and thrust-to-reverse faulted. Plutonic magmatism is also present as differentiated tholeiitic intrusions and as widespread Mesozoic Tethyan ophiolite.

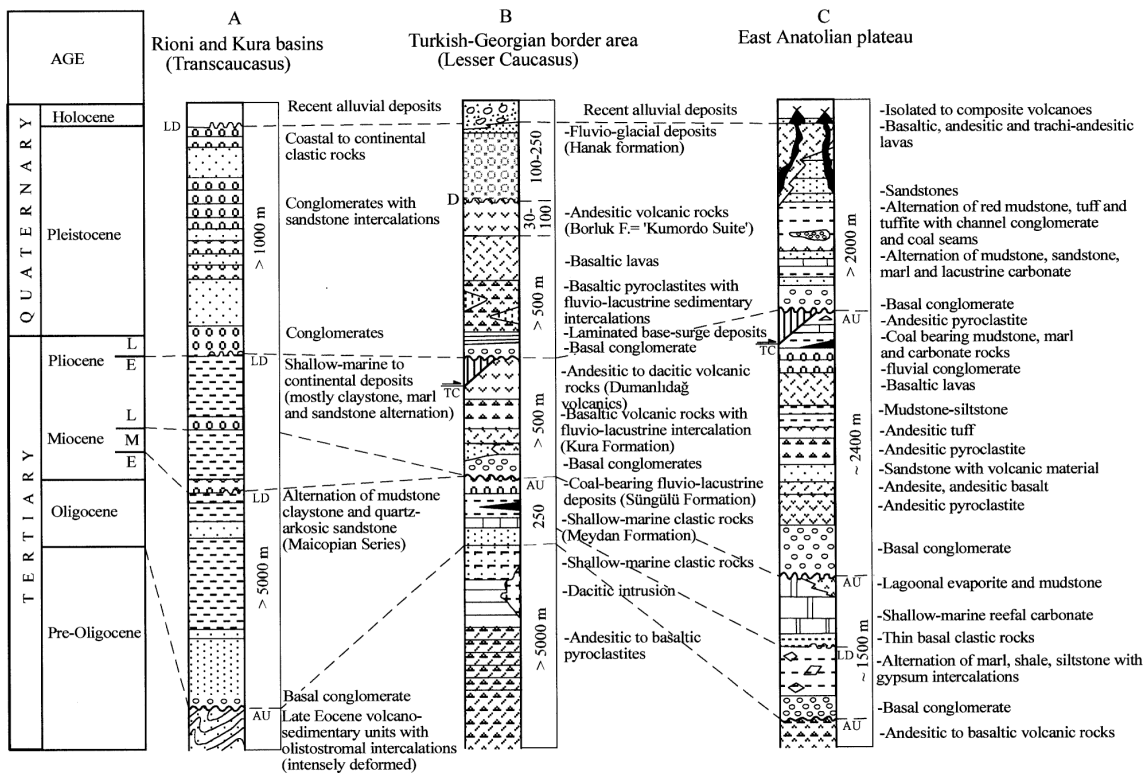


Fig. 2.12 Simplified stratigraphic columns of Oligocene-Quaternary neotectonic fill in the Rioni and Kura basins, Turkish-Georgia border area and East Anatolian basins. AU, angular unconformity; D, disconformity; E, early; L, late; LD, local disconformity; M, middle; TC, thrust-to-reverse fault contact [Koçyiğit et al., 2001].

In the Caucasian region, Precambrian rocks of Panafrican affinity form part of the structure of the metamorphic basement lying at the depth of 0 to 6,8 km to the south of the İzmir-Ankara-Erzincan-Sevan-Akera ophiolitic suture. They include gneissic granites, amphibolites, and gabbro-peridotite. North of the suture intrusive rocks are represented by Palaeozoic- Hercynian-related gabbroids, diorites, and quartz-diorites, Late Palaeozoic plagiogranites, granitoids, granodiorites, granites and quartz diorites. Late Jurassic granitoids and Late Cretaceous gabbro diorites and diorites are associated with northward subduction beneath the Eurasian continental margin. Eocene plagiogranites, gabbros, gabbros monzonite syenite and syenite diorite mark the late, to post-collisional phase related to the definitive closure of the eastern portion of the İzmir-Ankara-Erzincan-Sevan-Akera oceanic domain [Koçyiğit et al., 2001]. The plutonics listed above were of primary interest for this study as they represented primary targets for apatite fission-track analysis.

Three major elements characterize the Neogene fabric of the Lesser Caucasus: (i) NW, and NE-trending dextral to sinistral active strike-slip faults, (ii) N-S to NNW-trending fissures and/or Plio-Quaternary volcanoes, and (iii) a 5 km thick, hardly deformed Plio-Quaternary continental volcano-sedimentary succession accumulated in various strike-slip basins [Koçyiğit et al., 2001]. Starting from the southern foot of the Transcaucasus southward the nature of both the tectonic regime and geological structures vary gradationally. The N-S-directed compressional-contractual structures (folds, thrust to high-angle reverse fault, and ramp basins) are prominent to the north (Greater Caucasus and Transcaucasus), whereas the transtensional structures (both the sinistral and dextral strike-slip faults, various strike-slip basins, and N-S trending fissures become prominent to the south (the Lesser Caucasus and the East Anatolian Plateau). This is clearly an oversimplification, as significant shortening is evident in several parts of the otherwise strike-slip-dominated southern area. According to Koçyiğit et al. [2001] the strike-slip faults cut and displace dykes and other structures of Late Miocene age hence they are younger than Late Miocene. Therefore, they conclude that the time period between the Serravallian and the Late Early Pliocene is characterized by inversion in tectonic regime, basin type, and deformation pattern (from folding/thrusting to strike-slip faulting).

The collision stage in the Lesser Caucasus still needs to be thoroughly elucidated. For the Armenian sector, Sosson et al. [2010] proposed a new geodynamic evolutionary model since the Late Jurassic (Fig. 2.13). This model envisions the presence of two main subduction

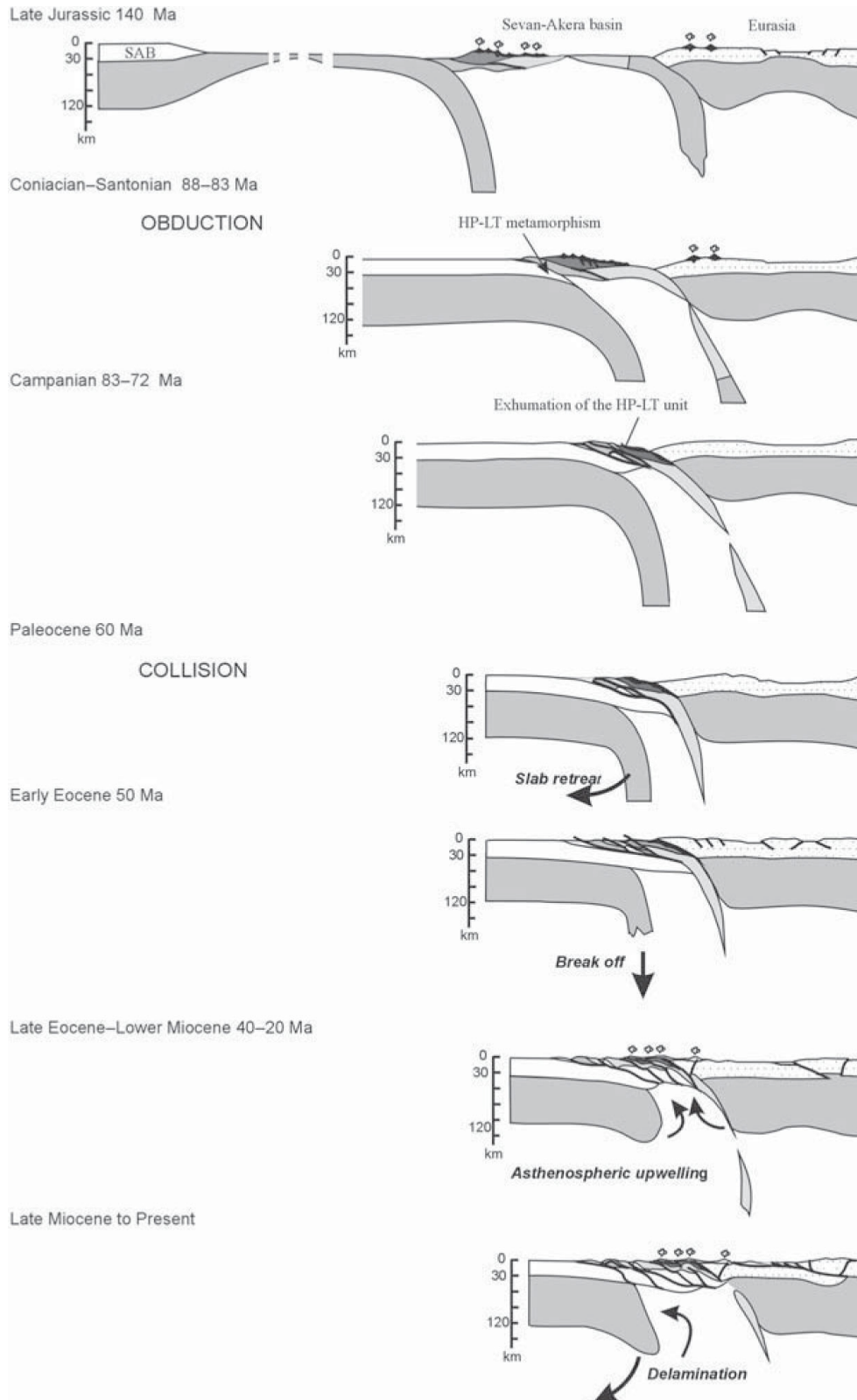


Fig. 2.13 Geodynamic model of the evolution of the Lesser Caucasus from the Late Jurassic to the present [Sosson et al., 2010].

zones and the South Armenian Block (SAB). According to this model, the onset of collision is dated as Palaeocene. This process occurred around 20 Ma later than the obduction (Late Coniacian-Santonian, 88-83 Ma) of the marginal basin over the SAB. From the Coniacian to the Palaeocene the intra-oceanic subduction (SSZ) evolved to a continental subduction of the SAB beneath the intra-oceanic arc and the marginal basin. This event is supported by HP-LT metamorphism at 94-90 Ma of oceanic formations identified within the accretionary prism in the Stepanavan area [Rolland et al., 2007; Galoyan et al., 2007]. From Palaeocene to Early Miocene time the occurrence of a foreland basin in front of the orogenic belt and the folding and erosion of the Sevan-Akera ophiolitic zone suggest the entrance of the SAB in the subduction zone beneath the Eurasia margin, pulled by the dense eclogitized oceanic slab to which it was still attached. The Early to Middle Eocene magmatism in the Sevan-Akera suture zone could correspond to the first stage of a slab retreat triggered by the continental subduction and to the slab break-off [Lordkipanidze et al., 1988]. Slab retreat and break-off lead to astenospheric upwelling below the suture zone, producing significant weakening of the SAB continental lithospheric mantle and the beginning of its delamination.

The recent geodynamics of the Caucasus and the adjacent territories is determined by its position between the still converging Eurasia and Arabia plates [Jackson & McKenzie, 1988; DeMets et al., 1990; Jackson & Ambraseys, 1997; Reilinger et al., 1997, 2006; Allen et al., 2004; Podgorosky et al., 2007; Forte et al., 2010]. According to geodetic data, the overall rate of convergence is ca. 20-30 mm/y.

Chapter Three

**METHODS**

The following section describes the methods applied during this work. Two different methods were employed: fission-track analysis of apatites (AFT) and (U-Th)/He analysis of zircons (ZHe). Both of them belong to the low-temperature thermochronology, aiming to the reconstruction of the thermal history of the samples, thus constraining the main evolutionary steps of an area. The methods hereafter described, including sampling, analysis and interpretation, follow the same routine currently adopted in most of the centers where thermochronometry is performed. Main references for this and the following are the synthetic works by Reiners [2005] and Reiners and Brandon [2006].

### *3.1. Thermochronometry: the theory*

Thermochronometry can be defined as the quantitative study of the thermal histories of rocks using temperature-sensitive radiometric dating methods, which are based on the comparison between the observed abundance of a naturally occurring radioactive isotope and its decay products. The dating is achieved through well-known decay rates equations, and the calibration on a vertical succession of strata previously recognized with basic geologic principles.

The term “thermochronometer” defines an isotopic system consisting of radioactive parent, radiogenic daughter or crystallographic feature, and the mineral in which they are found [Reiners et al., 2005]. Several isotopic systems can be evaluated, each one is characterized by a particular precision and, most importantly, a particular thermal sensitivity and closure temperature (Fig. 3.1). The thermal sensitivity of a thermochronometer describes its tendency to turn from an open to a closed system with decreasing temperatures. The closure temperature ( $T_c$ ) can be defined as the temperature of a system at the time of its thermochronometric cooling age, assuming a steady monotonic cooling history. The closure temperature concept can be seen as an oversimplification of the actual behaviour of the natural system. In fact, the closure of a thermochronometer occurs through a range of temperatures for which the retention of daughter products within the system (and hence the capability of registering thermochronometric ages) varies from 0% at the bottom (maximum temperature) to



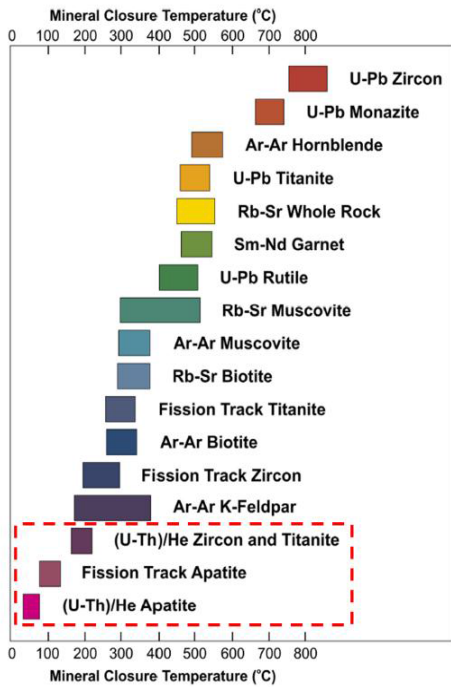


Figure 3.1. Nominal closure temperatures of various geochronometers and thermochronometers [from Gwilym, 2005]. Systems are ordered by closure temperature on the Y-axis; red-dashed rectangle indicates the low-temperature thermochronometers.

100% to the top (minimum temperature). This interval is called Partial Retention Zone (PRZ) and strictly speaking depends on a number of factors i.e., the chemical composition, morphology and internal integrity of the mineral, the hold time, the cooling rate (Fig. 3.2, 3.3). Closure temperatures and Partial Retention Zones for AFT and ZHe are discussed in their respective paragraphs. The thermochronometric age given by a particular thermochronometer represents the latest time of cooling of a sample above the  $T_c$  (or above the top of the PRZ). Conversely, when a sample is heated under the  $T_c$  (or under the base of the PRZ) the system re-opens and the previous thermochronometric age is obliterated; this process is called reset of the sample.

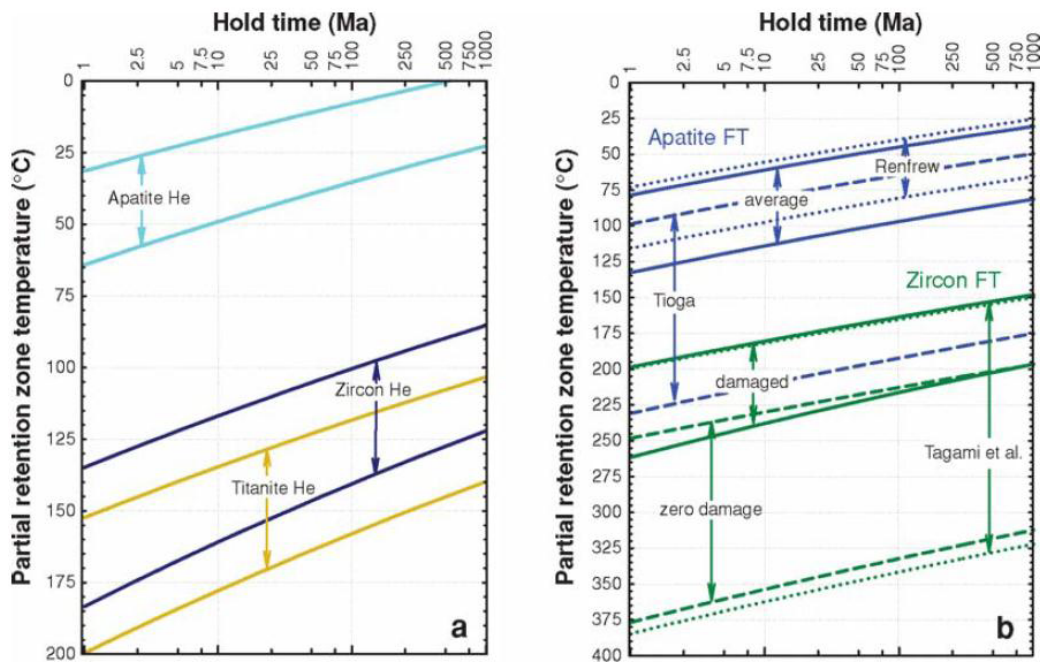


Figure 3.2. Partial Retention Zones for He and FT thermochronometers as a function of hold time [from Reiners and Brandon, 2006]. The upper and lower boundaries indicate respectively 90% and 10% retention; estimates were determined using the Closure program with parameters in Tab. 1 and 3 of Reiners and Brandon, 2006.

A vast array of thermochronometers are known nowadays; some of them are most sensitive to low temperatures (Fig. 3.1, red-dashed rectangle), typically within a range of 40°C and 200 °C (for durations of heating and cooling in excess of  $10^6$  years), and are used to investigate the thermal evolution within the upper part of the Earth's crust.

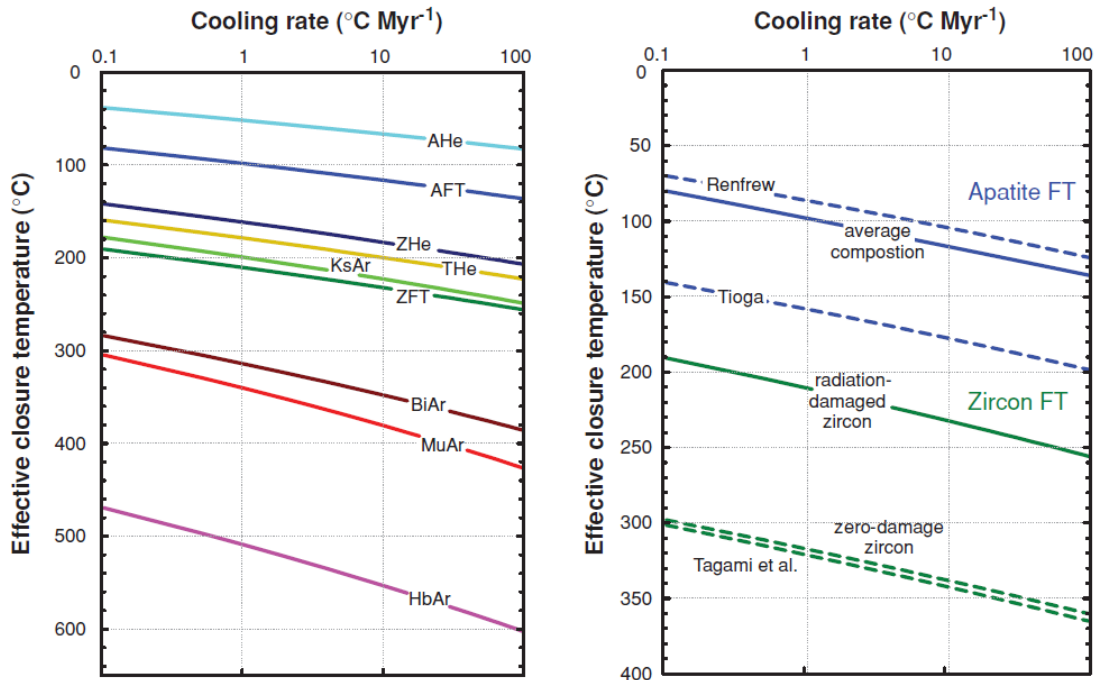


Figure 3.3. Effective closure temperature ( $T_c$ ) as a function of cooling rate for common He, FT, and Ar thermochronometers [from Reiners and Brandon, 2006].

### 3.2. Fission-track thermochronology

Fission track thermochronology is not based on the analysis of the amount of daughter product *per se*, rather it takes in account the evidence of the radioactive decay, namely the “fission tracks” (FT), damage trails produced by the spontaneous fission of U.

The spontaneous fission decay of  $^{238}\text{U}$  produces linear defects (latent fission tracks) in the lattice of U-bearing minerals [Fleischer et al., 1975], which are enlarged using a chemical etching process that enables the observation under an optical microscope.

A heavy, unstable  $^{238}\text{U}$  nucleus decays spontaneously and splits into two positively charged nuclear fragments, which are pushed away from each other by both strong coulomb

repulsion forces and the energy released by the nuclear fission and travel through the crystal affecting the electrostatic charge of the region they cross.

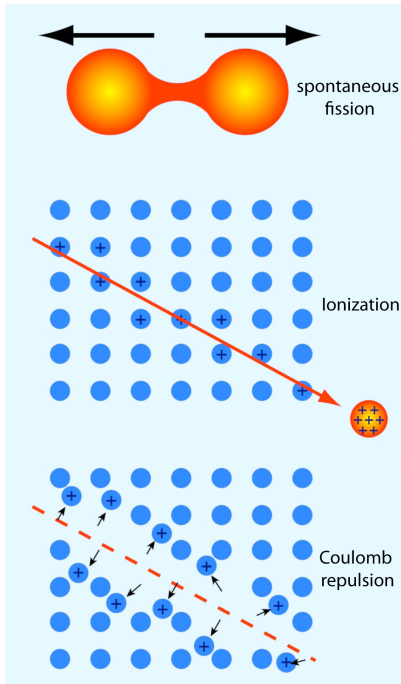


**Figure 3.4.** The “Ion Explosion Spike” model for FT formation (from Fleischer et al., 1975). The heavy nucleus splits in two nuclear fragments (a); the two positively charged fragments are pushed away from each other and along their track they tear off electrons from the atoms of the lattice (b); the positively charged atoms along the track dislocate from their lattice position due to repulsive electrostatic forces (c).

Electrons are ripped off from the atoms of the lattice and the ionized particles dislocated themselves from their original positions due to repulsive forces, then the stressed region relaxes elastically, straining the undamaged matrix (Ion Explosion Spike model for FT formation from Fleischer et al., 1975, Fig. 3.4).

The length of newly formed fission tracks is specific for the mineral involved; in apatite grains fission tracks have an initial width of approximately 10 nm and a length of ca. 16  $\mu\text{m}$  [Reiners & Brandon, 2006].

The determination of FT age depends on the same general equation as any radioactive decay scheme, modified considering that  $^{238}\text{U}$  decays not only by spontaneous fission but also by  $\alpha$ -decay [Tagami and O’Sullivan, 2005]. The technique can be applied to minerals which contain sufficient U (typically >10 ppm) to generate a statistically useful quantity of spontaneous fission tracks over geological time. In this work apatite has been the only mineral dated by FT, so the following

equations are specific to this thermochronometer.

Unlike other radioactive systems, AFT thermochronology measures the effect -rather than the product- of the radioactive decay scheme:

$$N_s = \frac{\lambda_f}{\lambda_\alpha} {}^{238}\text{N} (e^{\lambda_\alpha t} - 1)$$

where

$N_s$  = number of spontaneous fission tracks per unit volume

$\lambda_f$  = spontaneous fission decay constant ( $8.5 \cdot 10^{-17} \text{ yr}^{-1}$ )

$\lambda_\alpha$  =  $\alpha$ -decay constant ( $1.5 \cdot 10^{-10} \text{ yr}^{-1}$ )

$^{238}\text{N}$  = number of  $^{238}\text{U}$  atoms per unit volume

t = time.

The most common technique adopted in order to infer AFT single grain ages is the External Detector Method (EDM), which main stages are schematically indicated in Fig. 3.5. A detailed description of the method can be found in Gleadow, [1981], Hurford and Green [1982; 1983], Green [1985], Gleadow et al. [1986] and Hurford [1990a]. The mineral grains to be dated are mounted in epoxy resin, polished and chemically etched. By doing so, latent fission tracks are revealed and can be counted under an optical microscope, thus determining the spontaneous tracks density of single mineral grain. In order to determine the

$^{238}\text{U}$  initial concentration, a sheet of U-free mica is placed over the polished mount, then the mount-mica package is sent for neutron irradiation in a nuclear reactor. The mica records the fission tracks produced by the  $^{235}\text{U}$  decay and, when properly etched, provides the number of induced fission tracks ( $N_i$ ). The spontaneous and induced track densities are counted with an optical microscope implemented with a sliding table and a dedicated software and knowing the natural  $^{235}\text{U}/^{238}\text{U}$  ratio (a constant value of  $7.252 \times 10^{-3}$ ), the initial  $^{238}\text{U}$  content can be determined.

$$t_i = \frac{1}{\lambda_D} \ln \left( 1 + \lambda_D \zeta g \rho_d \frac{\rho_{s,i}}{\rho_{i,i}} \right)$$

where

$t_i$  = fission track age of the grain  $i$

$\lambda_D$  = total decay constant of  $^{238}\text{U}$

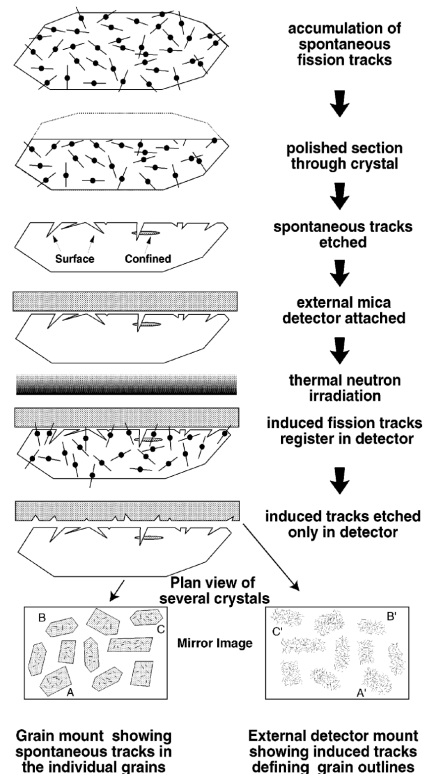


**Figure 3.5. schematic procedure for FT analysis with the EDM method (from Tagami and O'Sullivan, 2005).**

$\zeta$  = calibration factor different for each person [Hurford and Green, 1982; 1983]

$g$  = geometry factor for spontaneous fission track registration

$\rho_d$  = induced fission track density for a uranium standard corresponding to the sample position during neutron irradiation

$\rho_{s,i}$  = spontaneous track density for grain  $i$

$\rho_{i,i}$  = induced track density for grain  $i$

There is no accepted physical model of fission track annealing processes at the atomic level, since the process of fission track annealing is much more complicated than the diffusion of a single atomic species out of a mineral lattice, and still poorly known (Braun et al., 2006). Fission tracks annealing models have thus been developed using a completely empirical approach, looking at what form of the annealing relationship best fit the data statistically (Braun et al., 2006). Fission tracks are characterised by a semi-stable nature: all newly formed tracks in apatite have a length of approximately 16  $\mu\text{m}$  but they significantly shorten when heated within a particular interval of temperatures called Partial Annealing Zone (PAZ). FT annealing behaviour is independent on grain size, but it is demonstrated to vary with apatite chemistry, with retention increasing with increasing  $\text{Cl}/(\text{F}+\text{Cl})$  ratio [Green et al., 1985], although other cations and anions substitutions also play a role [Carlson et al., 1999; Donelick et al., 1999; Ketcham et al., 1999]. Moreover, the annealing behaviour also depends on the crystallographic orientation of the tracks, with higher annealing rate for tracks orthogonal than tracks parallel to the  $c$ -axis of the crystal [Green et al., 1986; Donelick et al., 1999; Ketcham et al., 2007]. The  $D_{\text{par}}$ , i.e. the mean width of fission tracks etch pits, is a commonly used proxy for track retentivity of single crystals, first proposed by Ketcham et al. [1999]. The effects of annealing can be quantified by measuring the lengths of horizontal confined tracks [Gleadow et al., 1986]. This depends on the fact that tracks form continuously, and thus each track experiences a different portion of the integrated thermal history [Braun et al., 2006]. Therefore, the track lengths distribution obtained by measuring a sufficient number of horizontal confined tracks (usually at least 50) contains information on the thermal history experienced by the sample [Braun et al., 2006; Fig 3.6].

The AFT PAZ values are usually comprised between 60 and 120°C, but can be significantly different depending on cooling rate and apatite chemistry (Fig. 3.2, 3.3); AFT closure temperatures generally vary between ca 80 and 120°C but are largely affected by apatite composition; an apatite of “average” composition [Ketcham et al., 1999] has  $T_c=116^\circ\text{C}$  for cooling rates of  $10^\circ\text{C}/\text{Ma}$ .

### 3.3. AFT data analysis

AFT thermochronometric age is achieved measuring the number of spontaneous and induced tracks, the relative areas and the mean  $D_{\text{par}}$  for usually 20-30 apatite grains from the same rock sample. Measured data were put into a specific software, the Trackkey software [Dunkl, 2000] which calculates the central age, tests the homogeneity of age populations and

generates radial plots for every analysed sample. The Y axis of a radial plot represents the standard error  $((a_g - a_c) / \sigma)$  of the single grain age ( $a_g$ ) with respect to the central age of the whole population ( $a_c$ ) and the X axis represents the relative error  $(1/\sigma)$  decreasing toward the radial scale. Single grain ages are read on the intercept with the radial axis (plotted on a logarithmic scale) of the line drawn through the single grain point and the origin. The  $\chi^2$  statistical test [Galbraith, 1981] is used to define the probability that all the grains counted belong to a single population of ages. A probability ( $P\chi^2$ ) of less than 5% is evidence of an asymmetric spread of single grain ages, and thus it indicates the presence of several age populations either due to inheritance of detrital grains from mixed detrital source areas, or differential annealing in grains of different compositions [Green et al., 1989]. If a sample passes the  $\chi^2$  test ( $P\chi^2 > 5\%$ ) the central age, which is essentially a weighted mean of the grain ages, reliably describes the AFT age of the sample.

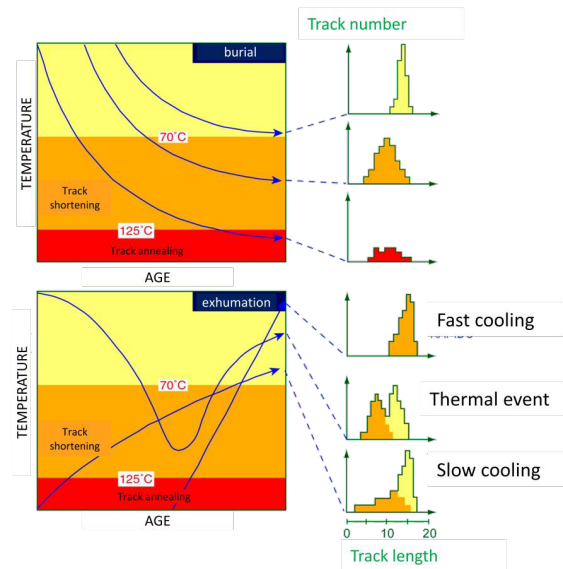


**Figure 3.6.** relationship between track length distribution and thermal history [Andreucci, 2013].

When possible, confined fission track are also measured for thermal modeling. A large number of confined FT (preferably > 50) is necessary to have enough statistical confidence, thus hindering this procedure for most of the samples. In suitable samples confined FT lengths are measured along with their orientation with respect to C-axis and mean  $D_{par}$ . More information about this process will be provided in the Thermal Modelling paragraph.

### 3.4. (U-Th)/He thermochronology

(U-Th)/He dating is based on the detection by mass spectrometry of both the parent ( $^{234}\text{U}$ ) and daughter ( $^{230}\text{Th}$ ) products of decay, through the emission of an alpha particle, as part of the much longer decay series beginning in  $^{238}\text{U}$  and ending in  $^{206}\text{Pb}$  [Reiners et al. 2005 and Lisker et al., 2013].

ZHe thermochronology relies on the accumulation of  $^4\text{He}$  during the  $\alpha$ -disintegration of  $^{238}\text{U}$ ,  $^{235}\text{U}$ ,  $^{232}\text{Th}$ , their daughter products and  $^{147}\text{Sm}$ . The  $T_c$  of mineral grains is dependent on activation energy, a geometry factor for the crystal shape, the thermal diffusivity ( $D_0$ ), the length of the average diffusion pathway from the interior to the surface of the grain and the cooling rate at  $T_c$ .

The He ingrowth equation assumes absence of  $^4\text{He}$ , both initial and produced by sources extraneous to the crystal, and secular equilibrium among all daughter products in the decay chain. Considering the normally high content of U and Th in zircons, these assumptions can be considered valid in most cases. A careful selection of the crystal is however required, in order to avoid grains affected by pervasive inclusions or broad coating.

The equation for He ingrowth in time (t) is:

$${}^4\text{He} = 8^{238}\text{U}(e^{\lambda_{238}t} - 1) + 7^{235}\text{U}(e^{\lambda_{235}t} - 1) + {}^{232}\text{UTh}(e^{\lambda_{232}t} - 1) + {}^{147}\text{Sm}(e^{\lambda_{147}t} - 1)$$

where He, U, Th and Sm refer to present-day amounts, and  $\lambda$  is the decay constant ( $\lambda_{238} = 1.551 \times 10^{-10}\text{yr}^{-1}$ ;  $\lambda_{235} = 9.849 \times 10^{-10}\text{yr}^{-1}$ ;  $\lambda_{232} = 4.948 \times 10^{-11}\text{yr}^{-1}$ ;  $\lambda_{147} = 0.654 \times 10^{-11}\text{yr}^{-1}$ ). This equation can be simplified, assuming that the ratio of  $^{238}\text{U}$  to  $^{235}\text{U}$  has in the solar

system a constant value of 137.88 in all rocks. However, new studies do not agree on this value, stating that many naturally occurring uranium-rich minerals, such as zircon, actually have a lower  $^{238}\text{U}/^{235}\text{U}$  ratio, with an average of  $137.818 \pm 0.045$  (the uncertainty assigned to this value relates to the variation observed between different samples). Agreement between these results, other rocks, and meteorites indicate that the new average  $^{238}\text{U}/^{235}\text{U}$  value and uncertainty may also be representative of the Earth's "bulk" uranium isotopic composition [British Geological Survey, 2012].

$${}^4\text{He} = 8^{238}\text{U}(e^{\lambda_{238}t} - 1) + 7\left(\frac{{}^{238}\text{U}}{137.88}\right)(e^{\lambda_{235}t} - 1) + {}^{232}\text{UTh}(e^{\lambda_{232}t} - 1) + {}^{147}\text{Sm}(e^{\lambda_{147}t} - 1)$$

The cooling age equation cannot however be directly solved, since the daughter  ${}^4\text{He}$  has different potential parent isotopes which can not be differentiated on the base of their role in the production of the  ${}^4\text{He}$ . On this purpose, the value of  $t_1$  is approximated using a Taylor series approximation, which can be simplified as:

$$t_1 \approx \frac{{}^4\text{He} - f(t_0) + t_0 f'(t_0)}{f'(t_0)}$$

The value of  $t_1$  is expressed as the "raw date" and represents the uncorrected cooling age of the sample, an underestimation of the true cooling age because of  $\alpha$ -particle ejection, which is discussed later.

PRZ for ZHe varies between ca. 90°C (for hold time higher than 250 My) and 185°C (for minimum hold time, Fig. 3.2), and  $T_c$  ranges between ca. 140°C and 200°C (Fig. 3.3) depending on the cooling rate [Reiners and Brandon, 2006].

### 3.5. $\alpha$ -ejection correction

As previously stated, the value of  $t_1$  expresses the "raw date", an underestimation of the true age of the sample. In fact, it is possible that some He is lost by ejection of  $\alpha$  particles outside the crystal domain, namely the " $\alpha$ -particle ejection".



When a parent isotope goes through  $\alpha$ -decay, the  $\alpha$  particles emitted travels a certain distance from the site of decay owing to the kinetic energy of the reaction. In zircons (and apatites) this distance is ca. 20  $\mu\text{m}$ . Should the decay occur within this span from the crystal edge, there is a statistical certainty that some daughter product will be ejected from the crystal lattice, injected in the surrounding phases and lost to the environment (Fig. 3.7). The loss of  $\alpha$  particles leads to an underestimation of the age of the crystal, which needs to be revised. Since the magnitude of  $\alpha$ -ejection is controlled by surface to volume ratio, spatial distribution of the parent atoms and medium specific diffusion values, the correction is mainly based on geometric parameters. Therefore, to account for  $\alpha$ -ejection it is a common practice to measure the physical dimensions of the crystal to be dated and to calculate a homogeneous  $\alpha$ -ejection correction factor (HAC), to which the raw date has to be multiplied, to obtain the age corrected for ejection (Farley, 2002).

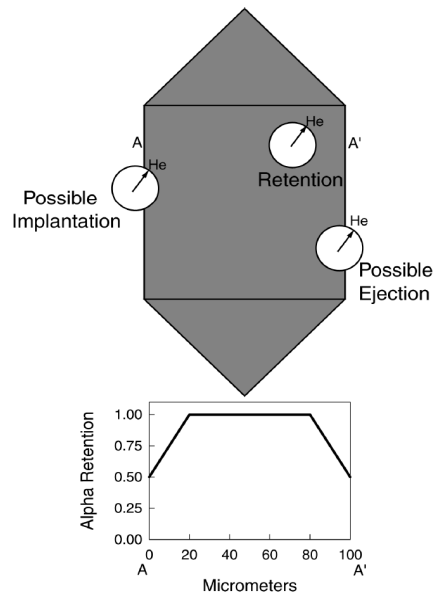


**Fig. 3.7. The effects of long  $\alpha$ -stopping distances on He retention [from Farley, 2002]. The upper figure illustrates the three possibilities within a schematic crystal:  $\alpha$  retention, possible  $\alpha$  ejection, and possible  $\alpha$  implantation. The centre of the circle denotes the site of the parent U or Th nuclide, and the edge of the white circle labelled He indicates the locus of points where the  $\alpha$  particle may come to rest; the arrow indicates one possible trajectory. The lower plot shows schematically how  $\alpha$  retention changes from rim to core to rim along the path A-A'; exact equations defining the shape of this curve as a function of grain size were given by Farley et al. [1996]**

### 3.6. (U-Th)/He data analysis

Usually, three to five grains from the same sample (replicates) are analysed. The comparison between single grain ages of the replicates gives information about the thermal history of the sample. Age reproducibility is firstly checked: if the age dispersion is low and the single grain ages cluster tightly, then the weighted mean of ages can be used for interpretation and the Tc concept can generally be applied [Fitzgerald et al., 2006], whereas high age dispersion is

usually related to a somehow complex thermal history i.e. slow cooling and a long permanence within the PRZ. The magnitude of the effect on age of subtle factors controlling He diffusion (like zonation, crystal size, kinetic parameters) increases with decreasing cooling rates [Ehlers & Farley, 2003] and these parameters tends to correlate with age.

The correlation between grain age and crystal size (radius) is particularly evident in case of slow cooling, since crystal size affects both  $\alpha$ -ejection and He diffusion kinetics; in this case age dispersion adds further information on the evolution of the samples and can be used to model the thermal history.

The correlation between grain age and eU indicates that the zircons where affected by radiation damages; also in this case dispersion do not preclude to use dates for reconstructing thermal histories, provided the RDAAM model of Flowes et al. [2009].

In this study, all the analysed samples display a high age reproducibility.

### 3.7. T-t modelling

In this dissertation, inverse modelling of track-length data was performed using the HeFTy program [Ehlers et al., 2005], in order to achieve realistic thermal modellings for the analysed samples. The software allows to integrate AFT and ZHe data, as well as other constrains inferred from stratigraphic relationships between strata and/or pre-existing radiometric ages. Time-temperature paths (T-t paths) are generated using a constrained Monte Carlo algorithm that allows the user to specify time-temperature regions through which each path is forced to pass. In general, all time-temperature histories should begin at a sufficiently high temperature to ensure that there is total annealing as an initial condition. Thus, the earliest T-t constraint should have a minimum temperature above the total annealing temperature of the most resistant apatite being modelled. An exception to this principle might be the modelling of rapidly cooled volcanic rocks where it is known a priori that the initial condition is represented by zero tracks present at some temperature below the total annealing temperature. The input parameters for AFT are single grain ages and confined fission track length, orientation and mean  $D_{par}$ . Modelling was based on the fission-track annealing model of Ketcham et al. [2007],

and the diffusion kinetics of and zircon after Reiners et al. [2004]. For zircons, a homogeneous distribution of U and Th was assumed. The gauge of the match between the modelled thermal history and the experimental data is given by the goodness-of-fit parameter (GOF), which indicates the probability of failing the null hypothesis that the model and data are different. In general, a value of 0.05 or higher is considered not to fail the null hypothesis, and thus reflects an acceptable fit between model and data [Ketcham, 2009]. GOF values higher than 0.5 are considered good and the closer the GOF gets to 1, the more the modelled T–t paths fits the data.



## REFERENCES – PART ONE

- Adamia, S. A., Chkhotua, T., Kekelia, M., Lordkipanidze, M., Shavishvili, I., & Zakariadze, G. (1981). Tectonics of the Caucasus and adjoining regions: implications for the evolution of the Tethys ocean. *Journal of Structural Geology*, 3(4), 437-447.
- Adamia, S. A., Belov, A., Kekelia, M., & Shavishvili, I. (1987). Paleozoic tectonic development of the Caucasus and Turkey (Geotraverse C). Pre-Variscan and Variscan Events in the Alpine–Mediterranean Mountain Belts, 22-50.
- Adamia, S., Mumladze, T., Sadradze, N., Tsereteli, E., Tsereteli, N., & Varazanashvili, O. (2008). Late Cenozoic tectonics and geodynamics of Georgia (SW Caucasus). *Georgian International Journal of Sciences and Technology*, 1, 77-107.
- Adamia, S., Chabukiani, A., Chkhotua, T. G., Sadradze, N., Zakaraia, D., & Zakariadze, G. (2010). Geology of the Caucasus and adjacent areas: 1: 2 500 000 scale geological map. *Επιστημονική Επετηρίδα του Τμήματος Γεωλογίας (ΑΠΘ)*, 99, 1-10.
- Adamia, S., Zakariadze, G., Chkhotua, T., Sadradze, N., Tsereteli, N., Chabukiani, A., & Gventsadze, A. (2011). Geology of the Caucasus: a review. *Turkish Journal of Earth Sciences*, 20(5), 489-544.
- Agard, P., Omrani, J., Jolivet, L., & Mouthereau, F. (2005). Convergence history across Zagros (Iran): constraints from collisional and earlier deformation. *International journal of earth sciences*, 94(3), 401-419.
- Akıncı, Ö. T. (1984). The Eastern Pontide volcano-sedimentary belt and associated massive sulphide deposits. *Geological Society, London, Special Publications*, 17(1), 415-428.
- Alavi, M. (1994). Tectonics of the Zagros orogenic belt of Iran: new data and interpretations. *Tectonophysics*, 229(3), 211-238.
- Allen, M., Jackson, J., & Walker, R. (2004). Late Cenozoic reorganization of the Arabia-Eurasia collision and the comparison of short-term and long-term deformation rates. *Tectonics*, 23(2).
- Allen, M. B., & Armstrong, H. A. (2008). Arabia–Eurasia collision and the forcing of mid-Cenozoic global cooling. *Palaeogeography, Palaeoclimatology, Palaeoecology*, 265(1), 52-58.
- Anderson, D. L. (2005). Large igneous provinces, delamination, and fertile mantle. *Elements*, 1(5), 271-275.
- Anderson, D. L. (2007). The eclogite engine: Chemical geodynamics as a Galileo thermometer. *Geological Society of America Special Papers*, 430, 47-64.
- Andreucci, B. (2013). Thermochronology of the Polish and Ukrainian Carpathians. Unpublished dissertation thesis, Alma Mater Studiorum Università di Bologna. DOI 10.6092/unibo/amsdottorato/5505.

- Aslanyan, A. T., & Satian, M. A. (1977). On the geological features of Transcaucasian ophiolitic zones. *Izvestia Acad. Sci. Armenian SSR, Nauki o Zemle*, 4(5), 13-26.
- Aslanyan, A. T., & Satian, M. A. (1982). Middle Cretaceous ophiolite zones of Transcaucasus and tectonic reconstructions. *Ofioliti*, 7(2-3), 131.
- Barka, A., Akyüz, S., Altunel, E., Sunal, G., Çakır, Z., Dikbaş, A., ... & Dawson, T. (1999). The August 17, 1999 İzmit earthquake, M= 7.4, eastern Marmara region, Turkey: study of surface rupture and slip distribution. *The 1999 İzmit and Duzce Earthquakes: Preliminary Results*, 15-30.
- Barka, A., Akyüz, H. S., Altunel, E., Sunal, G., Cakir, Z., Dikbas, A., ... & Rockwell, T. (2002). The surface rupture and slip distribution of the 17 August 1999 İzmit earthquake (M 7.4), North Anatolian fault. *Bulletin of the Seismological Society of America*, 92(1), 43-60.
- Bird, P. (1979). Continental delamination and the Colorado Plateau. *Journal of Geophysical Research: Solid Earth*, 84(B13), 7561-7571.
- Bozkurt, E. (2001). Neotectonics of Turkey—a synthesis. *Geodinamica acta*, 14(1-3), 3-30.
- Brun, J. P., & Nalpas, T. (1996). Graben inversion in nature and experiments. *Tectonics*, 15(3), 677-687.
- Braun, J., Van Der Beek, P., & Batt, G. (2006). *Quantitative thermochronology: numerical methods for the interpretation of thermochronological data*. Cambridge University Press.
- Carlson, W. D., Donelick, R. A., & Ketcham, R. A. (1999). Variability of apatite fission-track annealing kinetics: I. Experimental results. *American mineralogist*, 84(9), 1213-1223.
- Cavazza, W., Okay, A. I., & Zattin, M. (2009). Rapid early-middle Miocene exhumation of the Kazdağ Massif (western Anatolia). *International Journal of Earth Sciences*, 98(8), 1935-1947.
- Cavazza, W., Federici, I., Okay, A. I., & Zattin, M. (2012). Apatite fission-track thermochronology of the Western Pontides (NW Turkey). *Geological Magazine*, 149(1), 133-140.
- Chen, F., Siebel, W., Satir, M., Terzioğlu, M., & Saka, K. (2002). Geochronology of the Karadere basement (NW Turkey) and implications for the geological evolution of the Istanbul zone. *International Journal of Earth Sciences*, 91(3), 469-481.
- Cloetingh, S. A. P. L., Wortel, M. J. R., & Vlaar, N. J. (1982). State of Stress at Passive Margins and Initiation of Subduction Zones: Tectonic Processes: Model Investigations of Margin Environmental and Tectonic Processes.

- Cloetingh, S., Wortel, R., & Vlaar, N. J. (1989). On the initiation of subduction zones. *Pure and Applied Geophysics PAGEOPH*, 129(1-2), 7-25.
- Cloetingh, S. A. P. L., Ziegler, P. A., Beekman, F., Andriessen, P. A. M., Matenco, L., Bada, G., ... & Sokoutis, D. (2005). Lithospheric memory, state of stress and rheology: neotectonic controls on Europe's intraplate continental topography. *Quaternary Science Reviews*, 24(3), 241-304.
- Copley, A., & Jackson, J. (2006). Active tectonics of the Turkish-Iranian plateau. *Tectonics*, 25(6).
- Cosentino, D., Schildgen, T. F., Cipollari, P., Faranda, C., Gliozzi, E., Hudáčková, N., ... & Strecker, M. R. (2012). Late Miocene surface uplift of the southern margin of the Central Anatolian Plateau, Central Taurides, Turkey. *Geological Society of America Bulletin*, 124(1-2), 133-145.
- DeMets, C., Gordon, R. G., Argus, D. F., & Stein, S. (1990). Current plate motions. *Geophysical Journal International*, 101(2), 425-478.
- Dewey, J. F., Hempton, M. R., Kidd, W. S. F., Saroglu, F. A. M. C., & Şengör, A. M. C. (1986). Shortening of continental lithosphere: the neotectonics of Eastern Anatolia—a young collision zone. *Geological Society, London, Special Publications*, 19(1), 1-36.
- Dilek, Y. (2006). Collision tectonics of the Mediterranean region: causes and consequences. *Geological Society of America Special Papers*, 409, 1-13.
- Dilek, Y., & Whitney, D. L. (2000, September). Cenozoic crustal evolution in central Anatolia: Extension, magmatism and landscape development. In *Proceedings of the Third International Conference on the Geology of the Eastern Mediterranean*. Geological Survey Department, Nicosia (pp. 183-192).
- Donelick, R. A., Ketcham, R. A., & Carlson, W. D. (1999). Variability of apatite fission-track annealing kinetics: II. Crystallographic orientation effects. *American Mineralogist*, 84(9), 1224-1234.
- Dunkl, I. (2002). TRACKKEY: a Windows program for calculation and graphical presentation of fission track data. *Computers & Geosciences*, 28(1), 3-12.
- Ehlers, T. A. (2005). Crustal thermal processes and the interpretation of thermochronometer data. *Reviews in Mineralogy and Geochemistry*, 58(1), 315-350.
- Ehlers, T. A., & Farley, K. A. (2003). Apatite (U–Th)/He thermochronometry: methods and applications to problems in tectonic and surface processes. *Earth and Planetary Science Letters*, 206(1), 1-14.
- Faccenda, M., Gerya, T. V., & Chakraborty, S. (2008). Styles of post-subduction collisional orogeny: influence of convergence velocity, crustal rheology and radiogenic heat production. *Lithos*, 103(1-2), 257-287.

- Faccenda, M., Minelli, G., & Gerya, T. V. (2009). Coupled and decoupled regimes of continental collision: numerical modeling. *Earth and Planetary Science Letters*, 278(3-4), 337-349.
- Faccenna, C., Bellier, O., Martinod, J., Piromallo, C., & Regard, V. (2006). Slab detachment beneath eastern Anatolia: A possible cause for the formation of the North Anatolian fault. *Earth and Planetary Science Letters*, 242(1), 85-97.
- Farley, K. A. (2002). (U-Th)/He dating: Techniques, calibrations, and applications. *Reviews in Mineralogy and Geochemistry*, 47(1), 819-844.
- Federici, I., Cavazza, W., OKAY, A., Beyssac, O., Zattin, M., Corrado, S., & Dellisanti, F. (2010). Thermal evolution of the Permo– Triassic Karakaya subduction-accretion complex between the Biga Peninsula and the Tokat Massif (Anatolia). *Turkish Journal of Earth Sciences*, 19(4), 409-429.
- Fitzgerald, P. G., Baldwin, S. L., Webb, L. E., & O'Sullivan, P. B. (2006). Interpretation of (U–Th)/He single grain ages from slowly cooled crustal terranes: a case study from the Transantarctic Mountains of southern Victoria Land. *Chemical Geology*, 225(1), 91-120.
- Fleischer, R. L., Price, P. B., & Walker, R. M. (1975). *Nuclear tracks in solids: principles and applications*. Univ of California Press.
- Flowers, R. M., Ketcham, R. A., Shuster, D. L., & Farley, K. A. (2009). Apatite (U–Th)/He thermochronometry using a radiation damage accumulation and annealing model. *Geochimica et Cosmochimica Acta*, 73(8), 2347-2365.
- Forte, A. M., Cowgill, E., Bernardin, T., Kreylos, O., & Hamann, B. (2010). Late Cenozoic deformation of the Kura fold-thrust belt, southern Greater Caucasus. *Geological Society of America Bulletin*, 122(3-4), 465-486.
- Galoyan, G., Rolland, Y., Sosson, M., Corsini, M., & Melkonyan, R. (2007). Evidence for superposed MORB, oceanic plateau and volcanic arc series in the Lesser Caucasus (Stepanavan, Armenia). *Comptes Rendus Geoscience*, 339(7), 482-492.
- Gleadow, A. J. W., & Duddy, I. R. (1981). A natural long-term track annealing experiment for apatite. *Nuclear Tracks*, 5(1-2), 169-174.
- Gleadow, A. J. W., Duddy, I. R., Green, P. F., & Lovering, J. F. (1986). Confined fission track lengths in apatite: a diagnostic tool for thermal history analysis. *Contributions to Mineralogy and Petrology*, 94(4), 405-415.
- Göğüş, O. H., & Pysklywec, R. N. (2008). Mantle lithosphere delamination driving plateau uplift and synconvergent extension in eastern Anatolia. *Geology*, 36(9), 723-726.
- Gök, R., Sandvol, E., Türkelli, N., Seber, D., & Barazangi, M. (2003). Sn attenuation in the Anatolian and Iranian plateau and surrounding regions. *Geophysical Research Letters*, 30(24).



- Gök, R., Pasyanos, M. E., & Zor, E. (2007). Lithospheric structure of the continent–continent collision zone: eastern Turkey. *Geophysical Journal International*, 169(3), 1079-1088.
- Gök, R., Mellors, R. J., Sandvol, E., Pasyanos, M., Hauk, T., Takedatsu, R., ... & Javakishvirli, Z. (2011). Lithospheric velocity structure of the Anatolian plateau-Caucasus-Caspian region. *Journal of Geophysical Research: Solid Earth*, 116(B5).
- Green, P. F., Duddy, I. R., Gleadow, A. J. W., Tingate, P. R., & Laslett, G. M. (1985). Fission-track annealing in apatite: track length measurements and the form of the Arrhenius plot. *Nuclear Tracks and Radiation Measurements* (1982), 10(3), 323-328.
- Green, P. F., Duddy, I. R., Gleadow, A. J. W., Tingate, P. R., & Laslett, G. M. (1986). Thermal annealing of fission tracks in apatite: 1. A qualitative description. *Chemical Geology: Isotope Geoscience section*, 59, 237-253.
- Green, P. F., Duddy, I. R., Laslett, G. M., Hegarty, K. A., Gleadow, A. W., & Lovering, J. F. (1989). Thermal annealing of fission tracks in apatite 4. Quantitative modelling techniques and extension to geological timescales. *Chemical Geology: Isotope Geoscience Section*, 79(2), 155-182.
- Güleç, N., Hilton, D. R., & Mutlu, H. (2002). Helium isotope variations in Turkey: relationship to tectonics, volcanism and recent seismic activities. *Chemical Geology*, 187(1), 129-142.
- Hall, R. (1976). Ophiolite emplacement and the evolution of the Taurus suture zone, southeastern Turkey. *Geological Society of America Bulletin*, 87(7), 1078-1088.
- Holdsworth, R. E., Butler, C. A., & Roberts, A. M. (1997). The recognition of reactivation during continental deformation. *Journal of the Geological Society*, 154(1), 73-78.
- Hurford, A. J. (1990). Standardization of fission track dating calibration: Recommendation by the Fission Track Working Group of the IUGS Subcommittee on Geochronology. *Chemical Geology: Isotope Geoscience Section*, 80(2), 171-178.
- Hurford, A. J., & Green, P. F. (1982). A users' guide to fission track dating calibration. *Earth and Planetary Science Letters*, 59(2), 343-354.
- Hurford, A. J., & Green, P. F. (1983). The zeta age calibration of fission-track dating. *Chemical Geology*, 41, 285-317.
- Jackson, J., & McKenzie, D. (1988). The relationship between plate motions and seismic moment tensors, and the rates of active deformation in the Mediterranean and Middle East. *Geophysical Journal International*, 93(1), 45-73.
- Jackson, J. A., Ambraseys, N. N., Giardini, D., & Balassanian, S. (1997). Convergence between Eurasia and Arabia in eastern Turkey and the Caucasus. In *Historical and Prehistorical Earthquakes in the Caucasus* (Vol. 28, pp. 79-90). Kluwer.
- Jolivet, L., Huchon, P., & Rangin, C. (1989). Tectonic setting of Western Pacific marginal basins. *Tectonophysics*, 160(1-4), 23-47.

- Jolivet, L., & Faccenna, C. (2000). Mediterranean extension and the Africa-Eurasia collision. *Tectonics*, 19(6), 1095-1106.
- Kadinsky-Cade, K., Barazangi, M., Oliver, J., & Isacks, B. (1981). Lateral variations of high-frequency seismic wave propagation at regional distances across the Turkish and Iranian plateaus. *Journal of Geophysical Research: Solid Earth*, 86(B10), 9377-9396.
- Kaymakci, N., Aldanmaz, E., Langereis, C., Spell, T. L., Gurer, O. F., & Zanetti, K. A. (2007). Late Miocene transcurrent tectonics in NW Turkey: evidence from palaeomagnetism and  $^{40}\text{Ar}$ – $^{39}\text{Ar}$  dating of alkaline volcanic rocks. *Geological Magazine*, 144(2), 379-392.
- Keskin, M. (1994). Genesis of collision-related volcanism on the Erzurum-kars plateau, North eastern turkey (Doctoral dissertation, Durham University).
- Keskin, M. (2003). Magma generation by slab steepening and breakoff beneath a subduction-accretion complex: An alternative model for collision-related volcanism in Eastern Anatolia, Turkey. *Geophysical Research Letters*, 30(24).
- Ketcham, R. A., Donelick, R. A., & Carlson, W. D. (1999). Variability of apatite fission-track annealing kinetics: III. Extrapolation to geological time scales. *American Mineralogist*, 84(9), 1235-1255.
- Ketcham, R. A., Carter, A., Donelick, R. A., Barbarand, J., & Hurford, A. J. (2007). Improved modeling of fission-track annealing in apatite. *American Mineralogist*, 92(5-6), 799-810.
- Ketcham, R. A., 2009. HeFTy version 1.6.7. Manual
- Khain, V. E. (1975). Structure and main stages in the tectono-magmatic development of the Caucasus: an attempt at geodynamic interpretation. *American Journal of Science*, 275, 131-156.
- Koçyiğit, A., Yilmaz, A., Adamia, S., & Kuloshvili, S. (2001). Neotectonics of East Anatolian Plateau (Turkey) and Lesser Caucasus: implication for transition from thrusting to strike-slip faulting. *Geodinamica Acta*, 14(1-3), 177-195.
- Lei, J., & Zhao, D. (2007). Teleseismic evidence for a break-off subducting slab under Eastern Turkey. *Earth and Planetary Science Letters*, 257(1), 14-28.
- Lisker, F., Ventura, B., & Glasmacher, U. A. (2009). Apatite thermochronology in modern geology. Geological Society, London, Special Publications, 324(1), 1-23.
- Lordkipanidze, M. B., Meliksetian, B., & Djarbashian, R. (1989). Mesozoic–Cenozoic magmatic evolution of the Pontian–Crimean–Caucasian region. IGCP project, 198, 103-124.
- McKenzie, D. (1972). Active tectonics of the Mediterranean region. *Geophysical Journal International*, 30(2), 109-185.

- Nalpas, T., Le Douaran, S., Brun, J. P., Unternehr, P., & Richert, J. P. (1995). Inversion of the Broad Fourteens Basin (offshore Netherlands), a small-scale model investigation. *Sedimentary Geology*, 95(3-4), 237-250.
- Okay, A. I. (2008). Geology of Turkey: a synopsis. *Anschnitt*, 21, 19-42.
- Okay, A. I., & Sahinturk, O. (1997). AAPG Memoir 68: Regional and Petroleum Geology of the Black Sea and Surrounding Region. Chapter 15: Geology of the Eastern Pontides.
- Okay, A. I., & Tüysüz, O. (1999). Tethyan sutures of northern Turkey. *Geological Society, London, Special Publications*, 156(1), 475-515.
- Okay, A. I., Tansel, İ., & Tieysuez, O. K. A. N. (2001). Obduction, subduction and collision as reflected in the Upper Cretaceous–Lower Eocene sedimentary record of western Turkey. *Geological Magazine*, 138(2), 117-142.
- Okay, A. I., Tüysüz, O., & Kaya, Ş. (2004). From transpression to transtension: changes in morphology and structure around a bend on the North Anatolian Fault in the Marmara region. *Tectonophysics*, 391(1), 259-282.
- Okay, A. I., Zattin, M., & Cavazza, W. (2010). Apatite fission-track data for the Miocene Arabia-Eurasia collision. *Geology*, 38(1), 35-38.
- Reilinger, R., McClusky, S., Vernant, P., Lawrence, S., Ergintav, S., Cakmak, R., ... & Nadariya, M. (2006). GPS constraints on continental deformation in the Africa-Arabia-Eurasia continental collision zone and implications for the dynamics of plate interactions. *Journal of Geophysical Research: Solid Earth*, 111(B5).
- Pearce, J. A., Bender, J. F., De Long, S. E., Kidd, W. S. F., Low, P. J., Güner, Y., ... & Mitchell, J. G. (1990). Genesis of collision volcanism in Eastern Anatolia, Turkey. *Journal of Volcanology and Geothermal Research*, 44(1-2), 189-229.
- Philip, H., Avagyan, A., Karakhanian, A., Ritz, J. F., & Rebai, S. (2001). Estimating slip rates and recurrence intervals for strong earthquakes along an intracontinental fault: example of the Pambak–Sevan–Sunik fault (Armenia). *Tectonophysics*, 343(3), 205-232.
- Reilinger, R. E., McClusky, S. C., Souter, B. J., Hamburger, M. W., Prilepin, M. T., Mishin, A., ... & Balassanian, S. (1997). Preliminary estimates of plate convergence in the Caucasus collision zone from global positioning system measurements. *Geophysical research letters*, 24(14), 1815-1818.
- Reiners, P. W. (2005). Zircon (U-Th)/He thermochronometry. *Reviews in Mineralogy and Geochemistry*, 58(1), 151-179.
- Reiners, P. W., Ehlers, T. A., & Zeitler, P. K. (2005). Past, present, and future of thermochronology. *Reviews in Mineralogy and Geochemistry*, 58(1), 1-18.
- Reiners, P. W., & Brandon, M. T. (2006). Using thermochronology to understand orogenic erosion. *Annu. Rev. Earth Planet. Sci.*, 34, 419-466.

- Robertson, A. H. F. (2007). Overview of tectonic settings related to the rifting and opening of Mesozoic ocean basins in the Eastern Tethys: Oman, Himalayas and Eastern Mediterranean regions. Geological Society, London, Special Publications, 282(1), 325-388.
- Robinson, A. G., Banks, C. J., Rutherford, M. M., & Hirst, J. P. P. (1995). Stratigraphic and structural development of the Eastern Pontides, Turkey. *Journal of the Geological Society*, 152(5), 861-872.
- Rodgers, A. J., Ni, J. F., & Hearn, T. M. (1997). Propagation characteristics of short-period Sn and Lg in the Middle East. *Bulletin of the Seismological Society of America*, 87(2), 396-413.
- Rolland, Y., Billo, S., Corsini, M., Sosson, M., & Galoyan, G. (2007). Blueschists of the Amassia-Stepanavan suture zone (Armenia): linking Tethys subduction history from E-Turkey to W-Iran. *International Journal of Earth Sciences*, 98(3), 533-550.
- Rolland, Y., Galoyan, G., Bosch, D., Sosson, M., Corsini, M., Fornari, M., & Verati, C. (2009). Jurassic back-arc and Cretaceous hot-spot series In the Armenian ophiolites— Implications for the obduction process. *Lithos*, 112(3), 163-187.
- Sandvol, E., Al-Damegh, K., Calvert, A., Seber, D., Barazangi, M., Mohamad, R., ... & Gürbüz, C. (2001). Tomographic Imaging of Lg and Sn Propagation in the Middle East. *Monitoring the Comprehensive Nuclear-Test-Ban Treaty: Regional Wave Propagation and Crustal Structure*, 1121-1163.
- Şengör, A. M. C., & Yilmaz, Y. (1981). Tethyan evolution of Turkey: a plate tectonic approach. *Tectonophysics*, 75(3-4), 181-193, 203-190, 199-241.
- Şengör, A. C., Özeren, M. S., Keskin, M., Sakıncı, M., Özbakır, A. D., & Kayan, I. (2008). Eastern Turkish high plateau as a small Turkic-type orogen: Implications for post-collisional crust-forming processes in Turkic-type orogens. *Earth-Science Reviews*, 90(1), 1-48.
- Şengör, A. M. C., Görür, N., & Şaroğlu, F. (1985). Strike-slip faulting and related basin formation in zones of tectonic escape: Turkey as a case study.
- Şengör, A. M. C., Özeren, S., Genç, T., & Zor, E. (2003). East Anatolian high plateau as a mantle-supported, north-south shortened domal structure. *Geophysical Research Letters*, 30(24).
- Şengör, A. M. C., Tüysüz, O., İmren, C., Sakıncı, M., Eyidoğan, H., Görür, N., ... & Rangin, C. (2005). The North Anatolian fault: A new look. *Annu. Rev. Earth Planet. Sci.*, 33, 37-112.
- Seymen, I., & Aydın, A. (1972). The Bingöl earthquake fault and its relation to the North Anatolian fault zone. *Bull. Miner. Res. Explor. Inst. Turkey*, 79, 1-8.
- Sosson, M., Rolland, Y., Müller, C., Danelian, T., Melkonyan, R., Kekelia, S., ... & Galoyan, G. (2010). Subductions, obduction and collision in the Lesser Caucasus (Armenia,

- Azerbaijan, Georgia), new insights. Geological Society, London, Special Publications, 340(1), 329-352.
- Sokoutis, D., & Willingshofer, E. (2011). Decoupling during continental collision and intra-plate deformation. *Earth and Planetary Science Letters*, 305(3-4), 435-444.
- Stampfli, G. M., & Hochard, C. (2009). Plate tectonics of the Alpine realm. Geological Society, London, Special Publications, 327(1), 89-111.
- Sunal, G., Natal'in, B. A., Satir, M., & Toraman, E. (2006). Paleozoic magmatic events in the Strandja Massif, NW Turkey. *Geodinamica Acta*, 19(5), 283-300.
- Tagami, T., & O'Sullivan, P. B. (2005). Fundamentals of fission-track thermochronology. *Reviews in Mineralogy and Geochemistry*, 58(1), 19-47
- Ustaömer, T., & Robertson, A. H. F. (1994). Late Palaeozoic marginal basin and subduction-accretion: the Palaeotethyan Küre complex, central Pontides, northern Turkey. *Journal of the Geological Society*, 151(2), 291-305.
- Uysal, I. T., Mutlu, H., Altunel, E., Karabacak, V., & Golding, S. D. (2006). Clay mineralogical and isotopic (K–Ar,  $\delta^{18}\text{O}$ ,  $\delta\text{D}$ ) constraints on the evolution of the North Anatolian Fault Zone, Turkey. *Earth and Planetary Science Letters*, 243(1), 181-194.
- Yiğitbaş, E., & Yılmaz, Y. (1996). New evidence and solution to the Maden complex controversy of the Southeast Anatolian orogenic belt (Turkey). *Geologische Rundschau*, 85(2), 250-263.
- Yılmaz, Y. (1990). Comparison of young volcanic associations of western and eastern Anatolia formed under a compressional regime: a review. *Journal of Volcanology and Geothermal Research*, 44(1-2), 69-87.
- Yılmaz, Y. (1993). New evidence and model on the evolution of the southeast Anatolian orogen. *GSA Bulletin*, 105(2), 251-271.
- Yılmaz, Y., Şaroğlu, F., & Güner, Y. (1987). Initiation of the neomagmatism in East Anatolia. *Tectonophysics*, 134(1), 177-199.
- Yılmaz, A., Adamia, S., Chabukiani, A., Chkhotua, T., Erdoğan, K., Tuzcu, S., & Karabiyikoğlu, M. (2000). Structural correlation of the southern Transcaucasus (Georgia)-eastern Pontides (Turkey). Geological Society, London, Special Publications, 173(1), 171-182.
- Zakariadze, G. S., Dilek, Y., Adamia, S. A., Oberhänsli, R. E., Karpenko, S. F., Bazylev, B. A., & Solov'eva, N. (2007). Geochemistry and geochronology of the Neoproterozoic Pan-African Transcaucasian Massif (Republic of Georgia) and implications for island arc evolution of the late Precambrian Arabian–Nubian Shield. *Gondwana Research*, 11(1), 92-108.
- Zattin, M., Okay, A. I., & Cavazza, W. (2005). Fission-track evidence for late Oligocene and mid-Miocene activity along the North Anatolian Fault in south-western Thrace. *Terra Nova*, 17(2), 95-101.

- Zattin, M., Cavazza, W., Okay, A. I., Federici, I., Fellin, M. G., Pignalosa, A., & Reiners, P. (2010). A precursor of the North Anatolian Fault in the Marmara Sea region. *Journal of Asian Earth Sciences*, 39(3), 97-108.
- Ziegler, P. A. (1993). Plate-moving mechanisms: their relative importance William Smith Lecture 1992. *Journal of the Geological Society*, 150(5), 927-940.
- Ziegler, P. A., Cloetingh, S., & van Wees, J. D. (1995). Dynamics of intra-plate compressional deformation: the Alpine foreland and other examples. *Tectonophysics*, 252(1), 7-59.
- Ziegler, P. A., Van Wees, J. D., & Cloetingh, S. (1998). Mechanical controls on collision-related compressional intraplate deformation. *Tectonophysics*, 300(1), 103-129.
- Ziegler, P. A., Bertotti, G., & Cloetingh, S. A. P. L. (2002). Dynamic processes controlling foreland development – the role of mechanical (de) coupling of orogenic wedges and forelands. *Stephan Mueller Special Publication Series*, 1, 17-56.
- Zoback, M. L. (1992). First-and second-order patterns of stress in the lithosphere: The World Stress Map Project. *Journal of Geophysical Research: Solid Earth*, 97(B8), 11703-11728.
- Zor, E., Sandvol, E., Gürbüz, C., Türkelli, N., Seber, D., & Barazangi, M. (2003). The crustal structure of the East Anatolian plateau (Turkey) from receiver functions. *Geophysical Research Letters*, 30(24), TUR7(1-4).

PART TWO

Chapter Four

**MANUSCRIPT SUMMARY**

In this dissertation, three different case studies are taken in account. Three collisional orogens were studied and the discussion and comparison of their thermal histories point to distinct behaviors. The first manuscript discusses the Bitlis-Pütürge Massif, where there is evidence of a strong mid-Miocene episode of mechanical coupling between the indenter (Arabia) and the hinterland, with deformation of the orogenic wedge and reactivation of pre-existing structures over long distances. The second manuscript addresses the tectonic evolution of Lesser Caucasus and elaborates further on the topic of stress transfer from the Bitlis collision zone toward the north. In this region, thermal modellings indicate a heterogeneous distribution of collision-related stress: mid-Miocene mechanical coupling was active in some sectors whereas neighboring regions were left basically unaffected and retained the thermochronologic signature of an earlier orogeny. The final manuscript deals with the Strandja Massif, where thermal modelling indicates that the Alpine-age stress related to the collision mostly bypassed the older Cimmerian orogenic prism and focused along a rheologically weakened rift zone to the north.



#### **4.1. Manuscript 1**

*The Miocene Arabia-Eurasia collision zone of southeastern Turkey*

William Cavazza, Silvia Cattò, Massimiliano Zattin, Aral I. Okay, and Peter Reiners

Submitted to Geosphere (17 November 2017)

The Bitlis-Pütürge Massif is a collisional orogen developed in the area of maximum indentation along the >2,400 km-long Bitlis-Zagros suture between the Anatolide-Tauride terrane (in the north) and the Arabian plate (in the south). The dataset points to ubiquitous latest Cretaceous metamorphism of a passive margin sedimentary sequence and its igneous basement not only along the suture zone but across the entire width of the Anatolia-Tauride block north of the suture and farther to the lower case along the northern passive margin of the Arabian plate. This pervasive metamorphic event is related to ophiolite slabs obduction over the lower plate passive margin, in accordance with the model proposed by Ziegler et al. [1995], suggesting the likelihood of compressional reactivation and inception of subduction under the upper plate margin, weakened, and obduction of nappes over the lower plate passive margin, generally stronger than the oceanic lithosphere. During the Middle Miocene, the Bitlis-Pütürge orogenic wedge underwent a significant and discrete phase of rapid cooling/exhumation arguably related to frontal accretion and underplating. For the Eurasian foreland thermochronological and field evidences point out a coeval phase of cooling/exhumation focusing preferentially at rheological discontinuities as the Lesser Caucasus and the Eastern Pontides, suggesting tectonic stress efficient transfer over large distances, again in perfect accordance with Ziegler et al. [1995, 1998, 2002] and references therein. The enucleation since the late Middle Miocene of the North Anatolian and East Anatolian fault systems decoupled the thrust front from the foreland promoting a new tectonic regime where the plate convergence is mostly accommodated by strike-slip westward translation of the newly created (Anatolia) microplate and secondly by wholesome uplift of the Iranian continental plateau.

## 4.2. Manuscript 2

*Continental accretion and incremental deformation in the thermochronologic evolution of the Lesser Caucasus*

William Cavazza, Irene Albino, Ghazar Galoyan, Massimiliano Zattin, and Silvia Cattò

To be submitted to International Geology Review

Apatite fission-track (AFT) analysis and thermochronologic statistical modeling of basement rocks from the Lesser Caucasus differentiates two discrete cooling/exhumation phases correlated to major collisional orogenies and obduction episodes caused by accretion of large lithospheric terranes to the southern margin of Eurasia. The first cooling episode occurred in the Late Cretaceous (Turonian-Maastrichtian) and derived from collision along what is now the Sevan-Akera suture zone between the South Armenia block (i.e. the eastern prolongation of the Anatolide-Tauride terrane of Asia Minor) and the Somkheto-Karabakh magmatic arc, i.e. the product of Jurassic – Early Cretaceous northward subduction of Neotethyan oceanic lithosphere beneath the Eurasian southern margin. AFT analysis and thermochronologic modeling shows that some segments of the Sevan-Akera suture zone still retains the thermochronometric signature of this earlier collisional event whereas other segments have been overprinted by a mid-Miocene phase of rapid cooling. Such second episode of cooling/exhumation occurred where the trend of the trace of the suture changes from W-E to NW-SE. We argue that such tectonic reactivation was a far-field effect of the coeval Arabia-Eurasia collision along the Bitlis-Zagros suture zone to the south, in agreement with similar thermochronological evidence in the eastern Pontides of Turkey. Other segments of the Lesser Caucasus were not reactivated during the Miocene because the main structural discontinuities were not properly oriented.

From a broader perspective, we point out the existence of a widespread mid-Miocene episode of deformation along the northern borders of the Anatolian-Iranian Plateau, from the eastern Pontides to the Lesser Caucasus. During the Early and Middle Miocene continental deformation was concentrated along the Arabia-Eurasia (Bitlis-Zagros) collision zone but tectonic stress was transferred northward across eastern Anatolia, focusing along the eastern Black Sea continent-ocean rheological transition. The Black Sea (quasi)oceanic lithosphere is fundamentally stronger than the polydeformed continental lithosphere to the south and

therefore represented a “backstop” resisting deformation and deviating the impinging continental lithosphere (McClusky et al. 2000). The results of this study show that stress transfer was also efficient toward the northeast where segments of preexisting structural discontinuities like the Sevan-Akera suture properly oriented with respect to the prevalent stress field were reactivated with a significant dip-slip component.

### 4.3. Manuscript 3

*No significant Alpine tectonic overprint on the Cimmerian Strandja Massif (SE Bulgaria and NW Turkey)*

Silvia Cattò, William Cavazza , Massimiliano Zattin & Aral I. Okay

International Geology Review, DOI: 10.1080/00206814.2017.1350604

The Strandja Massif is a poly-deformed, deeply-eroded orogenic belt straddling the boundary between NW Turkey and SE Bulgaria. It was affected by the Variscan, Cimmerian and Alpine orogenies. Overall, the most conspicuous thermal and structural trait is the Cimmerian overprint characterized by pervasive regional metamorphism associated with thick-skinned thrust imbrication, arguably related to continent–continent collision with the Sakarya block. Nevertheless, the most peculiar feature is that from a thermochronometric viewpoint, the bulk of the Cimmerian Strandja orogen was largely unaffected by the compressional stress related to the closure of the Vardar–İzmir–Ankara oceanic domain(s) to the south, contrary to the adjacent Rhodopes. Evidence of Alpine-age tectonic is recorded only in the northern sector of the orogen, even though the poly-deformed, highly heterogeneous Strandja massif ostensibly seems an excellent rheological discontinuity. In this case, the Srednogorie magmatic arc, weakened by Late Cretaceous back-arc extension, happens to be a more suitable locus of deformation than the thick-skinned imbricated Strandja massif.

Chapter Five

**MANUSCRIPTS**



## 5.1. Manuscript 1

### **The Miocene Arabia-Eurasia collision zone of southeastern Turkey**

William Cavazza, Silvia Cattò, Massimiliano Zattin, Aral I. Okay, and Peter Reiners

*Submitted to Geosphere (17th November 2017)*

1 The Miocene Arabia-Eurasia collision zone of southeastern  
2 Turkey

3

4 **William Cavazza<sup>1</sup>, Silvia Cattò<sup>1</sup>, Massimiliano Zattin<sup>2</sup>, Aral I. Okay<sup>3</sup>, and Peter Reiners<sup>4</sup>**

5 *Department of Biological, Geological and Environmental Sciences, University of Bologna,*  
6 *40126 Bologna, Italy*

7 *<sup>2</sup>Department of Geosciences, University of Padua, 35131 Padua, Italy*

8 *<sup>3</sup>Eurasia Institute of Earth Sciences, Istanbul Technical University, Maslak 34469, Istanbul,*  
9 *Turkey*

10 *<sup>4</sup>Department of Geosciences, University of Arizona, Tucson, AZ 85721, USA*

11

12 **ABSTRACT**

13 The Bitlis-Pütürge collision zone of SE Turkey is the area of maximum indentation along  
14 the >2,400 km-long Assyrian-Zagros suture between Arabia and Eurasia. The integration of (i)  
15 fission-track analyses on apatites, (ii) (U-Th)/He analyses on zircons, (iii) field observations on  
16 stratigraphic and structural relationships, and (iv) preexisting U-Pb and Ar-Ar age determinations  
17 on zircons, amphiboles, and micas across provides for the first time an overall picture of the  
18 thermochronometric evolution of this collisional orogen. The dataset points to ubiquitous latest  
19 Cretaceous metamorphism of a passive margin sedimentary sequence and its igneous basement  
20 not only along the suture zone but across the entire width of the Anatolia-Tauride block north of  
21 the suture. The basement complex of the Bitlis and Pütürge massifs along the suture was rapidly  
22 exhumed between ca. 65 and 55 Ma and eventually overlain by Eocene shallow-marine  
23 sediments. The entire Oligocene is characterized by a rather flat thermochronometric evolution



24 in the Bitlis orogenic wedge, contrary to the widely held belief that this epoch marked the  
25 inception of the Arabia-Eurasia collision and was characterized by widespread deformation.  
26 During the Middle Miocene, the Bitlis-Pütürge orogenic wedge underwent a significant and  
27 discrete phase of rapid growth by both frontal accretion, as shown by cooling/exhumation of the  
28 foreland deposits on both sides of the orogenic prism, and underplating, as shown by  
29 cooling/exhumation of the central metamorphic core of the orogenic wedge. We conclude that  
30 continental collision started in the mid-Miocene, as also shown by coeval thick syntectonic  
31 clastic wedges deposited in flexural basins along the Arabian plate northern margin and  
32 contractional reactivation of a number of preexisting structures in the European foreland.

33

34 **Keywords:** Arabia-Eurasia continental collision; thermochronology; Bitlis-Pütürge massif;  
35 Assyrian suture; (U-Th)/He analysis on zircons; apatite fission-track analysis.

36

## 37 **INTRODUCTION**

38 The collision between Arabia and Eurasia along the >2,400km-long Bitlis-Zagros  
39 (Assyrian) suture zone in the Middle East (Fig. 1) is a major event in Earth's history which  
40 isolated the Mediterranean and the Indian ocean, and has been linked to mid-Cenozoic global  
41 cooling, Red Sea rifting, extension in the Aegean region, inception of the North and East  
42 Anatolian strike-slip fault systems, and development of the Anatolian-Iranian continental plateau  
43 (e.g., Şengör and Kidd, 1979; Dewey et al., 1986; Jolivet and Faccenna, 2000; Barazangi et al.,  
44 2006; Robertson et al., 2007; Allen and Armstrong, 2008; Yilmaz et al., 2010). The age of the  
45 continental collision has been the topic of much debate, with proposed ages ranging widely from  
46 the Late Cretaceous to the Pliocene (Hall, 1976; Berberian and King, 1981; Şengör et al., 1985;

47 Yılmaz, 1993; Alavi, 1994; Jolivet and Faccenna, 2000; Agard et al., 2005; Robertson et al.,  
48 2007; Allen and Armstrong, 2008; Okay et al., 2010; McQuarrie and van Hinsbergen, 2013).  
49 Exact determination of the timing of the continental collision is crucial not only for  
50 understanding the evolution of the Bitlis-Zagros collisional orogen but also for elucidating the  
51 chronology and causative mechanisms of more general syn- and post-collisional processes like  
52 (i) the development of large-scale strike-slip systems accomodating plate convergence and (ii)  
53 the inception of continental plateaux. In the Bitlis-Pütürge massifs of southeastern Turkey, i.e.  
54 the area of maximum continental indentation, high-temperature radiometric systems indicate a  
55 discrete episode of HP-LT metamorphism in the latest Cretaceous (Hempton, 1985; Okay et al.,  
56 1985, Oberhänsli et al., 2010, 2012, 2013; Rolland et al., 2012; Topuz et al., 2017) which has  
57 been interpreted as the result of the collision between Eurasia and either Arabia or a smaller  
58 microplate. The only low-temperature thermochronometric dataset available for the same region  
59 (Okay et al., 2010) –based on fission-track analyses on apatites of a number of samples from  
60 both the basement units and the sedimentary cover– points to a discrete phase of rapid mid-  
61 Miocene cooling/exhumation interpreted as the onset of the Arabia-Eurasia hard collision. The  
62 results by Okay et al. (2010) do not rule out the possibility that the documented episode of  
63 Miocene cooling was only the last stage of a longer thermochronometric evolution and that  
64 hence the collision could have started somewhat earlier. This paper advances further the state of  
65 the knowledge on this crucial area by integrating new AFT and ZrHe data with other radiometric  
66 data (U-Pb and Ar-Ar on zircons, amphiboles, and micas) from the literature, ultimately  
67 providing a complete picture of the thermo-tectonic evolution of selected segments of the  
68 Arabia-Eurasia collision zone.  
69

70 **GEOLOGICAL FRAMEWORK**

71 The Bitlis-Pütürge Massif of southeastern Anatolia (Fig. 2) is a 500 km-long arcuate belt of  
72 allochthonous metamorphic rocks bordering the Arabian Platform to the south, from which it is  
73 separated by a narrow belt of Upper Cretaceous-to-Early Miocene *mélange* made of flysch and  
74 ophiolitic units (Hall, 1976; Perinçek, 1990; Yılmaz, 1993; Okay, 2008). The massif is made of a  
75 Precambrian basement and an overlying Phanerozoic sequence (Çağlayan et al., 1984;  
76 Göncüoğlu and Turhan, 1984; Okay et al., 1985). The Precambrian basement consists of  
77 polymetamorphosed gneiss, amphibolite, micaschist and eclogite. The overlying Phanerozoic  
78 sequence is mostly made of schist, phyllite and marble, and represents the Palaeozoic-Mesozoic  
79 sedimentary cover of the Anatolide-Tauride terrane which suffered low-to-medium grade  
80 metamorphism in the latest Cretaceous (83-69 Ma; Campanian-Maastrichtian) (Hempton, 1985;  
81 Oberhänsli et al., 2010, 2012, 2013; Karaoglan et al., 2013; Rolland et al., 2012).

82 South-verging post-Eocene thrusting of the massif resulted in internal tectonic imbrication  
83 and the development of a series of north-dipping thrust sheets. To the north, such structure is  
84 largely concealed by the Plio-Quaternary volcano-sedimentary rocks of the Anatolian Plateau,  
85 whereas to the south the massif overlies tectonically *mélange* complexes of various ages (e.g.  
86 Hakkâri Complex), as well as the thick sedimentary succession of the Arabian plate northern  
87 margin (e.g., Yılmaz, 1993).

88 The Bitlis-Pütürge Massif is generally considered the southern deformed margin of the  
89 Anatolide-Tauride terrane, originally separated from the Arabian Platform by the southern  
90 branch of the Neotethys (Barrier and Vrielynck, 2008; Stampfli and Hochard, 2009). It marks the  
91 area of maximum collisional indentation between Arabia and Eurasia, with widespread  
92 exposures of metamorphic rocks. In this region, the Assyrian suture is <150 km from the Late

93 Cretaceous - Eocene Izmir-Ankara-Erzincan suture to the north (Fig. 1). These two suture zones  
94 mark the closure of the two branches of the western Neotethys (Barrier and Vrielynck, 2008;  
95 Stampfli and Hochard, 2009).

96 The area between the Izmir-Ankara-Erzincan and the Assyrian sutures is largely covered  
97 by the mostly Plio-Quaternary volcanics/volcaniclastics of the Anatolian Plateau. Paleozoic  
98 sedimentary rocks metamorphosed in the Late Cretaceous (Santonian-Campanian; Topuz et al.,  
99 2017) crop out sparsely as inliers and are similar –both in terms of lithology and age of  
100 metamorphism– to those of the Bitlis-Pütürge Massif. Such metamorphism is synchronous with  
101 the emplacement of a very large body of ophiolite and underlying tectonic slices of ophiolitic  
102 mélangé across the entire Anatolide-Tauride terrane (Şengör and Yılmaz, 1981; Okay and  
103 Tüysüz, 1999). Erosional remnants of this nappe of ophiolite and ophiolitic mélangé occur in the  
104 study area. Cenozoic sedimentation over the narrow area between the Izmir-Ankara-Erzincan  
105 and the Assyrian sutures was influenced by flexural processes due to the load exerted on the  
106 lithosphere by the orogenic wedges associated with the two suture zones. In general terms,  
107 outcrop areas of Eocene sedimentary successions tend to be concentrated to the north, i.e. close  
108 to the Izmir-Ankara-Erzincan suture, whereas Oligocene-Early Miocene successions are  
109 concentrated to the south, close to the Bitlis suture (Bilgic, 2002; Günay and Şenel, 2002; Şenel  
110 and Ercan, 2002; Tarhan, 2002). A large outcrop area of latest Eocene-to-Early Miocene  
111 sedimentary rocks to the west of Lake Van (Fig. 2) is commonly referred to as Muş Basin (e.g.,  
112 Akay et al., 1989; Sancay et al., 2006; Hüsing et al., 2009) but in reality is an inlier of a much  
113 larger sedimentary basin (Muş-Hınıs Basin) spanning virtually the entire area shown north of the  
114 Bitlis Massif in Figure 2 and for the most part concealed by the Plio-Quaternary volcano-  
115 sedimentary succession (Huvaz, 2009).

116

## 117 **SAMPLES AND METHODS**

118       Samples for apatite fission-track [AFT] and zircon (U-Th-Sm)/He [ZHe] analyses were  
119 collected along four transect across the Bitlis and Pütürge massifs and the collision zone,  
120 perpendicular to the strike of the main tectonic structures. Lithostratigraphic units from which  
121 the samples were taken comprise (i) the Bitlis and Pütürge metamorphic complexes, (ii) the  
122 Eocene sandstones of the Maden and Hakkäri complexes, (iii) the Oligocene sandstones of the  
123 Muş-Hınıs Basin, and (iv) the Paleozoic sandstone units in the collision-induced faulted  
124 anticlines on the Arabian Plate (Fig. 2; Table 1). Samples analysed for this paper are the same of  
125 Okay et al. (2010) except for an additional sample (TU255) from the Muş-Hınıs Basin. New,  
126 multiple mineral separations were made for each sample in order to obtain enough apatite grains  
127 and a statistically robust number of fission tracks.

128       Sample preparation and AFT analyses were carried out at the Department of Biological,  
129 Geological and Environmental Sciences of the University of Bologna. Apatite and zircon grains  
130 were concentrated by crushing and sieving, followed by hydrodynamic, magnetic, and heavy-  
131 liquid separation. Apatites were embedded in epoxy resin, polished in order to expose the  
132 internal surfaces within the grains, and the spontaneous FT were revealed by etching with 5N  
133 HNO<sub>3</sub> at 20°C for 20 seconds. The mounts were then coupled with a low-uranium fission-track-  
134 free muscovite mica sheet (external detector method) and sent for irradiation with thermal  
135 neutrons (see Donelick et al., 2005, for details) at the Radiation Center of Oregon State  
136 University. Nominal fluence of  $9 \times 10^{15}$  n cm<sup>-2</sup> was monitored with a CN5 uranium-doped silicate  
137 glass dosimeter. Induced fission tracks were revealed by etching of the mica sheets in 40% HF  
138 for 45 min at 20°C. Apatite grains from 24 samples were sent for irradiation, however, most

139 samples had too low uranium to generate enough tracks for a reliable age. Eight samples yielded  
140 apatites suitable for fission-track analysis. Spontaneous and induced fission tracks were counted  
141 under optical microscope at  $\times 1,250$  magnification, using an automatic stage (FTStage system)  
142 plus a digitizing tablet. Central ages were calculated with the zeta calibration approach (Hurford  
143 and Green, 1983), using Durango ( $31.3 \pm 0.3$  Ma) and Fish Canyon Tuff ( $27.8 \pm 0.2$  Ma) age  
144 standards within grains exposing *c*-axis-parallel crystallographic planes.

145         Apatite track-length distributions were calculated by measuring horizontal confined tracks  
146 together with the angle between the track and the *c*-axis. Confined tracks constitute a small part  
147 of the FT population, therefore additional concentrates were mounted, polished and etched for  
148 the analysis. Ultimately, four samples contained a statistically significant number of confined  
149 tracks. A quantitative evaluation of the thermal history of these four samples was carried out  
150 through modelling procedures, which find a range of cooling paths compatible with the apatite  
151 fission-track age and track-length distribution of each sample (Ketcham, 2005). In this work,  
152 inverse modelling of track-length data was performed using the HeFTy program (Ehlers et al.,  
153 2005), which generates the possible T–t paths by a Monte Carlo algorithm. Predicted AFT data  
154 were calculated according to the Ketcham et al. (2007) annealing model for fission tracks  
155 revealed by etching.  $D_{\text{par}}$  values (i.e. the etch pit length) were used to define the annealing kinetic  
156 parameters of the grains and the original track length. All available geological constraints  
157 (intrusion ages, metamorphic events, depositional ages, and stratigraphic relationships) and the  
158 results of ZHe analyses were incorporated into the thermochronometric modeling of the four  
159 selected samples (see next section).

160         Seven samples taken from the Bitlis-Pütürge metamorphic complex and the Eocene  
161 sandstones of the Hakkäri complex were prepared for ZHe analyses. Handpicked zircon grains

162 were photographed and measured for alpha-ejection correction following methods described in  
163 Reiners and Brandon (2006) and Hourigan et al. (2005). Helium analysis was performed at the  
164 Radiogenic Helium dating laboratory of the Department of Geosciences of the University of  
165 Arizona. The packets containing the single crystals to be analyzed and the standard crystals were  
166 placed in a stainless steel planchet inside a laser cell and degassed under vacuum by heating with  
167 a Nd-YAG laser for 15 minutes at 1-5 W. Helium blanks (0.1-0.05 fmol  $^4\text{He}$ ) were determined  
168 by heating empty packets with the same procedure. The gas was then spiked with 4pmol  $^3\text{He}$ ,  
169 condensed in a cryogenic trap at 16°K, then released at 37°K into a small volume with an  
170 activated getter and the source of a Balzer quadrupole mass spectrometer with Channeltron  
171 electron multiplier. Masses of HD and  $\text{H}^{3+}$  were measured to correct the  $^3\text{He}/^4\text{He}$  measured  
172 ratios. The obtained ratios were referenced to  $^4\text{He}$  standards measured in the same way. After  
173  $^4\text{He}$  measurement samples were retrieved from the laser cell, each packet was placed in a Teflon  
174 vial, spiked with calibrated  $^{229}\text{Th}$ ,  $^{233}\text{U}$ , and  $^{147}\text{Sm}$  solution and dissolved by 30%  $\text{NO}_3$ . Natural-  
175 to-spike isotope ratios were then measured on a high-resolution (single-collector) Element2 ICP-  
176 MS.

177

## 178 ANALYTICAL RESULTS AND INTERPRETATION

179 Results of AFT from the Bitlis-Pütürge collision zone and from the adjacent Muş-Hınıs  
180 Basin are reported in Table 1. AFT central ages from the orogenic wedge cluster tightly between  
181  $13.4 \pm 2.2$  and  $18.0 \pm 1.8$  Ma. Sample TU159 (an Eocene turbidite sandstone from the Hakkâri  
182 Complex) has a central age of  $25.2 \pm 7.2$  Ma, significantly older than all other samples. Sample  
183 TU255, an Oligocene turbidite sandstone from the Muş-Hınıs foreland basin, yielded an AFT  
184 central age of  $53.3 \pm 1.7$ , older than its depositional age. This implies that the sample was only

185 partially reset because it never reached temperatures corresponding to the base of the partial  
186 annealing zone of apatite (ca. 120°C), as discussed below. Analyzed samples do not show any  
187 particular age-elevation correlation. All the samples passed the  $\chi^2$  test indicating a single  
188 population of grains.

189 Table 2 provides a summary of (U-Th)/He analyses on zircons. All samples show a  
190 somewhat rapid cooling/exhumation through the partial retention zone. This is supported by (i)  
191 reproducible results of replicate analyses and (ii) no correlation of single grain ages with the  
192 equivalent sphere radius and eU (effective uranium). Therefore, the weighted mean of single  
193 grain ages adequately constrains the closure temperature of each sample. Most of the ZHe ages  
194 (samples TU-136, TU-142, TU-145, TU-149) cluster coherently between 44.2 and 37.0 Ma  
195 (Lutetian-Priabonian). The consistent results of replicate analyses of single samples indicates a  
196 rapid and widespread episode of cooling/exhumation in the Eocene. Sample TU-151  
197 (Precambrian chlorite schist) yielded an age of 60.4 Ma, in line with higher temperature  
198 radiometric systems employed in the same area (Oberhänsli et al., 2010, 2012, 2013), and was  
199 unaffected by later heating. Sample TU-138 (Precambrian gneiss) yielded an Early Miocene  
200 weighted mean age (22.4 Ma). All ZHe results were incorporated into the thermochronometric  
201 modeling (see below).

202 The thermochronometric modeling of sample TU149 (Precambrian gneiss; Pütürge Massif;  
203 Fig. 2) is well constrained by (i) a  $77.5 \pm 0.7$  Ma Ar/Ar age on phengites from micaschists of the  
204 overlying Paleozoic metasedimentary section nearby (Rolland et al., 2012), (ii) mid-Eocene  
205 sedimentary rocks nonconformably overlying the Pütürge basement complex (e.g., Bilgic, 2002)  
206 (Fig. 3), and by our own (iii) ZHe (Table 2) and (iv) AFT (Table 1) analyses. Integration of these  
207 data provide for the first time a comprehensive reconstruction of the overall thermochronometric



208 development of this sector of the Pütürge Massif (Fig. 3B). Following Late Cretaceous  
209 metamorphism, the sample underwent fairly rapid cooling and exhumation to near-surface  
210 conditions, and was covered by the Maden Complex, a thick volcano-sedimentary succession  
211 deposited in a short-lived backarc basin (Yiğitbaş and Yılmaz, 1996). Deposition of the Maden  
212 Complex induced progressive burial heating of basement sample TU149 between ca. 45 and 39  
213 Ma. The Oligocene thermal evolution of the sample is rather flat until ca. 19 Ma (Burdigalian),  
214 when the best-fit curve derived from the study of the apatite fission-track length distribution (Fig.  
215 3B) shows a sudden increase in the cooling rate.

216       Thermochronometric modeling of sample TU136 (Paleozoic metasandstone; central Bitlis  
217 Massif; Fig. 2) is constrained by (i) two Late Cretaceous (Campanian; 84.4-73.8 Ma) (Oberhänsli  
218 et al., 2012, 2013) metamorphic ages from similar rock units along tectonic strike to the southeast  
219 (Table 3), (ii) Middle-Late Eocene sedimentary rocks nonconformably overlying the Bitlis  
220 basement complex (e.g., Tarhan, 2002) (Fig. 4), and by our own (iii) ZHe analyses (Table 2) and  
221 (iv) AFT analysis (Table 1). Track-length frequency distribution is platykurtic -the result of a  
222 long residence time in the partial annealing zone- with abundant long tracks (15-17  $\mu\text{m}$ )  
223 indicating a later phase of rapid cooling (Fig. 4C). The thermochronometric evolution of this  
224 metasedimentary sample from the Bitlis Massif is similar to the one described above for the  
225 Precambrian gneisses of the Pütürge Massif. Again, the entire duration of the Oligocene (and  
226 Early Miocene) is characterized by the residence of the sample at stable temperatures,  
227 corresponding at the base of the partial annealing zone of apatite (ca. 120°C). A sudden increase  
228 in the rate of cooling occurred at 15-12 Ma (Middle Miocene) depending on whether we consider  
229 the mean or best-fit curve (Fig. 4B).

230       An Early Oligocene sandstone sample (TU255) from the lower portion of the Muş Basin

231 sedimentary fill (Yazledere Fm., Figs. 2 and 3) yielded a broad single-grain age distribution (Fig.  
232 4E) and a bimodal track-length distribution (Fig. 4G), indicating a complex thermal history. AFT  
233 central age for this sample is 53.2 Ma (Table 1), i.e. older than its depositional age. This implies  
234 that the sample has not been completely reset, thus partially retaining the original thermal  
235 signature of the sediment source rocks contributing detritus to the Muş-Hınıs Basin. In such  
236 cases, central ages are hardly significant and only the statistical modeling of FT length  
237 distributions can constrain the T-t path. Inverse modeling (Fig. 4F) depicts clearly a phase of  
238 post-depositional heating (ca. 28-16 Ma; Late Oligocene – Early Miocene), likely resulting from  
239 progressive sedimentary burial, followed by rapid cooling/exhumation starting at ca. 15 Ma.

240 Sample TU155 (Eocene sandstone from the Hakkâri Complex mélange; Fig. 2) shows a  
241 fairly tight single-grain age distribution and a leptokurtic and unimodal track-length distribution  
242 (Fig. 5A, C). This translates in a simple thermochrometric evolution (Fig. 5B). The best-fit curve  
243 (Fig. 5B) shows (i) a phase of progressive heating ranging from deposition to approximately 29  
244 Ma (latest Early Oligocene), followed by a phase of rather stable temperatures (29-13 Ma), in  
245 turn followed by rapid uplift starting in the mid-Miocene at about 12 Ma.

246 In summary, modeled samples come from a variety of rock types and tectonostratigraphic  
247 units, ranging from (i) polymetamorphosed Precambrian basement and (ii) its Paleozoic  
248 metasedimentary cover, to (iii) Eocene sediments incorporated in the frontal part of the Bitlis  
249 orogenic wedge and (iv) Early Oligocene foreland deposits from the Muş-Hınıs Basin north of  
250 the Bitlis-Pütürge Massif. Despite such heterogeneity, all analyzed samples point to a coherent  
251 thermochronometric history. Most remarkably, they show rather flat T-t paths during the  
252 Oligocene in the orogenic wedge and a sudden increase in the cooling/exhumation rate in the  
253 mid-Miocene, both in the orogenic wedge and the adjacent foreland.

254 Areal distribution of radiometric ages (Fig. 6) provide important clues as to the strain  
255 distribution pattern through time, both in the collision zone and its European hinterland. Lower  
256 temperature radiometric systems (AFT and ZHe) yielded younger ages along a narrow belt  
257 coincident with the Bitlis-Pütürge collision zone. In the central portion of such belt AFT central  
258 ages cluster tightly between  $13.4 \pm 2.2$  and  $14.6 \pm 2.5$  Ma, i.e. in the mid-Miocene. This cluster  
259 resulted from the rapid passage of the samples across the apatite PAZ (ca. 120-60°C) and  
260 registered the last significant cooling/exhumation event suffered by the analyzed rock units.  
261 Integrated statistical modeling of all available thermochronological constraints (Ar/Ar, Rb/Sr,  
262 U/Pb, ZHe, AFT, stratigraphic relationships) confirm the importance of this sharp and discrete  
263 mid-Miocene cooling episode (Figs. 3-5).

264 AFT central ages from samples taken north of the Bitlis collision zone range consistently  
265 between 48.8 and 35.9 Ma (Middle-Late Eocene), not only in the study area but across a wide  
266 area comprising most of the eastern Anatolian plateau (Albino et al., 2014), and were not affected  
267 by later cooling/exhumation. Middle-Late Eocene cooling is coeval with final closure of the  
268 northern Neotethyan branch and the development of the Izmir-Ankara-Erzincan suture zone  
269 (Okay and Tüysüz, 1999; Stampfli and Hochard, 2004).

270 Results yielded by radiometric systems characterized by a higher closure temperature are  
271 age coherent and do not show any areal variation (Fig. 6). In fact, metamorphic rocks of the  
272 Bitlis-Pütürge Massif, as well as the other scattered outcrop of metamorphic rocks farther to the  
273 north all yielded Late Cretaceous (Campanian-Maastrichtian) metamorphic ages (Hempton,  
274 1985; Oberhänsli et al., 2010, 2012, 2013; Karaoglan et al., 2013; Rolland et al., 2012). Recent  
275 radiometric data by Topuz et al. (2017) indicate that the entire width of the eastern Anatolian  
276 Plateau, from the Erzincan-Sevan-Akera suture zone to the north to the Bitlis suture zone to the

277 south bears the marks of such Late Cretaceous metamorphic event. This implies that the cause of  
278 such metamorphism is not to be searched along the Bitlis collision zone.

279

## 280 **DISCUSSION**

281       The stratigraphy of the northernmost sector of the Arabian platform provides a compelling  
282 record of the tectonic evolution of the adjacent Bitlis-Pütürge orogenic prism as it has been the  
283 lower plate of the Arabia-Eurasia subduction/collision zone during the entire Cenozoic. Two  
284 coarse-grained clastic inputs punctuate the stratigraphy of the northern Arabian platform south of  
285 the collision zone. (1) The first one occurred in the Late Cretaceous (Late Campanian –  
286 Maastrichtian: Antak Fm, Tanjero Fm, and equivalents) and was related to the creation of  
287 structural relief, lithospheric flexure, and creation of accommodation resulting from widespread  
288 ophiolite obduction and related crustal shortening. Such discrete and important episode of  
289 ophiolite obduction along the Anatolide-Tauride and Arabian northern continental margins has  
290 been described from western Anatolia to Oman (e.g. Coleman, 1981; Okay et al., 2001;  
291 Robertson, 2002) and is discussed below. (2) The second influx of coarse-grained clastics  
292 occurred in the Late Miocene (Şelmo Fm and its lateral equivalents) and it is commonly  
293 interpreted as the onset of hard collision. These two clastic intervals are separated by Paleogene  
294 carbonate sediments and no coherent collision-related foreland basin stratigraphy for the  
295 Oligocene can be outlined (Fig. 7). If the Arabia-Eurasia collision took place in the Oligocene  
296 one would expect the presence of large volumes of orogen-derived sediments on the flexured  
297 lower (Arabian) plate, whereas the Oligocene succession south of the Bitlis-Pütürge orogenic  
298 prism lacks any evidence of synorogenic sedimentation. The Oligocene stratigraphic hiatus -  
299 considered by some as evidence of collision-related tectonic deformation- may well be explained

300 taking into account the Oligocene eustatic sealevel lowstand, one of the largest in Earth's history.  
301 Miller et al. (2008) concluded that a glacioeustatic selevel lowering of 55 m occurred in the  
302 Early Oligocene (35.7-33.5 Ma). Such sealevel fall produced dramatic paleoenvironmental and  
303 stratigraphic changes in the Arabian flatlands (Nairn and Alsharhan, 1997; Jassim and Goff,  
304 2006) and can account for the widespread Oligocene nondepositional hiatus. Therefore, we  
305 conclude that there is no stratigraphic evidence on the Arabian margin for an Oligocene collision  
306 with the Anatolide-Tauride terrane to the north. The thermochronometric reconstructions  
307 presented here (Figs. 3-5) underline the absence of significant Oligocene cooling/exhumation  
308 along the southern margin of the Anatolide-Tauride terrane and point instead to rapid  
309 cooling/exhumation in the Miocene, in agreement with field stratigraphic and structural  
310 relationships. A subsidence curve from the portion of the Muş-Hınıs retroarc foreland basin north  
311 of Lake Van also show a discrete episode of uplift in the mid-Miocene within the overall context  
312 of protracted subsidence typical of upper-plate (retroarc) foreland basins (Fig. 8).

313 Geological field evidence indicates that a large area south of the Erzincan-Sevan suture  
314 was covered by mid-Campanian time by a series of large obducted ophiolites. These took the  
315 form of either large, relatively coherent slabs now cropping out as klippen or widespread  
316 *mélange* bodies (Bilgic, 2002; Günay and Şenel, 2002; Şenel and Ercan, 2002; Tarhan, 2002). At  
317 the same time, the same area experienced HP/LT metamorphism (Hempton, 1985; Okay et al.,  
318 1995, Oberhaensli et al., 2010, 2012, 2013; Rolland et al., 2012; Topuz et al., 2017). For  
319 example, across the Pütürge Massif the basement complex and the metamorphic sole of the  
320 overlying ophiolitic nappes yielded virtually the same Late Cretaceous metamorphic ages  
321 [ $77.5 \pm 0.7$  Ma (Ar/Ar on phengites) and  $78.7 \pm 1.0$  Ma (Ar/Ar on amphibole), respectively)] (Fig.  
322 3D, Table 3). North of the Pütürge Massif other scattered inliers of metasedimentary rocks

323 interspersed within the widespread volcano-sedimentary cover of the Anatolian Plateau yielded  
324 consistent Late Cretaceous metamorphic ages (Topuz et al., 2017). The radiometric dataset is far  
325 from being complete, but the picture emerging in eastern Anatolia is one of a coherent  
326 metamorphic event across the entire area comprised between the Erzincan-Sevan suture to the  
327 north and the Assyrian suture to the south. This metamorphism is coeval with massive southward  
328 ophiolite obduction from the northern branch of the Neotethys onto the Anatolide-Tauride  
329 terrane (Stampfli and Hochard, 2009) (Fig. 9A).

330         In the past, the pre-Neogene basement of the Eastern Anatolia plateau has been interpreted  
331 as consisting largely of an accretionary prism spanning –north to south– the distance from the  
332 eastern Pontides to the Bitlis collision zone (Eastern Anatolia accretionary complex–EAAC;  
333 Şengör and Yılmaz, 1981; Şengör et al., 2003). The EAAC concept has had wide resonance and  
334 is now ingrained in the scientific literature. More recent field and laboratory data indicate that  
335 eastern Anatolia is instead characterized by continental rock assemblages that underwent high-  
336 temperature and medium-pressure metamorphism at middle- to lower-crustal depths during the  
337 Late Cretaceous (Yılmaz et al., 2010; Topuz et al., 2017), as discussed above. These continental  
338 rock assemblages are tectonically overlain by disrupted ophiolites or ophiolitic mélange  
339 obducted in the Late Cretaceous and then pushed southward during the closure of the northern  
340 branch of the Neotethys and the ensuing development of the Izmir-Ankara-Erzincan suture zone  
341 (e.g., Okay and Tüysüz, 1999). The synchronicity of obduction and widespread metamorphism  
342 as well as the structural relationship between the ophiolites and the underlying continental  
343 basement support the hypothesis that the emplacement of a large ophiolitic nappe complex was  
344 responsible for diffuse deformation and metamorphism of the underlying Paleozoic sedimentary  
345 cover of the Proterozoic basement complex of the Anatolide-Tauride terrane. According to

346 Topuz et al. (2017), there is no indication of major strike-slip faults which might have interposed  
347 the continental fragments within the ophiolites and hence the scattered metamorphic inliers are  
348 the evidence of a more or less continuous continental substrate overthrust by the ophiolitic nappe  
349 complex. Ophiolite obduction took place in the Campanian (Fig. 9A), but southward tectonic  
350 transport of ophiolitic nappes (possibly including also sections of the underlying metamorphosed  
351 Paleozoic sedimentary cover of the Anatolide-Tauride terrane) continued during the  
352 Maastrichtian and the Paleocene (Fig. 9B) as the collision between the Anatolide-Tauride and  
353 Sakarya terranes was progressing. By the Middle Eocene (Fig. 9C) collision along the Izmir-  
354 Ankara-Erzincan suture zone was complete and subduction jumped to the southern margin of the  
355 Anatolide-Tauride terrane. The convergence rate between Africa and the southern margin of  
356 Eurasia –actually a collage of Gondwana-derived exotic terranes– had decreased, the subducting  
357 slab was affected by roll-back, and the upper plate was being extended. Such extension is  
358 recorded by the Maden Complex, a mid-Eocene volcano-sedimentary succession developed in a  
359 back-arc basin (Yiğitbaş and Yılmaz, 1996) and presently occurring as intensely deformed  
360 tectonostratigraphic units within the Bitlis-Puturge orogenic wedge. Widespread extension along  
361 the southern margin of the Anatolide-Tauride terrane as recorded by the Maden basin(s) is hardly  
362 compatible with the notion of an Eocene Arabia-Eurasia collision.

363         Low-temperature thermochronological data for the Eurasian foreland north of the Bitlis-  
364 Pütürge suture zone suggest that the tectonic stresses related to the Arabian collision were  
365 transmitted efficiently over large distances, focusing preferentially at rheological discontinuities  
366 located as far as the Eastern Pontides and the Lesser Caucasus (Albino et al., 2014; Cavazza et  
367 al., 2015). Stress focused either (i) along the marked rheological difference between the  
368 polydeformed continental lithosphere of the Eastern Pontides and the relatively pristine quasi-

369 oceanic lithosphere of the eastern Black Sea or (ii) along properly oriented segments of the  
370 Erzincan-Sevan-Akera suture zone. Since the late Middle Miocene a new tectonic regime is  
371 active as the westward translation of Anatolia is accommodating most of the Arabia-Eurasia  
372 convergence, thus decoupling the foreland from the orogenic wedge and precluding efficient  
373 northward stress transfer. As soon as the two plates were mechanically coupled, the inception of  
374 the Northern and Eastern Anatolian fault systems absorbed much of the plate convergence.  
375 Tectonic escape of Anatolia was preconditioned and facilitated by slab rollback along the  
376 Aegean subduction zone (Jolivet and Brun, 2010).

377

## 378 **CONCLUSIONS**

379 Noble gas and fission-track thermochronometric data -integrated with radiometric data  
380 from the literature and the analysis of field stratigraphic and structural relationships- constrain  
381 the overall thermal history of the Bitlis-Pütürge metamorphic complex, i.e. the area of maximum  
382 indentation along the Assyrian-Zagros continental collision zone. The dataset indicates  
383 widespread latest Cretaceous metamorphism of a passive margin sedimentary sequence and its  
384 igneous basement along the suture zone and across the entire width of the Anatolia-Tauride  
385 block north of the suture. Such metamorphism is likely related to extensive southward obduction  
386 of oceanic lithosphere from the northern branch of the Neotethys onto the northern continental  
387 margin of the Anatolide-Tauride block. Evidence for this interpretation lies in the occurrence of  
388 Late Cretaceous metamorphic rocks extending from the Izmir-Ankara-Erzincan suture to the  
389 north to the Bitlis-Pütürge metamorphic complex to the south. The basement complex of the  
390 Bitlis and Pütürge massifs along the suture was then rapidly exhumed between ca. 65 and 55 Ma  
391 and eventually overlain by Eocene shallow marine sediments. Integrated statistical modeling



392 shows that the Oligocene thermochronometric evolution of the orogen was rather featureless,  
393 contrary to the widely held belief that this epoch marked the beginning of the Arabia-Eurasia  
394 collision and was thus characterized by widespread deformation. Conversely, during the Middle  
395 Miocene, the Bitlis-Pütürge orogenic wedge was rapidly and significantly deformed both by (i)  
396 frontal accretion, as shown by cooling/exhumation of the foreland deposits on both sides of the  
397 orogenic prism, and (ii) underplating, as shown by cooling/exhumation of the central  
398 metamorphic core of the orogenic wedge. Orogenic growth is also substantiated by the  
399 stratigraphy of the lower (Arabian) plate which shows the presence of a coarse-grained clastic  
400 wedge in the Middle Miocene as well as evidence of growth structures.

401       Taking into consideration that colliding continental margins are morphologically irregular  
402 and strain sequences are commonly diachronous along the strike of suture zones (Dewey et al.,  
403 1986), we emphasize that the results of this study applies only to the Bitlis- Pütürge sector of the  
404 Arabia-Eurasia collision zone and should not be necessarily applied also to the Zagros collision  
405 front to the southeast.

406

#### 407 **ACKNOWLEDGMENTS**

408       Thanks to Olivier Lacombe, Federico Rossetti and Gerard Stampfli for fruitful discussions.  
409 This research was funded by MIUR (Italian Ministry of Education, University and Research) and  
410 the University of Bologna (RFO funds).

411

#### 412 **REFERENCES CITED**

- 413 Agard, P., Omrani, J., Jolivet, L., and Mouthereau, F., 2005, Convergence history across Zagros  
414 (Iran): constraints from collisional and earlier deformation. *International Journal of Earth*  
415 *Sciences*, v. 94, p. 401-419.
- 416 Akay, E., Erkan, E., and Ünay, E., 1989, Stratigraphy of the Tertiary Muş basin [in Turkish]:  
417 *MTA Journal*, v. 109, p. 59-76.
- 418 Alavi, M., 1994, Tectonics of the Zagros orogenic belt of Iran: new data and interpretations.  
419 *Tectonophysics*, v. 229, p. 211-238.
- 420 Albino, I., Cavazza, W., Zattin, M., Okay, A.I., Adamia, S., and Sadradze N., 2014, Far-field  
421 tectonic effects of the Arabia-Eurasia collision and the inception of the North Anatolian  
422 Fault system: *Geological Magazine*, v. 151, p. 372-379.
- 423 Allen, M.B., and Armstrong, H.A., 2008, Arabia–Eurasia collision and the forcing of mid-  
424 Cenozoic global cooling: *Palaeogeography, Palaeoclimatology, Palaeoecology*, v. 265, p.  
425 52-58.
- 426 Barazangi, M., Sandvol, E., and Seber, D., 2006, Structure and tectonic evolution of the  
427 Anatolian plateau in eastern Turkey: *Geological Society of America Special Papers*, v. 409,  
428 p. 463-473.
- 429 Barrier, E., and Vrielynck, B., eds. 2008, *Palaeotectonic maps of the Middle East – Middle East*  
430 *Basins Evolution (MEBE) Programme: Commission for the Geological Map of the World*  
431 (Paris).
- 432 Berberian, M., and King, G.C.P., 1981, Towards a paleogeography and tectonic evolution of  
433 Iran: *Canadian Journal of Earth Sciences*, v. 18, p. 210-265.
- 434 Bilgic, T., 2002, 1: 500,000 Turkey Geological Map. Sheet Sivas.
- 435 Cavazza, W., Albino, I., Zattin, M., Galoyan, G., Imamverdiyev, N. and Melkonyan, R., 2015,

436           Thermochronometric evidence for Miocene tectonic reactivation of the Sevan-Akera suture  
437           zone (Lesser Caucasus): a far-field tectonic effect of the Arabia-Eurasia collision?  
438           Geological Society of London Special Publication 428, doi: 10.1144/SP428.4.

439 Coleman, R.G., 1981, Tectonic setting for ophiolite obduction in Oman. *Journal of Geophysical*  
440           *Research: Solid Earth*, v. 86, p. 2497-2508.

441 Dewey, J.F., Hempton, M.R., Kidd, W.S.F., Saroglu, F.A.M.C., and Şengör, A.M.C., 1986,  
442           Shortening of continental lithosphere: the neotectonics of Eastern Anatolia—a young  
443           collision zone: Geological Society, London, Special Publications, v. 19, p. 1-36.

444 Donelick, R.A., O’Sullivan, P.B., and Ketcham, R.A., 2005, Apatite fission-track analysis:  
445           Reviews in Mineralogy and Geochemistry, v. 58, p. 49-94.

446 Ehlers, T.A., Chaudhri, T., Kumar, S., Fuller, C.W., Willett, S.D., Ketcham, R.A., Brandon,  
447           M.T., Belton, D.X., Kohn, B.P., Gleadow, A.J. and Dunai, T.J., 2005, Computational tools  
448           for low-temperature thermochronometer interpretation: *Reviews in Mineralogy and*  
449           *Geochemistry*, v. 58, p. 589-622.

450 Gleadow, A.J.W., and Fitzgerald, P.G., 1987, Uplift history and structure of the Transantarctic  
451           Mountains: new evidence from fission track dating of basement apatites in the Dry Valleys  
452           area, southern Victoria Land: *Earth and Planetary Science Letters*, v. 82, p. 1-14.

453 Göncüoğlu, M.C., and Turhan, N., 1984, Geology of the Bitlis metamorphic belt. In *International*  
454           *Symposium on Geology of the Taurus Belt: Proceedings of the Mineral Research and*  
455           *Exploration Institute of Turkey, Ankara*, p. 237-244.

456 Günay, Y. and Şenel, M., 2002, 1: 500,000 Turkey Geological Map. Sheet Cizre.

457 Hall, R., 1976, Ophiolite emplacement and the evolution of the Taurus suture zone, southeastern  
458           Turkey. *Geological Society of America Bulletin*, 87(7), pp.1078-1088.

- 459 Hempton, M.R., 1985, Structure and deformation history of the Bitlis suture near Lake Hazar,  
460 southeastern Turkey: *Geological Society of America Bulletin*, v. 96, p. 233-243.
- 461 Hourigan, J.K., Reiners, P.W., and Brandon, M.T., 2005, U-Th zonation-dependent alpha-  
462 ejection in (U-Th)/He chronometry: *Geochimica et Cosmochimica Acta*, v. 69, p. 3349-  
463 3365.
- 464 Hurford, A.J., and Green, P.F., 1983, The zeta age calibration of fission-track dating: *Chemical*  
465 *Geology*, v. 41, p. 285-317.
- 466 Hüsing, S.K., Zachariasse, W.J., Van Hinsbergen, D.J., Krijgsman, W., Inceöz, M., Harzhauser,  
467 M., Mandic, O., and Kroh, A., 2009, Oligocene–Miocene basin evolution in SE Anatolia,  
468 Turkey: constraints on the closure of the eastern Tethys gateway: *Geological Society*,  
469 *London, Special Publications*, v. 311, p. 107-132.
- 470 Huvaz, O., 2009, Comparative petroleum systems analysis of the interior basins of Turkey:  
471 implications for petroleum potential: *Marine and Petroleum Geology*, v. 26, p. 1656-1676.
- 472 Jassim, S.Z., and Goff, J.C. (eds.), 2006, *Geology of Iraq*. DOLIN sro, distributed by Geological  
473 Society of London, 341 p.
- 474 Jolivet, L., and Brun, J.P., 2010, Cenozoic geodynamic evolution of the Aegean: *International*  
475 *Journal of Earth Sciences*, v. 99, p. 109-138.
- 476 Jolivet, L., and Faccenna, C., 2000, Mediterranean extension and the Africa- Eurasia collision:  
477 *Tectonics*, v. 19(6), p. 1095-1106.
- 478 Karaoğlan, F., Parlak, O., Robertson, A., Thöni, M., Klötzli, U., Koller, F., and Okay, A.I., 2013,  
479 Evidence of Eocene high-temperature/high-pressure metamorphism of ophiolitic rocks and  
480 granitoid intrusion related to Neotethyan subduction processes (Doğanşehir area, SE  
481 Anatolia): *Geological Society, London, Special Publications*, v. 372, p. 249-272.

- 482 Ketcham, R.A., 2005, Forward and inverse modeling of low-temperature thermochronometry  
483 data: *Reviews in Mineralogy and Geochemistry*, v. 58(1), p. 275-314.
- 484 Ketcham, R.A., Donelick, R.A., and Carlson, W.D., 1999, Variability of apatite fission-track  
485 annealing kinetics: III. Extrapolation to geological time scales: *American Mineralogist*, v.  
486 84(9), p. 1235-1255.
- 487 Ketcham, R.A., Carter, A., Donelick, R.A., Barbarand, J., and Hurford, A.J., 2007, Improved  
488 modeling of fission-track annealing in apatite: *American Mineralogist*, v. 92(5-6), p. 799-  
489 810.
- 490 Kiliç, A.D., and Ateş, C., 2015, Geochronology of the Late Cretaceous magmatism and  
491 metamorphism, Pütürge massif, Turkey: *Acta Petrologica Sinica*, v. 31, p. 1485-1493.
- 492 Le Pichon, X., and Kreemer, C., 2010, The Miocene-to-present kinematic evolution of the  
493 eastern Mediterranean and Middle East and its implications for dynamics: *Annual Review*  
494 *of Earth and Planetary Sciences*, v. 38, p. 323-351.
- 495 McQuarrie, N., and van Hinsbergen, D. J., 2013, Retrodeforming the Arabia-Eurasia collision  
496 zone: Age of collision versus magnitude of continental subduction: *Geology*, v. 41, p. 315-  
497 318.
- 498 Miller, K.G., Browning, J.V., Aubry, M.P., Wade, B.S., Katz, M.E., Kulpecz, A.A., and Wright,  
499 J.D., 2008, Eocene–Oligocene global climate and sea-level changes: St. Stephens Quarry,  
500 Alabama: *Geological Society of America Bulletin*, v. 120, p. 34-53.
- 501 Nairn, A.E.M., and Alsharhan, A.S., 1997, Sedimentary basins and petroleum geology of the  
502 Middle East: Elsevier, 878 p.
- 503 Oberhänsli, R., Bousquet, R., Candan, O., and Okay, A.I., 2012, Dating subduction events in East  
504 Anatolia, Turkey: *Turkish Journal of Earth Sciences*, v. 21, p. 1-17.

- 505 Oberhänsli, R., Candan, O., Bousquet, R., Rimmele, G., Okay, A.I., and Goff, J., 2010, Alpine  
506 high pressure evolution of the eastern Bitlis complex, SE Turkey: Geological Society,  
507 London, Special Publications, vol. 340, p. 461-483.
- 508 Oberhänsli, R., Koralay, E., Candan, O., Pourteau, A., and Bousquet, R., 2013, Late Cretaceous  
509 eclogitic high-pressure relics in the Bitlis Massif: *Geodinamica Acta*, v. 26, p. 175-190.
- 510 Okay, A.I., 2008, Geology of Turkey: a synopsis: *Anschnitt*, v. 21, p. 19-42.
- 511 Okay, A.I., Arman, M.B., and Göncüoğlu, M.C., 1985, Petrology and phase relations of the  
512 kyanite-eclogites from eastern Turkey: *Contributions to Mineralogy and Petrology*, v. 91,  
513 p. 196-204.
- 514 Okay, A.I., Tansel, İ., and Tüysüz, O., 2001, Obduction, subduction and collision as reflected in  
515 the Upper Cretaceous–Lower Eocene sedimentary record of western Turkey. *Geological*  
516 *Magazine*, v. 138, p. 117-142.
- 517 Okay, A.I., and Tüysüz, O., 1999, Tethyan sutures of northern Turkey: Geological Society,  
518 London, Special Publications, v. 156, p. 475-515.
- 519 Okay, A.I., Zattin, M., and Cavazza, W., 2010, Apatite fission-track data for the Miocene  
520 Arabia-Eurasia collision: *Geology*, v. 38, p. 35–38.
- 521 Perinçek, D., 1990, Stratigraphy of the Hakkâri province, southeast Turkey [in Turkish]: *TAPG*  
522 *Bulletin*, v. 2/1, p. 21-68.
- 523 Reiners, P.W., and Brandon, M.T., 2006, Using thermochronology to understand orogenic  
524 erosion. *Annual Review Earth Planetary Sciences*, v. 34, p. 419-466.
- 525 Robertson, A.H.F., 2002, Overview of the genesis and emplacement of Mesozoic ophiolites in  
526 the Eastern Mediterranean Tethyan region: *Lithos*, v. 65, p. 1-67.

- 527 Robertson, A.H.F., Parlak, O., Rizaoglu, T., Ünlügenç, Ü., İnan, N., Tasli, K., and Ustaömer, T.,  
528 2007, Tectonic evolution of the South Tethyan ocean: evidence from the Eastern Taurus  
529 Mountains (Elazığ region, SE Turkey): Geological Society, London, Special Publications,  
530 v. 272, p. 231-270.
- 531 Rolland, Y., Perinçek, D., Kaymakci, N., Sosson, M., Barrier, E., and Avagyan, A., 2012,  
532 Evidence for ~80–75Ma subduction jump during Anatolide–Tauride–Armenian block  
533 accretion and ~48Ma Arabia–Eurasia collision in Lesser Caucasus–East Anatolia: Journal  
534 of Geodynamics, v. 56, p. 76-85.
- 535 Sancay, R.H., Bati, Z., and Işik, U., 2006, Palynomorph, foraminifera, and calcareous  
536 nannoplankton biostratigraphy of Oligo–Miocene sediments in the Muş basin, eastern  
537 Anatolia, Turkey: Turkish Journal of Earth Sciences, v. 15, p. 259-319.
- 538 Şenel, M., and Ercan, T., 2002, 1: 500,000 Turkey Geological Map. Sheet Van.
- 539 Şengör, A.M.C., Özeren, S., Genc, T., and Zor, E., 2003, East Anatolian high plateau as a  
540 mantle-supported, north-south shortened domal structure: Geophysical Research Letters, v.  
541 30, p. 8045, doi:10.1029/2003GL017858.
- 542 Şengör, A.M.C., and Kidd, W.S.F., 1979, Post-collisional tectonics of the Turkish-Iranian  
543 plateau and a comparison with Tibet: Tectonophysics, v. 55, p. 361-376.
- 544 Şengör, A.M.C., and Yılmaz, Y., 1981, Tethyan evolution of Turkey: A plate tectonic approach:  
545 Tectonophysics, v. 75, p. 181–241.
- 546 Stampfli, G. M., and Hochard, C., 2009, Plate tectonics of the Alpine realm: Geological Society,  
547 London, Special Publication 327, p. 89-111.
- 548 Tarhan, N., 2002, 1: 500,000 Turkey Geological Map. Sheet Erzurum. Maden Tetkik ve Arama  
549 Genel Müdürlüğü, Ankara, 2nd edition.

- 550 Topuz, G., Candan, O., Zack, T., and Yılmaz, A., 2017, East Anatolian Plateau constructed over  
551 a continental basement: No evidence for the East Anatolian Accretionary Complex:  
552 Geology, in press.
- 553 Yazgan, E., Michard, A., Whitechurch, H., and Montigny, R., 1983, Le Taurus de Malatya  
554 (Turquie orientale), élément de la suture sud-téthysienne: Bull. Soc. Géol. France, v. 25, p.  
555 59-69.
- 556 Yiğitbaş, E., and Yılmaz, Y., 1996, New evidence and solution to the Maden complex  
557 controversy of the Southeast Anatolian orogenic belt (Turkey): Geologische Rundschau, v.  
558 85, p.250-263.
- 559 Yılmaz, A., Adamia, S., and Yılmaz, H., 2014, Comparisons of the suture zones along a  
560 geotraverse from the Scythian Platform to the Arabian Platform: Geoscience Frontiers, v.  
561 5, p. 855-875.
- 562 Yılmaz, A., Yılmaz, H., Kaya, C., and Boztug, D., 2010, The nature of the crustal structure of the  
563 Eastern Anatolian Plateau, Turkey: Geodinamica Acta, v. 23, p. 167-183.
- 564 Yılmaz, E., and Duran, O., 1997, Stratigraphic lexicon for the autochthonous and allochthonous  
565 units of Southeast Anatolia [in Turkish]. Türkiye Petrolleri A.O. Research Center,  
566 Publication No. 31, 460 p.
- 567 Yılmaz, Y., 1993, New evidence and model on the evolution of the southeast Anatolian orogen:  
568 Geological Society of America Bulletin, v. 105, p. 251-271.

569

## 570 **FIGURE CAPTIONS**

- 571 Figure 1. Overall tectonic sketch map of the Middle East. The box indicates the area shown in  
572 Fig. 2. AT–Anatolide-Tauride terrane, IZ–Istanbul Zone, SkZ–Sakarya Zone, KM–Kırşehir



573 Massif, NAF–North Anatolian Fault, EAF–Eastern Anatolian Fault, EP–Eastern Pontides,  
574 IAESZ–Izmir-Ankara-Erzincan suture zone, SASZ–Sevan-Akera suture zone, GC–Greater  
575 Caucasus, LC–Lesser Caucasus. GPS vectors from LePichon and Kreemer (2010).

576 Figure 2. Geological sketch map of the Bitlis–Pütürge collision zone of southeastern Turkey  
577 (after Bilgic, 2002; Günay and Şenel, 2002; Şenel and Ercan, 2002; Tarhan, 2002).

578 Figure 3. Summary of analytical results for sample TU-149 (Precambrian gneiss; Pütürge  
579 Massif) and geological cross-section A-A' (see Figure 2 for location). For details on  
580 radiometric ages reported in the figure, see Table 3. EAF–East Anatolian fault. A. Radial  
581 plots of single-grain apatite fission-track ages. B. Time-temperature paths obtained from  
582 integrated inverse modeling of apatite fission-track data (this study), (U-Th)/He analyses  
583 on zircons (this study), Ar-Ar analysis on biotites, U/Pb on zircons (Kiliç and Ateş, 2014).  
584 Green areas mark envelopes of statistically acceptable fit, and the thicker lines correspond  
585 to the most probable thermal histories: red line is the mean of all statistically acceptable  
586 paths; blue line is the best-fit T-t path. Parameters related to inverse modeling are reported:  
587 GOF, goodness-of-fit gives an indication about the fit between observed and predicted data  
588 (values closer to 1 are best). C. Histogram showing the confined-track length distributions  
589 of apatite grains. D. Geological cross-section of the Pütürge Massif (redrawn from Yazgan  
590 et al., 1983). No vertical exaggeration. See Figure 2 for location of trace of section.

591 Figure 4. Summary of analytical results for samples TU-136 (Precambrian gneiss; Bitlis Massif)  
592 and TU-255 (Oligocene sandstone; Muş-Hınıs Basin). See Figure 2 for location. A. Radial  
593 plots of single-grain apatite fission-track ages. B. Time-temperature paths obtained from  
594 integrated inverse modeling of apatite fission-track data (this study), (U-Th)/He analyses  
595 on zircons (this study), Ar-Ar analysis on biotites, U/Pb on zircons (Kiliç and Ateş, 2014).

596 Green areas mark envelopes of statistically acceptable fit, and the thicker lines correspond  
597 to the most probable thermal histories: red line is the mean of all statistically acceptable  
598 paths; blue line is the best-fit T-t path. Parameters related to inverse modeling are reported:  
599 GOF, goodness-of-fit gives an indication about the fit between observed and predicted data  
600 (values closer to 1 are best). C. Histogram showing the confined-track length distributions  
601 of apatite grains. D. Geological cross-section of the central Bitlis Massif (redrawn from  
602 Yazgan et al., 1983). See Figure 2 for location of trace of section.

603 Figure 5. Summary of analytical results for sample TU-155 (Eocene sandstone). See Figure 2 for  
604 location. A. Radial plots of single-grain apatite fission-track ages. B. Time-temperature  
605 paths obtained from integrated inverse modeling of apatite fission-track data (this study)  
606 and (U-Th)/He analyses on zircons (this study). Green areas mark envelopes of statistically  
607 acceptable fit, and the thicker lines correspond to the most probable thermal histories: red  
608 line is the mean of all statistically acceptable paths; blue line is the best-fit T-t path.  
609 Parameters related to inverse modeling are reported: GOF, goodness-of-fit gives an  
610 indication about the fit between observed and predicted data (values closer to 1 are best). C.  
611 Histogram showing the confined-track length distributions of apatite grains. D. Geological  
612 cross-section of the eastern Bitlis Massif (redrawn from Perinçek, 1990).

613 Figure 6. Areal distribution of radiometric ages along the Bitlis- Pütürge collision zone and the  
614 Anatolian foreland. Apatite fission-track ages are from Table 1; ZrHe ages are from Table  
615 2; all other radiometric ages are from Table 3. Dashed orange line includes all AFT ages  
616 younger than 20 Ma; dashed red line includes all AFT ages younger than 15 Ma. Sources  
617 of data: <sup>a</sup>Okay et al., 2010; <sup>b</sup>Albino et al., 2013; <sup>c</sup>this paper; <sup>d</sup>Oberhänsli et al.,

618 2012; <sup>e</sup>Rolland et al., 2012; <sup>f</sup>Karaoglan et al., 2013; <sup>g</sup>Hempton, 1985; <sup>h</sup>Oberhänsli et al.,  
619 2013; <sup>i</sup>Topuz et al., 2017; <sup>j</sup>Oberhänsli et al., 2010.

620 Figure 7. Chronolithostratigraphic chart for the northernmost Arabian platform in Turkish  
621 territory (from Yılmaz and Duran, 1997).

622 Figure 8. Burial and subsidence history, isotherms, and vitrinite reflectance (%Ro) profile for the  
623 Malazgirt-1 well (for location, see Fig. 2) in the eastern Muş-Hınıs Basin (redrawn from  
624 Huvaz, 2009). Inception of subsidence at the Middle-Late Eocene transition coincides with  
625 the beginning of subduction along the southern margin of the Anatolide-Tauride block.  
626 Subsidence continued until the mid-Miocene in a foreland basin setting, when a discrete  
627 phase of inversion occurred.

628 Figure 9. Paleogeographic sketch maps for the Arabia-Eurasia collision (modified from Barrier  
629 and Vrielynck, 2008). EAP–eastern Anatolia platform, BPB–Bitlis-Pütürge block, EBB–  
630 eastern Black Sea basin, GCB–Greater Caucasus Basin, ION–Izmir-Ankara-Erzincan  
631 ophiolite nappes, KCN–Kizildag-Cilo ophiolite nappe, KsM–Kirsehir Massif, MoP–  
632 Moesian Platform, PAM–peri-Arabian massif, PoV–Pontide volcanic arc, SAM–Sevan-  
633 Akera ophiolitic massif, SkB–Sakarya Basin, SSB–Sanandaj-Sirjan block, TaP–Tauride  
634 platform, WBB–western Black Sea basin.

Table 1

**Table 1.** Apatite fission-track analytical data.

Sample	Coordinates (UTM)	Elevation (m)	Rock type	No. of crystals	Spontaneous		Induced		$P(\chi^2)$	Dosimeter		Age (Ma) $\pm$ 1 $\sigma$	Mean confined track length ( $\mu\text{m}$ ) $\pm$ std. err.	Std. dev.	No. of tracks measured
					$r_s$	$N_s$	$r_i$	$N_i$		$r_d$	$N_d$				
TU136	38S0251160 4260508	1642	Metasandstone	20	0.72	40	0.89	496	100.0	0.90	4293	13.4 $\pm$ 2.2	14.4 $\pm$ 0.2	1.24	51
TU138	38S0241967 4249698	1285	Gneiss	16	0.46	22	0.55	264	100.0	0.90	4281	13.8 $\pm$ 3.1	—	—	—
TU140	37S0753971 4234870	871	Sandstone	4	5.14	43	4.84	405	91.1	0.90	4256	17.5 $\pm$ 2.8	—	—	—
TU142	37S0634579 4267009	1208	Gneiss	—	—	—	—	—	—	—	—	—	—	—	—
TU145	37S0630748 4277901	1175	Metagranite	20	0.55	38	0.62	425	82.5	0.89	4219	14.6 $\pm$ 2.5	—	—	—
TU149	37S0476619 4240707	1395	Gneiss	20	1.60	112	1.44	1006	87.0	0.88	4181	18.0 $\pm$ 1.8	14.1 $\pm$ 0.2	1.35	72
TU151	38S0340100 4221763	2025	Chlorite schist	—	—	—	—	—	—	—	—	—	—	—	—
TU155	38S0321648 4195176	1607	Sandstone	20	0.88	53	1.18	711	65.1	1.01	4818	13.9 $\pm$ 2.1	15.2 $\pm$ 0.2	1.08	51
TU159	38S0396240 4162747	1342	Sandstone	6	0.53	14	0.39	102	75.4	1.00	4771	25.2 $\pm$ 7.2	—	—	—
TU255	37S 0750864 4293994	1339	Sandstone	17	1.98	122	0.65	481	76.4	14.30	4679	53.3 $\pm$ 1.7	13.7 $\pm$ 0.2	1.38	62

Note: Central ages were calculated using dosimeter glass CN5 and  $\zeta$ -CN5 = 367.45  $\pm$  4.35 (analyst MZ).  $\rho_s$ —spontaneous track densities ( $\times 10^5 \text{ cm}^{-2}$ ) measured in internal mineral surfaces;  $N_s$ —total number of spontaneous tracks;  $\rho_i$  and  $\rho_d$ —induced and dosimeter track densities ( $\times 10^6 \text{ cm}^{-2}$ ) on external mica detectors ( $g = 0.5$ );  $N_i$  and  $N_d$ —total numbers of tracks;  $P(\chi^2)$ —probability of obtaining  $\chi^2$  value for degrees of freedom (where  $v =$  number of crystals  $- 1$ ); a probability  $> 5\%$  is indicative of a homogeneous population. Samples with a probability  $< 5\%$  were analyzed with the binomial peak-fitting method.

Table 2

Table 2. Zircon (U-Th)/He analytical data.

Sample	Raw age $\pm 2\sigma$ (Ma)	$R_s$ (mm)	U (ppm)	Th (ppm)	$^4\text{He}$ (nmol/g)	eU (ppm)	$F_T$ $^{238}\text{U}$	$F_T$ $^{235}\text{U}$	$F_T$ $^{232}\text{Th}$	Fully $F_T$ corrected age $\pm \sigma$ (Ma)
<b>TU136</b>										
TU136_Zr2	29.1 $\pm$ 2.2	68.14	435.88	108.64	72.54	461.41	0.82	0.79	0.79	35.6 $\pm$ 1.3
TU136_Zr3	32.3 $\pm$ 2.4	42.95	481.88	47.34	85.92	493.00	0.72	0.68	0.68	44.7 $\pm$ 1.6
<b>TU138</b>										
TU138_Zr1	18.5 $\pm$ 0.4	47.77	124.65	99.64	14.84	148.07	0.75	0.71	0.71	25.0 $\pm$ 0.3
TU138_Zr2	14.6 $\pm$ 0.4	49.51	165.00	94.11	14.77	187.12	0.76	0.72	0.72	19.5 $\pm$ 0.3
TU138_Zr4	16.4 $\pm$ 1.2	43.92	179.84	129.11	18.58	210.18	0.73	0.69	0.69	22.7 $\pm$ 0.8
<b>TU142</b>										
TU142_Zr2	34.3 $\pm$ 1.0	45.66	290.36	165.57	60.99	329.27	0.74	0.70	0.70	46.7 $\pm$ 0.7
TU142_Zr3	31.0 $\pm$ 0.8	38.94	242.46	103.56	44.69	266.80	0.70	0.66	0.66	44.8 $\pm$ 0.6
TU142_Zr4	27.7 $\pm$ 0.8	37.19	848.49	1087.09	165.33	1103.95	0.68	0.64	0.64	41.1 $\pm$ 0.5
<b>TU145</b>										
TU145_Zr1	27.9 $\pm$ 0.8	47.59	2167.91	1338.95	374.41	2482.57	0.75	0.71	0.71	37.6 $\pm$ 0.5
TU145_Zr2	25.8 $\pm$ 0.6	46.71	2571.73	1405.04	403.87	2901.92	0.74	0.71	0.71	34.9 $\pm$ 0.4
TU145_3Zr	26.7 $\pm$ 0.8	39.25	1763.48	1100.76	292.26	2022.16	0.70	0.66	0.66	38.6 $\pm$ 0.5
<b>TU149</b>										
TU149_Zr1	22.7 $\pm$ 0.6	30.93	1266.33	152.64	159.53	1302.21	0.63	0.58	0.58	36.3 $\pm$ 0.5
TU149_Zr2	26.0 $\pm$ 0.8	35.12	957.69	161.95	139.60	995.75	0.67	0.62	0.62	39.0 $\pm$ 0.6
<b>TU151</b>										
TU151_Zr1	53.3 $\pm$ 1.4	57.85	187.51	62.56	58.40	202.21	0.790	0.759	0.759	67.7 $\pm$ 0.9
TU151_Zr2	37.9 $\pm$ 1.2	35.96	300.57	49.24	63.99	312.14	0.675	0.630	0.630	56.4 $\pm$ 0.8
TU151_Zr3	46.8 $\pm$ 1.4	68.42	571.51	108.53	151.36	597.02	0.820	0.794	0.794	57.2 $\pm$ 0.8
<b>TU155</b>										
TU155_Zr3	17.5 $\pm$ 0.4	35.69	327.44	262.55	36.75	389.14	0.672	0.628	0.628	26.3 $\pm$ 0.3

$F_T$  = retentivity of alpha particle in a sphere of varying radius;  $R_s$  = equivalent sphere radius.

Table 3

**Table 3.** Compilation of preexisting radiometric data.

Sample	Rock type	Coordinates (UTM)	Dated mineral	Method	Age (Ma)	$\pm\sigma$ (Ma)
<b>Bitlis</b>						
VAN 26 <sup>a</sup>	metapelite	-	muscovite	<sup>40</sup> Ar/ <sup>39</sup> Ar	69.8	0.4
VAN 27 <sup>a</sup>	metapelite	-	muscovite	<sup>40</sup> Ar/ <sup>39</sup> Ar	69.2	0.7
VAN 29 <sup>a</sup>	metapelite	-	muscovite	<sup>40</sup> Ar/ <sup>39</sup> Ar	68.8	2.2
VAN 36 <sup>a</sup>	metapelite	-	muscovite	<sup>40</sup> Ar/ <sup>39</sup> Ar	68.0	0.7
VAN 75 <sup>a</sup>	metapelite	-	muscovite	<sup>40</sup> Ar/ <sup>39</sup> Ar	73.8	7.7
VAN 75A <sup>a</sup>	metapelite	-	muscovite	<sup>40</sup> Ar/ <sup>39</sup> Ar	73.8	7.7
VAN 76 <sup>a</sup>	metapelite	-	muscovite	<sup>40</sup> Ar/ <sup>39</sup> Ar	76.0	0.7
VAN 77 <sup>a</sup>	metapelite	-	muscovite	<sup>40</sup> Ar/ <sup>39</sup> Ar	78.8	0.6
VAN 75 <sup>b</sup>	metapelite	-	phengite	<sup>40</sup> Ar/ <sup>39</sup> Ar	73.8	7.7
VAN 75A <sup>b</sup>	metapelite	-	phengite	<sup>40</sup> Ar/ <sup>39</sup> Ar	73.6	4.4
B157-1 <sup>g</sup>	eclogite	-	zircon	U–Pb	82.4	0.9
B157-2 <sup>g</sup>	eclogite	-	zircon	U–Pb	84.4	0.9
<b>Pütürge</b>						
Loc28 <sup>c</sup>	micaschist	37N 477060.9 4217244.7	phengite	<sup>40</sup> Ar/ <sup>39</sup> Ar	77.5	0.7
Loc59 <sup>c</sup>	amphibolites	37N 431046.1 4230447.3	amphibole	<sup>40</sup> Ar/ <sup>39</sup> Ar	47.1	1.2
13TK51 <sup>d</sup>	augen gneiss	-	zircon	U–Pb	551	6
13TK54 <sup>d</sup>	augen gneiss	-	zircon	U–Pb	544	4
Sample <sup>f</sup>	micaschist	-	whole-rock	K–Ar	71.2	3.6
dk704 <sup>h</sup>	metagranitic gneiss	-	zircon	U–Pb	84.2	1.1
dk173.8 <sup>h</sup>	metapelitic shist	-	biotite	<sup>40</sup> Ar/ <sup>39</sup> Ar	83.21	0.07
<b>Maden</b>						
Loc46 <sup>c</sup>	gabbro	37N 484693.9 4254696.6	amphibole	<sup>40</sup> Ar/ <sup>39</sup> Ar	79.9	0.4
Loc46(duplicate) <sup>c</sup>	gabbro	37N 484693.9 4254696.7	amphibole	<sup>40</sup> Ar/ <sup>39</sup> Ar	77.5	0.7
<b>Keban-Malatya</b>						
Loc49 <sup>c</sup>	marble	37N 476355.5 4296643.1	muscovite	<sup>40</sup> Ar/ <sup>39</sup> Ar	73.0	0.5
<b>Ophiolite</b>						
FK10 <sup>e</sup>	rhyolite	-	zircon	U–Pb	74.6	4.4
FK48 <sup>e</sup>	rhyolite	-	zircon	U–Pb	83.1	2.2

<sup>a</sup> Oberhänsli et al., 2012<sup>d</sup> Oberhänsli et al., 2010<sup>c</sup> Rolland et al., 2012<sup>a</sup> Beyarslan et al., 2016<sup>e</sup> Karaoglan et al., 2013<sup>f</sup> Hempton, 1985<sup>g</sup> Oberhänsli et al., 2013<sup>h</sup> Kiliç et Ateş, 2013

Figure 1

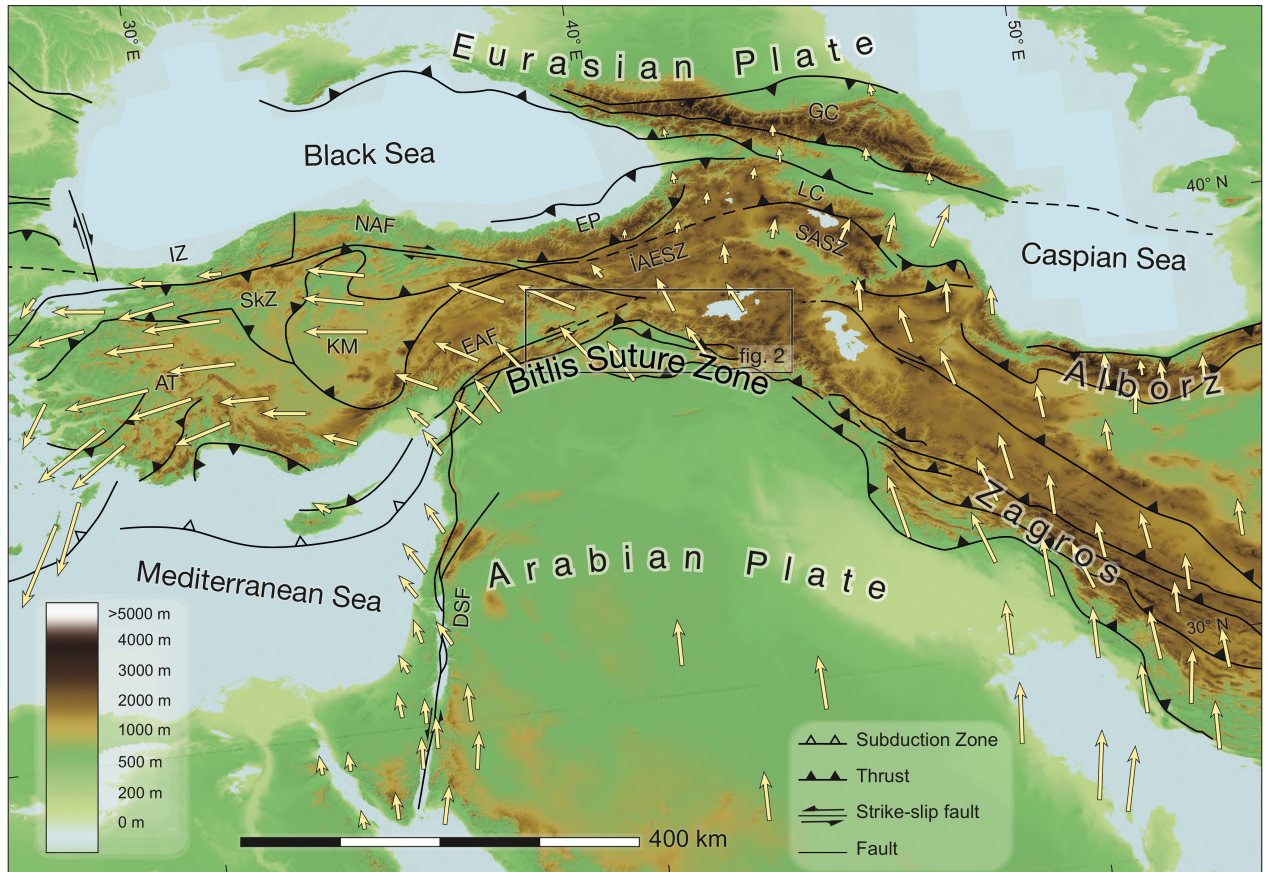


Figure 2

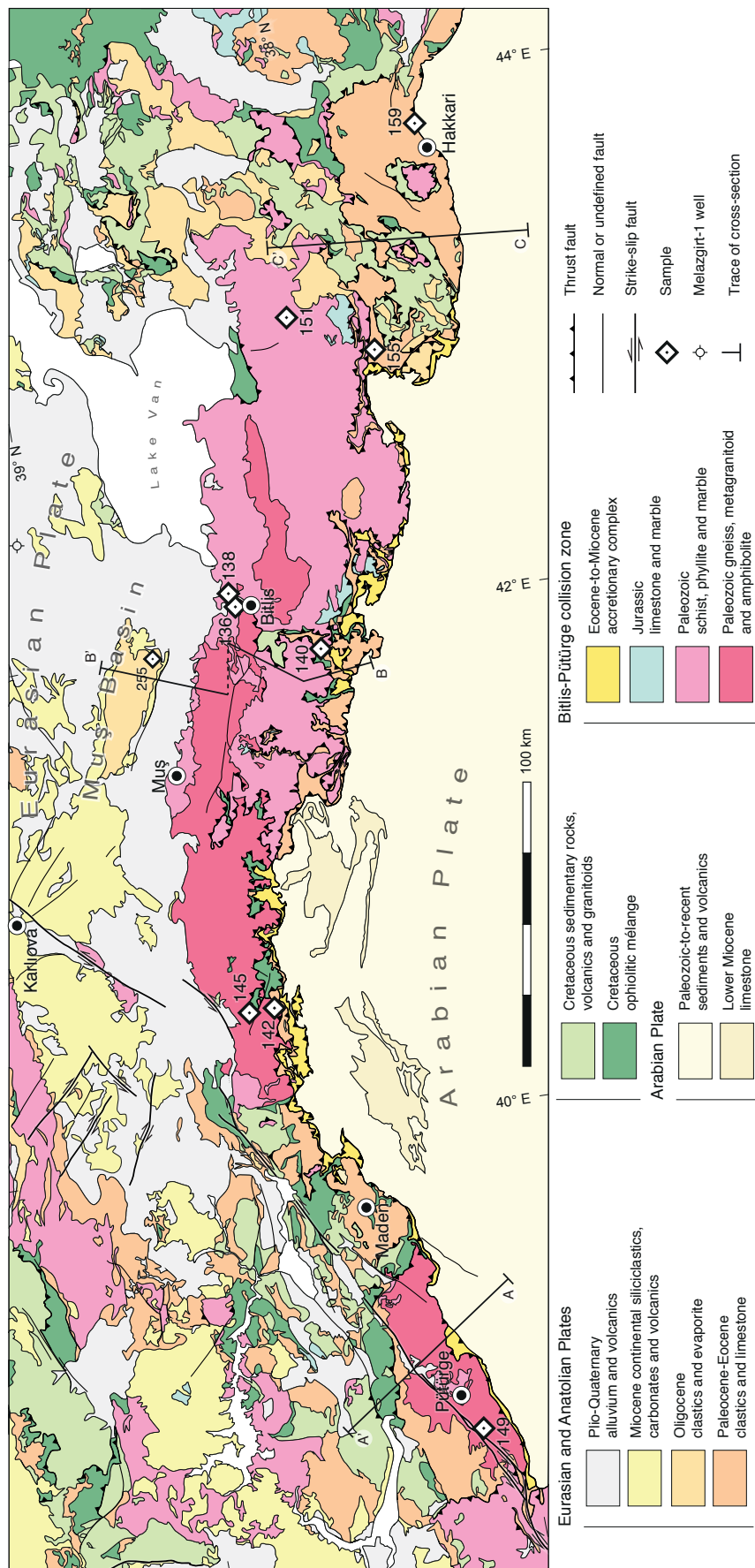




Figure 3

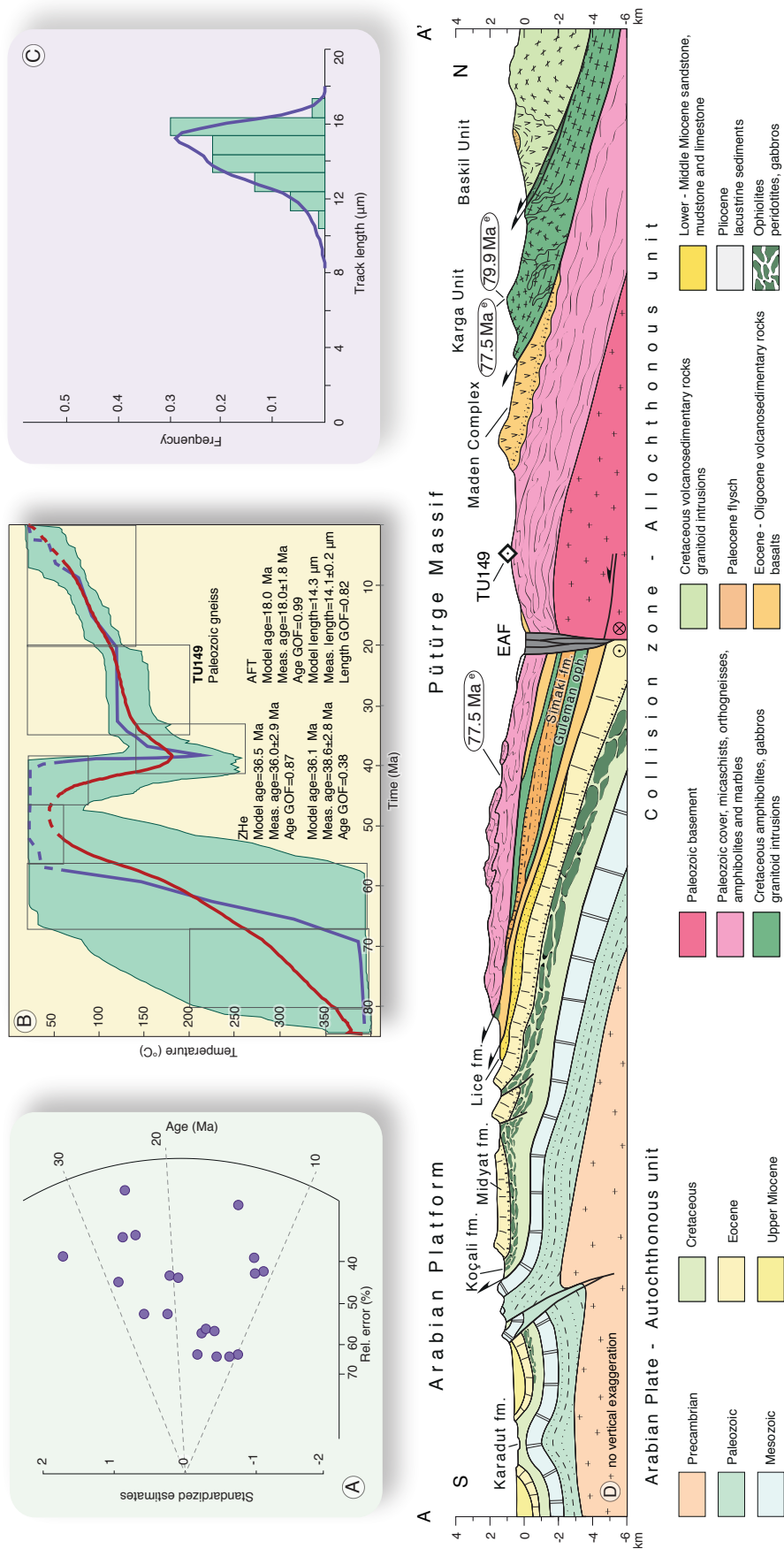


Figure 4

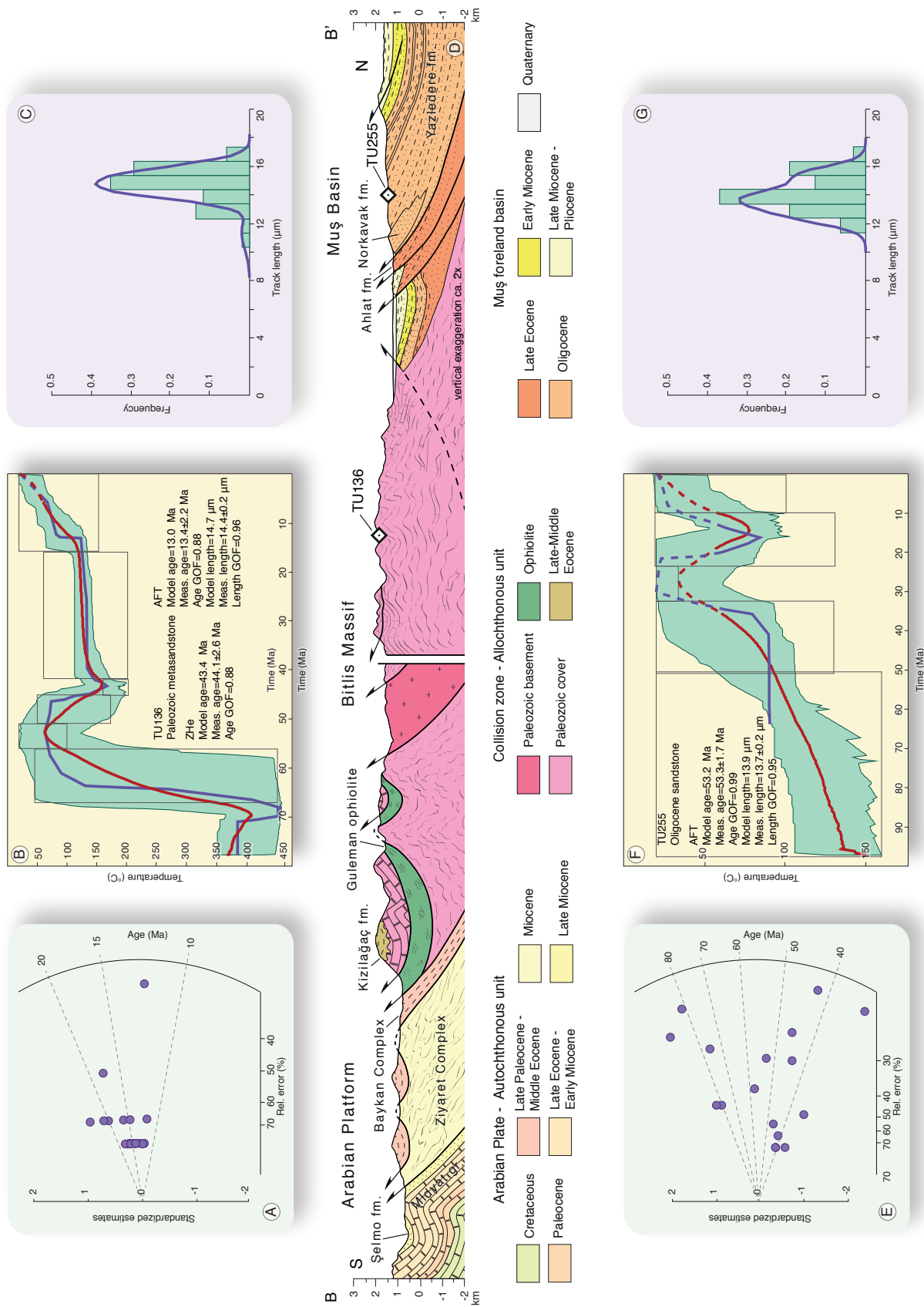


Figure 5

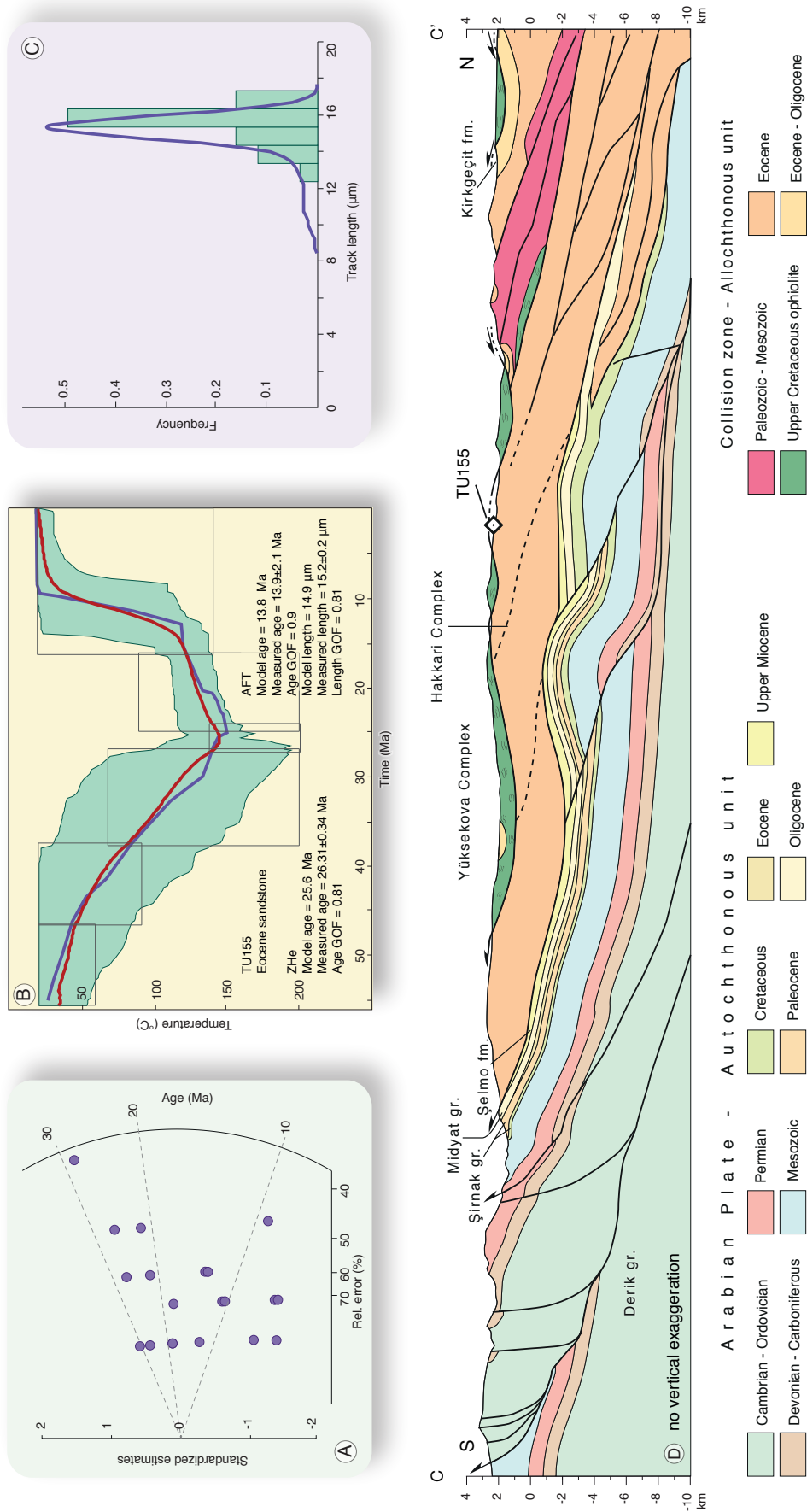


Figure 6

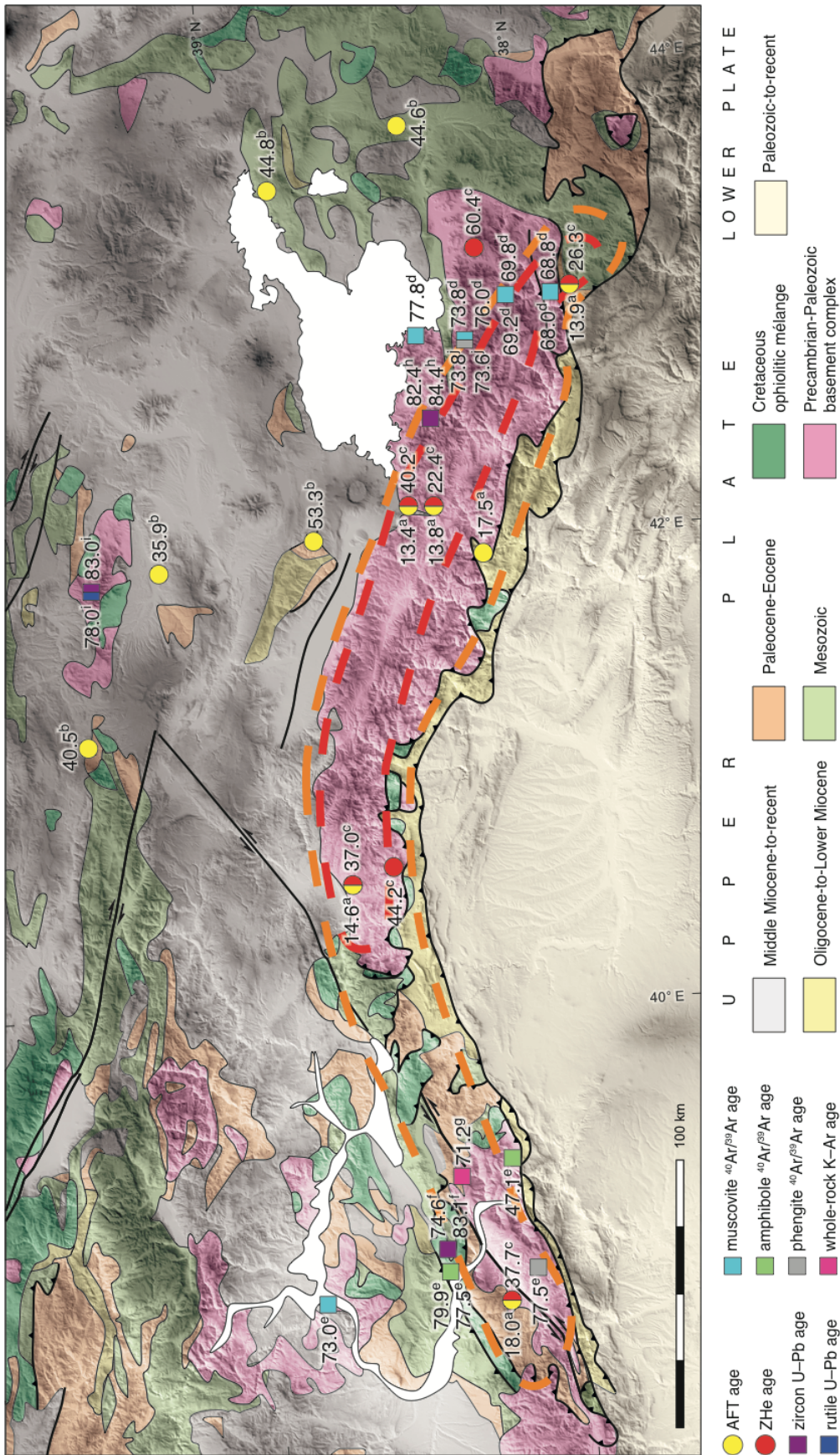


Figure 7

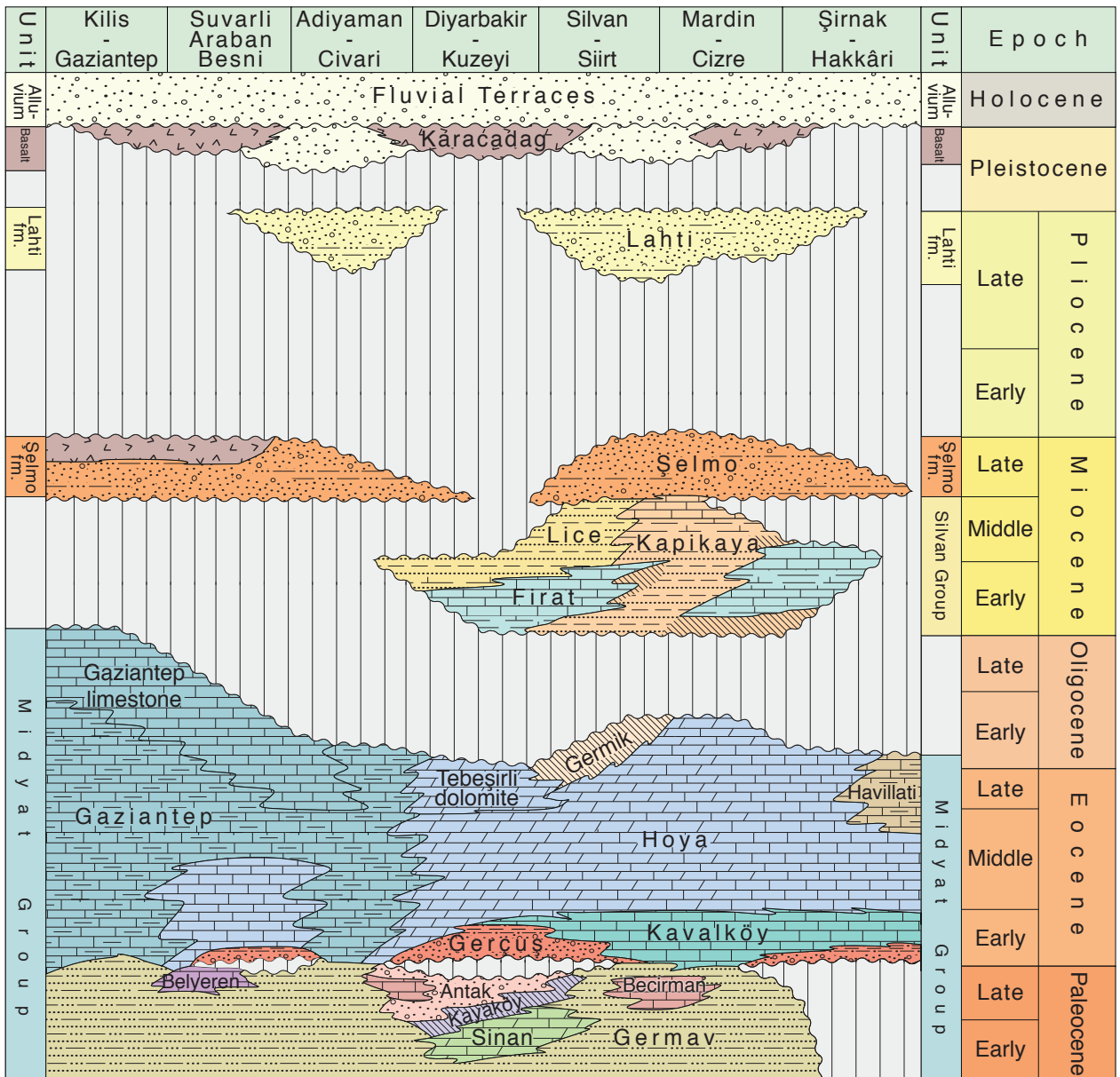


Figure 8

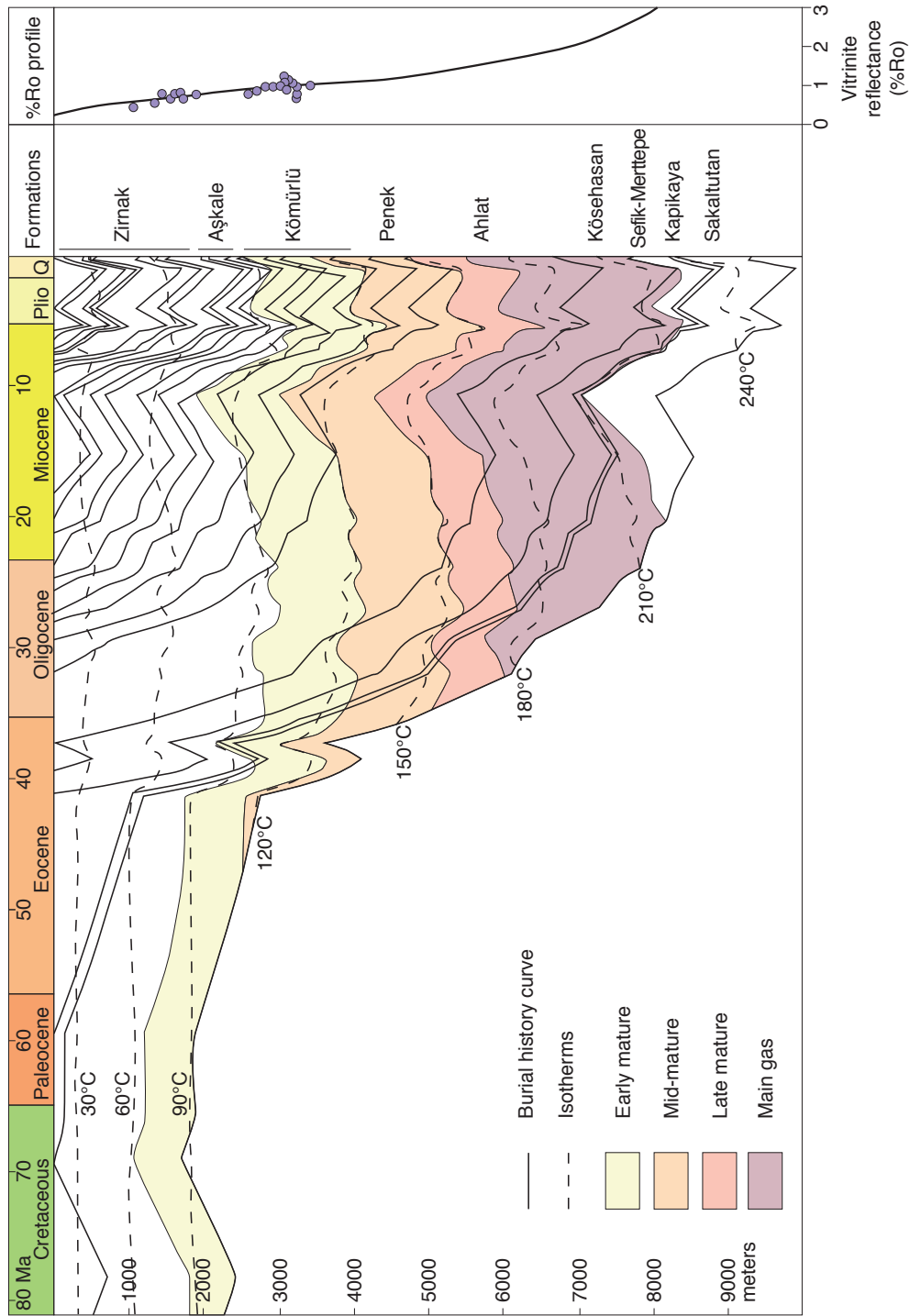
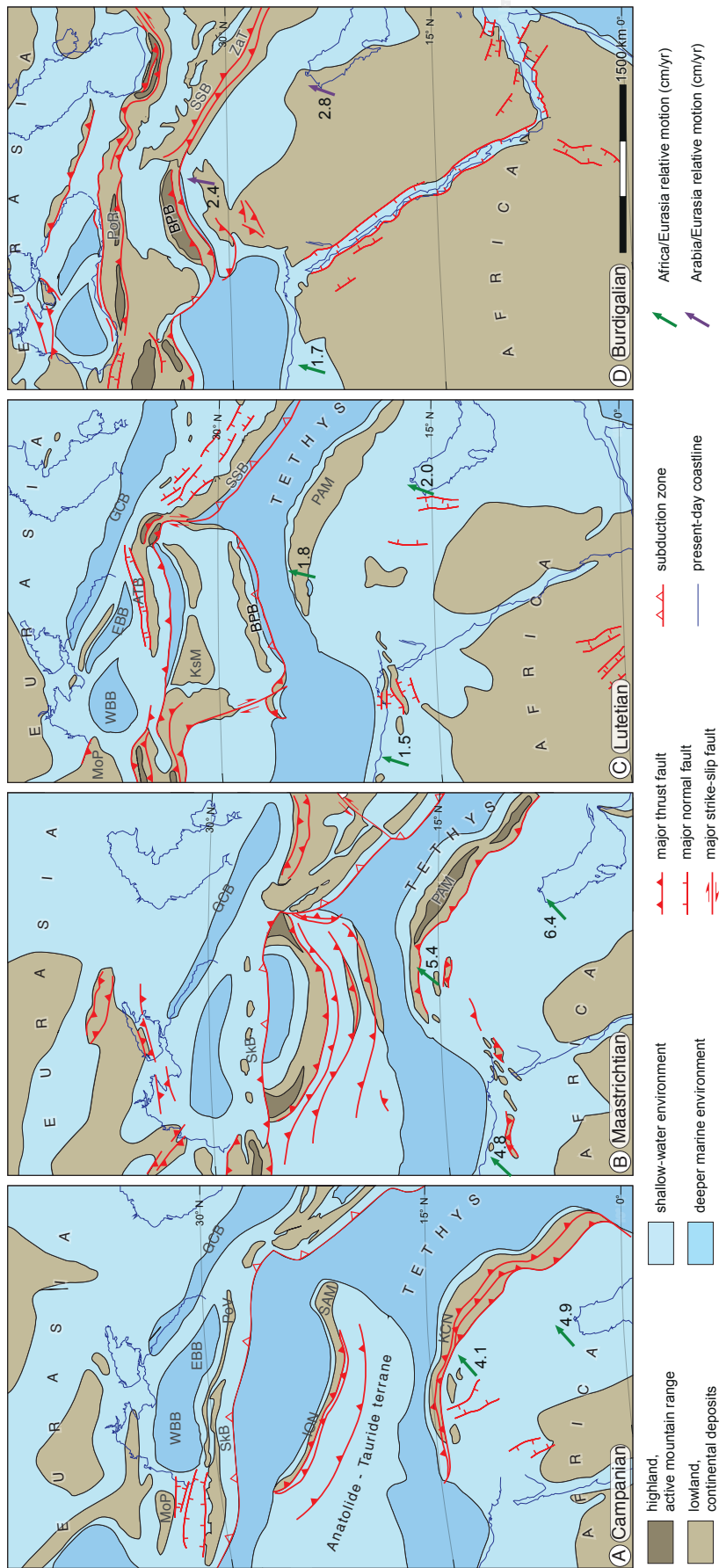


Figure 9







## 5.2. Manuscript 2

**Continental accretion and incremental deformation  
in the thermochronologic evolution of the Lesser Caucasus**

William Cavazza, Irene Albino, Ghazar Galoyan, Massimiliano Zattin, and Silvia Cattò

*To be submitted to International Geology Review*

## **Abstract**

Apatite fission-track analysis and thermochronologic statistical modeling of Precambrian-to-Oligocene plutonic and metamorphic rocks from the Lesser Caucasus differentiates two discrete cooling episodes correlatable to major accretion/obduction events along the margins of the northern branch of the Neotethys. The first cooling episode occurred in the Late Cretaceous (Turonian-Maastrichtian) and is coeval with widespread southward ophiolite obduction; the thermochronometric record of such first event is still predominant only in a relatively small area of the Somkheto-Karabakh magmatic arc which has not been overprinted by significant later exhumation. The second cooling episode occurred in the Early Miocene and reactivated most of the Amasia-Sevan-Akera (ASA) suture zone, i.e. the suture marking the final closure of the northern Neotethys during the Paleogene. Miocene cooling/exhumation is widespread both in the lower and upper plates of the ASA suture zone, and overprinted any previous thermochronologic signature.

Compilation of available thermochronologic, structural, and stratigraphic data across eastern Anatolia and Transcaucasia points to widespread and rapid Early-to-Middle Miocene cooling/exhumation along the borders of the Anatolian Plateau. Miocene collisional stress focused along the Bitlis suture zone (i.e. the belt marking the closure of the southern branch of the Neotethys and the ensuing Arabia-Eurasia collision) and was transmitted northward across the Anatolian hinterland, focusing along preexisting structural discontinuities: the Black Sea continent-ocean transition along the eastern Pontides and the ASA suture zone.

**Keywords:** Lesser Caucasus; low-temperature thermochronology; apatite fission-track analysis; structural reactivation; far-field tectonics

## **Introduction**

Horizontal compressional stress can travel far from continent-continent collision zones inducing an array of compressional/transpressional structural features such as lithosphere-scale folding, basement upthrusting, and basin inversion both in the foreland and the

hinterland (Zoback 1992; Ziegler *et al.* 1995, 1998, 2002; Cloetingh *et al.* 2005). Collision-related stresses can bypass the orogenic wedge and focus along rheological discontinuities at distances in excess of  $10^3$  km from the collisional front (Ziegler *et al.* 2002). Strong mechanical coupling between the collisional orogenic wedge and its foreland/hinterland is a crucial prerequisite for efficient far-field stress transfer and the ensuing onset and evolution of intraplate compressional features. Variations in mechanical coupling can be controlled by plate convergence rates and direction, the geometry of the collisional zone, and the rheology and structural fabric of the plates (Cloetingh *et al.* 1982, 1989; Jolivet *et al.* 1989; Ziegler 1993).

The collision between Arabia and Eurasia led to the development of the Bitlis-Zagros orogenic prism and a number of hinterland/foreland structural features, including (i) the North and East Anatolian Fault systems, (ii) the structural inversion of the Transcaucasian basin(s), (iii) widespread deformation in what is now the Anatolian-Armenian-Iranian plateau, and (iv) faulted anticlines in the flexured Arabian lower plate (Fig. 1). Despite the importance of the event, the timing of collision-related deformation has been long debated, with estimates ranging from Late Cretaceous (Hall 1976; Berberian and King 1981; Alavi, 1994), to Late Eocene-Oligocene (35-25 Ma; Jolivet and Faccenna 2000; Agard *et al.* 2005; Allen and Armstrong 2008), to Miocene (Şengör *et al.* 1985; Dewey *et al.* 1986; Yılmaz 1993; Robertson *et al.* 2007). Recent thermochronologic data has shown that the Bitlis orogenic wedge underwent a significant and discrete mid-Miocene phase of rapid growth by both frontal accretion, as shown by cooling/exhumation of the foreland deposits on both sides of the orogenic prism, and underplating, as shown by cooling/exhumation of the central metamorphic core of the orogenic wedge (Okay *et al.* 2010; Cavazza *et al.* 2018). The thermochronologic analysis of the Bitlis orogenic prism does not support the notion of a pre-Miocene collision (Cavazza *et al.* 2018). In addition, there is no evidence of a coherent collision-related foreland basin stratigraphy for the Paleogene. If the Arabia-Eurasia collision took place in the Paleogene one would expect the presence of large volumes of orogen-derived sediments on the flexured lower (Arabian) plate, whereas the Paleogene succession south of the Bitlis-Pütürge orogenic prism lacks evidence of synorogenic sedimentation. It can be concluded that Arabia-Eurasia continental collision started in the Miocene, as also shown by coeval thick

syntectonic clastic wedges deposited in flexural basins along the Arabian plate northern margin.

Low-temperature thermochronological data for the Eurasian hinterland north of the Bitlis- Pütürge suture zone suggest that Miocene tectonic stresses related to the Arabian collision were transmitted efficiently over large distances, focusing preferentially at preexisting rheological discontinuities (Albino *et al.* 2014; Cavazza *et al.* 2017). Stress concentrated along the marked rheological difference between the polydeformed continental lithosphere of the Eastern Pontides and the relatively pristine quasi-oceanic lithosphere of the eastern Black Sea. Cavazza *et al.* (2017) showed preliminary data on the northern segment of the Amasia-Sevan-Akera suture zone (Lesser Caucasus) indicating significant mid-Miocene reactivation of this structure. In this paper, we examine the thermochronological evolution of the entire Lesser Caucasus, concluding that portions of the Lesser Caucasus have preserved the tectonostratigraphic and thermotectonic record of an earlier episode of oceanic obduction and continental accretion, i.e. the result of the Late Cretaceous – Eocene obliteration of the northern Neotethys and the ensuing collision between Eurasia and the Anatolide-Tauride terrane. Other properly oriented segments of the Amasia-Sevan-Akera suture zone were reactivated during the Miocene, synchronously with maximum mechanical coupling along the Arabia-Eurasia collision front ca. 250 km to the south.

### **Geological setting**

The Amasia-Sevan-Akera (ASA) ophiolite belt (Knipper 1975; Adamia *et al.* 1981) stretches in a NW-SE direction for about 400 km along the axis of the Lesser Caucasus (Caucasus Minor) (Figs. 2, 3). The belt is made of outcrops of heavily deformed Middle Jurassic ultrabasic rocks, gabbros, and basalts overlain by pelagic sedimentary deposits. The ophiolite belt is thrust to the southwest and it is floored by a basal tectonic mélange made of greenschist facies metaophiolites and lenses of amphibolite and blueschist. Scattered outcrops of ophiolites occurring southwest of the ASA belt occur in the Vedi (Knipper & Sokolov 1977; Zakariadze *et al.* 1983) and Zangezur (Aslanyan and Satian 1977; Knipper and Khain 1980; Adamia *et al.* 1981) regions of Armenia, as far as 70 km away from the main

suture. These two ophiolite bodies are now considered as klippen of the main ASA ophiolite belt (Sosson *et al.* 2010). The petrochemical characteristics of the ophiolite belt and the associated klippen indicate an overall tholeiitic tendency influenced by a subduction component (for a review, see Rolland *et al.* 2010).

The ASA ophiolite belt separates Variscan terranes of Eurasian affinity to the north from Panafrican terranes of Gondwanian affinity to the south (Rolland *et al.* 2012 and refs. therein). From this viewpoint, it plays the same role of the Izmir-Ankara-Erzincan suture of Anatolia of which it can be considered the eastward prolongation (Khain 1994; Okay and Tüysüz 1999; Adamia *et al.* 2011). The geographic proximity and similarity in the geological units suggests a parallel evolution between northeastern Anatolia and Caucasus Minor (Adamia 1975; Knipper 1975; Okay and Tüysüz 1999; Hassig *et al.* 2013). In the Lesser Caucasus the southwestward obduction of oceanic lithosphere on the Anatolide-Tauride block (also called South Armenian block) (Knipper 1975; Knipper and Khain 1980; Zonenshain *et al.* 1990) occurred during the Late Cretaceous (Sokolov 1977; Knipper and Khain 1980). Traditionally, it was thought that the obduction was directly related to the collision between the SAB and Eurasia but more recent paleogeographic reconstructions envision an early (Campanian) episode of ophiolite obduction unrelated to collision along the northern continental margin of the Anatolide-Tauride block followed by diachronous collision of irregular continental margins in the Maastrichtian-Ypresian (Stampfli *et al.* 2001; Cavazza *et al.* 2004; Barrier and Vrielynck 2008). During continental collision the Eurasian plate overthrust the ophiolite southward but large outcrops of the obducted ophiolite remain either as isolated klippen or reworked mélange.

Subduction of the northern Neotethys underneath the southern European continental margin prior to collision is evidenced by the Somkheto-Karabakh magmatic arc, a thick and mainly calcalkaline, Andean-type magmatic arc and associated volcanoclastic series dated as Bajocian to Santonian (Knipper 1975; Adamia *et al.* 1977, 1987; Adamia *et al.* 1981; Ricou *et al.* 1986; Sosson *et al.* 2010). The basement complex of the European margin crops out in three metamorphic salients in Georgian territory: the Dzirula, Khrami and Loki massifs (Fig. 2). The overlying stratigraphic succession is relatively well exposed along the northeastern part of

the Lesser Caucasus and can be summarized as follows (for details, see Sosson *et al.* 2010). A ca. 3,000 m thick Bajocian–Bathonian section dominated by basalts, volcanoclastic turbidites and andesite overlies the Variscan basement, indicating major magmatic activity during the Middle Jurassic. The Late Jurassic succession represents a transgressive trend

with conglomerate, mudrock, and reef limestone. The Kimmeridgian features widespread intrusions (granodiorites, gabbros, quartz-diorites, plagiogranites) (Melkonian 1976; Lordkipanidze *et al.* 1988) with a number of associated ore deposits. The Early Cretaceous - early Late Cretaceous units have reduced thickness and display a variety of terrestrial and shallow marine environments. Late Turonian or Coniacian formations overlie unconformably the Late Jurassic intrusions and the earlier Cretaceous units. This unconformity is a supraregional feature and can be traced southeastward along the northeastern flank of Caucasus Minor to Karabakh, where it covers a relatively short time span within the Turonian. The Senonian succession comprises pillow- and massive basalt lava flows. Thus the magmatic arc was still active during this period of time along this part of the Eurasian margin. The end of magmatic activity occurred in Campanian to Maastrichtian times.

The terrane south of ASA suture zone has been termed South Armenia block (or, alternatively, Daralagez terrane) and is considered as the eastern continuation of the Anatolide-Tauride terrane of Turkey (Adamia 1975; Knipper 1975; Okay and Tüysüz 1999). Its basement -well exposed in the Dzarkuniats massif northeast of Yerevan (Fig. 2)- is made of a Proterozoic metamorphic rocks (gneiss, micaschist) intruded by leucogranite. The overlying incomplete Palaeozoic sedimentary succession crops out in southwestern Armenia and Nakhijevan. It is made of a >1,500 m thick section of Late Devonian (Frasnian-Famennian) sandstone/mudrock and Carboniferous reefal limestone, disconformably overlain by Permian - Early Triassic carbonates evolving upsection into Middle-Late Triassic siliciclastic sandstone and mudrock. The Jurassic is cropping out only at a distance from the ASA suture zone in northern Iran and Nakhijevan, where carbonate platform are predominant. Thick Early Cretaceous reef limestone overlie unconformably all previous formations and are overlain by a Late Cenomanian flysch and by Late Coniacian–Santonian olistostrome bodies (Sokolov 1977; Sosson *et al.* 2010) made of ophiolitic blocks in a pelitic matrix. These olistostromes are

considered as forerunners of the widespread ophiolite obduction episode characterizing the northern margin of the Anatolide-Tauride-Armenia terrane during the latest Cretaceous (e.g. Hassig *et al.* 2013). The onset of collision or the continental subduction of the Anatolide-Tauride-Armenia terrane below the Eurasian margin in the Lesser Caucasus is dated as Paleocene (Sosson *et al.* 2010). This process occurred around 20 Ma later than southward ophiolite obduction (Late Coniacian–Santonian, 88–83 Ma) and led to the uplift of the Sevan–Akera suture zone, its folding, erosion and to the transfer of detritus in a flexural basin in front of the belt, above the obduction structures. Throughout the Paleocene and the Early-Middle Eocene a flexural basin covered the obducted ophiolite and related structures, and was progressively deformed along thrusts in its internal (northeastern) sector. It was generally considered that the Miocene marked a transition to mostly strike-slip deformation in the region (e.g. Avagyan *et al.* 2015) but preliminary thermochronologic data has proved considerable dip-slip movements during this epoch along properly oriented segments of the Sevan-Akera suture zone, both in the lower and upper plates (Cavazza *et al.* 2017).

## **Methods**

### *Apatite fission-track analysis and modeling*

Fission tracks are linear radiation damages within the crystal lattice, caused by nuclear fission of radioactive isotope  $^{238}\text{U}$ , that can be etched and counted under an optical microscope. Concurrently, neutron irradiation is used to induce the decay of  $^{235}\text{U}$ , generating radiation damages on the surface of an external detector. Grain-by-grain determination of both spontaneous and induced fission-track densities yields a single-grain age representing the cooling of the grain below a closure temperature of  $\sim 100^\circ\text{C}$ . Fission-track dating is a useful tool to unravel the cooling histories experienced by rocks in the upper crustal levels and to give a measure of their exhumation (for a review of the method, see Donelick *et al.* 2005). Fission tracks in apatites all have the same initial length of about  $16\ \mu\text{m}$  (e.g. Ketcham *et al.* 1999) but anneal at rates proportional to temperatures, starting at about  $60\ ^\circ\text{C}$ . Over geological time periods, partial annealing of fission tracks occurs at temperatures between about  $60$  and  $125\ ^\circ\text{C}$  (i.e. the Partial-Annealing Zone: PAZ; Gleadow and Fitzgerald 1987).

Because tracks shorten in relation to the degree and duration of heating, the measurement of fission-track lengths gives information about the thermal evolution in the PAZ temperature range. A quantitative evaluation of the thermal history can be carried out through modelling procedures, which find a range of cooling paths compatible with the apatite fission-track (AFT) data (Ketcham 2005). In this work, inverse modelling of track length data was performed using the HeFTy program (Ehlers *et al.* 2005), which generates the possible T–t paths by a Monte Carlo algorithm. Predicted AFT data were calculated according to the Ketcham *et al.* (2007) annealing model for fission tracks revealed by etching.  $D_{\text{par}}$  values (i.e. the etch pit length) were used to define the annealing kinetic parameters of the grains and the original track length.

#### *Sampling strategy and sample preparation*

Forty-one samples were taken on both sides of the Sevan-Akera suture zone, covering the length of the Lesser Caucasus from the Proterozoic Tzaghkuniats Massif to the northwest to the southern end of the mostly Jurassic Somkheto-Karabakh magmatic arc to the southeast (Fig. 2). Most samples are from plutonic and metamorphic rocks ranging in age from Precambrian to Jurassic. Younger Oligo-Miocene intrusives from the Armenian highlands were also sampled. Apatite grains were concentrated by crushing and sieving, followed by hydrodynamic, magnetic, and heavy-liquid separations. Apatites were embedded in epoxy resin, polished in order to expose the internal surfaces within the grains, and the spontaneous FT were revealed by etching with 5N HNO<sub>3</sub> at 20°C for 20 seconds. The mounts were then coupled with a low-uranium fission-track-free muscovite mica sheet (external detector method) and sent for irradiation with thermal neutrons (see Donelick *et al.* 2005, for details) at the Radiation Center of Oregon State University. Nominal fluence of  $9 \times 10^{15}$  n cm<sup>-2</sup> was monitored with a CN5 uranium-doped silicate glass dosimeter. Induced fission tracks were revealed by etching of the mica sheets in 40% HF for 45 min at 20°C. Spontaneous and induced fission tracks were counted under an optical microscope at  $\times 1,250$  magnification, using an automatic stage (FTStage system) and a digitizing tablet.

Twenty-one samples of the original set yielded apatites suitable for dating (Table 1). Central ages were calculated with the zeta calibration approach (Hurford and Green 1983),



using Durango ( $31.3 \pm 0.3$  Ma) and Fish Canyon Tuff ( $27.8 \pm 0.2$  Ma) age standards within grains exposing *c*-axis-parallel crystallographic planes. Track-length distributions were calculated by measuring horizontal confined tracks together with the angle between the track and the *c*-axis. Confined tracks constitute a small part of the FT population, therefore additional concentrates were mounted, polished and etched for the analysis. Ultimately, six samples contained a statistically significant number of confined tracks. All available geological constraints (intrusion ages, depositional ages, and stratigraphic relationships) were incorporated into the modeling. A first batch of thousands simulations was performed with very large time-temperature constraints. Once a broad range of possible solutions was achieved, the program was forced to work on more restricted time-temperature region (boxes in Figs. 3, 4 and 5). The distribution of fission-track lengths and geological information support a general picture of simple cooling paths, without relevant post-exhumation burial and additional cooling events. The modeled cooling paths thus provide important constraints on the cooling/exhumation chronology of the study area.

### **Analytical results**

Table 1 and Figure 2 provide a summary of the AFT data. Central ages cluster into two distinct groups. The older age cluster ranges from  $92.1 \pm 1.7$  Ma to  $64.4.7 \pm 1.5$  Ma (Late Cretaceous). The younger age cluster range from  $23.3 \pm 1.7$  Ma to  $11.9 \pm 1.7$  Ma to (Early-Middle Miocene). All the samples passed the  $\chi^2$  test indicating a single population of grains and do not show any correlation between age and elevation. The two age groups show a well defined geographic position, with the older age samples clustering in the hanging wall of ASA suture zone in the central portion of the Somkheto-Karabakh magmatic arc (Fig. 2). AFT central ages provide an average indication of how the samples cooled across the partial annealing zone (PAZ) of apatite (ca. 120-60°C) but can be somewhat misleading if the sample resided within the PAZ for a long time. More precise t-T paths can be obtained through statistical modeling of fission-track length distributions. Following are the results of thermochronometric modeling of six samples containing a statistically significant number of confined tracks. We will describe first the AFT analytical results obtained from the samples

taken along the European margin (i.e. northeast of the ASA suture zone) and then those from the samples taken along the Anatolide-Tauride-Armenian margin. Results of the statistical forward modeling are shown in Figures 3, 4, and 5.

#### *AFT results from the European margin*

Sample TU348 is a Late Jurassic diorite dike intruding a granodiorite pluton in the central portion of the Somkheto-Karabakh magmatic arc (Gedabey mine) (Figures 2, 4, Table 1). Track-length frequency distribution is platykurtic (Fig. 6); inverse modeling indicates very rapid cooling across the apatite PAZ between 80 and 77 Ma (Campanian).

Sample TU351 is a Middle Jurassic granite from the Ertepe pluton of the central Somkheto-Karabakh magmatic arc (Figures 2, 4, Table 1). It yielded a tight cluster of single-grain ages (98-85 Ma), a central age of  $92.1 \pm 1.7$  Ma, a leptokurtic track-length distribution with a single peak, and a relatively short mean track length of  $12.16 \pm 1.13$   $\mu\text{m}$  (Fig. 6). The overall shape of the reconstructed time-temperature path of this sample is similar to the one of sample TU348 from the same region (Fig. 4) despite an older AFT central age.

Three other samples from the central Somkheto-Karabakh magmatic arc were analyzed but did not yield enough confined tracks for a statistically robust inverse modeling. Two granodiorite samples (TU344 and 345) from the Late Jurassic Dashkesan pluton yielded central ages of  $64.4 \pm 1.5$  and  $75.5 \pm 2.1$ , respectively (Fig. 2; Table 1). The third sample (TU352) was taken from the Early Cretaceous Uchtepe pluton and provided a central age of  $87.6 \pm 1.5$  Ma. Another latest Cretaceous AFT central age came from a Late Paleozoic granitic sample (TU354) from the Khrami Massif of southern Georgia, a Variscan metamorphic salient.

Sample TU297 is a leucogranite from a Late Jurassic granitic-tonalitic body intruding the volcanics/volcaniclastics of the northern Somkheto-Karabakh magmatic arc (Table 1; Figs. 2). The geological setting of this sample is identical to those of samples from the central portion of the arc (see above) but its low-temperature thermochronological evolution (Fig. 3) indicates a discrete, much younger episode of cooling at about 12 Ma (Middle Miocene). Two other samples from the northern Somkheto-Karabakh magmatic arc were analyzed and also yielded Miocene central ages: TU298 (Middle Jurassic plagiogranite from the Alaverdi district;

12.4 ± 1.1 Ma) and TU380 (Middle Jurassic granite from the Berdadzor pluton; 23.3±1.7) (fig. 2). Both samples did not contain enough confined tracks for inverse statistical modeling.

Two samples from the Late Jurassic Mehmana pluton in the southern part of the Somkheto-Karabakh magmatic arc yielded again consistent Miocene AFT central ages. Sample TU382 (tonalite from the Kashen mine) provided an age of 20.3 ± 1.1 Ma. Sample TU384 (coarse-grained tonalite) provided an age of 19.7 ± 3.2 Ma (Table 1; Figs. 2, 4).

Two samples (TU385 tonalite, TU387 diorite) from the Tsav pluton of the Kapan zone yielded Early Miocene apatite fission-track ages of 21.2 ± 1.1 and 23.1 ± 2.3 Ma, respectively (Fig. 2).

#### *AFT results from the Anatolide-Tauride-Armenian margin*

Irrispective of their age (Precambrian to Miocene) and lithology (from orthogneiss to granitoid rocks) all samples from the Anatolide margin yielded coherent Early Miocene apatite fission-track central ages, ranging from 22.1 ± 1.1 to 16.2 ± 2.8 Ma (Fig. 2). Three samples were taken from the crystalline rocks of the Tzaghuniats Massif. Sample TU290 is from an Upper Eocene monzonite/monzodiorite body intruding the Proterozoic basement complex of the massif (Table 1; Fig. 2). It yielded a tight cluster of single-grain ages (25-12 Ma), a central age of 16.8 ± 2.5 Ma, and a leptokurtic track-length distribution with a single peak and relatively long mean track length of 14.50 ± 0.14 μm (Figure 6). The best-fit t-T path shows fast cooling through the PAZ between ca. 19 Ma and 16 Ma (Figure 4). Both samples TU291 (Precambrian orthogneiss) and TU292 (Late Jurassic tonalite) did not contain enough confined tracks for inverse modeling but yielded quite consistent Burdigalian (late Early Miocene) FT central ages.

Sample TU391 (porphyritic granite from the northern Meghri-Ordubad pluton in southernmost Armenia) was taken from a pluton which yielded a magmatic age of 22 Ma (earliest Miocene; U-Pb on zircons; Moritz *et al.* 2016). The AFT central age of this sample is 16.2 ± 2.8 Ma (Table 1) thus implying that cooling to temperatures within the range of the apatite PAZ occurred soon after its emplacement. Inverse modeling (Figure 5) shows a long residence time within the PAZ and the overall t-T can be interpreted as the result of emplacement at shallow crustal levels (2-3 km).

Sample TU395 is from a Late Oligocene-Early Miocene dike cutting the thick Middle Eocene volcano-sedimentary succession of the Vayots Dzor province of Armenia. It yielded a tight cluster of single-grain ages (24-17 Ma), a central age of  $19.2 \pm 1.1$  Ma, and a moderately platykurtic track-length distribution with a single peak and a short mean track length of  $12.62 \pm 0.11 \mu\text{m}$  (Figure 6). Overall, this intrusion shows a cooling history very similar to that of TU391, i.e. magmatic cooling followed by a relatively long residence time (from ca. 20 to 2 Ma) within the temperature range of the PAZ (Figure 4). This dike was emplaced at shallow crustal levels as shown also by the unmetamorphosed Eocene succession nearby. Residence within the PAZ was somehow complicated by two minor heating episodes at about 16-12 and 5-2 Ma. Within the same region, two additional samples (TU396 Late Oligocene – Early Miocene granodiorite; TU397 Late Eocene diorite) did not contain enough confined fission track for inverse modeling but yielded coherent Early Miocene central ages of  $18.2 \pm 3.0$  and  $17.7 \pm 1.0$  Ma, respectively (Figure 2, Table 1).

A granodiorite sample (TU392) from the Sisian stocks of southern Armenia (Fig. 2) yielded an AFT central age of  $22.1 \pm 1.1$  Ma (Table 1).

## **Discussion**

The correlation between low-temperature thermochronometric data and specific geological structures is a difficult task requiring a thorough understanding of the structural setting of the study area. This prerequisite is not met by the Lesser Caucasus, a region where a combination of geological complexity and political fragmentation has hampered the development of a satisfactory structural framework. From this viewpoint, the cross-sections of Figures 3, 4, and 5 ought to be considered rough, tentative depictions of a complex geological structure resulting from incremental deformation and contrasting structural styles. Nevertheless, this paper presents the first low-temperature thermochronometric dataset for the Lesser Caucasus; such dataset is relevant for any future structural interpretation of the region as it provides compelling constraints on its geological evolution. Based on the existing literature, following is an attempt at interpreting our dataset within the geological context of the Lesser Caucasus and the surrounding regions.

The AFT thermochronometric dataset presented here is coherent and documents two distinct episodes of cooling/exhumation in the Lesser Caucasus: during the Late Cretaceous and in Early-Middle Miocene times. These two cooling events can be correlated to the stratigraphic and structural record of the study area and the adjoining regions, as described in the available literature. For example, all along the northeastern flank of the Lesser Caucasus a widespread Turonian unconformity separates either the Middle-Late Jurassic Somkheto-Karabakh magmatic arc (or Early Cretaceous shallow marine sedimentary rocks) from the overlying latest Turonian - Coniacian sedimentary formations (Sosson *et al.* 2010). The age of such unconformity is in agreement with our Turonian AFT ages (92-88 Ma) in the eastern portion of the Somkheto-Karabakh magmatic arc of northern Azerbaijan west of the city of Ganja (Fig. 2). Portions of the eastern Somkheto-Karabakh magmatic arc were thus exhumed in pre-Coniacian times (see also the modeling of sample TU351 in Fig. 4), concomitant with the southwestward obduction of the Sevan-Akera ophiolites on the Anatolide-Tauride terrane (88-87 Ma; Rolland *et al.* 2007, 2010; Sosson *et al.* 2010). Our data show that in the western part of the magmatic arc at the latitude of Ganja the AFT record of the obduction was overprinted by the exhumation of a new apatite partial annealing zone at 75-64 Ma (Late Campanian – Early Danian) (Table 1; Figs. 2, 4; see also sample TU348 in Fig. 4) during final oceanic closure (74-71 Ma; Rolland *et al.* 2007, 2010; Galoyan *et al.* 2009, 2013; Sosson *et al.* 2010) and the ensuing continental indentation, lithospheric coupling, and thrusting. Alternatively, one might envision the Cretaceous AFT age pattern found in the southeastern portion of the study area as the result of a single, prolonged exhumation episode.

Late Cretaceous ophiolite obduction along the Anatolide-Tauride-Armenian (and Arabian) northern continental margin has been described from western Anatolia to Oman (e.g. Coleman 1981; Okay *et al.* 2001; Robertson 2002). Such discrete and important episode of ophiolite obduction had significant tectonic effects, including the development of structural relief, lithospheric flexure, and creation of accommodation space for sedimentation. Crustal shortening might have also played an important role during obduction as recent studies in eastern Anatolia (Cavazza *et al.* 2018; Topuz *et al.* 2017) point to a coherent metamorphic event across the entire area comprised between the Erzincan-Sevan suture to the north and

the Bitlis-Zagros suture to the south. Late Cretaceous metamorphism is coeval with massive southward ophiolite obduction from the northern branch of the Neotethys onto the Anatolide-Tauride terrane (Stampfli and Hochard 2009).

Coherent Neogene AFT ages characterize all other portions of the study area on both sides of the Sevan-Akera suture zone (Fig. 2), ranging from 23.3 to 11.9 Ma (Early-Middle Miocene) (Table 1). Correlation between the thermochronometric data presented here and the activity of specific geological structures of the Lesser Caucasus would require a detailed structural analysis and goes beyond the scope of this work. Nonetheless, the analysis of published literature (including the available geological maps) and preliminary field data point to a few large structures which might have driven to a large extent the thermal evolution of the study area. For example, the complex fault system northeast of the town of Dilijan in the hanging wall of the Sevan-Akera suture (Fig. 2) separates the two groups of FT ages and must have played a role in the differential exhumation of the samples analyzed in this paper. Such complex structure comprises (i) a large east-west-trending, south-dipping reverse fault and (ii) a NE-SW-trending transpressional fault system separating not reset Late Cretaceous FT ages to the NW from Miocene ages to the SE. This fault array does not seem to continue into the footwall block, whose western part is also characterized by Miocene cooling ages (a few Ma older than those in the hanging wall). The fact that Miocene cooling ages occur both in the hanging wall and footwall of the Sevan-Akera main thrust fault suggests that the overall exhumation pattern in this portion of the Lesser Caucasus cannot be simply the result of the reactivation of that thrust, although such a reactivation could account for the offset of ca. 5 Ma in the AFT cooling ages between hanging wall and footwall blocks (~12 vs. ~17 Ma, respectively) across the thrust.

The Lesser Caucasus low-temperature thermochronologic evolution during the Neogene -with particular reference to Miocene cooling- can be framed within a broader context by comparing it to the results of recent thermochronometric studies in adjacent regions of eastern Anatolia, as shown in Fig. 7 and discussed below. Exhumation of Cretaceous-to-Eocene granitoids along the Black Sea coast in the eastern Pontides region also occurred in the Miocene (Albino *et al.* 2014), mirroring the age of maximum tectonic coupling between the

Eurasia and Arabia plates along the 2,400 km long Bitlis-Zagros suture zone, some 200 km to the south (Okay *et al.* 2010). Long-range deformation focused along the Black Sea coast at the boundary between polydeformed continental lithosphere and pristine -and rheologically stronger- oceanic lithosphere of the Eastern Black Sea. Conversely, apatite FT ages across the Anatolian Plateau are consistently Paleogene (with a cluster of ages in the Middle-Late Eocene). Over this wide region, Eocene cooling was the last thermochronologically significant result of the contractional deformation related to the closure of the Izmir-Ankara-Erzincan ocean and the ensuing collision between the Sakarya and Anatolide-Tauride terranes. The memory of this continental accretion has been retained by the AFT thermochronometer because exhumation during the creation of the Anatolian Plateau was insufficient to unroof a new apatite partial annealing zone (Cavazza *et al.* 2017, 2018). Stress from the Bitlis collision zone was transmitted heterogeneously in the region of the Lesser Caucasus. The Adjara-Trialeti zone of western Georgia was structurally affected but exhumation was insufficient to expose a new apatite PAZ (Albino *et al.* 2014). This paper documents that in other areas of the Lesser Caucasus exhumation (i) was large enough to expose to the surface a new PAZ, (ii) was coeval with the Arabia-Eurasia collision, and (iii) focused along preexisting structural discontinuities, i.e. segments of the Sevan-Akera suture zone.

From a wider, more interpretative perspective, the integration of present-day crustal dynamics and low-temperature thermochronometric data available for Asia Minor -as summarized in Fig. 7- provides a comparison between short- and long-term deformation

patterns for the entire eastern Anatolian-Transcaucasian region and has some bearing on the timing of the overall westward “tectonic escape” of Anatolia. Present-day GPS velocity patterns indicate that most of the Arabia-Eurasia convergence is now accommodated by the westward movement of the Anatolian plate (Fig. 8) which has largely decoupled the Anatolian hinterland from the Bitlis collision zone. GPS velocities (and seismicity) are now very low in the Eastern Pontides and the Lesser Caucasus, where contractional exhumation was rapid during the Early-Middle Miocene (Albino *et al.* 2014; Cavazza *et al.* 2017, 2018; this paper). Two successive stages of Neogene deformation of the hinterland of the Arabia-Eurasia collision zone can thus be inferred (Figure 9). (1) During the Early Miocene, continental deformation

was concentrated along the Arabia-Eurasia (Bitlis) collision zone but tectonic stresses were transmitted over a wider area and focused along the coast of the eastern Black Sea and in the Caucasus, inducing significant shortening and exhumation. The Black Sea (quasi)oceanic lithosphere is rheologically stronger than the polydeformed Anatolian continental lithosphere to the south and therefore acted as a “backstop” resisting deformation and deviating the impinging continental lithosphere (McClusky *et al.* 2000). Other small areas along kinematic block boundaries may have been affected. From this viewpoint, it should be noted that the set of Miocene AFT ages in NW Armenia presented by Albino *et al.* (2014) and compiled in this paper was yielded by samples straddling the boundary between kinematic blocks proposed by Reilinger *et al.* (2006) based on the analysis of GPS motion vectors. (2) Since late Middle Miocene time the activation of the North and Eastern Anatolian Fault systems and the connate westward translation of Anatolia have reduced efficient northward stress transfer. In this new tectonic regime -still active today- most of the Arabia-Eurasia convergence is being accommodated by the westward motion of Anatolia whereas the eastern Pontides are mechanically decoupled from the Bitlis collision zone. It could be argued that the transition between the two successive deformation stages may have occurred any time between the Middle Miocene and the present, but independent stratigraphic and structural data indicate clearly that the North Anatolian Fault system was activated in the mid-Miocene (for a review, see Şengör *et al.*, 2005). Thus, the transition between shortening-dominated and strike-slip-dominated deformation occurred most likely in the Middle Miocene, shortly after maximum mechanical coupling between Arabia and Eurasia.

## **Conclusions**

This paper presents the first comprehensive low-temperature thermochronologic survey of the entire Lesser Caucasus. The integration of the thermochronometric data presented here and preexisting stratigraphic-structural data generates constraints relevant to the overall geological evolution of the Lesser Caucasus and the Middle East as a whole. AFT analyses point to a coherent Early-Middle Miocene episode of cooling/exhumation along the Paleocene-Eocene ASA suture zone which was likely reactivated by far-field stresses during Miocene collision along



the Arabia-Eurasia collision zone, some 250 km to the south. The Miocene AFT ages along the ASA suture zone correlate well with other evidences of coeval cooling to the west. A compilation of all available fission-track data for the Bitlis-Zagros collision zone, the eastern Anatolian Plateau, the eastern Pontides, the Adjara-Trialeti fold-and-thrust belt of western Georgia, and the Lesser Caucasus shows clearly that Miocene cooling/exhumation occurred not only along the Arabia-Eurasia collision front but affected also selected portions of the Eurasian hinterland, i.e. the easternmost Pontides and the Lesser Caucasus. Conversely, cooling at temperatures below the apatite partial annealing zone in the Anatolian Plateau occurred in the Paleogene (with a cluster of ages in the Middle-Late Eocene), coevally with the development of the İzmir-Ankara-Erzincan suture (e.g. Okay and Tüysüz 1999). This indicates that the entire region occupied nowadays by the plateau was largely bypassed by the tectonic stresses related to the collision and never underwent significant exhumation.

Despite the vastity of the area compared to the relatively small number of samples and the widespread cover of mostly Plio-Quaternary volcanics characterizing eastern Anatolia and Transcaucasia, this study shows clearly that significant Miocene-age deformation occurred only at the margins of the Anatolian-Iranian Plateau. Synchronous deformation at the opposing ends of the Anatolian continental plateau reproduces the results of recent studies that identified deformation at the northern margin of the Tibetan Plateau, synchronous with the early stage of India-Asia collision (e.g. Clark *et al.* 2010). The area affected by faulting increased very little through time as the northern margin of Tibet was established early; deformation has propagated northward by only a minor amount during the entire period of collision.

### **Acknowledgments**

Stimulating field discussions with S. Adamia (Inst. of Geophysics, Tbilisi), N. Imamverdiyev (Baku State Univ.), R. Melkonyan (Acad. of Sciences, Yerevan), A.I. Okay (Istanbul Technical Univ.) and N. Sadradze (Inst. of Geology, Tbilisi) were instrumental for introducing the senior author to the geology of the Lesser Caucasus. Funding for this research was provided by

MIUR (Italian Ministry of University and Research) PRIN funds and the University of Bologna RFO funds. Thanks to the National Academy of Sciences (Yerevan) for logistical support.

## References

- Adamia, S., Zakariadze, G., Chkhotua, T., Sadradze, N., Tsereteli, N., Chabukian, A. and Gventsadze, A., 2011, Geology of the Caucasus: a review: *Turkish Journal of Earth Sciences*, 20, p. 489-544.
- Alavi, M., 1994, Tectonics of the Zagros orogenic belt of Iran: new data and interpretations: *Tectonophysics*, v. 229, p. 211-238.
- Albino, I., Cavazza, W., Zattin, M., Okay, A.I., Adamia, S., and Sadradze, N., 2014, Far-field tectonic effects of the Arabia-Eurasia collision and the inception of the North Anatolian Fault system. *Geological Magazine*, v. 151, p. 372-379.
- Allen, M.B., and Armstrong, H.A. 2008, Arabia–Eurasia collision and the forcing of mid-Cenozoic global cooling: *Palaeogeography Palaeoclimatology Palaeoecology*, v. 265, p. 52–58.
- Aslanyan, A.T., and Satian, M. A., 1977, On the geological features of Transcaucasian ophiolitic zones: *Izvestia Acad. Sci. Armenian SSR, Nauki o Zemle* 4–5, 13–26 (in Russian).
- Avagyan, A., Sosson, M., Philip, H., Karakhanian, A., Rolland, Y., Melkonyan, R., Rebaï, S., and Davtyan, V., 2005, Neogene to Quaternary stress field evolution in Lesser Caucasus and adjacent regions using fault kinematics analysis and volcanic cluster data: *Geodinamica Acta*, v. 18, p.401-416.
- Barrier, E., and Vrielynck, B., 2008, Paleotectonic Maps of the Middle East – Tectono-sedimentary-palinspastic maps from Late Norian to Pliocene: Commission for the Geological Map of the World.
- Berberian, M., and King, G.C.P., 1981, Towards a paleogeography and tectonic evolution of Iran: *Canadian Journal of Earth Sciences*, v. 18, p. 210-265.
- Cavazza, W., Albino, I., Zattin, M., Galoyan, G., Imamverdiyev, N. and Melkonyan, R., 2017a, Thermochronometric evidence for Miocene tectonic reactivation of the Sevan-Akera suture zone (Lesser Caucasus): a far-field tectonic effect of the Arabia-Eurasia collision? In: M. Sosson, R. A. Stephenson and S. A. Adamia, eds., *Tectonic Evolution of the Eastern Black Sea and Caucasus: Geological Society of London Special Publication 428*, p. 187-198, doi: 10.1144/SP428.4.
- Cavazza, W., Cattò, S., Zattin, M., Okay, A.I., and Reiners, P., 2017b, The Miocene Arabia-Eurasia collision zone of southeastern Turkey: *Geosphere*, submitted.

- Cavazza, W., Roure, F., Spakman, Stampfli, G.M., and Ziegler, P.A., eds., 2004, The TRANSMED Atlas: the Mediterranean Region from Crust to Mantle: Heidelberg, Springer-Verlag, 141 pp. + CD-ROM.
- Clark, M.K, Farley, K.A., Zheng, D., Wang, Z., and Duvall, A.R., 2010, Early Cenozoic faulting of the northern Tibetan Plateau margin from apatite (U–Th)/He ages: *Earth and Planetary Science Letters*, v. 296, p. 78–88.
- Cloetingh, S.A.P.L., Wortel, M.J.R., and Vlaar, N.J., 1982, State of stress at passive margins and initiation of subduction zones: tectonic processes: model investigations of margin environmental and tectonic processes, p. 717-723.
- Cloetingh, S., Wortel, R., and Vlaar, N. J., 1989, On the initiation of subduction zones. *Pure and Applied Geophysics PAGEOPH*, v. 129, p. 7-25.
- Cloetingh, S. A. P. L., Ziegler, P. A., Beekman, F., Andriessen, P. A. M., Matenco, L., Bada, G., Garcia-Castellanos, D., Hardebol., N., Dèzes, P., and Sokoutis, D., 2005, Lithospheric memory, state of stress and rheology: neotectonic controls on Europe's intraplate continental topography. *Quaternary Science Reviews*, v. 24, p. 241-304.
- Dewey, J.F., Hempton, M.R., Kidd, W.S.F., Saroglu, F., and Şengör, A.M.C., 1986, Shortening of continental lithosphere: the neotectonics of Eastern Anatolia—a young collision zone: Geological Society, London, Special Publications, v. 19, p. 1-36.
- Donelick, R. A., O’Sullivan, P. B., and Ketcham, R.A., 2005, Apatite fission-track analysis: *Reviews in Mineralogy and Geochemistry*, v. 58(1), p. 49-94.
- Ehlers, T.A., Chaudhri, T., Kumar, S., Fuller, C.W., Willett, S.D., Ketcham, R.A., Brandon, M.T., Belton, D.X., Kohn, B.P., Gleadow, A.J. and Dunai, T.J., 2005, Computational tools for low-temperature thermochronometer interpretation: *Reviews in Mineralogy and Geochemistry*, v. 58(1), p. 589-622.
- Galoyan, G.L., Melkonyan, R.L., Chung, S.-L., Khorenyan, R.H., Atayan, L.S., Hung, C.-H., and Amiraghyan, S.V., 2013, On the petrology and geochemistry of Jurassic Island-arc magmatics of the Karabagh segment of the Somkheto–Karabagh terrain: *Proceedings of the NAS of the Republic of Armenia, Earth Sciences*, v. 66, p. 3–22 (in Russian).
- Galoyan, G., Rolland, Y., Sosson, M., Corsini, M., Billo, S., Verati, C., and Melkonyan, R. 2009, *Geology, geochemistry and <sup>40</sup>Ar/<sup>39</sup>Ar dating of Sevan ophiolites (Lesser Caucasus, Armenia): evidence for Jurassic back-arc opening and hot spot event between the South Armenian Block and Eurasia: *Journal of Asian Earth Sciences*, v. 34, p. 135–153.*
- Gleadow, A.J.W., and Fitzgerald, P.G., 1987, Uplift history and structure of the Transantarctic Mountains: new evidence from fission track dating of basement apatites in the Dry Valleys area, southern Victoria Land: *Earth and Planetary Science Letters*, v. 82, p. 1-14.
- Hall, R., 1976, Ophiolite emplacement and the evolution of the Taurus suture zone, southeastern Turkey: *Geological Society of America Bulletin*, v. 87, p. 1078-1088.

- Hassig, M., Rolland, Y., Sosson, M., Galoyan, G., Muller, C., Avagyan, A., and Sahakyan, L. 2013, New structural and petrological data on the Amasia ophiolites (NW Sevan–Akera suture zone, Lesser Caucasus): Insights for a large-scale obduction in Armenia and NE Turkey: *Tectonophysics*, v. 588, p. 135–153.
- Hurford, A.J., and Green, P.F., 1983, The zeta age calibration of fission-track dating: *Chemical Geology*, v. 41, p. 285-317.
- Jolivet, L., and Faccenna, C., 2000, Mediterranean extension and the Africa-Eurasia collision: *Tectonics*, v. 19, p. 1095-1106.
- Jolivet, L., Huchon, P., and Rangin, C., 1989, Tectonic setting of Western Pacific marginal basins: *Tectonophysics*, v. 160, p. 23-47.
- Ketcham, R.A., 2005, Forward and inverse modeling of low-temperature thermochronometry data: *Reviews in Mineralogy and Geochemistry*, v. 58(1), p. 275-314.
- Ketcham, R.A., Carter, A., Donelick, R.A., Barbarand, J., and Hurford, A.J., 2007, Improved modeling of fission-track annealing in apatite: *American Mineralogist*, v. 92(5-6), p. 799-810.
- Ketcham, R.A., Donelick, R.A., and Carlson, W.D., 1999, Variability of apatite fission-track annealing kinetics: III. Extrapolation to geological time scales: *American Mineralogist*, v. 84(9), p. 1235-1255.
- Khain, V.E., 1994, *Geology of Northern Eurasia (Ex-USSR). Second Part: Phanerozoic fold belts and young platforms*: Gebrüder Borntraeger, Berlin, 404 pp.
- Knipper, A.L. 1975, The oceanic crust in the structure of the Alpine Folded Belt (South Europe, western part of Asia and Cuba): *Transactions*, 267, Moscow 'Nauka' (in Russian).
- Knipper, A.L., and Khain, E.V., 1980, Structural position of ophiolites of the Caucasus: *Ofioliti*, Special Issue, 2, p. 297–314.
- Le Pichon, X., and Kreemer, C., 2010, The Miocene-to-present kinematic evolution of the eastern Mediterranean and Middle East and its implications for dynamics: *Annual Review of Earth and Planetary Sciences*, v. 38, p. 323-351.
- McClusky, S. et al., 2000, Global Positioning System constraints on plate kinematics and dynamics in the eastern Mediterranean and Caucasus: *Journal of Geophysical Research*, v. 105, p. 5695– 5719.
- Melkonyan, R.L., 1989, *Petrology and ore-bearing capacity of the Mesozoic island-arc granitoid formations of the Lesser Caucasus: Summary of Sciences Thesis*, Moscow, 50 p. (in Russian).
- Ministry of Geology of the USSR, 1952a. *Geological Map of the USSR*, 1:200,000 scale, sheet K-38-XXVII.

- Ministry of Geology of the USSR, 1952b. Geological Map of the USSR, 1:200,000 scale, sheet K-38-XXXIII.
- Ministry of Geology of the USSR, 1952c. Geological Map of the USSR, 1:200,000 scale, sheet K-38-XXXV.
- Ministry of Geology of the USSR, 1952d. Geological Map of the USSR, 1:200,000 scale, sheet J-38-V.
- Ministry of Geology of the USSR, 1959. Geological Map of the USSR, 1:200,000 scale, sheet K-38-XXVIII.
- Ministry of Geology of the USSR, 1971. Geological Map of the USSR, 1:200,000 scale, sheet J-38-XI.
- Moritz, R., Rezeau, H., Ovtcharova, M., Tayan, R., Melkonyan, R., Hovakimyan, S., Ramazanov, V., Selby, D., Ulianov, A., Chiaradia, M., and Putlitz, B., 2016, Long-lived, stationary magmatism and pulsed porphyry systems during Tethyan subduction to post-collision evolution in the southernmost Lesser Caucasus, Armenia and Nakhitchevan: *Gondwana Research*, v. 37, p. 465-503.
- Okay, A. I., and Tüysüz, O., 1999, Tethyan sutures of the northern Turkey. In *The Mediterranean Basins: Tertiary Extension within the Alpine Orogen* (eds B. Durand, L. Jolivet, F. Horvát & M. Serrane): Geological Society of London Special Publication no. 156, p. 475-515.
- Okay, A.I., Zattin, M., and Cavazza, W., 2010, Apatite fission-track data for the Miocene Arabia-Eurasia collision: *Geology*, v. 38, p. 35–38.
- Reilinger, R., McClusky, S., Vernant, P., Lawrence, S., Ergintav, S., Cakmak, R., Ozener, H., Kadirov, F., Guliev, I., Stepanyan, R., Nadariya, M., Hahubia, G., Mahmoud, S., Sakr, K., Arrajehi, A., Paradissis, D., Al-Aydrus, A., Prilepin, M., Guseva, T., Evren, E., Dmitrotsa, A., Filikov, S.V., Gomez, F., Al-Ghazzi, R., and Karam, G., 2006. GPS constraints on continental deformation in the Africa-Arabia-Eurasia continental collision zone and implications for the dynamics of plate interactions: *Journal of Geophysical Research*, v. 111, No. B5, B05411.
- Ricou, L.E., Dercourt, J., Geyssant, J., Grandjacquet, C., Lepvrier, C., and Biju-Duval, B., 1986, Geological constraints on the Alpine evolution of the Mediterranean Tethys: *Tectonophysics*, v. 123, p. 83–122.
- Robertson, A.H.F., 2002, Overview of the genesis and emplacement of Mesozoic ophiolites in the Eastern Mediterranean Tethyan region: *Lithos*, v. 65, p. 1-67.
- Robertson, A.H.F., Parlak, O., Rızaoğlu, T., Ünlügenç, Ü., İnan, N., Taslı, K., and Ustaömer, T., 2007, Tectonic evolution of the South Tethyan ocean: evidence from the Eastern Taurus Mountains (Elazığ region, SE Turkey). In: *Deformation of continental crust* (eds A.C. Ries, R.W.H. Butler & R.H. Graham), p. 231-270. Geological Society, London, Special Publication, 272.

- Rolland, R., Galoyan, G., Bosch, D., Sosson, M., Corsini, M., Fornari, M., and Verati, C., 2009, Jurassic back-arc and Cretaceous hot-spot series in the Armenian ophiolites – Implications for the obduction process: *Lithos*, v. 112, p. 163–187.
- Rolland, Y., Galoyan, G., Sosson, M., Melkonyan, R., and Avagyan, A., 2010, The Armenian Ophiolite: insights for Jurassic back-arc formation, Lower Cretaceous hot spot magmatism and Upper Cretaceous obduction over the South Armenian Block. In: Stephenson, R.A., Starostenko, V., and Bergerat, F. (eds), *Sedimentary Basins Tectonics from the Black Sea to the Arabian Platform*: Geological Society, London, Special Publications, v. 340, p. 353-382.
- Rolland, Y., Billo, S., Corsini, M., Sosson, M., and Galoyan, G., 2007, Blueschists of the Amassia-Stepanavan Suture Zone (Armenia): linking Tethys subduction history from E-Turkey to W-Iran: *International Journal of Earth Sciences*, doi: 10.1007/s00531-007-0286-8.
- Rolland, Y., Perincek, D., Kaymakci, N., Sosson, M., Barrier, E., and Avagyan, A., 2012, Evidence for ~ 80-75Ma subduction jump during Anatolide-Tauride-Armenian block accretion and ~ 48Ma Arabia-Eurasia collision in Lesser Caucasus-East Anatolia: *Journal of Geodynamics*, v. 56, p. 76-85.
- Şengör, A.M.C., Tüysüz, O., İmren, C., Sakiñç, M., Eyidoğan, H., Görür, N., Le Pichon, X., and Rangin, C., 2005, The North Anatolian fault: A new look. *Annu. Rev. Earth Planet. Sci.*, v. 33, p.37-112.
- Sokolov, S.D., 1977, *The Olistostromes and Ophiolitic Nappes of the Lesser Caucasus*: Izdatelstvo 'Nauka', Moscow (in Russian).
- Sosson, M., Rolland, Y., Müller, C., Danelian, T., Melkonyan, R., Kekelia, S., Adamia, S., Babazadeh, V., Kangarli, T., Avagyan, A., Galoyan, G. and Mosar, J., 2010, Subductions, obduction and collision in the Lesser Caucasus (Armenia, Azerbaijan, Georgia), new insights: Geological Society of London Special Publication no. 340, p. 329-352.
- Stampfli, G., Borel, G., Cavazza, W., Mosar, J. and Ziegler, P.A. (Eds.), 2001, *The Paleotectonic Atlas of the PeriTethyan Domain*: CD-ROM, European Geophysical Society.
- Stampfli, G. M., and Hochard, C., 2009, *Plate tectonics of the Alpine realm*: Geological Society, London, Special Publication 327, p. 89-111.
- Ziegler, P.A., 1993, Plate-moving mechanisms: their relative importance: *Journal of the Geological Society*, v. 150, p. 927-940.
- Ziegler, P.A., Cloetingh, S., and Van Wees, J.-D., 1995, Dynamics of intra-plate compressional deformation: the Alpine foreland and other examples: *Tectonophysics*, v. 252, p. 7–59.
- Ziegler, P.A., Van Wees, J.-D., and Cloetingh, S. 1998, Mechanical controls on collision-related compressional intraplate deformation: *Tectonophysics*, v. 300, p. 103-129.

- Ziegler, P.A., Bertotti, G., and Cloetingh, S.A.P.L., 2002, Dynamic processes controlling foreland development - the role of mechanical (de) coupling of orogenic wedges and forelands. *Stephan Mueller Special Publication Series*, 1, 17-56.
- Zoback, M.L., 1992, First-and second-order patterns of stress in the lithosphere: The World Stress Map Project: *Journal of Geophysical Research: Solid Earth*, v. 97, p. 11703-11728.
- Zonenshein, L.P., Kuzmin, M.I., and Natapov, L.M. 1990, *Geology of the USSR: A Plate-Tectonic Synthesis*: American Geophysical Union Geodynamics Series, v. 21, 242 p.

## Figure Captions

Figure 1. Tectonic sketch map of Asia Minor and the Caucasian region. Modified after Sosson *et al.* (2010) and Cavazza *et al.* (2017). Location of Fig. 2 is shown.

Figure 2. Geological sketch map of the Lesser Caucasus (after Sosson *et al.* 2010; Cavazza *et al.* 2017). Apatite fission-track model ages are shown (for analytical details and exact sample locations, see Table 1). Traces of geological cross-sections of Figures 3, 4, and 5 are also shown.

Figure 3. Schematic geological section across the northern Lesser Caucasus (see Fig. 2 for location). Modified after Ministry of Geology USSR (1952a, b). The extent of a large slab of southwestward-obducted ophiolite along the Sevan-Akera suture is inferential. Only the fission-track ages closest to the trace of the cross-section are shown; see Fig. 2 and Table 1 for the complete dataset. Time-temperature paths obtained from integrated inverse modeling of apatite fission-track data from samples TU290 and TU297. Green areas mark envelopes of statistically acceptable fit, and the lines correspond to the most probable thermal histories: red line is the mean of all statistically acceptable paths; blue line is the best-fit T-t path. Parameters related to inverse modeling are reported: GOF, goodness-of-fit gives an indication about the fit between observed and predicted data (values closer to 1 are best).

Figure 4. Schematic geological section across the central Lesser Caucasus (see Fig. 2 for location). Modified after Sosson *et al.* (2010). The section emphasizes the structural pattern produced by shortening during continental collision; the effects of late-stage strike-slip tectonics are largely ignored. Only the fission-track ages closest to the traces of geological cross-sections are shown; see Fig. 2 for the complete dataset. Time-temperature paths obtained from integrated inverse modeling of apatite fission-track data from samples TU395, 348 and 351. Green areas mark envelopes of statistically acceptable fit, and the lines correspond to the most probable thermal histories: red line is the mean of all statistically acceptable paths; blue line is the best-fit T-t path. Parameters related to inverse modeling are



reported: GOF, goodness-of-fit gives an indication about the fit between observed and predicted data (values closer to 1 are best).

Figure 5. Schematic geological section across the southern Lesser Caucasus (see Fig. 2 for location). Modified after Ministry of Geology USSR (1952c, 1952d, 1971). Interpretation of this cross-section subscribes to the notion that the Kapan Zone represents a section of the Somkheto-Karabakh magmatic arc displaced by large-scale sinistral strike-slip. Only the fission-track ages closest to the traces of geological cross-sections are shown; see Fig. 2 for the complete dataset. Time-temperature paths obtained from integrated inverse modeling of apatite fission-track data from samples TU391. Green areas mark envelopes of statistically acceptable fit, and the lines correspond to the most probable thermal histories: red line is the mean of all statistically acceptable paths; blue line is the best-fit T-t path. Parameters related to inverse modeling are reported: GOF, goodness-of-fit gives an indication about the fit between observed and predicted data (values closer to 1 are best).

Figure 6. Radial plots of single-grain apatite fission-track ages and histograms showing the confined-track length distributions of apatite grains for the six samples employed for statistical modeling. For analytical details on AFT ages reported in the figure, see Table 1.

Figure 7. Areal distribution of apatite fission-track ages in eastern Anatolia and Transcaucasia. Dark orange: ages <15 Ma; light orange: ages 22-15 Ma. All other FT ages are older than 22 Ma. IAESZ: Izmir-Ankara-Erzincan suture zone. Sources of data: Okay *et al.* 2010; Albino *et al.* 2014; Cavazza *et al.* 2017, 2018; this study.

Figure 8. GPS motion vectors in the Middle East (from LePichon and Kreemer 2010). DSF-Dead Sea Fault; EAF-East Anatolian Fault system; EP-Eastern Pontides; GC-Greater Caucasus; IAESZ: Izmir-Ankara-Erzincan suture zone; IZ-Istanbul Zone; KM-Kirsehir Massif; LC-Lesser Caucasus; NAF-North Anatolian Fault system; SASZ-Sevan-Akera suture zone; SkZ-Sakarya Zone.

Figure 9. Stages of Neogene deformation patterns in the Eurasian hinterland of the Bitlis-Zagros collision zone. The development and westward movement of the Anatolian Plate has decoupled to a large extent the collision zone from its hinterland. Dark red indicates areas of focused deformation/exhumation, as determined by fission-track analysis. The plate velocity field is only schematically shown.

Table 1

Table 1. Results of apatite fission-track analyses (see Fig.2 for location of samples).

Sample	Rock Type	Location	Age	Elevation (m)	UTM Coordinates (38T)	No. crystals	Spontaneous			Induced			P(X) <sup>2</sup>
							$\rho_s$	$N_s$	$\rho_i$	$N_i$	$\rho_i$	$N_i$	
TU290*	Monzonite	Aghavnadzor	Late Eocene	1,846	475087 4492519	17	1.75	57	17.32	559	99.43		
TU291*	Orthogneiss	Bjni	Precambrian	1,788	469751 4480111	20	1.91	80	18.45	773	80.92		
TU292*	Tonalite	NW of Arzakan	Late Jurassic	1,923	463243 4484734	20	2.05	101	18.30	898	95.68		
TU297*	Leucogranite	Mets Ayrum	Late Jurassic	665	484745 4558283	21	1.53	59	18.83	722	98.77		
TU298*	Plagiogranite	E of Alaverdi	Middle Jurassic	661	475628 4551062	20	2.26	179	16.83	1,134	100.00		
TU344*	Granodiorite	Dashkesan pluton	Late Jurassic	1,438	591398 4483554	20	4.73	257	11.90	648	100.00		
TU345*	Granodiorite	Dashkesan pluton	Late Jurassic	1,545	592153 4482654	20	5.01	276	12.92	713	98.20		
TU348*	Diorite	Gedabey mine	Late Jurassic	1,539	567870 4492625	18	5.09	281	12.89	711	100.00		
TU351*	Granite	Ertepe pluton	Middle Jurassic	1,677	575265 4498811	21	8.29	442	17.92	955	89.98		
TU352*	Granodiorite	Uchtepe pluton	Early Cretaceous	507	612216 4500380	20	8.43	456	17.64	940	87.68		
TU354	Granite	Khrami Massif	Late Paleozoic	1,524	426185 4599082	21	3.40	175	10.9	540	99.83		
TU380	Granite	Berdadzor pluton	Middle-Late Jurassic?	1,523	635850 4393421	16	1.79	62	20.20	702	90.14		
TU382	Tonalite	Mehmana pluton	Late Jurassic (153 Ma)	713	650829 4443990	21	2.85	180	35.32	2,226	89.95		
TU384	Granodiorite	Mehmana pluton	Late Jurassic	605	656216 4438175	20	2.73	169	39.20	1,979	97.31		
TU385	Tonalite	Tsav pluton	Late Jurassic - Early Cretaceous	1,238	627336 4329451	20	1.65	184	28.71	2,078	90.21		
TU387	Diorite	Tsav pluton	Late Jurassic - Early Cretaceous	1,069	626859 4323628	23	2.66	133	18.60	933	95.21		
TU391	Granite	Meghri pluton	latest Oligocene - earliest Miocene	2,153	601645 4327242	16	3.02	151	24.22	1,989	99.24		
TU392	Granodiorite	Sisian stocks	Middle Eocene	1,783	588031 4362302	25	4.82	374	34.70	2,696	80.81		
TU395	Granodiorite	Jermuk/Vaik stocks	Late Oligocene - Early Miocene?	1,320	544108 4393482	17	2.73	170	40.77	2,345	89.91		
TU396	Granodiorite	Yeghegnadzor	Late Oligocene - Early Miocene?	1,113	528198 4398800	25	2.61	160	22.26	1,364	99.94		
TU397	Diorite	Salli	Late Eocene	1,580	523785 4413779	18	2.29	107	26.51	1,213	91.12		

MCTL: mean confined track length. Central ages calculated using dosimeter glass CN5 and z-CN5=336.34±16.24 (analyst I. Albino).  $\rho_s$ : spontaneous track densities ( $\times 10^5 \text{ cm}^{-2}$ ); measured in internal mine dosimeter track densities ( $\times 10^6 \text{ cm}^{-2}$ ) on external mica detectors ( $g = 0.5$ );  $N_i$  and  $N_s$ : total numbers of tracks;  $P(X)^2$ : probability of obtaining  $X^2$ -value for n degrees of freedom (where n=number of crystals from Cavazza et al. (2017) (analyst I. Albino).

Figure 1

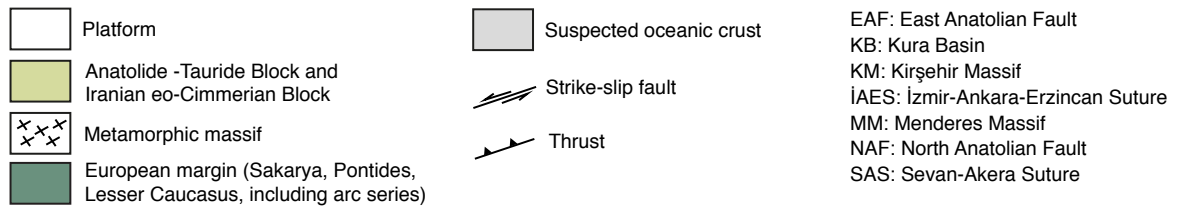
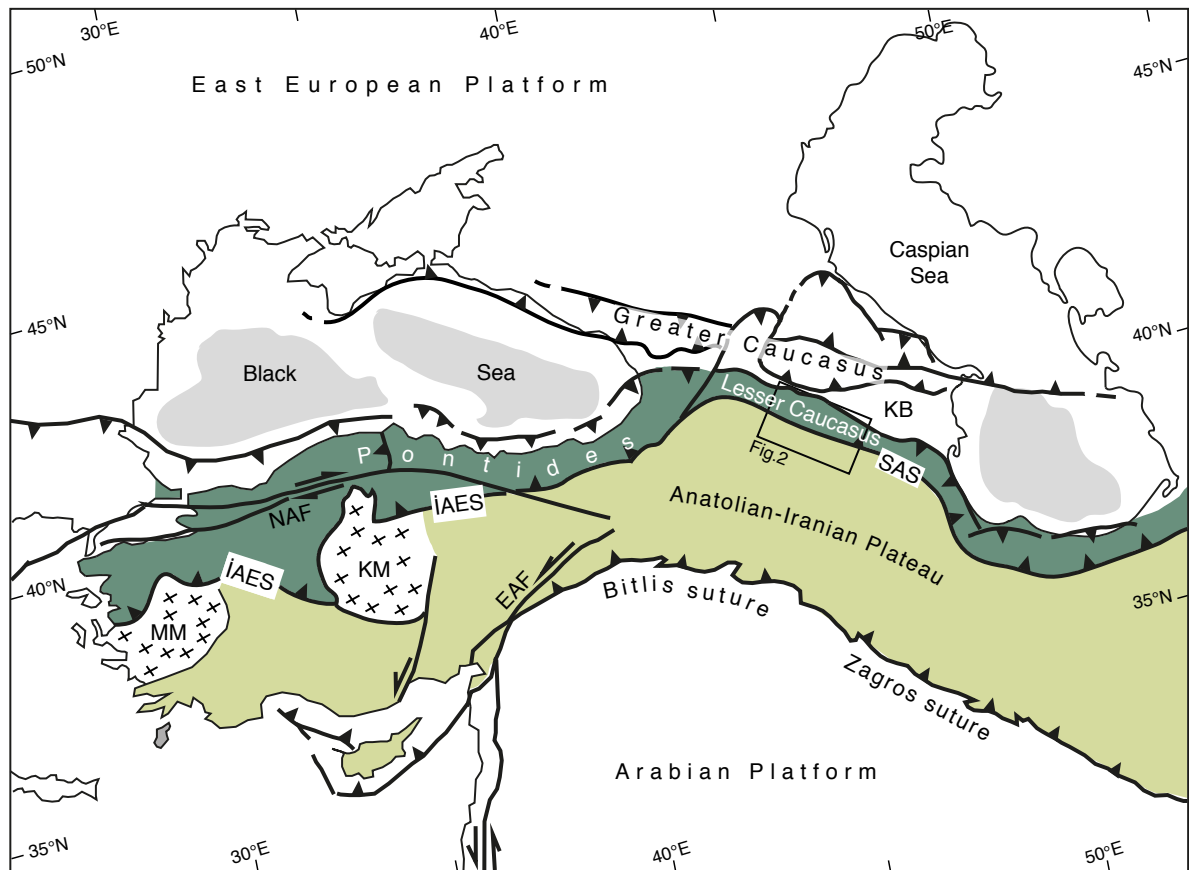


Figure 2

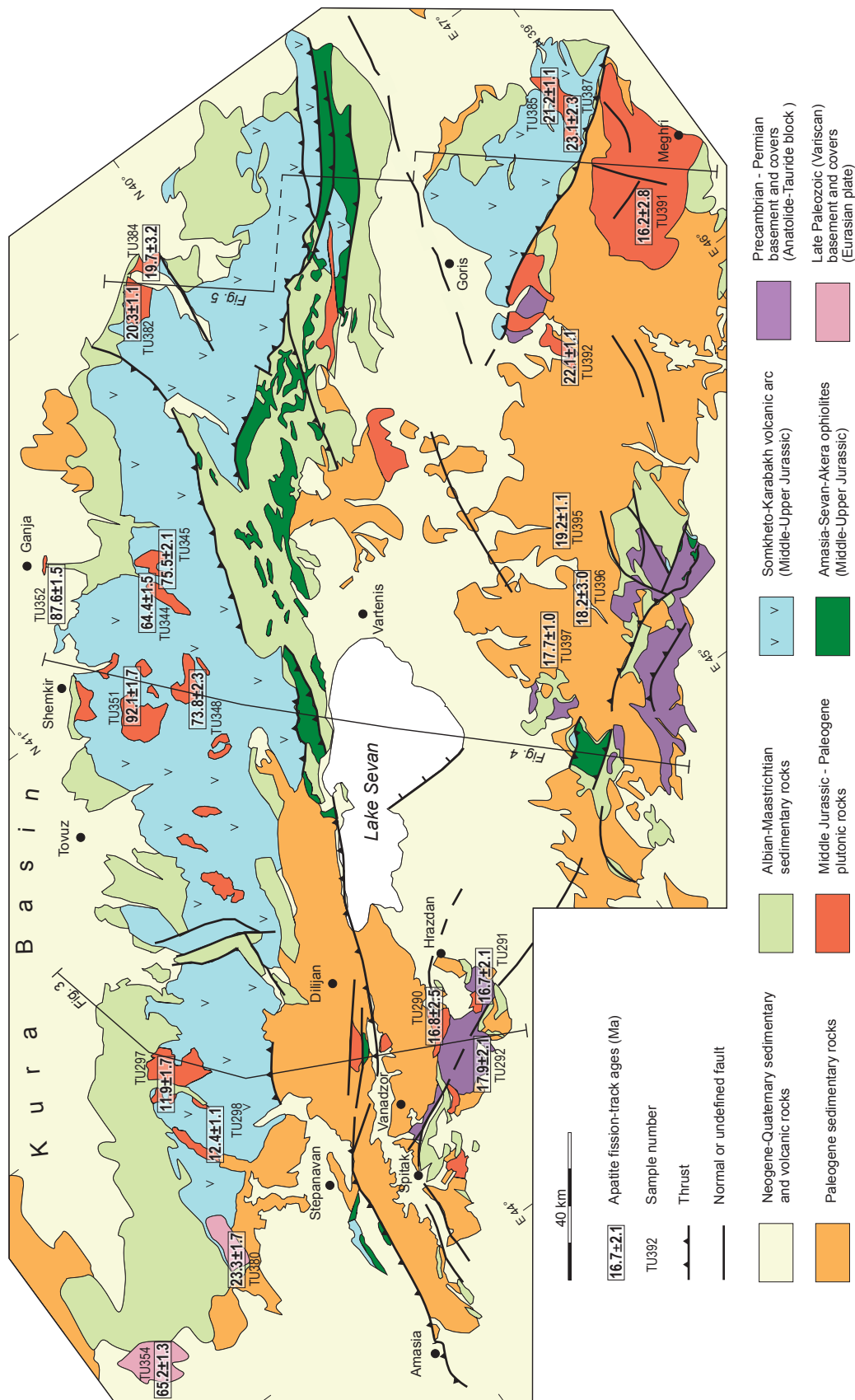


Figure 3

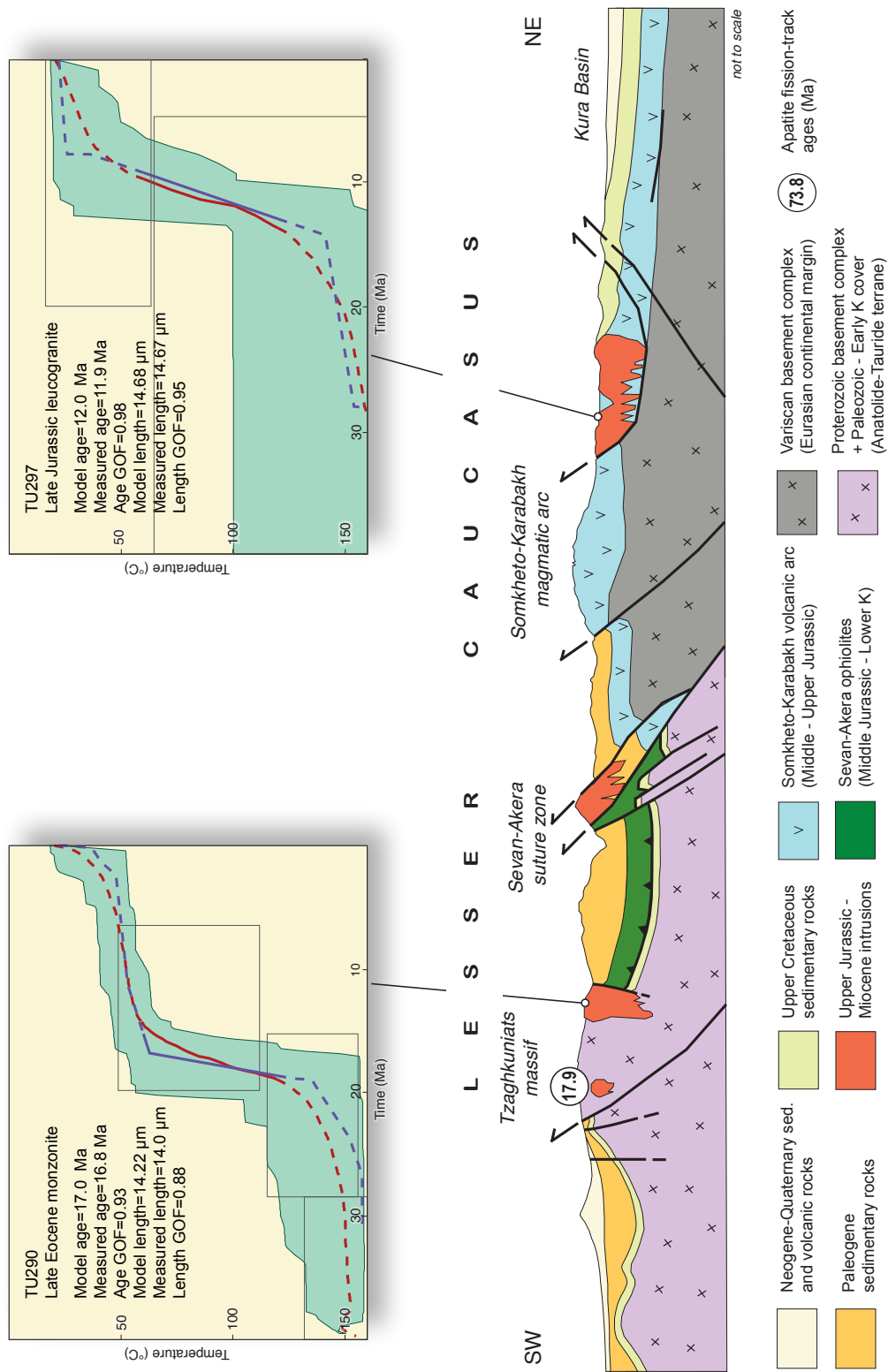


Figure 4

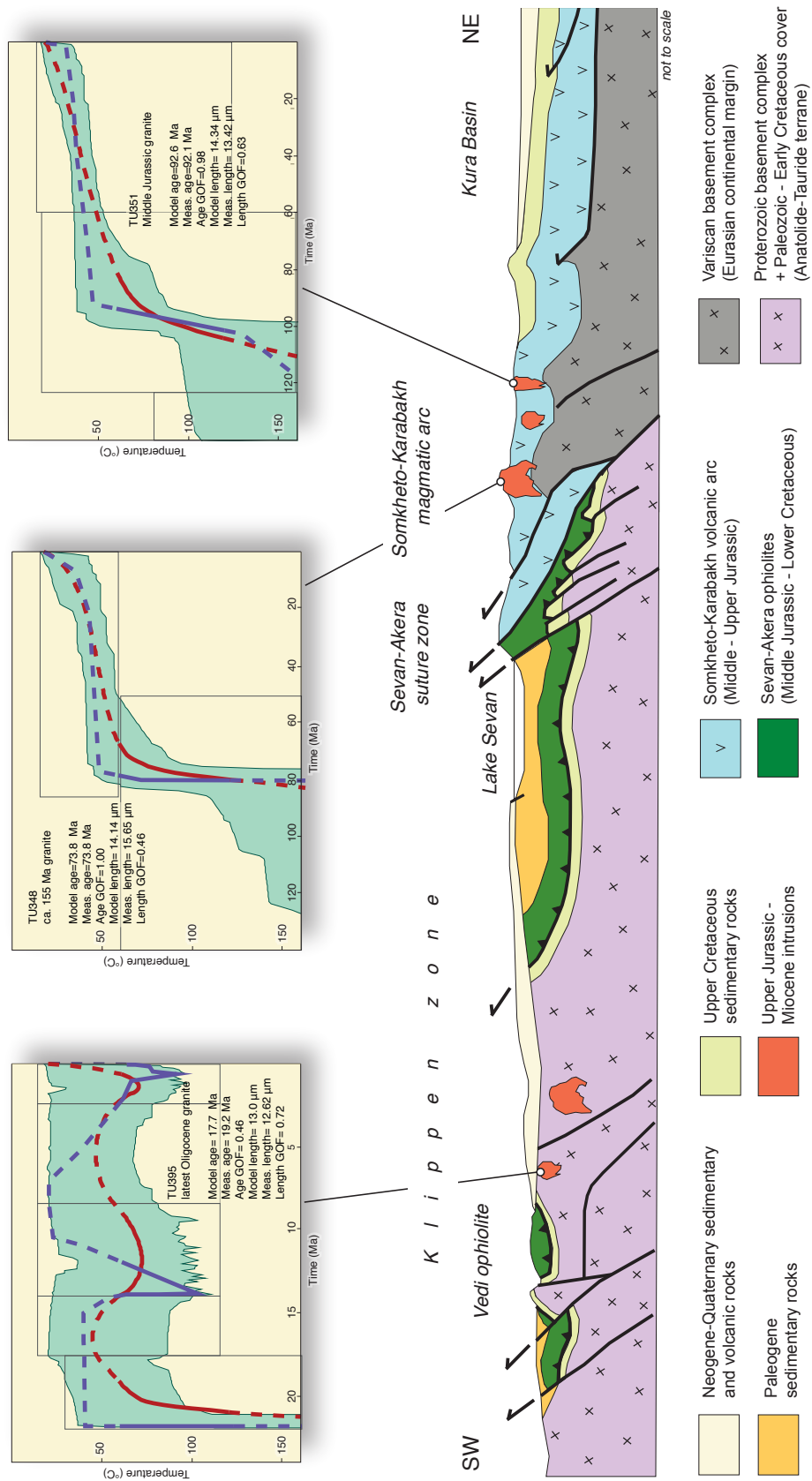


Figure 5

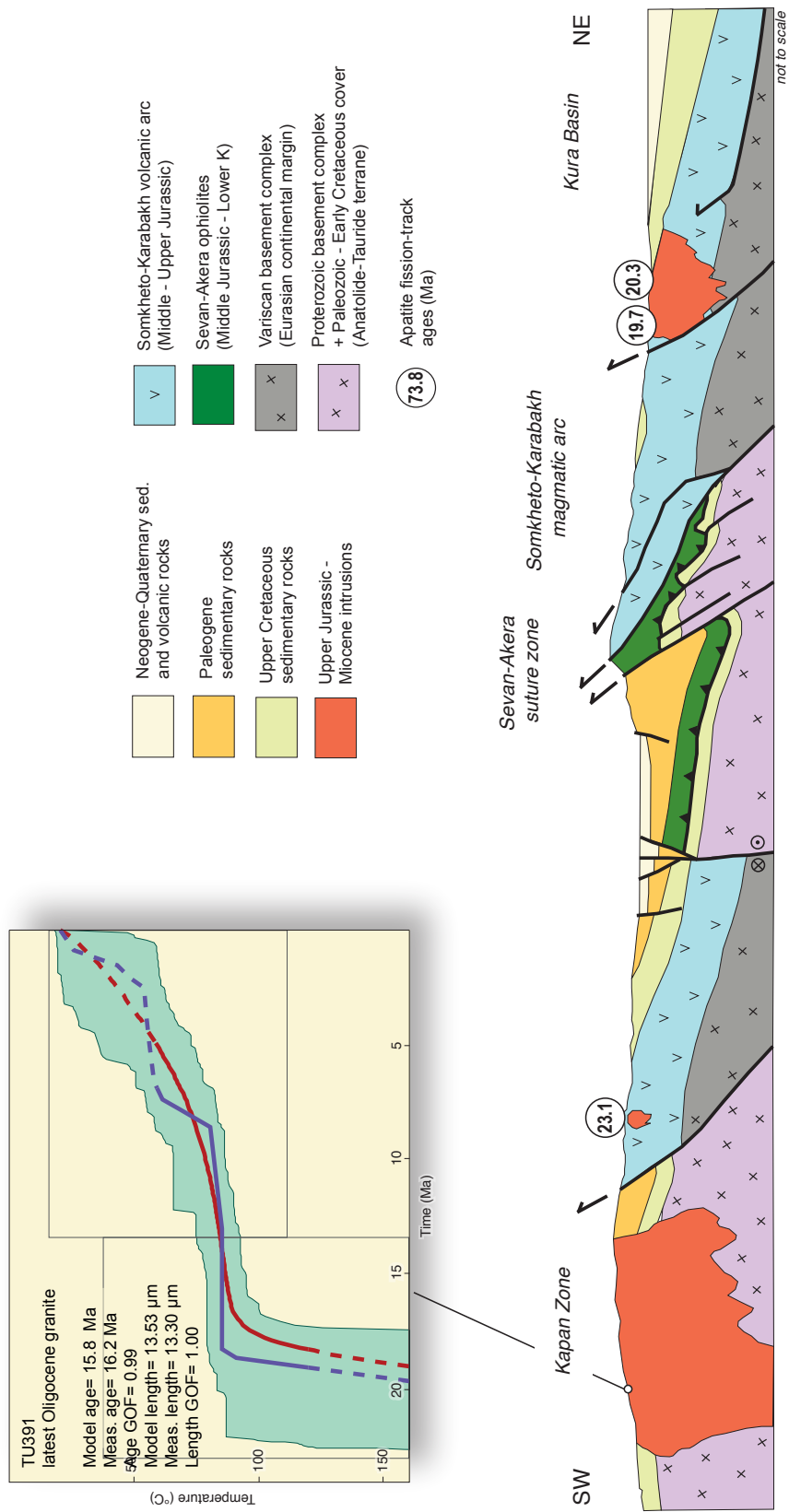




Figure 6

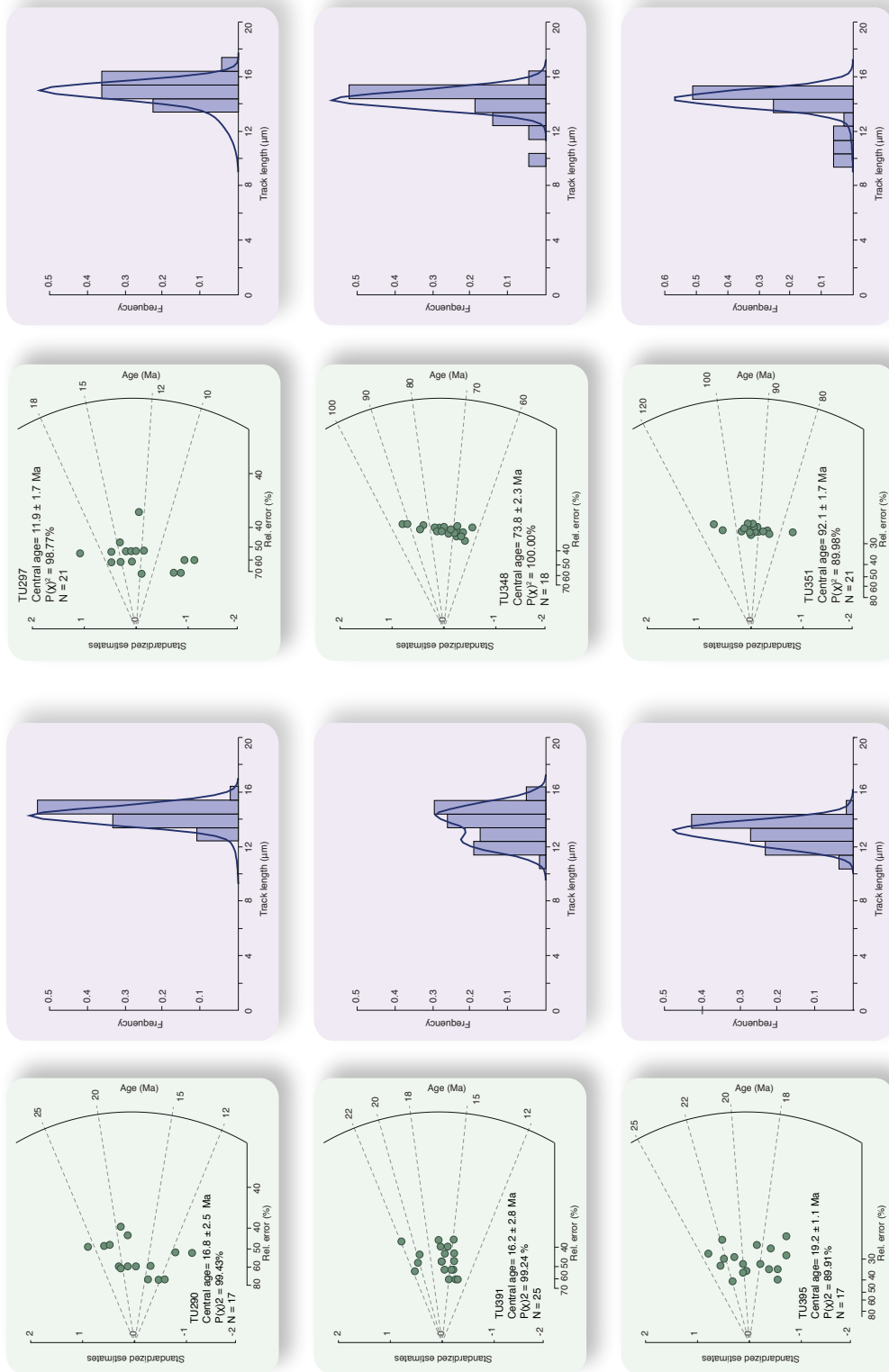


Figure 7

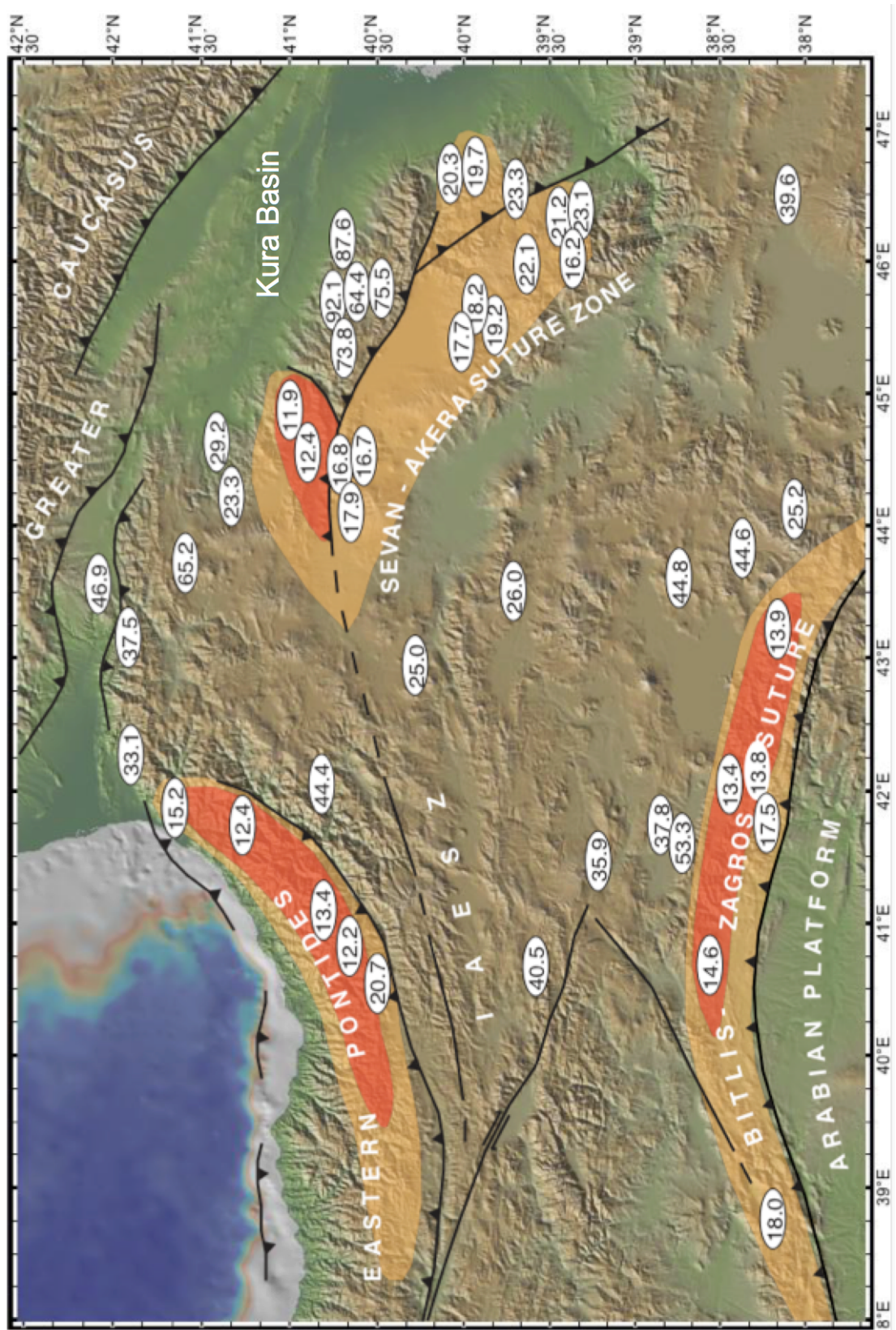


Figure 8

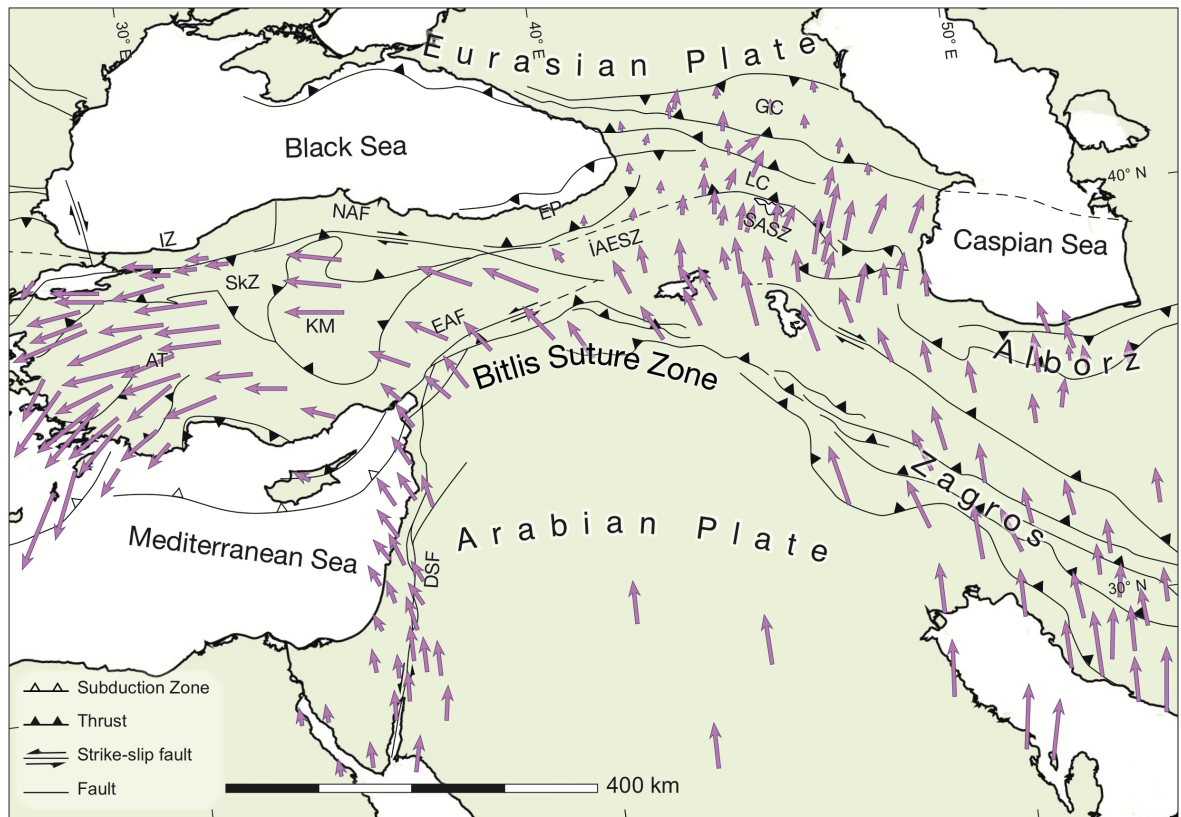
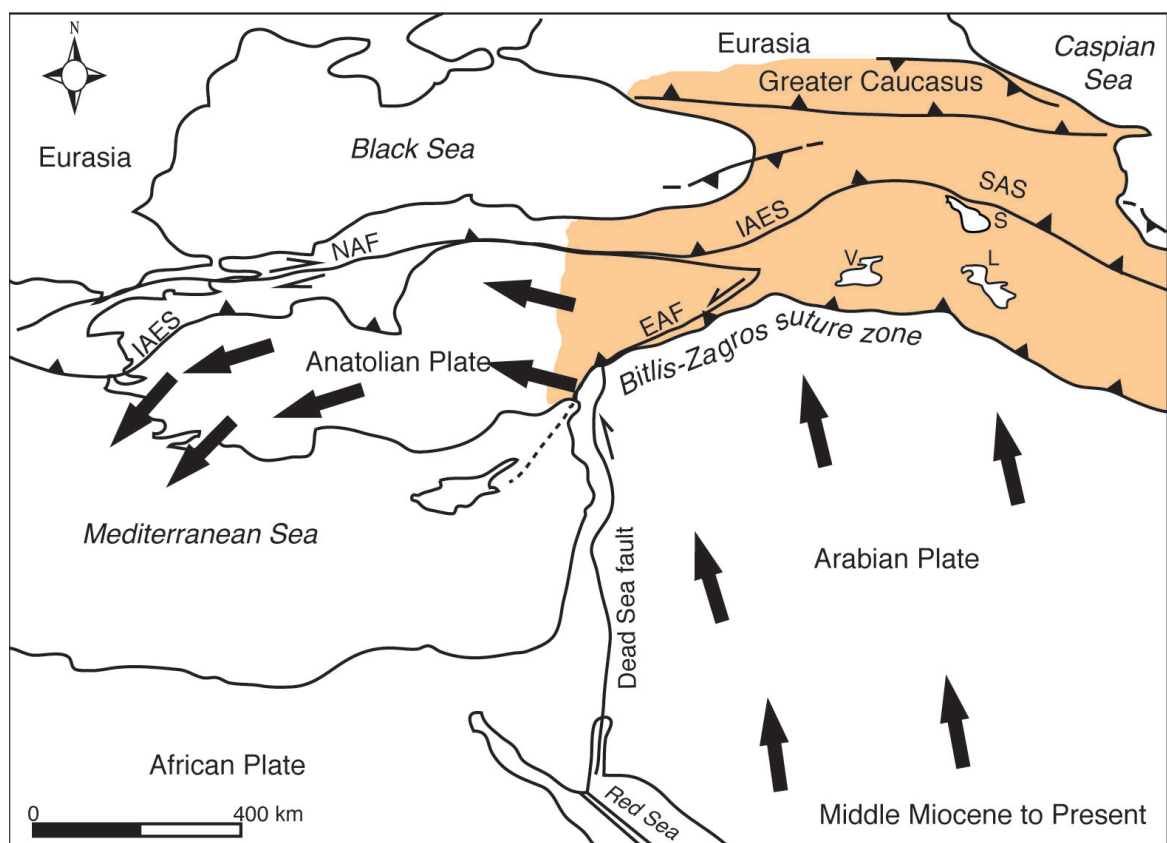
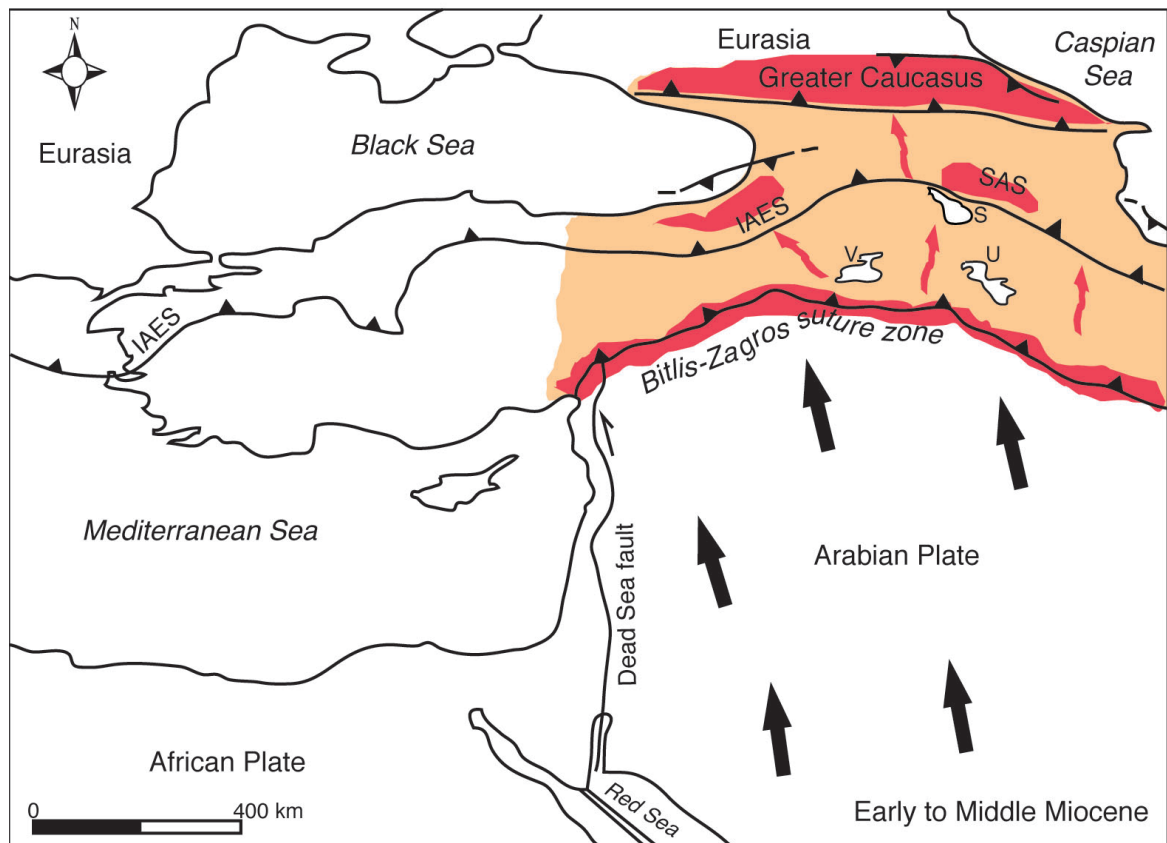


Figure 9



### **5.3. Manuscript 3**

#### **No significant Alpine tectonic overprint on the Cimmerian Strandja Massif**

**(SE Bulgaria and NW Turkey)**

Silvia Cattò, William Cavazza, Massimiliano Zattin & Aral I. Okay

International Geology Review, DOI: 10.1080/00206814.2017.1350604





## No significant Alpine tectonic overprint on the Cimmerian Strandja Massif (SE Bulgaria and NW Turkey)


Silvia Cattò, William Cavazza , Massimiliano Zattin & Aral I. Okay


To cite this article: Silvia Cattò, William Cavazza , Massimiliano Zattin & Aral I. Okay (2017): No significant Alpine tectonic overprint on the Cimmerian Strandja Massif (SE Bulgaria and NW Turkey), International Geology Review, DOI: [10.1080/00206814.2017.1350604](https://doi.org/10.1080/00206814.2017.1350604)

To link to this article: <http://dx.doi.org/10.1080/00206814.2017.1350604>

 Published online: 17 Jul 2017.

 Submit your article to this journal [↗](#)

 View related articles [↗](#)

 View Crossmark data [↗](#)

Full Terms & Conditions of access and use can be found at  
<http://www.tandfonline.com/action/journalInformation?journalCode=tigr20>


Download by: [Cornell University Library]

Date: 18 July 2017, At: 06:30

ARTICLE



## No significant Alpine tectonic overprint on the Cimmerian Strandja Massif (SE Bulgaria and NW Turkey)

Silvia Cattò<sup>a</sup>, William Cavazza <sup>a</sup>, Massimiliano Zattin<sup>b</sup> and Aral I. Okay<sup>c</sup>

<sup>a</sup>Department of Biological, Geological, and Environmental Sciences, University of Bologna, Bologna, Italy; <sup>b</sup>Department of Geosciences, University of Padua, Padua, Italy; <sup>c</sup>Eurasia Institute of Earth Sciences, Istanbul Technical University, Istanbul, Turkey

### ABSTRACT

We provide the first comprehensive picture of the thermochronometric evolution of the Cimmerian Strandja metamorphic massif of SE Bulgaria and NW Turkey, concluding that the bulk of the massif has escaped significant Alpine-age deformation. Following Late Jurassic heating, the central part of the massif underwent a Kimmeridgian-Berriasian phase of relatively rapid cooling followed by very slow cooling in Cretaceous-to-Early Eocene times. These results are consistent with a Late Jurassic–Early Cretaceous Neocimmerian (palaeo-Alpine) phase of north-verging thrust imbrication and regional metamorphism, followed by slow cooling/exhumation driven by erosion. From a thermochronometric viewpoint, the bulk of the Cimmerian Strandja orogen was largely unaffected by the compressional stress related to the closure of the Vardar–İzmir–Ankara oceanic domain(s) to the south, contrary to the adjacent Rhodopes. Evidence of Alpine-age deformation is recorded only in the northern sector of the Strandja massif, where both basement and sedimentary rocks underwent cooling/exhumation associated with an important phase of shortening of the East Balkan fold-and-thrust belt starting in the Middle–Late Eocene. Such shortening focused in the former Srednogorie rift zone because this area had been rheologically weakened by Late Cretaceous extension.

### ARTICLE HISTORY

Received 28 March 2017  
Accepted 30 June 2017

### KEYWORDS



Strandja Massif;  
low-temperature  
thermochronology; apatite  
fission-track analysis;  
Cimmerian orogeny; Balkans

### Introduction

The term ‘Cimmerian orogeny’ loosely refers to tectonic deformation ranging in age from the Late Triassic to the Early Cretaceous – a timespan of about 100 Ma – and covering a wide area stretching west to east from the eastern Alps to the Far East over a distance in excess of 8000 km (see Şengör 1984, for a review). The notion of a continent–continent collision between a Gondwana-derived ribbon continent and the southern margin of Laurasia as the driving mechanism for Cimmerian deformation was first proposed by Şengör (1979) and has influenced geological thinking ever since, with minor variations (e.g. Dercourt *et al.* 1993; Ricou 1995). More recent geological research is pointing to a series of discrete and largely diachronous Cimmerian deformation events (Stampfli and Borel 2004; Stampfli and Hochard 2009; Okay *et al.* 2013, 2015; Topuz *et al.* 2013). From this viewpoint, the composite Cimmerian tectonic belt comprises a variety of geological objects, including the remnants of: (i) several oceanic basins, which opened starting from the Middle Permian and closed between the Late Triassic and the Cretaceous; (ii)

a number of amalgamated pre-Alpine continental terranes resulting from the rifting of the Gondwanan margin, northward drift, and accretion to the European margin; and (iii) several oceanic volcanic arcs and plateaux locally accreted to the Laurasian margin without any large-scale continental collision. Such variety of accreted objects agrees well with the diachroneity and large geographic extent of the composite Cimmerian tectonic belt.

Main orogenic events related to terrane accretion along the southern Laurasian margin have been traditionally identified as Late Triassic – Liassic (Eocimmerian orogeny), Late Jurassic – Early Cretaceous (Neocimmerian orogeny), and Late Cretaceous – Miocene (Alpine orogeny *lato sensu*) (Şengör 1984; Khain 1994; Okay and Tüysüz 1999; Cavazza *et al.* 2004; Papanikolaou *et al.* 2004; Okay *et al.* 2010). Broadly speaking, Cimmerian-age tectonic elements are clearly distinguishable from the Far East to Iran, whereas they are more difficult to recognize across Asia Minor and the Balkan peninsula, where they were overprinted during later orogenic pulses. The distinction between Cimmerian and Alpine structural patterns

**CONTACT** William Cavazza  william.cavazza@unibo.it  Department of Biological, Geological, and Environmental Sciences, University of Bologna, Piazza di Porta San Donato 1, Bologna 40126, Italy

© 2017 Informa UK Limited, trading as Taylor & Francis Group

is rather difficult. The picture is further complicated by back-arc oceanic basins (Halstatt-Meliata, Maliac, Pindos, and Crimea-Svanetia) which opened along the southern margin of Eurasia during subduction of Palaeotethys and which were mostly destroyed during the docking of the Cimmerian continental terranes (e.g. Stampfli and Hochard 2009).

The southern Balkan region bears evidence of Cimmerian-age deformation (e.g. Stampfli *et al.* 2001; Papanikolaou *et al.* 2004; Stampfli and Kozur 2006). This region features a large metamorphic assemblage comprising – west to east – the Serbo-Macedonian,

Rhodope, and Strandja massifs. The relationship between these metamorphic domains, and their ages of metamorphism are still poorly known (see Burchfiel and Nakov 2015, for a review). Such southern Balkan metamorphic assemblage is bound to the north by the Eocene–Oligocene Balkan thrust belt and to the south by the early Tertiary Vardar suture and the Intra-Pontide suture (Figure 1). The least known portion of the southern Balkan metamorphic province is the Strandja Massif to the northeast. In this paper, we provide the first low-temperature thermochronometric data along a transect covering the whole width of the Strandja Massif, both

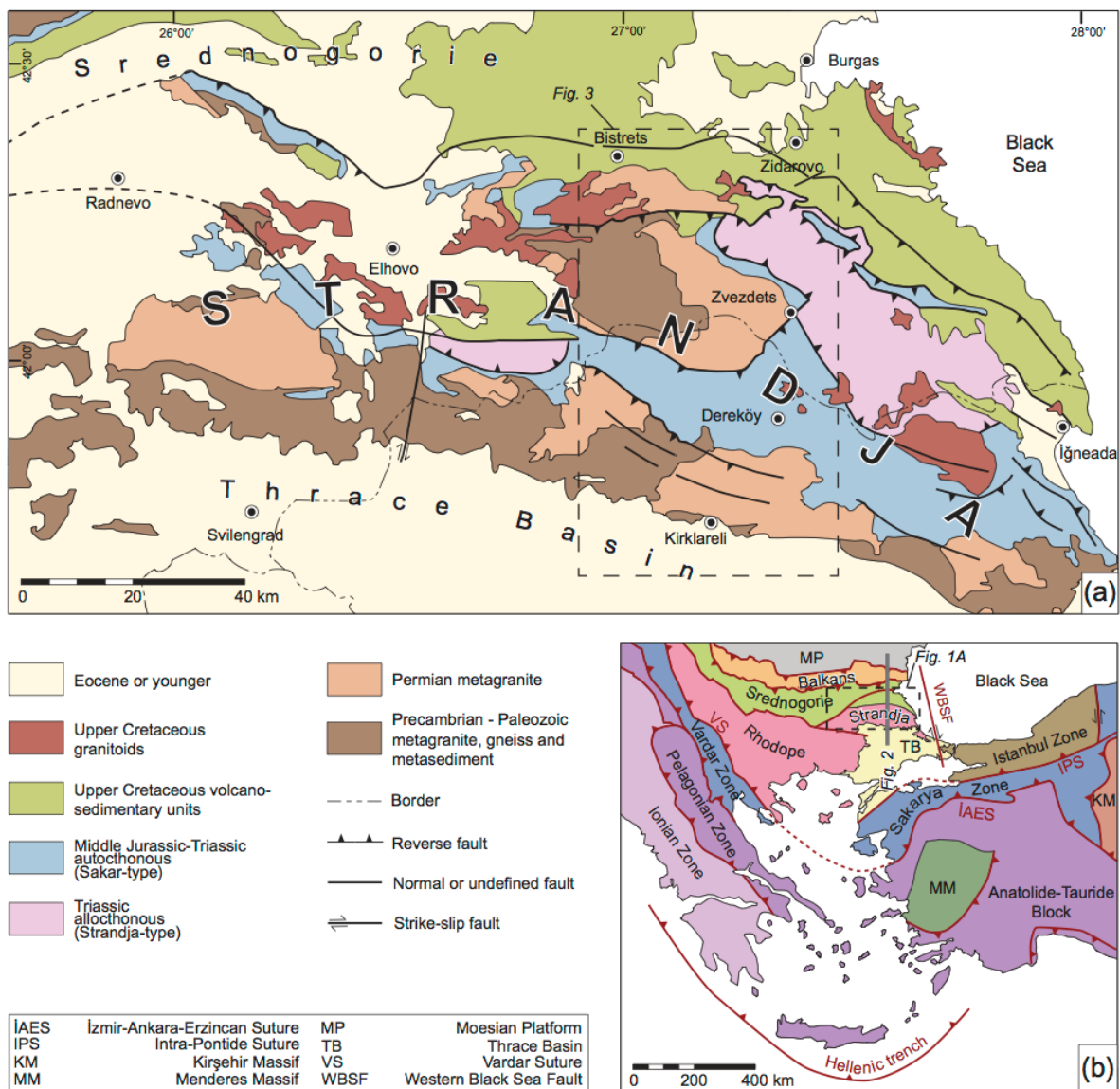


**Figure 1.** (a) Simplified geological map of the Strandja Massif; location of study area (Figure 3) is shown as a dashed box. (b) Main tectonic divisions and boundaries of the Aegean and periAegean region.



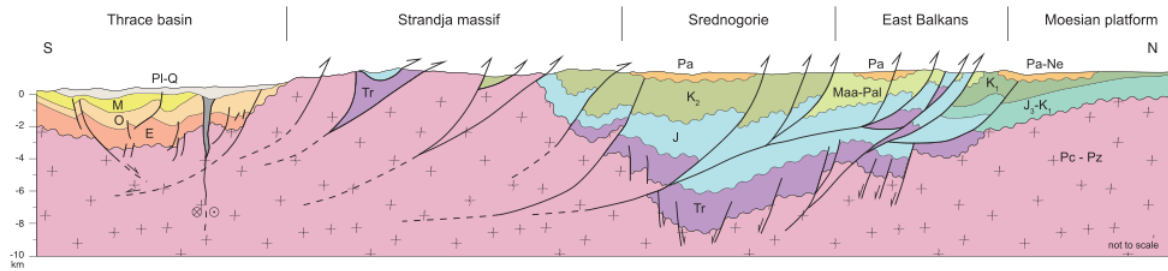


**Figure 2.** Schematic structural cross-section across the northern Thrace Basin, the Strandja Massif, the Srednogorie rift zone, and the southern Moesian Platform. Modified from Görür and Okay (1996), Georgiev *et al.* (2001), and Natal'in *et al.* (2012). Location of cross-section is shown in Figure 1.

in Bulgarian and Turkish territory. The integration of apatite fission-track (AFT) data with preexisting structural and radiometric data shows that the bulk of the massif did not undergo any significant thermal evolution during the Alpine tectonic cycle, thus basically retaining its Cimmerian-age structure. Alpine-age contractional deformation focused instead to the north of the massif to create the East Balkan thrust belt, whereas to the south late Eocene–Oligocene extension created the accommodation space for the thick deposits of the Thrace Basin (d'Atri *et al.* 2012; Cavazza *et al.* 2013) (Figure 2). From this viewpoint, the Strandja Massif is therefore one of very few areas in the perimediterranean region where Cimmerian-age tectonics can be studied without a significant Alpine structural overprint.

### Geological setting

The Strandja (Strandhza, Istanca) Massif is a poly-deformed, deeply eroded orogenic belt cropping out in a W–E direction in NW Turkey and SE Bulgaria over a distance of about 230 km and a width of about 60 km (Figure 1). Its internal structure results from the superposed effects of the Variscan, Cimmerian, and Alpine orogenic cycles (Okay *et al.* 2001; Lilov *et al.* 2004; Gerdjikov *et al.* 2005; Elmas *et al.* 2011; Sunal *et al.* 2011; Natal'in *et al.* 2012; Şahin *et al.* 2013; Machev *et al.* 2015). To the north, the Strandja Massif is thrust over the volcanics/volcaniclastics of the Late Cretaceous Eastern Srednogorie extensional basin (Georgiev *et al.* 2001; Stampfli *et al.* 2001) (Figure 2). The Western Black Sea fault, a NS-trending dextral strike-slip fault, which originated in the Cretaceous (Okay *et al.* 1994), defines the eastern boundary of the massif, separating it from the Western Black Sea basin and from the İstanbul exotic terrane (Figure 1). To the south, the thick Eocene-to-present sediments of the Thrace Basin lie non-conformably over the metamorphic rocks of the Strandja Massif

(Turgut *et al.* 1991; Less *et al.* 2011) (Figure 2). The western Strandja has been interpreted as thrust over the Eastern Rhodope Massif to the west (Papanikolaou *et al.* 2004) but the contact is covered by the sediments of the northwestern propagation of the Thrace Basin.

Despite several studies tackling the stratigraphy and structure of the Strandja Massif (e.g. Aydın 1974; Chatalov 1980, 1988, 1990, 1982; Gocev 1985; Dabovski and Savov 1988; Çağlayan 1996; Çağlayan and Yurtsever 1998; Okay *et al.* 2001; Dabovski *et al.* 2002; Gerdjikov 2005; Vasilev and Dabovski 2010; Natal'in *et al.* 2012, 2016), structural correlations and age attributions are still uncertain. An integrated, supranational overview of the Strandja Massif as a whole has been hindered by the scarce collaboration among the researchers from the two neighbouring countries. Most previous studies, often in native language, focus on either the Turkish or the Bulgarian side, ultimately preventing correlation between units and structures. Official maps published by the Committee of Geology and Mineral Resources (Sofia) and the General Directorate of Mineral Research and Exploration (MTA, Ankara) do not match across the border. Limited bilateral mapping and correlation by Bedi *et al.* (2013) somewhat improved the situation but as of today there is still no consensus as to the overall stratigraphy, structural arrangement, and palaeogeographic interpretation of the massif. Our geological sketch map (Figure 3) and cross-section (Figure 4) is modified after Okay *et al.* (2001), Sunal *et al.* (2006), Natal'in *et al.* (2012) for the Turkish side and based on Chatalov *et al.* (1995) for the Bulgarian side, with few modifications. More detailed explanations about the petrography and the stratigraphy of the units are provided in those works.

The overall structure of the massif has been traditionally interpreted as a Palaeozoic basement intruded by Permian granitoids and overlain by a Permo-Jurassic metasedimentary cover deposited in an amagmatic epicontinental basin (Aydın 1974, 1982; Çağlayan and

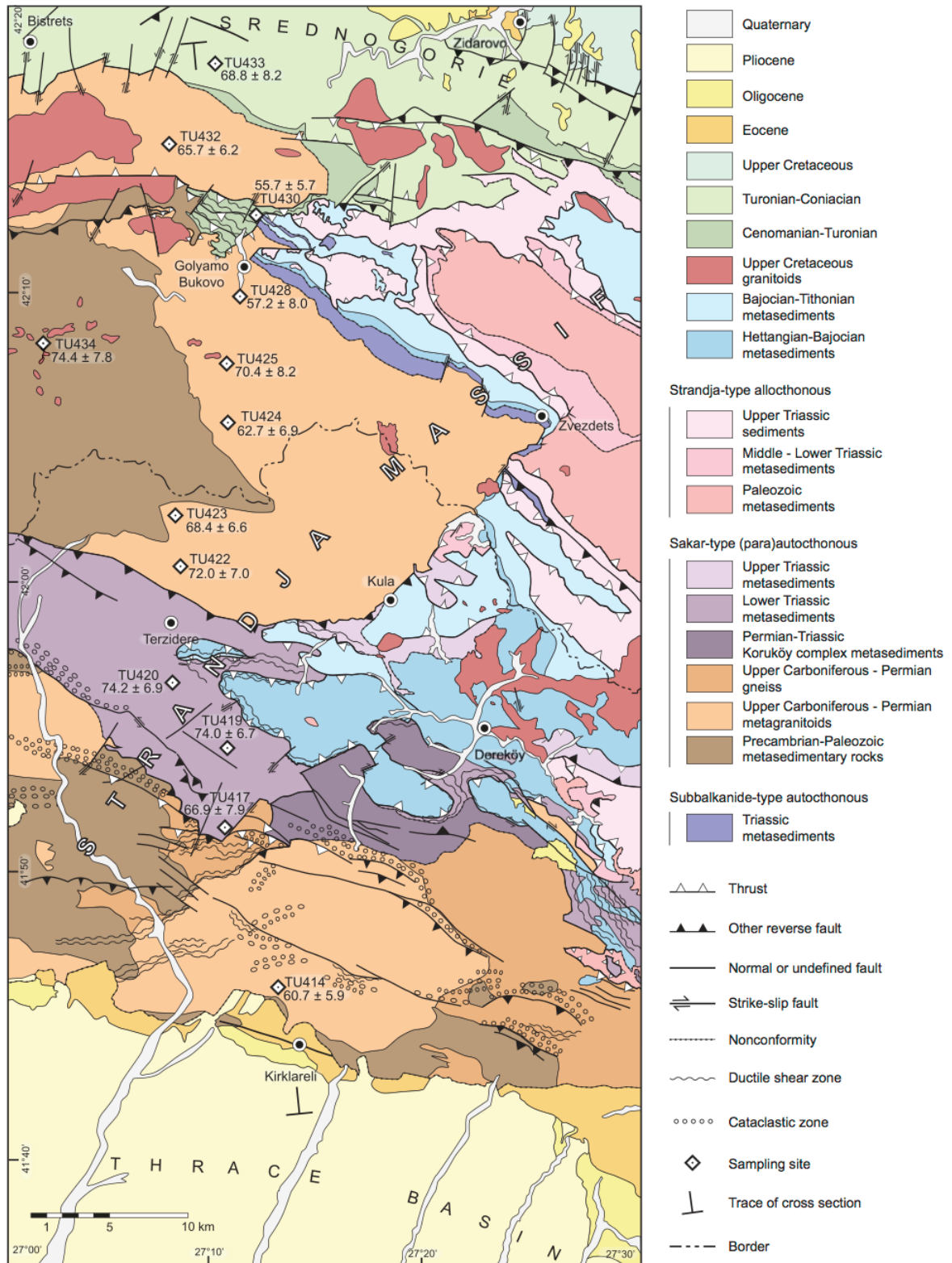


**Figure 3.** Geological map of the study area, modified after Chatalov *et al.* (1995), Çağlayan and Yurtsever (1998), Okay *et al.* (2001), Sunal *et al.* (2006), Natal'in *et al.* (2012), and Bedi *et al.* (2013). Diamonds indicate sample sites, numbers, and apatite fission-track mean ages in Ma ±1 standard deviation from the mean.

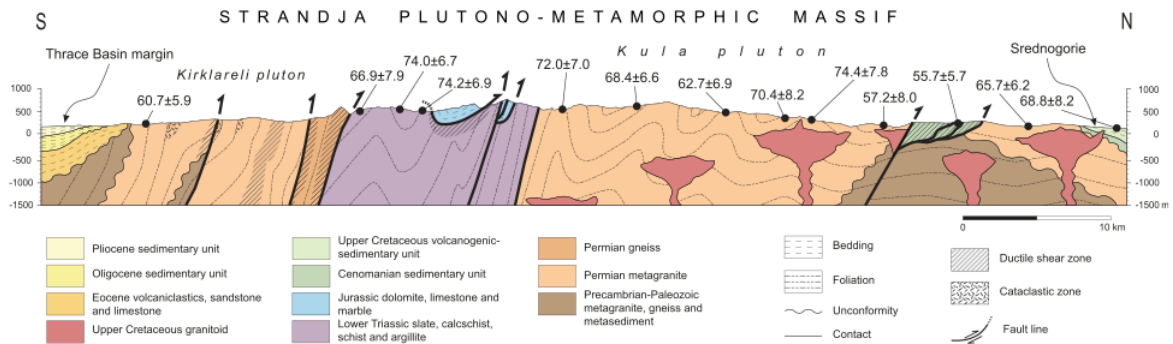


**Figure 4.** Geological cross-section of the Strandja Massif (see Figure 3 for the location of the trace of the section). Numbers in ellipses are apatite fission-track mean ages in Ma  $\pm$  1 standard deviation from the mean. Modified after Natal'in *et al.* (2012).

Yurtsever 1998; Okay *et al.* 2001). More recent studies have proved that the oldest rocks of the Strandja Massif are Precambrian (e.g. Lilov *et al.* 2004; Şahin *et al.* 2014; Natal'in *et al.* 2016).

The older tectonic history of the massif is loosely constrained due to intense Cimmerian-age structural overprint. Nonetheless, several studies locate the Strandja Massif along the northern margin of Gondwana in Late Proterozoic–Early Cambrian times (Yanev *et al.* 2006; Sunal *et al.* 2008; Şahin *et al.* 2014). A number of continental blocks rifted from Gondwana during the Devonian and drifted towards Eurasia (Stampfli and Borel 2002). Collision of these blocks and their accretion along the southern Eurasian margin took place during the Middle-to-Late Carboniferous with the development of the central European Variscan belt of which the Strandja Massif arguably represents the eastern continuation (Okay *et al.* 2001). A widespread episode of magmatism occurred in the Late Permian (Okay *et al.* 2001; Sunal *et al.* 2006) with the emplacement of the Kirklareli-type plutons along a subduction-related magmatic arc (Sunal *et al.* 2006; Natal'in *et al.* 2012).

A latest Permian–Jurassic sedimentary succession was deposited on the Variscan basement complex along the northern margin of the Palaeotethys (Chatalov 1990; Stampfli and Hochard 2009). The Triassic succession shows affinities to the central European Germanic facies, with a basal continental clastic series overlain by Middle Triassic shallow-marine carbonates (Chatalov 1988, 1990). On the other hand, in the so-called Strandja-type allochthonous tectonic units (Figure 3), the Triassic is deep marine (Chatalov 1988, 1990; Zagorchev and Budurov 1997; Dabovski *et al.* 2002; Tchoumatchenco and Tronkov 2010). Marine sedimentation continued into the mid-Jurassic (Bathonian), and came to an end in the Late Jurassic, when the continuing opening of the İzmir–Ankara ocean to the

south – forcing the Sakarya zone northward – led eventually to continental collision and thick-skinned thrusts imbrication (Stampfli and Hochard 2009). Ensuing regional metamorphism was of lower amphibolite and greenschist facies but locally the Variscan basement and its covers were brought at depths >20 km (Okay *et al.* 2001). The northward vergence of the nappes and the absence of Late Jurassic–Early Cretaceous back-arc magmatism in the area corroborate the idea of a Rhodope–Strandja passive margin involved in the S-dipping subduction of Küre oceanic crust under the Sakarya terrane, followed by continent–continent collision (Figure 5(a,b)).

The non-metamorphic Late Cretaceous volcano-sedimentary cover of the Srednogorie Zone overlies with an angular unconformity the older units all along the northern margin of the Strandja Massif, providing a Cenomanian minimum age limit for the mid-Mesozoic regional metamorphism. This cover is widespread in Bulgaria (Vârşilo, Grudovo, and Mičurin groups) and crops out more sparsely in Turkey (İğneada Group), outside the study area (e.g. Okay *et al.* 2001). The volcano-sedimentary succession sequence as well as all older units are intruded by scattered Late Santonian–Campanian biotite- and hornblende-bearing granodiorite stocks (Dereköy–Demirköy granite).

The Cenozoic sediments of the Thrace Basin lap on the eroded metamorphic basement along the southern limb of the Strandja Massif (Figures 2 and 3). The sequence starts with Upper Eocene basal medium-to-coarse conglomerate and sandstone on the margin of the basin, switching to fine-to-medium sandstone interbedded with shale moving towards the centre, topped by a partly dolomitized reef complex (Less *et al.* 2011). These sediments are overlain by Oligocene marls interbedded with tuff and followed upsection by shale, micritic limestone, and tuff, switching gradually to fine-to-medium sandstone intercalated with shale and

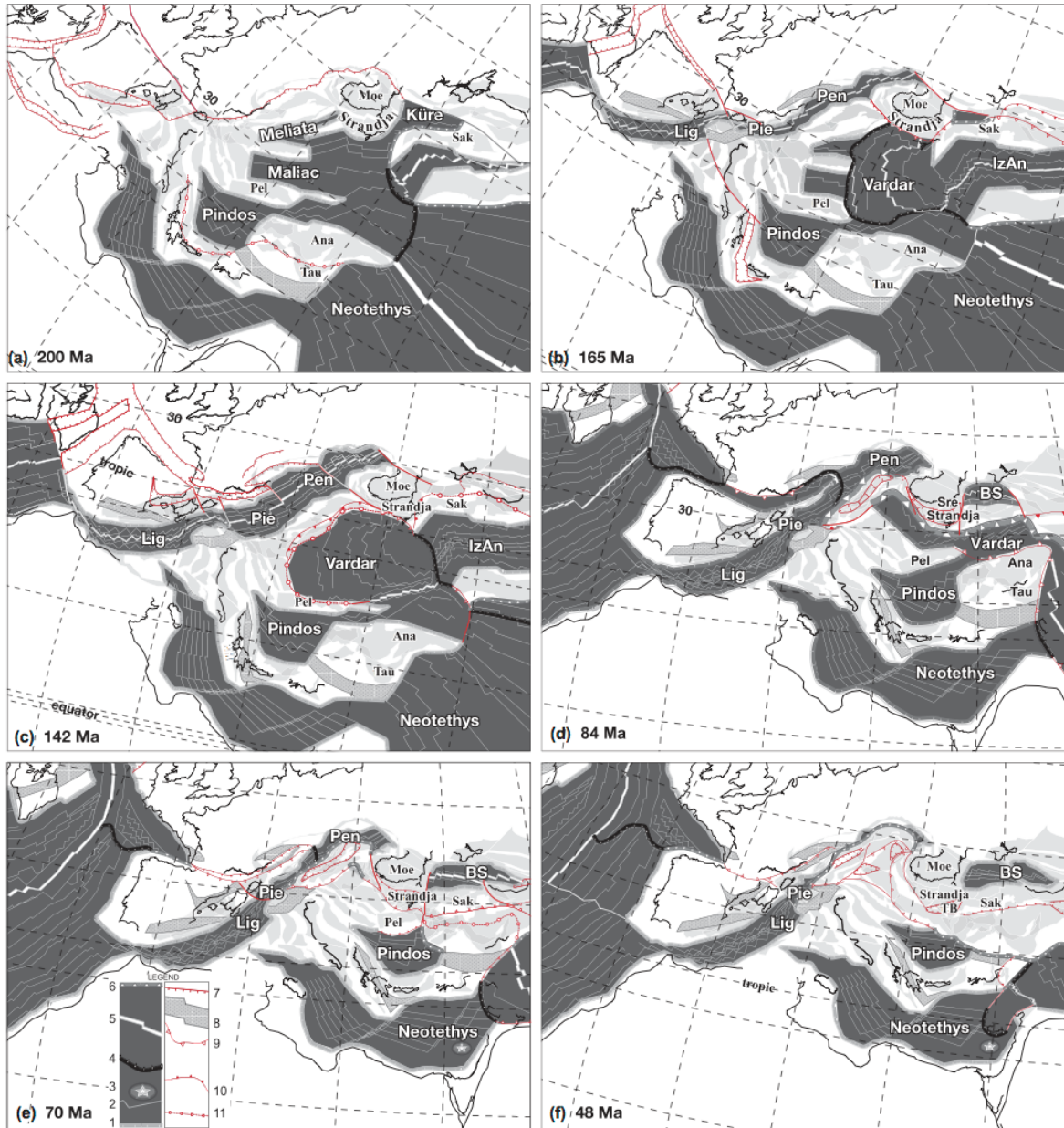


**Figure 5.** Palaeostructural/palaeoenvironmental reconstructions of the western Tethyan region from the earliest Jurassic (200 Ma) to the Early Eocene (48 Ma) (modified after Stampfli and Hochard 2009). Symbols: 1: passive margins; 2: magmatic or synthetic anomaly; 3: seamount; 4: intraoceanic subduction; 5: mid-ocean ridge; 6: active margin; 7: active rift; 8: inactive rift (basin); 9: collision zone; 10: thrust; 11: suture. Ana: Anatolides; BS: Black Sea; IzAn: İzmir–Ankara ocean; Lig: Ligurian ocean; Moe: Moesia; Pel: Pelagonia; Pen: Penninic; Pie: Piedmont; Sak: Sakarya; Sre: Srednogorie; Tau: Taurus; TB: Thrace Basin.

thin lignite layers and lacustrine claystone and siltstone (Çağlayan and Yurtsever 1998).

From a structural viewpoint, the Strandja Massif can be broadly defined as a metamorphosed, north-verging imbricated orogenic belt (Figures 2–4) made of a poly-deformed Variscan basement and its Late Permian-to-

Jurassic cover. The massif was then deeply eroded in Early Cretaceous time and intruded in the Late Cretaceous (Okay *et al.* 2001; Gerdjikov 2005; Elmas *et al.* 2011; Natal'in *et al.* 2012; Şahin *et al.* 2014; Machev *et al.* 2015). Pre-Cretaceous units were metamorphosed into greenschist to low-grade amphibolite

facies during Late Jurassic–Early Cretaceous times (Aydin 1982; Okay *et al.* 2001; Lilov *et al.* 2004; Sunal *et al.* 2011). Peak-metamorphism reached temperatures ranging between ~500°C in the south (Sunal *et al.* 2011) and ~400°C in the north (Lilov *et al.* 2004). The Palaeozoic basement complex as well as the Permo-Jurassic metasedimentary cover display a strong, penetrative SW-dipping foliation reworking all previous structures (Figure 4), in addition to a stretching lineation displaying top-to-north, northwest, or northeast sense of shear (Sunal *et al.* 2006, 2008; Natal'in *et al.* 2012, 2016). This foliation is late Middle Jurassic–Early Cretaceous (Natal'in *et al.* 2012; Sunal *et al.* 2011) and it is consistent with a phase of thick-skinned deformation, nappe imbrication, and metamorphism.

## Methods

### Apatite fission-track analysis and modelling

Fission tracks are radiation damages within the crystal lattice, caused by nuclear fission of radioactive isotope  $^{238}\text{U}$  that can be etched and counted under an optical microscope. Concurrently, neutron irradiation is employed to induce the decay of  $^{235}\text{U}$ , eliciting radiation damages on the surface of an external detector. Grain-by-grain determination of both spontaneous and induced fission-track densities yields a single-grain age representing the cooling of the grain below a closure temperature of ~100°C. Fission-track dating is a useful tool to unravel the cooling histories experienced by rocks in the upper crustal levels and to give a measure of their exhumation (for a review of the method, see Donelick *et al.* 2005). Fission tracks in apatites all have the same initial length of about 16  $\mu\text{m}$  (the specific length depending on composition; e.g. Ketcham *et al.* 1999) but anneal at rates proportional to temperatures, starting from about 60°C. Over geological time periods, partial annealing of fission tracks occurs at temperatures between about 60°C and 125°C (i.e. the partial-annealing zone: PAZ; Gleadow and Fitzgerald 1987). Because tracks shorten in relation to the degree and duration of heating, the measurement of fission track lengths gives information about the thermal evolution in the PAZ temperature range. A quantitative evaluation of the thermal history can be carried out through modelling procedures, which find a range of cooling paths compatible with the AFT data (Ketcham 2005). In this work, inverse modelling of track length data was performed using the HeFTy program (Ehlers *et al.* 2005), which generates the possible  $T-t$  paths by a Monte Carlo algorithm. Predicted AFT data were calculated according to the Ketcham *et al.* (2007) annealing

model for fission tracks revealed by etching.  $D_{\text{par}}$  values (i.e. the etch pit length) were used to define the annealing kinetic parameters of the grains and the original track length.

### Sampling strategy and sample preparation

Twenty-one samples were taken from the metamorphosed late-Variscan intrusives and Triassic sedimentary cover of the massif, and from the Late Cretaceous volcanoclastics and granitoid intrusions (Table 1). The samples were collected along a N–S transect (see Figures 3 and 4 for the exact location) perpendicular to the strike of the main tectonic structures. Apatite grains were concentrated by crushing and sieving, followed by hydrodynamic, magnetic, and heavy-liquid separation. Apatites were embedded in epoxy resin, polished in order to expose the internal surfaces within the grains, and the spontaneous FT were revealed by etching with 5N  $\text{HNO}_3$  at 20°C for 20 s. The mounts were then coupled with a low-uranium fission-track-free muscovite mica sheet (external detector method) and sent for irradiation with thermal neutrons (see Donelick *et al.* 2005, for details) at the Radiation Center of Oregon State University. Nominal fluence of  $9 \times 10^{15} \text{ n cm}^{-2}$  was monitored with a CN5 uranium-doped silicate glass dosimeter. Induced fission tracks were revealed by etching of the mica sheets in 40% HF for 45 min at 20°C. Spontaneous and induced fission tracks were counted under optical microscope at 1250 $\times$  magnification, using an automatic stage (FTStage system) plus a digitizing tablet.

Central ages were calculated with the zeta calibration approach (Hurford and Green 1983), using Durango ( $31.3 \pm 0.3 \text{ Ma}$ ) and Fish Canyon Tuff ( $27.8 \pm 0.2 \text{ Ma}$ ) age standards within grains exposing  $c$ -axis-parallel crystallographic planes. Thirteen samples of the original set yielded suitable apatites. Track-length distributions were calculated by measuring horizontal confined tracks together with the angle between the track and the  $c$ -axis. Confined tracks constitute a small part of the FT population, therefore additional concentrates were mounted, polished, and etched for the analysis. Ultimately, eight samples contained a statistically significant number of confined tracks.

### Geological constraints for thermochronometric modelling

All available geological constraints (intrusion ages, metamorphic events, depositional ages, and stratigraphic relationships) were incorporated into the modelling. The intrusion age of the Kirklareli and Kula

**Table 1.** Apatite fission-track analytical data.

Sample number	Rock type	Age	Coordinates (UTM)	Elevation (m)	Number of grains	Spontaneous			Induced			Dosimeter			Age (Ma) $\pm 1\sigma$	Number of measured tracks	Mean TL ( $\mu\text{m}$ ) $\pm$ standard error	SD	Mean $D_{\text{pair}}$ ( $\mu\text{m}$ )
						$\rho_s$	$N_s$	$\rho_i$	$N_i$	$P(\chi^2)$	$\rho_d$	$N_d$	$P(\chi^2)$						
TU414	Metagranite	Permian	35T 0517238 4625267	160	32	7.36	613	20.05	1670	97.68	9.18	4368	60.7 $\pm$ 5.9	43	11.62 $\pm$ 0.25	1.67	1.91		
TU417	Metasandstone	Early Triassic	35T 0514359 4634886	393	19	3.29	203	8.77	541	99.25	9.9	4712	66.9 $\pm$ 7.9	23	11.74 $\pm$ 0.43	2.1	1.34		
TU419	Metasandstone	Early Triassic	35T 0514268 4640788	439	21	14.96	1325	35.88	3179	99.79	9.86	4689	74.0 $\pm$ 6.7	83	13.81 $\pm$ 0.15	1.42	1.68		
TU420	Metasandstone	Early Triassic	35T 0512791 4644346	497	25	8.23	878	19.58	2090	97.79	9.81	4666	74.2 $\pm$ 6.9	13	13.32 $\pm$ 0.48	1.75	1.54		
TU422	Metagranite	Permian	35T 0510578 4653799	439	28	5.73	617	12.83	1380	99.7	8.95	4262	72.0 $\pm$ 7.0	25	12.23 $\pm$ 0.42	2.13	2.2		
TU423	Metagranite	Permian	35T 0510501 4655777	467	20	17.84	1087	40.87	2491	97.79	8.7	4155	68.4 $\pm$ 6.6	60	12.94 $\pm$ 0.17	1.34	1.82		
TU424	Granitoid	Permian	35T 0514117 4661733	443	26	3.95	281	10.58	752	99.96	9.31	4429	62.7 $\pm$ 6.9	3	13.15 $\pm$ 0.72	1.25	2.49		
TU425	Granitoid	Permian	35T 0514184 4664635	430	27	4.11	220	9.12	488	99.99	8.67	4124	70.4 $\pm$ 8.2	4	12.33 $\pm$ 0.69	1.39	1.97		
TU428	Granitoid	Permian	35T 0515172 4670097	136	9	3.87	118	11.65	355	74.96	9.76	4643	57.2 $\pm$ 8.0	56	13.1 $\pm$ 0.28	2.1	1.49		
TU430	Sandstone	Cenomanian– Turonian	35T 0515221 4673634	187	20	9.25	422	26.52	1210	99.46	8.86	4216	55.7 $\pm$ 5.7	46	13.24 $\pm$ 0.25	1.74	2.64		
TU432	Granitoid	Permian	35T 0509676 4678113	318	13	11.29	705	27.27	1702	89.42	8.8	4185	65.7 $\pm$ 6.2	55	13.76 $\pm$ 0.18	1.38	2.0		
TU433	Sandstone	Turonian– Coniacian	35T 0512480 4682179	274	22	2.79	197	7.08	500	99.92	9.71	4620	68.8 $\pm$ 8.2	44	14.13 $\pm$ 0.23	1.58	2.03		
TU434	Quartz-diorite	Late Cretaceous	35T 0501514 4666354	241	25	5.08	389	10.45	809	99.55	8.6	4094	74.4 $\pm$ 7.8	70	13.92 $\pm$ 0.19	1.66	2.41		

Central ages calculated using dosimeter glass CN5 and  $\zeta\text{-CN5} = 369.01 \pm 3.3$ .  $\rho_s$ : spontaneous track densities ( $\times 10^5 \text{ cm}^{-2}$ ) measured in internal mineral surfaces;  $N_s$ : total number of spontaneous tracks;  $\rho_i$  and  $\rho_d$ : induced and dosimeter track densities ( $\times 10^6 \text{ cm}^{-2}$ ) on external mica detectors ( $g = 0.5$ );  $N_i$  and  $N_d$ : total numbers of tracks;  $P(\chi^2)$ : probability of obtaining  $\chi^2$  value for  $\nu$  degrees of freedom (where  $\nu = \text{number of crystals} - 1$ ); a probability  $>5\%$  is indicative of a homogeneous population.

metagranites (samples TU414, TU423, TU428, TU432) is ~271 Ma (Okay *et al.* 2001), while their temperature of emplacement was between 750°C and 850°C (Miller *et al.* 2003). Triassic metasandstones (e.g. sample TU419) are Olenekian-Induan in age (Evciler Formation in Bedi *et al.* 2013). By extension, we assumed widespread Early Triassic subaerial/shallow-marine sedimentation above the Permian granitoids, implying that in Olenekian-Induan times samples TU414, TU423, TU428, TU432 were also near the surface (~20°C). Sunal *et al.* (2011) constrained the peak of Late Jurassic–Early Cretaceous regional metamorphism in the Turkish part of the Strandja Massif between  $162.3 \pm 1.6$  and  $157.7 \pm 1.5$  Ma with progressively younger cooling ages from south to north. Estimated temperature conditions reached 485–530°C in the south and 450–500°C in the northern part (within epidote-amphibolite facies conditions). As to the Bulgarian part, Lilov *et al.* (2004) proposed a peak of regional greenschist-facies metamorphism at 160–170 Ma, with temperatures ranging between 350°C and 450°C.

Depositional ages of Late Cretaceous sedimentary rocks, namely the Vârșilo (TU430) and Grudovo groups (TU433) are reckoned as Cenomanian–Turonian and Turonian–Coniacian, respectively (Chatalov *et al.* 1995). We considered that those samples were in subaerial conditions (~20°C) alongside sample TU432 from the underlying Permian bedrock being eroded. Finally, the Permian metagranite cropping out along the margin of the Thrace Basin is non-conformably overlain by Late Bartonian to Oligocene basal conglomerate, sandstone, and limestone (Less *et al.* 2011), thus implying that sample TU414 was near the surface (~20°C) during that time.

### Analytical results

Table 1 and Figure 6 provide a summary of the AFT data. Central ages range from  $74.4 \pm 7.8$  to  $55.7 \pm 5.7$  Ma (Late Campanian–Early Ypresian), without any particular geographic trend or age-elevation correlation. All the samples passed the  $\chi^2$  test indicating a single population of grains. Such central ages could be mistaken as evidence of an Alpine phase of cooling/exhumation, but the results of thermochronometric modelling based on statistical analysis of fission-track length distributions indicate slow cooling throughout the Late Cretaceous and the Palaeocene for most samples (Figure 7). In such a case, central ages are not significant and only the statistical modelling of fission-track length distributions can constrain the  $T-t$  paths, as discussed below.

The southernmost sample TU414 is a late Palaeozoic metagranite from the Kirklareli pluton (Figures 3 and 4, Table 1). Its bimodal track-length distribution indicates that sample TU414 underwent a complex thermal history. Inverse modelling best-fit path shows rapid cooling through the PAZ between 145 and 138 Ma (earliest Cretaceous; Figure 7), followed by a long period at near-surface conditions. In the Late Oligocene, a new episode of moderate heating brought the sample back in the PAZ, followed by Neogene cooling.

Moving northward, sample TU417 (Early Triassic metasandstone) also yielded an earliest Cretaceous central age, similar to sample TU414. This sample did not contain enough confined FT for inverse modelling. Sample TU419 (Early Triassic metasandstone) yielded a tight cluster of single-grain ages (80–70 Ma), a central age of  $74.0 \pm 6.7$  Ma, and a leptokurtic track-length distribution with a single peak and relatively long mean track length of  $13.81 \pm 0.15$   $\mu\text{m}$ . The best-fit  $t-T$  path shows slow cooling through the PAZ between ca. 105 and 65 Ma (Figure 7). Both samples TU420 (Triassic metasandstone) and TU422 (metagranite) did not contain enough confined tracks for inverse modelling.

Sample TU423 (metagranite; Kula pluton) yielded relatively broad single-grain age and track-length distributions. The modelling indicates extremely slow cooling through the PAZ from ca. 110 to 30 Ma (Figure 7). Samples TU424 and TU425 are also from the Kula pluton and are both characterized by the virtual absence of confined tracks, hindering inverse modelling. Sample TU434 was taken from a Santonian granitic intrusion (Aydin 1982) ~10 km west of the transect line. It yielded the oldest AFT central age of the set ( $74.4 \pm 7.8$  Ma) and displayed relatively long confined tracks (mean track length =  $13.92 \pm 0.19$   $\mu\text{m}$ ). In accordance with the overall trend, slow cooling within the PAZ occurred between 95 and 50 Ma, with an acceleration in the cooling rate at ~50 Ma (Figure 7).

Sample TU428 (Permian metagranite in the northern part of the Kula pluton) is characterized by a platykurtic (and bimodal) track-length frequency distribution (Figure 6). Inverse modelling of this sample describes a very slow cooling and a long residence time within the PAZ (Figure 7), with an acceleration in the cooling rate since the mid-Eocene (from ~40 Ma). Sample TU430 was collected from a mélange derived from tectonic disruption of Cenomanian sandstone in the footwall of a major north-verging nappe (Figures 3 and 4). This sample yielded a broad track-length distribution with two scarcely distinguishable peaks. Inverse modelling indicates slow heating from surficial conditions at about 95 Ma (depositional age), entering the 60°C isotherm at 70 Ma, maximum heating (~110°C) at

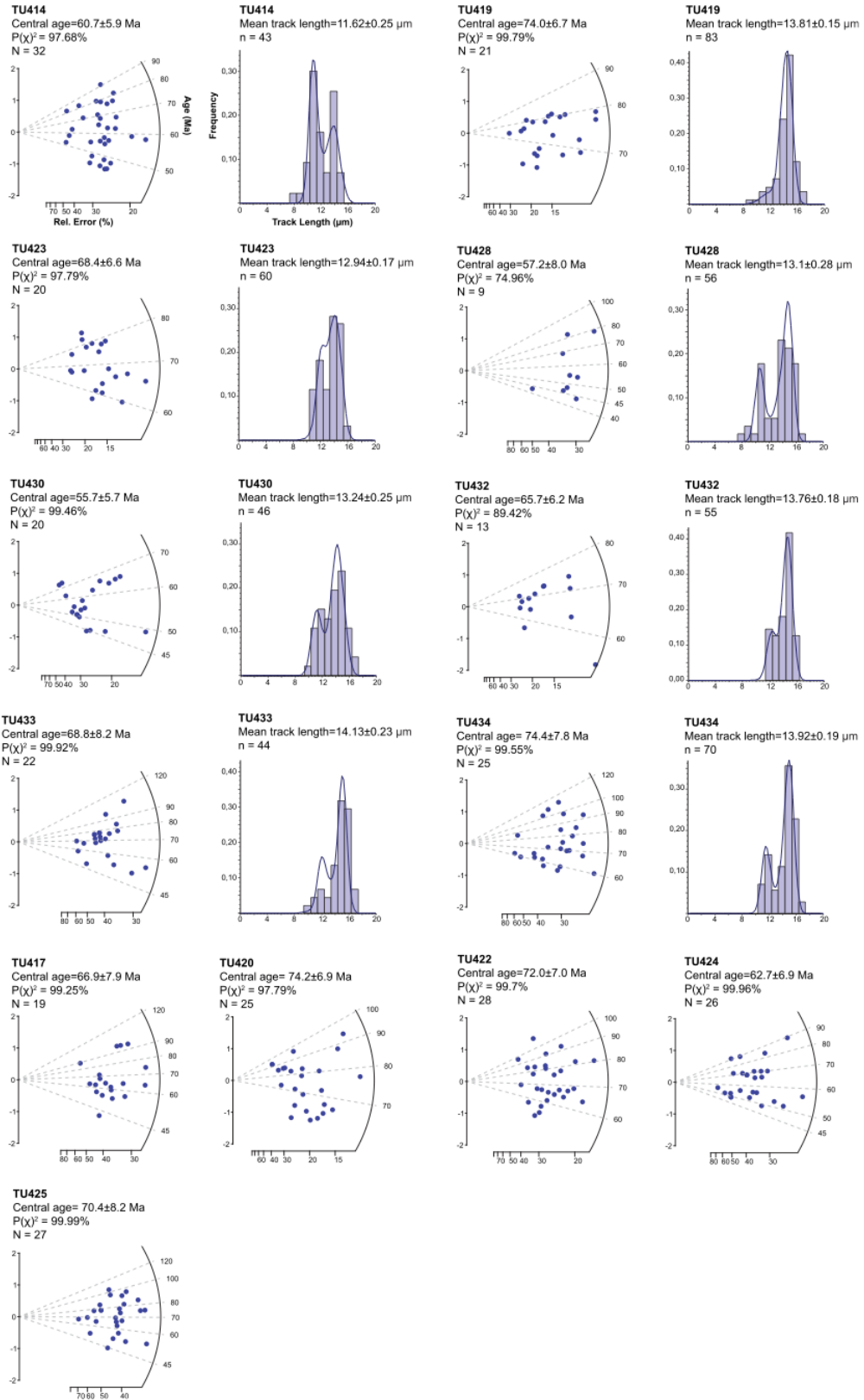


**Figure 6.** Radial plots of single-grain apatite fission-track ages. Histograms show the confined-track length distributions of the eight samples whose time–temperature paths are shown in Figure 7.



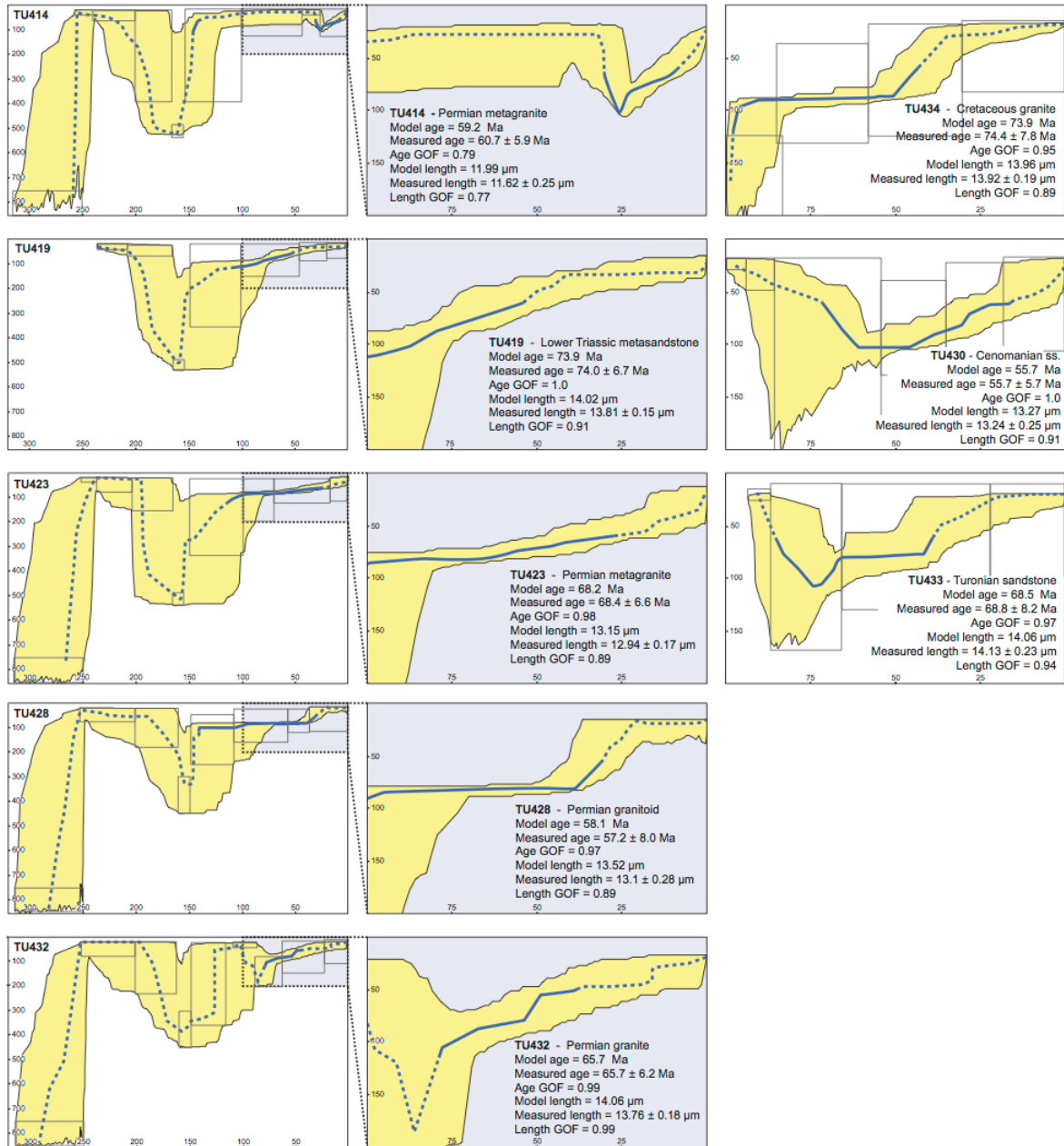


**Figure 7.** Time–temperature paths obtained from inverse modelling of apatite fission-track data. Graphs in the central column are enlargements of portions of those to the left. X-axes and Y-axes of all diagrams refer to age (Ma) and temperature (°C), respectively. Yellow areas mark envelopes of statistically acceptable fit, and the thicker lines correspond to the most probable thermal histories (best-fit curves). Boxes represent *T–t* domains constrained by available data (radiometric ages, stratigraphic relationships, AFT analyses). Parameters related to inverse modelling are reported: *n*, number of measured track lengths; GOF, goodness-of-fit gives an indication about the fit between observed and predicted data (values closer to 1 are best).

60–45 Ma, followed by progressive cooling (Figure 7). Sample TU430 never suffered temperatures higher than 120°C (i.e. the base of the partial annealing zone), nonetheless no single grain-ages older than 75 Ma were

determined from this detrital sample, possibly the result of the long residence time within the PAZ and the maximum temperature very close to the 120°C isotherm. Alternatively, considering the envelopes of

statistically acceptable fit in Figure 6, one might conclude that total annealing might have occurred below the bottom of the PAZ.

The two northernmost samples display a fairly similar thermochronometric evolution. Sample TU432 was taken from the northern rim of the Kula pluton, separated from the main body by a thrust fault (Figures 3 and 4), and yielded a unimodal track-length distribution (Figure 6). The thermochronometric modelling constrains two discrete phases of cooling, in the Campanian and in the Middle–Late Eocene (Figure 7). The northernmost sample (TU433) was taken from the Turonian sandstones at the base of the Yambol–Burgas basin fill (Figure 3). The sample yielded a range of single-grain ages, from 110 to 45 Ma. Again, two discrete phases of cooling occurred: in the Late Cretaceous and in the Late Eocene (Figure 7). The slight difference in the reconstructed thermochronometric evolution of the two samples may result from their relative position within the north-verging Strandja orogenic wedge, with somewhat higher temperatures and earlier deformation to the south.

## Discussion

The extent of the late stage of the Cimmerian orogenic cycle in the Rhodopes and the Strandja Massif has been a matter of much debate, to the point of being underestimated or ignored altogether in several palaeostructural/palaeoenvironmental reconstructions (e.g. Dercourt *et al.* 1985, 1993, 2000; Barrier and Vrielynck 2008). In the Strandja massif, geochronological evidences and field observations (Tchoumatchenco *et al.* 1989; Okay *et al.* 2001; Lilov *et al.* 2004; Sunal *et al.* 2011; Natal'in *et al.* 2012) contrast with these reconstructions and entail the occurrence of significant shortening – plausibly the result of collision – at the Jurassic–Cretaceous boundary. Such shortening induced thick-skinned thrust imbrication and metamorphism in the area. Peak metamorphic temperatures, amount of deformation, and kinematic indicators indicate northward propagation of the orogeny (Okay *et al.* 2001; Lilov *et al.* 2004; Sunal *et al.* 2011). As for the tectonic setting in that period, the Strandja massif underwent an initial condition of passive continental margin along the Eurasian plate, followed by collision with the northwestern end of the Sakarya continental element (Figure 5(b, c)). This event determined the main internal structure of the massif and of the western Pontides as well.

Many uncertainties persist on the geological evolution of the Strandja Massif and its palaeogeographic position through time as the area was affected by multiple deformations during the Variscan, Cimmerian,

and Alpine orogenic cycles (Okay *et al.* 2001; Stampfli *et al.* 2001; Stampfli and Borel 2002; Stampfli and Kozur 2006; Sunal *et al.* 2008; Von Raumer and Stampfli 2008; Stampfli and Hochard 2009; Natal'in *et al.* 2012). Despite the complexities introduced by single geological structures, broad-scale low-temperature thermochronometric patterns provide first-order information on the tectonic processes that cause rock cooling. The AFT analyses presented in this paper place a number of compelling constraints which needs to be integrated in any reconstruction of the tectonic evolution of the Strandja Massif.

In our study area, the integration of available Neocimmerian peak-metamorphic ages/temperatures with our AFT-derived thermochronologic modelling points to a rapid Late Jurassic heating followed by similarly rapid cooling (Figure 7). Integrated thermochronometric modelling shows a slightly diachronous inception of Neocimmerian peak metamorphism from south to north. Following Neocimmerian metamorphism, cooling of the southernmost sample (TU414; Late Permian metagranite from the Kirklareli pluton) across the PAZ is well constrained in the Berriasian. Conversely, samples TU419 and TU423 from the central portion of the massif both entered the PAZ later in the Early Cretaceous. Despite coming from different structural positions (Figures 3 and 4), these two samples display a very similar subsequent thermochronometric evolution, characterized by a long residence time within the PAZ (>55 Ma) during the Late Cretaceous and most of the Palaeogene. Sample TU428 in the Bulgarian portion of the massif resembles TU414, with lower temperature of metamorphism (Lilov *et al.* 2004), drastic cooling in Berriasian as well, but never exiting the PAZ.

During the Aptian–Albian rifting began in the western Black Sea back-arc (Zonenshein and Le Pichon 1986; Nikishin *et al.* 2015) due to progressive southward slab roll-back within the context of continued northward subduction of the Vardar–İzmir–Ankara oceanic domain underneath the southern Eurasian continental margin. Black Sea extensional tectonics extended westward into the Srednogorie zone of central Bulgaria (Figure 5(d)) (Georgiev *et al.* 2001), where rift-related Cenomanian–Turonian conglomerate and sandstone overlie non-conformably the basement complex (Figures 3 and 4) and grade upsection into the thick volcano-sedimentary succession of the Yambol–Burgas basin. Continued extension led to the intrusion of a number of shallow latest Cretaceous stocks piercing both the basement complex and its Cretaceous sedimentary cover (Georgiev *et al.* 2012). This thermal event is registered in the northernmost portion of the study area where samples TU432 (Permian granite) and TU433

(Turonian sandstone) both show a discrete episode of heating in the Campanian, in agreement with available U-Pb zircon ages from plutonic rocks of the same region clustering at ~80 Ma (Georgiev *et al.* 2012). Sample TU434 – taken from a Late Cretaceous shallow intrusion (Figure 3) – resided within the apatite PAZ (~60–120°C) from the latest Cretaceous until the late Early Eocene when it started to undergo rapid cooling/exhumation (Figure 7).

North of Golyamo Bukovo in Bulgaria (Figure 3) the basal Cenomanian–Turonian sedimentary rocks suffered intense deformation along a prominent brittle shear zone trending west-east and dipping to the SSW at an angle of about 45°, to become a tectonic mélange. Sample TU430 was taken from the mélange: it shows (i) progressive burial-driven heating during the Late Cretaceous, followed by (ii) permanence at the base of the PAZ in the Palaeocene–Early Eocene, and (iii) progressive cooling/exhumation since the Middle Eocene (Figure 7). From a broader perspective, all samples from the northern part of the study area underwent cooling starting from the late Early–Middle Eocene. This matches an important phase of thrusting in the development of the East Balkan thrust belt (Banks 1997; Sinclair *et al.* 1997; Stewart *et al.* 2011). Considering the pervasive Late Jurassic–Early Cretaceous structural fabric of the Strandja Massif, the Golyamo Bukovo and the other major N-verging overthrusts of the northern massif likely have an older Neocimmerian thermal signature which was overprinted and erased by younger deformation.

Immediately south of the study area lies the Thrace Basin, a large Middle Eocene to Quaternary sedimentary basin. Basin-floor geometry features a number of structural highs and deep depocenters; as a consequence the sedimentary fill – reaching a maximum thickness of 9000 m – is characterized by abrupt lateral variations in thickness and facies types (Turgut and Eseller 2000; Siyako and Huvaz 2007; d'Atri *et al.* 2012; Cavazza *et al.* 2013). Limited deep borehole information as well as geophysical data indicate that the floor of the Thrace Basin is made of basement rocks similar to those of the Strandja and Rhodope massifs, which raises the question of the true areal extent of the Cimmerian orogenic wedge to the south. (The same consideration applies for its northern termination, concealed by the volcano-sedimentary succession of the Yambol–Burgas basin of the Srednogorie zone.)

The geodynamic setting and structural evolution of the Thrace Basin is far from being understood. Following Görür and Okay (1996), it was long interpreted as a forearc basin which developed in a context of northward subduction. This interpretation was

challenged by more recent data emphasizing the lack of both a coeval magmatic arc and a subduction complex associated with the basin (d'Atri *et al.* 2012; Cavazza *et al.* 2013). All these elements – along with the correspondence between subsidence pulses in the basin and lithospheric stretching in the metamorphic core complexes of southern Bulgaria and the northern Aegean region – indicate instead that the Thrace Basin was likely the result of post-orogenic collapse after the continental collision related to the closure of the Vardar–İzmir–Ankara ocean in the latest Cretaceous (Figure 5(e)). The role of the structural inversion of preexisting Cimmerian structures in the development of the basin should also be considered.

Our thermochronometric transect across the Strandja Massif spans the transition between a region of Eocene compression (i.e. the eastern Balkans) to the north and a region of marked Eocene subsidence (the Thrace Basin) to the south (Figure 2). The AFT dataset presented in this paper records such transition. Late Early–Middle Eocene contraction was thermochronologically recorded only in the northern part of the Strandja Massif. As discussed above, all northern samples show a phase of contractional cooling/exhumation during the Eocene. Conversely, irrespective of their lithologic nature, the samples from the central and southern portions of the massif underwent slow erosional cooling throughout the Cenozoic (Figure 7). The southernmost sample (TU414; Figure 3), a Palaeozoic metagranite along the northern margin of the Thrace Basin, is the only sample in the entire dataset showing a phase of heating in the Oligocene (Figure 7), the result of regional basinal subsidence and progressive sediment burial. This sample was then exhumed during the Neogene, possibly due to the activity of a complex array of blind strike-slip faults forming the main present-day boundary between the outcropping portion of the Strandja Massif and the Thrace Basin (Perinçek 1991; Turgut *et al.* 1991).

Alpine-age orogenic events in the Balkan peninsula are related to the successive closures of the Vardar (latest Cretaceous) and Pindos (Middle–Late Eocene) oceans and the associated accretion of the Pelagonian and Greater Apulia continental blocks along the southern Eurasian margin (Stampfli and Hochard 2009) (Figure 5). The Cimmerian orogenic wedge of the Strandja Massif has not registered these events in terms of low-temperature thermochronology as our AFT analyses and modelling from the main body of the massif do not show any significant thermal event coeval with these collisional orogenies. Most Alpine-age deformation focused instead to the north, with the development of the thin-skinned thrust belt of the

Eastern Balkans and coeval widespread syntectonic deposition within a foreland basin (e.g. Nachev 1981; Doglioni *et al.* 1996; Bergerat *et al.* 2010; Stewart *et al.* 2011). Alpine-age deformation focused in the Srednogie region because it had been rheologically weakened by Late Cretaceous back-arc extension. Other studies described Late Eocene–Miocene inversion structures in various locations along the western Black Sea margin (Doglioni *et al.* 1996; Stovba *et al.* 2009). Munteanu *et al.* (2011) identified a coherent thick-skinned thrust system with northward vergence in the Romanian offshore. In this region, thrusting inverted a number of Cretaceous grabens; shortening started during the Late Eocene and affected all areas of the Western Black Sea Basin during Oligocene and Miocene times, gradually migrating northward.

It cannot be excluded that the basement floor of the Thrace Basin was deformed following the closure of the Vardar–İzmir–Ankara oceanic domain before experiencing subsidence from the Middle Eocene due to orogenic collapse induced by slab rollback. In particular, the role of the blind Terzili strike-slip fault system for the geodynamics of the whole southern Balkan region might have been greatly underestimated as such system might represent a long-lived major tectonic contact repeatedly reactivated with different kinematics. Further thermochronological and structural works in the region are needed to clarify these issues.

## Conclusions

This work presents the first low-temperature thermochronology results for the Strandja Massif, based on AFT analysis of Permian, Triassic, and Cretaceous rock samples. Thermal evolution was investigated along a transect extending from the Cenozoic sediments of the Thrace Basin in the south to the Late Cretaceous volcanics/volcaniclastics of the Srednogie zone in the north. The integration of our new thermochronometric data with radiometric, structural, and stratigraphic data from the literature provides cogent constraints on the geological evolution of the Strandja Massif and the palaeogeographic/palaeotectonic reconstructions of the entire Balkan region.

Following Late Jurassic crustal shortening and regional metamorphism, the central part of the Strandja Massif underwent a Kimmeridgian–Berriasian phase of relatively rapid cooling/exhumation. Conversely, the overall thermal evolution in the massif during the Late Cretaceous is one of slow erosional cooling – possibly driven by erosion – with the exception of its northernmost part which was involved in Srednogie back-arc rifting. In this region, the intrusion of small plutons at

shallow crustal levels (cooling ages of ca. 80 Ma; Campanian) reset locally the AFT system, as shown by our thermochronologic modelling. If the local thermal effects of such plutonism are filtered from the models, the entire post-Cimmerian thermochronometric evolution of the Strandja Massif indicates tectonic quiescence from the Late Cretaceous to the Early Eocene. Such tectonic inactivity continued in the central portion of the Strandja Massif, whereas its northern portion and the southern Srednogie back-arc basin underwent rapid contractional exhumation starting between 50 and 40 Ma (Middle Eocene). Alpine-age stresses related to the closure of the northern branch of Neotethys and the ensuing development of the Vardar–İzmir–Ankara suture zone were transmitted over a long distance through the Strandja Cimmerian orogenic wedge and focused preferentially to the north, in the area previously weakened by Srednogie extensional tectonics.

## Acknowledgements

We thank two anonymous reviewers for their comments which improved the clarity of the manuscript. Thanks to Irene Albino for technical help in the first stages of this research.

## Disclosure statement

No potential conflict of interest was reported by the authors.

## Funding

Funding for this research was provided by the University of Bologna RFO funds.

## ORCID

William Cavazza  <http://orcid.org/0000-0002-6030-9689>

## References

- Aydin, Y., 1974, Etude pétrographique et géochimique de la partie centrale du Massif d'Istanbul (Turquie). PhD dissertation, University of Nancy, 131 pp. [in French].
- Aydin, Y., 1982, Geology of the Yildiz Mountains (Istanbul) massif. Istanbul Technical University Engineering and Architecture Faculty, Associate Professor Thesis [in Turkish].
- Banks, C.J., 1997, Basins and thrust belts of the Balkan coast and the Black Sea, in Robinson, A.G., Ed., Regional and petroleum geology of the Black Sea and surrounding region: AAPG Memoir 68: p. 115–128.
- Barrier, E., Vrielynck, B., Bergerat, F., Brunet, M.F., Mosar, J., Poisson, A., and Sosson, M., 2008, Palaeotectonic maps of the Middle East: Tectono-sedimentary-palinspastic maps from Late Norian to Pliocene. MEBE Project.

- Bedi, Y., Vasilev, E., Dabovski, C., Ergen, A., Okuyucu, C., Doğan, A., Tekin, U., Ivanova, D., Boncheva, I., Lakova, I., Sachanski, V., Kuşcu, I., Tuncay, E., Demiray, G., Soycan, H., and Göncüoğlu, M.C., 2013, New age data from the tectonostratigraphic units of the Istranca "Massif" in NW Turkey: A correlation with SE Bulgaria: *Geologica Carpathica*, v. 64, p. 255–277. [10.2478/geoca-2013-0019](https://doi.org/10.2478/geoca-2013-0019)
- Bergerat, F., Vangelov, D., and Dimov, D., 2010, Brittle deformation, paleostress field reconstruction and tectonic evolution of the Eastern Balkanides (Bulgaria) during Mesozoic and Cenozoic times: *Geological Society London Special Publication*, v. 340, p. 77–111. [10.1144/SP340.6](https://doi.org/10.1144/SP340.6)
- Burchfiel, B.C., and Nakov, R., 2015, The multiply deformed foreland fold-thrust belt of the Balkan orogen, northern Bulgaria: *Geosphere*, v. 11(2), p. 463–490. [10.1130/GES01020.1](https://doi.org/10.1130/GES01020.1)
- Çağlayan, M.A., 1996, Evolution of Strandja Massif in Mesozoic-Lower Tertiary and its role in the evolution of Thrace Basin: *Bulletin Turkish Association Petrol Geological*, v. 81, p. 82–93.
- Çağlayan, M.A., and Yurtsever, A., 1998, Geological Map of Turkey 1:100,000 scale, no. 20, 21, 22, 23, Burgaz-A3, Edirne-B2 and B3, Burgaz-A4 and Kırklareli-B4; Kırklareli-B5 and B6; Kırklareli-C6 Sheets: Ankara, Mineral Research and Exploration Institute (MTA) of Turkey.
- Cavazza, W., Caracciolo, L., Critelli, S., d'Atri, A., and Zuffa, G.G., 2013, Petrostratigraphic evolution of the Thrace Basin (Bulgaria, Greece, Turkey) within the context of Eocene-Oligocene post-collisional evolution of the Vardar-Izmir-Ankara suture zone: *Geodinamica Acta*, v. 26(1–2), p. 12–26. [10.1080/09853111.2013.858943](https://doi.org/10.1080/09853111.2013.858943)
- Cavazza, W., Roure, F., and Ziegler, P.A., 2004, The Mediterranean area and the surrounding regions: Active processes, remnants of former Tethyan oceans and related thrustbelts, in Cavazza, W., Roure, F., Spakman, W., Stampfli, G.M., and Ziegler, P.A., eds., *The TRANSMED Atlas: The Mediterranean Region from Crust to Mantle*: Heidelberg, Springer-Verlag, p. 1–29.
- Chatalov, G., 1990, Geology of the Strandja zone in Bulgaria: Sofia Publishing House Bulgarian Academy of Sciences, p. 1–263.
- Chatalov, G., Dabovski, C., Savov, S., Filipov, L., Nikolov, G., and Aneva, T., 1995, Zeljazkovo sheet, 1:100,000 scale Geological Map of Bulgaria: Sofia, Committee of Geology and Mineral Resources.
- Chatalov, G.A., 1980, Two facies type of Triassic in Strandza mountain, SE Bulgaria: *Rivista Italiana Paleontologia*, v. 85, p. 1029–1046.
- Chatalov, G.A., 1988, Recent developments in geology of the Strandzha zone in Bulgaria: *Bulletin Technical University Istanbul*, v. 41, p. 433–465. [in Turkish].
- d'Atri, A., Zuffa, G.G., Cavazza, W., Okay, A.I., and Di Vincenzo, G., 2012, Detrital supply from subduction/accretion complexes to the Eocene-Oligocene post-collisional southern Thrace Basin (NW Turkey and NE Greece): *Sedimentary Geology*, v. 243–244, p. 117–129. [10.1016/j.sedgeo.2011.10.008](https://doi.org/10.1016/j.sedgeo.2011.10.008)
- Dabovski, C., Boyanov, I., Zagorchev, I., Nikolov, T., Sapunov, I., Khrishev, K., and Yanev, Y., 2002, Structure and Alpine evolution of Bulgaria: *Geologica Balcanica*, v. 32(2/4), p. 9–16.
- Dabovski, C., and Savov, S.S., 1988, Structural studies in the nappes of Southeast Strandza: *Geologica Balcanica*, v. 18, p. 19–36.
- Dercourt, J., Gaetani, M., Vrielynck, B., Barrier, E., Biju-Duval, B., Brunet, M.F., Cadet, J.P., Crasquin, S., and Sandulescu, M., 2000, *Atlas Peri-Tethys Palaeogeographical Maps*: Paris, Commission de la Carte Géologique du Monde.
- Dercourt, J., Ricou, L.E., and Vrielynck, B., 1993, *Atlas Tethys palaeoenvironmental maps*: Paris, Gauthier-Villars.
- Dercourt, J., Zonenshain, L.P., Ricou, L.E., Kazmin, V.G., Le Pichon, X., Knipper, A.L., Grandjacquet, C., Sborshchikov, I. M., Boulin, J., Sorokhtin, O., Geysant, J., Lepvrier, C., Biju-Duval, B., Sibuet, J.-C., Savostin, L.A., Westphal, M., and Lauer, J.-P., 1985, Presentation de 9 cartes paleogeographiques au 1/2,000,000 s' etendant de l'Atlantique au Pamir pour la periode du Lias a l'Actuel: *Bulletin De La Société Géologique De France*, v. 1(5), p. 637–652.
- Dogliani, C., Busatta, C., Bolis, G., Mariannini, L., and Zanella, M., 1996, Structural evolution of the Eastern Balkans (Bulgaria): *Marine and Petroleum Geology*, v. 13(2), p. 225–251. [10.1016/0264-8172\(95\)00045-3](https://doi.org/10.1016/0264-8172(95)00045-3)
- Donelick, R.A., O'Sullivan, P.B., and Ketcham, R.A., 2005, Apatite fission-track analysis: Reviews in Mineralogy and Geochemistry, v. 58(1), p. 49–94. [10.2138/rmg.2005.58.3](https://doi.org/10.2138/rmg.2005.58.3)
- Ehlers, T.A., Chaudhri, T., Kumar, S., Fuller, C.W., Willett, S.D., Ketcham, R.A., Brandon, M.T., Belton, D.X., Kohn, B.P., Gleadow, A.J., and Dunai, T.J., 2005, Computational tools for low-temperature thermochronometer interpretation: Reviews in Mineralogy and Geochemistry, v. 58(1), p. 589–622. [10.2138/rmg.2005.58.22](https://doi.org/10.2138/rmg.2005.58.22)
- Elmas, A., Yılmaz, İ., Yiğitbaşı, E., and Ullrich, T., 2011, A Late Jurassic–Early Cretaceous metamorphic core complex, Strandja Massif, NW Turkey: *International Journal of Earth Sciences*, v. 100(6), p. 1251–1263. [10.1007/s00531-010-0540-3](https://doi.org/10.1007/s00531-010-0540-3)
- Georgiev, G., Dabovski, C., and Stanisheva-Vassileva, G., 2001, East Srednogie-Balkan Rift Zone, in Ziegler, P.A., Cavazza, W., Robertson, A.H.F., and Crasquin-Soleau, S., eds., *Peritethyan Rift/Wrench Basins and Passive Margins*: Paris, Mémoires du Muséum National d'Histoire Naturelle, v. 186, p. 259–293.
- Georgiev, S., Von Quadt, A., Heinrich, C.A., Peytcheva, I., and Marchev, P., 2012, Time evolution of a rifted continental arc: Integrated ID-TIMS and LA-ICPMS study of magmatic zircons from the Eastern Srednogie, Bulgaria: *Lithos*, v. 154, p. 53–67. [10.1016/j.lithos.2012.06.020](https://doi.org/10.1016/j.lithos.2012.06.020)
- Gerdjikov, I., 2005, Alpine metamorphism and granitoid magmatism in the Strandja zone: New data from the Sakar unit, SE Bulgaria: *Turkish Journal of Earth Sciences*, v. 14(2), p. 167–183.
- Gleadow, A.J.W., and Fitzgerald, P.G., 1987, Uplift history and structure of the Transantarctic Mountains: New evidence from fission track dating of basement apatites in the Dry Valleys area, southern Victoria Land: *Earth and Planetary Science Letters*, v. 82, p. 1–14. [10.1016/0012-821X\(87\)90102-6](https://doi.org/10.1016/0012-821X(87)90102-6)
- Gocev, P.M., 1985, Strandzides: Geotectonics, Tectonophysics and Geodynamics, v. 18, p. 28–54.
- Görür, N., and Okay, A.I., 1996, A fore-arc origin for the Thrace Basin, NW Turkey: *Geologische Rundschau*, v. 85, p. 662–668. [10.1007/BF02440103](https://doi.org/10.1007/BF02440103)

- Hurford, A.J., and Green, P.F., 1983, The zeta age calibration of fission-track dating: *Chemical Geology*, v. 41, p. 285–317. [10.1016/S0009-2541\(83\)80026-6](https://doi.org/10.1016/S0009-2541(83)80026-6)
- Ketcham, R.A., 2005, Forward and inverse modeling of low-temperature thermochronometry data: *Reviews in Mineralogy and Geochemistry*, v. 58(1), p. 275–314. [10.2138/rmg.2005.58.11](https://doi.org/10.2138/rmg.2005.58.11)
- Ketcham, R.A., Carter, A., Donelick, R.A., Barbarand, J., and Hurford, A.J., 2007, Improved modeling of fission-track annealing in apatite: *American Mineralogist*, v. 92(5–6), p. 799–810. [10.2138/am.2007.2281](https://doi.org/10.2138/am.2007.2281)
- Ketcham, R.A., Donelick, R.A., and Carlson, W.D., 1999, Variability of apatite fission-track annealing kinetics: III. Extrapolation to geological time scales: *American Mineralogist*, v. 84(9), p. 1235–1255. [10.2138/am-1999-0903](https://doi.org/10.2138/am-1999-0903)
- Khain, V.E., 1994, *Geology of Northern Eurasia (Ex-USSR). Second Part: Phanerozoic fold belts and young platforms*: Berlin, Gebrüder Borntraeger, 404p.
- Less, G., Özcan, E., and Okay, A.I., 2011, Stratigraphy and larger foraminifera of the Middle Eocene to Lower Oligocene shallow-marine units in the northern and eastern parts of the Thrace Basin, NW Turkey: *Turkish Journal of Earth Sciences*, v. 20(6), p. 793–845.
- Lilov, P., Maliakov, Y., and Balogh, K., 2004, K-Ar dating of metamorphic rocks from Strandja massif, SE Bulgaria: *Bulgarian Academy of Sciences, Geochemistry, Mineralogy and Petrology*, v. 41, p. 107–120.
- Machev, P., Ganev, V., and Klain, L., 2015, New LA-ICP-MS U-Pb zircon dating for Strandja granitoids (SE Bulgaria): Evidence for two-stage late Variscan magmatism in the internal Balkanides: *Turkish Journal of Earth Sciences*, v. 24(3), p. 230–248. [10.3906/yer-1407-21](https://doi.org/10.3906/yer-1407-21)
- Miller, C.F., McDowell, S.M., and Mapes, R.W., 2003, Hot and cold granites? Implications of zircon saturation temperatures and preservation of inheritance: *Geology*, v. 31(6), p. 529–532. [10.1130/0091-7613\(2003\)031<0529:HACGIO>2.0.CO;2](https://doi.org/10.1130/0091-7613(2003)031<0529:HACGIO>2.0.CO;2)
- Munteanu, I., Matenco, L., Dinu, C., and Cloetingh, S., 2011, Kinematics of back-arc inversion of the Western Black Sea Basin: *Tectonics*, v. 30, p. TC5004. [10.1029/2011TC002865](https://doi.org/10.1029/2011TC002865)
- Nachev, I.K., 1981, On the origin of Flysch in Bulgaria: *Review of the Bulgarian Geological Society*, v. 42(2), p. 143–152.
- Natal'in, B.A., Sunal, G., Gün, E., Wang, B., and Zhiqing, Y., 2016, Precambrian to Early Cretaceous rocks of the Strandja Massif (northwestern Turkey): Evolution of a long lasting magmatic arc: *Canadian Journal of Earth Sciences*, v. 53(11), p. 1312–1335. [10.1139/cjes-2016-0026](https://doi.org/10.1139/cjes-2016-0026)
- Natal'in, B.A., Sunal, G., Satir, M., and Toraman, E., 2012, Tectonics of the Strandja Massif, NW Turkey: History of a long-lived arc at the northern margin of Palaeo-Tethys: *Turkish Journal of Earth Sciences*, v. 21(5), p. 755–798.
- Nikishin, A.M., Okay, A., Tüysüz, O., Demirer, A., Wannier, M., Amelin, N., and Petrov, E., 2015, The Black Sea Basins structure and history: New model based on new deep penetration regional seismic data. Part 2: Tectonic history and paleogeography: *Marine and Petroleum Geology*, v. 59, p. 656–670. [10.1016/j.marpetgeo.2014.08.018](https://doi.org/10.1016/j.marpetgeo.2014.08.018)
- Okay, A.I., Altiner, D., and Kiliç, A.M., 2015, Triassic limestone, turbidites and serpentinite – the Cimmeride orogeny in the Central Pontides: *Geological Magazine*, v. 152, p. 460–479. [10.1017/S0016756814000429](https://doi.org/10.1017/S0016756814000429)
- Okay, A.I., Satir, M., Tüysüz, O., Akyüz, S., and Chen, F., 2001, The tectonics of the Strandja Massif: Late-Variscan and mid-Mesozoic deformation and metamorphism in the northern Aegean: *International Journal of Earth Sciences*, v. 90(2), p. 217–233. [10.1007/s005310000104](https://doi.org/10.1007/s005310000104)
- Okay, A.I., Şengör, A.C., and Görür, N., 1994, Kinematic history of the opening of the Black Sea and its effect on the surrounding regions: *Geology*, v. 22(3), p. 267–270. [10.1130/0091-7613\(1994\)022<0267:KHOTOO>2.3.CO;2](https://doi.org/10.1130/0091-7613(1994)022<0267:KHOTOO>2.3.CO;2)
- Okay, A.I., Sunal, G., Sherlock, S., Altiner, D., Tüysüz, O., Kylander-Clark, A.R.C., and Aygül, M., 2013, Early Cretaceous sedimentation and orogeny on the southern active margin of Eurasia: Central Pontides, Turkey: *Tectonics*, v. 32, p. 1247–1271. [10.1002/tect.20077](https://doi.org/10.1002/tect.20077)
- Okay, A.I., and Tüysüz, O., 1999, Tethyan sutures of the northern Turkey, in Durand, B., Jolivet, L., Horvát, F., and Sérrane, M., eds, *The Mediterranean Basins: Tertiary Extension within the Alpine Orogen*: London, Geological Society of London Special Publication no. 156, p. 475–515.
- Okay, A.I., Zattin, M., and Cavazza, W., 2010, Apatite fission-track data for the Miocene Arabia-Eurasia collision: *Geology*, v. 38, p. 35–38.
- Papanikolaou, D., Barghathi, H., Dabovski, C., Dimitriu, R., El-Hawat, A., Ioane, D., Kranis, H., Obeidi, A., Oaie, C., Seghedi, A., and Zagorchev, I., 2004, TRANSMED Transect VII: East European Craton - Scythian Platform - Dobrogea - Balkanides - Rhodope Massif - Hellenides - East Mediterranean - Cyrenaica, in Cavazza, W., Roure, F., Spakman, W., Stampfli, G.M., and Ziegler, P.A., eds., *The TRANSMED Atlas: The Mediterranean Region from Crust to Mantle*: Heidelberg, Springer-Verlag.
- Perinçek, D., 1991, Possible strand of the North Anatolian fault in the Thrace Basin, Turkey - An interpretation: *American Association of Petroleum Geologists Bulletin*, v. 75, p. 241–257.
- Ricou, L.E., 1995, The plate tectonic history of the past Tethys Ocean, in Nairn, A.E.M., Ricou, L.E., Vrielynck, B., and Dercourt, J., eds., *The Tethys Ocean*: New York, Plenum Press.
- Şahin, S.Y., Aysal, N., Güngör, Y., Peytcheva, I., and Neubauer, F., 2014, Geochemistry and U–Pb zircon geochronology of metagranites in Istraanca (Strandja) Zone, NW Pontides, Turkey: Implications for the geodynamic evolution of Cadomian orogeny: *Gondwana Research*, v. 26(2), p. 755–771. [10.1016/j.gr.2013.07.011](https://doi.org/10.1016/j.gr.2013.07.011)
- Şengör, A.M.C., 1979, Mid-Mesozoic closure of Permo-Triassic Tethys and its implications: *Nature*, v. 279, p. 590–593. [10.1038/279590a0](https://doi.org/10.1038/279590a0)
- Şengör, A.M.C., 1984, The Cimmeride orogenic system and the tectonics of Eurasia: Boulder, CO, Geological Society of America Special Paper 195, 82 p.
- Sinclair, H.D., Juranov, S.G., Georgiev, G., Byrne, P., and Mountney, N.P., 1997, The Balkan thrust wedge and foreland basin of eastern Bulgaria: Structural and stratigraphic development, in Robinson, A.G., ed., *Regional and petroleum geology of the Black Sea and surrounding region*: Tulsa OK, American Association of Petroleum Geologists Memoir: v. 68, p. 91–114.
- Siyako, M., and Huvaz, O., 2007, Eocene stratigraphic evolution of the Thrace Basin, Turkey: *Sedimentary Geology*, v. 198, p. 75–91. [10.1016/j.sedgeo.2006.11.008](https://doi.org/10.1016/j.sedgeo.2006.11.008)
- Stampfli, G., Borel, G., Cavazza, W., Mosar, J., and Ziegler, P.A., Eds., 2001, *The Paleotectonic Atlas of the Peri-Tethyan*

- Domain: CD-ROM: Kathlenburg-Lindau, European Geophysical Society.
- Stampfli, G.M., and Borel, G.D., 2002, A plate tectonic model for the Paleozoic and Mesozoic constrained by dynamic plate boundaries and restored synthetic oceanic isochrons: *Earth and Planetary Science Letters*, v. 196(1), p. 17–33. [10.1016/S0012-821X\(01\)00588-X](https://doi.org/10.1016/S0012-821X(01)00588-X)
- Stampfli, G.M., and Borel, G.D., 2004, The TRANSMED transects in space and time: Constraints on the Paleotectonic evolution of the Mediterranean domain, *in* Cavazza, W., Roure, F., Spakman, W., Stampfli, G.M., and Ziegler, P., eds., *The TRANSMED Atlas: The Mediterranean Region from Crust to Mantle*: Berlin, Springer Verlag, p. 53–80.
- Stampfli, G.M., and Hochard, C., 2009, Plate tectonics of the Alpine realm: London, Geological Society, Special Publication 327, p. 89–111.
- Stampfli, G.M., and Kozur, H., 2006, Europe from the Variscan to the Alpine cycles: *Geological Society of London Memoir*, v. 32, p. 57–82. [10.1144/GSL.MEM.2006.032.01.04](https://doi.org/10.1144/GSL.MEM.2006.032.01.04)
- Stewart, C., Nemčok, M., Vangelov, D., Higgins, E., Welker, C., and Meaux, D., 2011, Structural and depositional evolution of the East Balkan thrust belt, Bulgaria: *AAPG Bulletin*, v. 95(4), p. 649–673. [10.1306/08181008061](https://doi.org/10.1306/08181008061)
- Stovba, S., Khriachtchevskaia, O., and Popadyuk, I., 2009, Hydrocarbon-bearing areas in the eastern part of the Ukrainian Black Sea: *Leading Edge*, v. 28(9), p. 1042–1045. [10.1190/1.3236373](https://doi.org/10.1190/1.3236373)
- Sunal, G., Natal'in, B.A., Satir, M., and Toraman, E., 2006, Paleozoic magmatic events in the Strandja Massif, NW Turkey: *Geodinamica Acta*, v. 19(5), p. 283–300. [10.3166/ga.19.283-300](https://doi.org/10.3166/ga.19.283-300)
- Sunal, G., Satir, M., Natal'in, B.A., Topuz, G., and Vonderschmidt, O., 2011, Metamorphism and diachronous cooling in a contractional orogen: The Strandja Massif, NW Turkey: *Geological Magazine*, v. 148, p. 580–596. [10.1017/S0016756810001020](https://doi.org/10.1017/S0016756810001020)
- Sunal, G., Satir, M., Natal'in, B.A., and Toraman, E., 2008, Paleotectonic position of the Strandja Massif and surrounding continental blocks based on zircon Pb-Pb age studies: *International Geology Review*, v. 50(6), p. 519–545. [10.2747/0020-6814.50.6.519](https://doi.org/10.2747/0020-6814.50.6.519)
- Tchoumatchenco, P., Nikolov, T., and Sapunov, I., 1989, Outline of the Jurassic and Early Cretaceous tectonic evolution in Bulgaria: *CR Bulgarian Academy Sciences*, v. 42, p. 99–102.
- Tchoumatchenco, P., and Tronkov, D., 2010, Lithostratigraphic units of Tethyan Type of East Stara Planina Mts and Strandzha Mt. (Veleka Unit), south-east Bulgaria. Correlation essay: *CR Academic Bulg Sciences*, v. 63, p. 285–294.
- Topuz, G., Göçmengil, G., Rolland, Y., Çelik, Ö.F., Zack, T., and Schmitt, A.K., 2013, Jurassic accretionary complex and ophiolite from northeast Turkey: No evidence for the Cimmerian continental ribbon: *Geology*, v. 41, p. 255–258. [10.1130/G33577.1](https://doi.org/10.1130/G33577.1)
- Turgut, S., and Eseller, G., 2000, Sequence stratigraphy, tectonics and depositional history in eastern Thrace Basin, NW Turkey: *Marine and Petroleum Geology*, v. 17(1), p. 61–100. [10.1016/S0264-8172\(99\)00015-X](https://doi.org/10.1016/S0264-8172(99)00015-X)
- Turgut, S., Türkaslan, M., and Perinçek, D., 1991, Evolution of the Thrace sedimentary basin and its hydrocarbon prospectivity, *in* Spencer, A.M., Ed., *Generation, Accumulation, and Production of Europe's Hydrocarbons: Special Publication of European Association of Petroleum Geoscientists 1*, p. 415–437.
- Vasilev, E., and Dabovski, C., 2010, Tectonostratigraphy of Strandzha Massif: Correlations across the Turkish-Bulgarian Border: *Sofia, BAS Guide Book*, p. 1–58.
- Von Raumer, J.F., and Stampfli, G.M., 2008, The birth of the Rhenic Ocean-Early Palaeozoic subsidence patterns and subsequent tectonic plate scenarios: *Tectonophysics*, 461(1), p. 9–20. [10.1016/j.tecto.2008.04.012](https://doi.org/10.1016/j.tecto.2008.04.012)
- Yanev, S., Göncüoğlu, M.C., Gedik, I., Lakova, I., Boncheva, I., Sachanski, V., Okuyucu, C., Özgül, N., Timur, E., Maliakov, Y., and Saydam, G., 2006, Stratigraphy, correlations and palaeogeography of Paleozoic terranes of Bulgaria and NW Turkey: A review of recent data, *in* Robertson, A.H.F., and Mountrakis, D., Eds., *Tectonic development of the Eastern Mediterranean Region*: London, Geol. Soc. London, Spec. Publ. 260, p. 51–67.
- Zagorchev, I., and Budurov, K., 1997, Outline of the Triassic palaeogeography of Bulgaria: *Albertiana*, 19, p. 12–24.
- Zonenshain, L.R., and LePichon, X., 1986, Deep basins of the Black sea and Caspian Sea as remnants of Mesozoic back-arc basins: *Tectonophysics*, v. 123, p. 181–212. [10.1016/0040-1951\(86\)90197-6](https://doi.org/10.1016/0040-1951(86)90197-6)





Chapter Six  
**CONCLUSIONS**

Mechanical coupling of a collisional front and its forelands can induce far-field tectonic stresses and significant compressional structures at distances of over 1,700 km from a collision front [e.g. Ziegler et al., 1998, 2002]. Localization of compressional deformations far from the collision zone is mainly controlled by spatial and temporal strength variations of the lithosphere and their orientation within the compressional stress field evidence [e.g. Zoback, 1992; Ziegler et al., 1995, 1998, 2002; Cloetingh et al., 2005]. Decoupling between plates is important in determining the evolution of lithospheric structures, localizing the strain, controlling the dominant deformation mechanism and as a result determining the locus of uplift and subsidence [Sokoutis and Willingshofer, 2011]. In particular, Sokoutis and Willingshofer [2011] point out that deformation by thrusting along the decoupled boundary, often associated with underthrusting and subduction of the incoming plate is a typical rheological indicator for decoupling between a weak zone and its foreland plate. The weakness at plate interfaces arguably plays a major role for horizontal decoupling, as the strain is usually accommodated along weak plate contacts, such as subduction channels and weak intraplate faults (see Willingshofer & Sokoutis [2009] for a review). The models presented in Willingshofer & Sokoutis [2009] indicate that strong mechanical coupling between plates and orogenic wedges leads to deformation of the lithosphere by folding of the strong indenter, the foreland plate(s) and the weak orogenic wedge as well. In contrast, strong decoupling between the orogenic wedge and the foreland induces crustal- and lithospheric-scale thrusting, and most of the shortening is taken up by shear along the decoupled boundary.

In this regard, thermochronometric techniques are exceptional tools for better understanding the stress partitioning within the (supposedly) unaffected foreland/hinterland. Although it is indisputable that cooling may result from many processes, in collisional orogens it widely derives from shortening-driven erosion and exhumation. Cooling ages can thus be considered representative of collision-related deformation. However, a complication to this approach is that cooling ages are not always indicative of a distinct, temporarily well-constrained event, but may derive from either (i) more slow-paced processes, e.g. a moderately slow exhumation [Reiners and Brandon, 2006] or (ii) superposed and incremental deformation. In this regard, integration with other data (i.e. stratigraphic and structural

observations in the field, confined-tracks annealing models, pre-existing radiometric age determinations) is crucial. The reconstruction of thermal histories can be used to pinpoint and estimate in a (semi)quantitative way the spatial and temporal distribution of stress-related deformations, thus pointing out the geodynamic processes affecting the structure and the development of a collisional setting. Under these assumptions, three collisional orogens (the Bitlis-Pütürge Massif, the Lesser Caucasus and the Strandja Massif) were chosen for thermochronological study. The first two areas have been involved and directly affected by the Arabia-Eurasia continental collision. The Arabia-Eurasia collision zone is part of the larger Alpine-Himalaya orogenic belt and accommodates the northward motion of the Arabian plate with respect to Eurasia. This geodynamic setting is regarded as one of the best examples of ongoing continental collision in the world [e.g. Reilinger et al., 2006; Jackson et al., 1997; Allen et al., 2004; Okay et al., 2010], thus providing an excellent place to study far-field stress transmission and partitioning.

The Bitlis-Pütürge metamorphic complex, i.e. the area of maximum indentation along the collision zone, displays a composite thermal evolution reflecting the complex nature of the eastern Mediterranean region, characterized by the presence of multiple terrane accreted against the plate margins and then pinched and squeezed in between the two colliding plates and the several oceanic domains in the middle [Okay, 2008; Okay et al., 2010]. The dataset indicates widespread latest Cretaceous metamorphism of a passive margin related to extensive southward obduction of ophiolites from the northern Izmir-Ankara-Erzincan suture onto the northern continental margin of the Anatolide-Tauride block. The massif was then rapidly exhumed during the Paleocene, spent most of the Eocene and the whole Oligocene in a state of tectonic quiescence and was rapidly exhumed and significantly deformed during the Middle Miocene. In spite of the complexity of the thermal histories, the Miocene exhumation event is extremely coherent and well recognizable in all the samples. This thermochronometric evidence is further corroborated by field stratigraphic and structural relationships.

In the Lesser Caucasus along the Sevan-Akera suture zone, i.e. the most striking structural element of the area, marking the boundary between the Gondwana-type and Laurasia-type terranes, an analogous clustering of ages can be observed, with Late

Cretaceous ages arguably related to oceanic lithosphere obduction and coherent Miocene ages coeval with the collision taking place to the south. The coexistence of coherent but somehow more scattered Late Cretaceous to Early - Middle Eocene ages with extremely coherent Miocene ages constitutes a *leitmotiv* for all the Anatolide-Tauride block [Albino et al., 2014; Cavazza et al., 2015]. Notably, the Miocene ages are found in close proximity of major structures (i.e. segments of the Izmir-Ankara-Erzincan-Sevan-Akera suture zone) whereas Late Cretaceous to Early - Middle Eocene ages are sparsely present both within the foreland and along the structures. This strongly suggests mechanical coupling between the orogenic wedge and Eurasian foreland north of the Bitlis-Pütürge suture zone during the Miocene, with efficient stress transmission northward over large distances [Ziegler et al., 1998, 2002; Cloetingh et al., 2005]. The stress focused preferentially at rheological discontinuities located as far as the Lesser Caucasus and the Eastern Pontides, and even then, only where the structures were conveniently oriented within the stress field. Since the late Middle Miocene, a new tectonic regime is active as the Arabian Plate and the Eurasian Plate decoupled. Nowadays, the westward translation of Anatolia is accommodating most of the Arabia-Eurasia convergence for the western part of the collision zone, efficiently decoupling the foreland from the orogenic wedge and precluding efficient northward stress transfer. The extrusion of Anatolia is made possible by the enucleation of the dextral North Anatolian (NAF) and sinistral East Anatolian (EAF) fault systems and actually facilitated by the extensive forces driven by the slab roll-back in the Aegean Sea. In the eastern part of the collision zone convergence is accommodated mainly via shortening along the Zagros, the Alborz, the Kura fold-and-thrust belt and the Apsheron Sill, and via transpression along the Main Recent Fault [e.g., Axen et al., 2001; Allen et al., 2002; Guest et al., 2006; Forte et al., 2013]. In the central part the collision stress is accommodated by a complex and widespread network of strike-slip faults in the East Anatolian Plateau and Lesser Caucasus and by wholesome uplift of the Plateau.

In the Strandja Massif the situation is rather different. The Cimmerian Strandja metamorphic massif, standing along the southern margin of Laurasia, is characterized by a complex thermal history, having been affected by the Variscan, Cimmerian and Alpine orogenies. However, the mechanical behaviour of this orogen in response to collision-related

stress was remarkably diverse in respect to the other two. The massif underwent an episode of Late Jurassic heating consistent with a Neocimmerian (palaeo-Alpine) phase of northverging thrust imbrication and regional metamorphism, then the central part of the massif was affected by latest Jurassic - earliest Cretaceous relatively rapid cooling. In Cretaceous-to-Early Eocene times the massif cooled very slowly and was (thermally) almost completely unaffected by Alpine-age deformations that dominated adjacent areas (e.g. the Rhodope Massif), in spite of the intrinsic rheological weakness of the massif (poly-deformed, pervasively faulted, lithologically dishomogeneous) and the relatively proximity to the collision front. Evidence of Alpine-age deformation is recorded only in the northern sector of the Strandja massif, where both basement and sedimentary rocks underwent cooling/exhumation associated with an important phase of shortening of the East Balkan fold-and-thrust belt starting in the Middle–Late Eocene.

The burial/exhumation histories inferred for the Bitlis and Strandja orogens show two very different mechanisms of collisional stress transmission. In the Bitlis orogen the stress focused both on the orogenic prism and on the foreland, where it reactivated conveniently oriented older structures. Conversely, in the Strandja orogen the stress mostly bypassed the orogenic prism and focused on the Srednogorie rift basin to the north, rheologically weakened by previous Late Cretaceous back-arc extension. We argue that the overstretched crust of that rift basin offered far less resistance to the stress than the thick-skinned, basement nappe stack of the Strandja Massif.



## REFERENCES – PART TWO

- Albino, I., Cavazza, W., Zattin, M., Okay, A. I., Adamia, S., & Sadradze, N. (2014). Far-field tectonic effects of the Arabia–Eurasia collision and the inception of the North Anatolian Fault system. *Geological Magazine*, 151(2), 372-379.
- Allen, M. B., Jones, S., Ismail-Zadeh, A., Simmons, M., & Anderson, L. (2002). Onset of subduction as the cause of rapid Pliocene-Quaternary subsidence in the South Caspian basin. *Geology*, 30(9), 775-778.
- Allen, M., Jackson, J., & Walker, R. (2004). Late Cenozoic reorganization of the Arabia-Eurasia collision and the comparison of short-term and long-term deformation rates. *Tectonics*, 23(2).
- Axen, G. J., Lam, P. S., Grove, M., Stockli, D. F., & Hassanzadeh, J. (2001). Exhumation of the west-central Alborz Mountains, Iran, Caspian subsidence, and collision-related tectonics. *Geology*, 29(6), 559-562.
- Cavazza, W., Albino, I., Zattin, M., Galoyan, G., Imamverdiyev, N., & Melkonyan, R. (2015). Thermochronometric evidence for Miocene tectonic reactivation of the Sevan–Akera suture zone (Lesser Caucasus): a far-field tectonic effect of the Arabia–Eurasia collision?. *Geological Society, London, Special Publications*, 428(1), 187-198.
- Forte, A. M., Cowgill, E., Murtuzayev, I., Kangarli, T., & Stoica, M. (2013). Structural geometries and magnitude of shortening in the eastern Kura fold-thrust belt, Azerbaijan: Implications for the development of the Greater Caucasus Mountains. *Tectonics*, 32(3), 688-717.
- Jackson, J. A., Ambraseys, N. N., Giardini, D., & Balassanian, S. (1997). Convergence between Eurasia and Arabia in eastern Turkey and the Caucasus. In *Historical and Prehistorical Earthquakes in the Caucasus* (Vol. 28, pp. 79-90). Kluwer.
- Okay, A. I. (2008). Geology of Turkey: a synopsis. *Anschnitt*, 21, 19-42
- Okay, A. I., Zattin, M., & Cavazza, W. (2010). Apatite fission-track data for the Miocene Arabia-Eurasia collision. *Geology*, 38(1), 35-38.
- Reillinger, R. E., McClusky, S. C., Souter, B. J., Hamburger, M. W., Prilepin, M. T., Mishin, A., ... & Balassanian, S. (1997). Preliminary estimates of plate convergence in the Caucasus collision zone from global positioning system measurements. *Geophysical Research Letters*, 24(14), 1815-1818.
- Reiners, P. W., & Brandon, M. T. (2006). Using thermochronology to understand orogenic erosion. *Annual Reviews of Earth and Planetary Sciences*, 34, 419-466.
- Sokoutis, D., & Willingshofer, E. (2011). Decoupling during continental collision and intra-plate deformation. *Earth and Planetary Science Letters*, 305(3-4), 435-444.

- Willingshofer, E., & Sokoutis, D. (2009). Decoupling along plate boundaries: Key variable controlling the mode of deformation and the geometry of collisional mountain belts. *Geology*, 37(1), 39-42.
- Ziegler, P. A., Cloetingh, S., & van Wees, J. D. (1995). Dynamics of intra-plate compressional deformation: the Alpine foreland and other examples. *Tectonophysics*, 252(1), 7-59.
- Ziegler, P. A., Van Wees, J. D., & Cloetingh, S. (1998). Mechanical controls on collision-related compressional intraplate deformation. *Tectonophysics*, 300(1), 103-129.
- Ziegler, P. A., Bertotti, G., & Cloetingh, S. A. P. L. (2002). Dynamic processes controlling foreland development – the role of mechanical (de) coupling of orogenic wedges and forelands. *Stephan Mueller Special Publication Series*, 1, 17-56.
- Zoback, M. L. (1992). First-and second-order patterns of stress in the lithosphere: The World Stress Map Project. *Journal of Geophysical Research: Solid Earth*, 97(B8), 11703-11728.



APPENDIX A

**THERMOCHRONOLOGICAL EVOLUTION OF NORTHWESTERN IRAN**

As illustrated in previous chapters, the thermochronologic evolution of three different collisional orogens located within the Western Tethyan domain has been studied in order to understand the dynamics of stress partitioning and transmission and, from a more general viewpoint, to clarify the tectonic evolution of the northern foreland of the Arabia-Eurasia collision. To the same end, another area was investigated during this PhD project. This region constitutes the northern deformed foreland of the Zagros fold-and-thrust belt, NW Iran (Urumieh Lake region). The study area extends over a wide region ( $\sim 1,200 \text{ km}^2$ ) in close proximity to the locus of maximum indentation between the Arabian and Eurasian plates (Figure A.1). We produced a compilation of all the thermochronological data available [fission-track analysis on apatite and zircons, (U-Th)/He analysis on apatite and zircons] for a huge area comprising a wide sector of the Middle East, then we proceeded selecting the sampling sites for maximum covering of uninvestigated areas. Forty samples were collected from a vast array of rock types, twenty-five of them yielded suitable grains for the AFT analysis constituting the first available thermochronological dataset for the region (sample locations are reported in Figure A.2). AFT central ages range between  $55.8 \pm 9.1 \text{ Ma}$  and  $14.6 \pm 1.3 \text{ Ma}$  (Ypresian-Langhian), ultimately clustering in two groups. The older group displays Priabonian to Chattian AFT ages and arguably represents the time of first collision between the two plates. The younger group shows Early-Middle Miocene AFT ages and represents a phase of fast cooling and increased exhumation also observable within the Turkish part of the foreland, namely in the easternmost Pontides [Albino et al., 2014] and in adequately oriented segments of the Sevan-Akera suture zone (Lesser Caucasus of Armenia and Azerbaijan) [Cavazza et al., 2015]. Coeval exhumation along the the Bitlis suture [Okay et al., 2010] suggests far-field stress transmission from the collision zone across its foreland.

Radial plots showing single-grain age distributions are shown in Figures 3 to 10. Twelve T-t paths have been achieved for the whole area, significantly implementing the knowledge of the thermal evolution of the region (Figure A.5 to A.10). Generally speaking, these preliminary results seem to corroborate the hypothesis of mechanical coupling, efficient stress transmission and reactivation of pre-existing weakened structures, but the modalities and the geological causes leading to these events are still to be discussed.

## FIGURE CAPTIONS

Figure A.1 Overall tectonic sketch map of the Middle East. The box indicates the area shown in Fig.2.

Figure A.2 Geological sketch map of the study area. Apatite fission-track sample locations are shown (for analytical details and exact sample locations, see Table 1).

Figure A.3 Radial plots of single-grain apatite fission-track ages. For analytical details on AFT ages reported in the figure, see Table 1.

Figure A.4 Radial plots of single-grain apatite fission-track ages. For analytical details on AFT ages reported in the figure, see Table 1.

Figure A.5 to A.10 Summary of analytical results, Time-temperature paths obtained from inverse modeling of apatite fission-track data; green areas mark envelopes of statistically acceptable fit, and the thicker lines correspond to the most probable thermal histories: red line is the mean of all statistically acceptable paths; blue line is the best-fit T-t path. Parameters related to inverse modeling are reported: GOF, goodness-of-fit gives an indication about the fit between observed and predicted data (values closer to 1 are best). Histogram showing the confined-track length distributions of apatite grains.

Table A.1

Sample number	Rock type	Age	Coordinates (UTM)	Elevation (m)	No. of grains	Spontaneous		Induced		$P(\chi^2)$	Dosimeter		Age (Ma) $\pm 1\sigma$	No. of measured tracks	Mean TL ( $\mu\text{m}$ ) $\pm$ standard error	SD	Mean Dpar ( $\mu\text{m}$ )
						$\rho_s$	$N_s$	$\beta$	$N_i$		$\rho_d$	$N_d$					
TU435	Granite	Oligocene	38N 663717 418489	1780	16	1.04	71	10.54	725	97.27	10.38	4933	18.4 $\pm$ 2.8	8	14.16 $\pm$ 0.4	1.13	2.09
TU436	Granite	Oligocene	38N 676714 4171658	1777	30	1.24	299	15.52	3723	99.97	10.29	4890	14.9 $\pm$ 1.5	41	14.07 $\pm$ 0.28	1.78	1.98
TU437	Granite porphyroid	Oligocene	38N 719497 4151961	1336	22	0.75	127	4.93	826	97.98	10.19	4843	28.4 $\pm$ 3.6	9	13.18 $\pm$ 0.69	2.07	2.59
TU438	Granodiorite	Late Paleogene	39N 245055 4117232	1730	23	2.52	361	16.35	2338	93.51	10.10	4800	28.2 $\pm$ 2.0	53	15 $\pm$ 0.13	0.98	2.53
TU439	Sandstone	Permian	38N 595416 4152624	1536	16	1.85	95	9.35	479	83.54	10.01	4757	35.8 $\pm$ 5.0	3	-	-	1.84
TU441	Sandstone	Cretaceous	38N 587478 4150364	1394	21	1.56	83	4.35	231	74.71	9.92	4714	64.2 $\pm$ 9.8	4	-	-	2.51
TU443	Granitoid	Middle Triassic	38N 553296 4247005	1699	20	2.71	316	18.42	2144	95.68	9.82	4667	21.1 $\pm$ 2.7	16	12.08 $\pm$ 0.29	1.14	1.79
TU444	Alkali syenite	Oligocene	38N 689662 4267298	1634	20	2.48	361	29.45	4275	87.15	9.72	4624	14.9 $\pm$ 1.5	51	13.26 $\pm$ 0.17	1.21	2.5
TU445	Monzonite	Oligocene	38N 690855 4279125	1690	22	1.16	193	8.53	1420	99.49	9.64	4581	23.7 $\pm$ 2.7	51	13.2 $\pm$ 0.14	0.97	2.58
TU446	Syenite	Oligocene	38N 678809 4298311	1261	22	0.79	133	5.44	907	99.99	9.55	4539	25.3 $\pm$ 3.2	6	-	-	2.26
TU447	Syenite	Oligocene	38N 678475 4298973	1262	17	1.15	93	7.97	645	99.97	9.45	4491	24.1 $\pm$ 3.4	14	13.13 $\pm$ 0.21	0.78	2.1
TU448	Monzonite	Oligocene	38N 703611 4268421	1070	23	1.46	271	15.37	2843	97.35	9.36	4448	16.3 $\pm$ 1.7	54	13.4 $\pm$ 0.09	0.66	2.21
TU449	Granite	Post-Early Eocene	39N 296631 4060052	2005	20	1.65	189	9.64	1100	97.33	9.27	4406	29.0 $\pm$ 3.3	56	13.06 $\pm$ 0.15	1.13	2.38
TU450	Granite	Post-Early Eocene	39N 309924 4074255	1700	21	2.02	314	11.48	1783	99.61	9.18	4363	29.2 $\pm$ 3.0	52	12.88 $\pm$ 0.15	1.08	1.9
TU452	Paragneiss	Precambrian	38N 730022 4067308	2092	21	0.94	168	5.81	1030	99.70	9.08	4315	26.8 $\pm$ 3.2	1	-	-	2.21
TU453	Granite	Precambrian	38N 734820 4064468	2165	21	0.73	93	7.28	922	100.00	8.99	4272	16.4 $\pm$ 2.3	1	-	-	2.00
TU454	Granite	Precambrian	38N 664029 4041202	2214	20	3.98	540	18.96	2569	99.90	8.90	4230	33.8 $\pm$ 3.3	52	12.82 $\pm$ 0.12	0.89	2.61
TU455	Granite	Cretaceous	38N 650819 4045875	1532	20	1.69	255	9.29	1395	99.97	8.80	4182	29.1 $\pm$ 3.1	54	13.39 $\pm$ 0.20	1.46	2.06
TU456	Diorite	Tertiary	38N 622455 4083863	1532	20	1.63	174	7.77	826	99.96	8.71	4139	33.1 $\pm$ 3.9	48	13.43 $\pm$ 0.12	0.81	4.02
TU457	Granite	Post-Cretaceous	38N 532825 4069236	1729	22	1.55	106	10.96	760	99.12	8.57	4073	22.0 $\pm$ 2.9	1	-	-	1.86
TU458	Granite	Post-Cretaceous	38N 525461 4086064	1459	20	2.06	281	13.05	1775	99.88	8.43	4006	24.1 $\pm$ 2.6	46	12.9 $\pm$ 0.13	0.9	2.72
TU462	Gneiss	Precambrian	38N 470289 4182720	1695	20	3.78	195	37.1	1911	99.92	8.34	3964	15.4 $\pm$ 1.7	54	12.07 $\pm$ 0.26	1.9	1.86
TU471	Monzo-syenite	Late Eocene	38N 601766 4299693	561	20	1.15	101	4.63	406	99.80	8.16	3878	36.6 $\pm$ 5.1	1	-	-	2.57
TU473	Sandstone	Eocene	38N 565361 4297158	1287	18	2.09	166	9.17	727	4.73	8.06	3830	34.3 $\pm$ 4.9	1	-	-	3.14
TU474	Sandstone	Eocene	38N 573683 4272088	1781	20	1.33	198	8.02	1195	2.08	7.97	3788	25.2 $\pm$ 3.3	11	-	-	3.74

Central ages calculated using dosimeter glass CN5 and  $\zeta$  CN5 = 369.01  $\pm$  3.3.  $\rho_s$ , spontaneous track densities ( $\times 10^4$  cm $^{-2}$ ) measured in internal mineral surfaces;  $N_s$ , total number of spontaneous tracks;  $\rho$  and  $\rho_i$ , induced and dosimeter track densities ( $\times 10^6$  cm $^{-2}$ ) on external mica detectors (g = 0.5);  $N_i$  and  $N_d$ , total numbers of tracks;  $P(\chi^2)$ , probability of obtaining  $\chi^2$  value for  $\nu$  degrees of freedom (where  $\nu$  = number of crystals - 1); a probability >5% is indicative of a homogeneous population.

Figure A.1

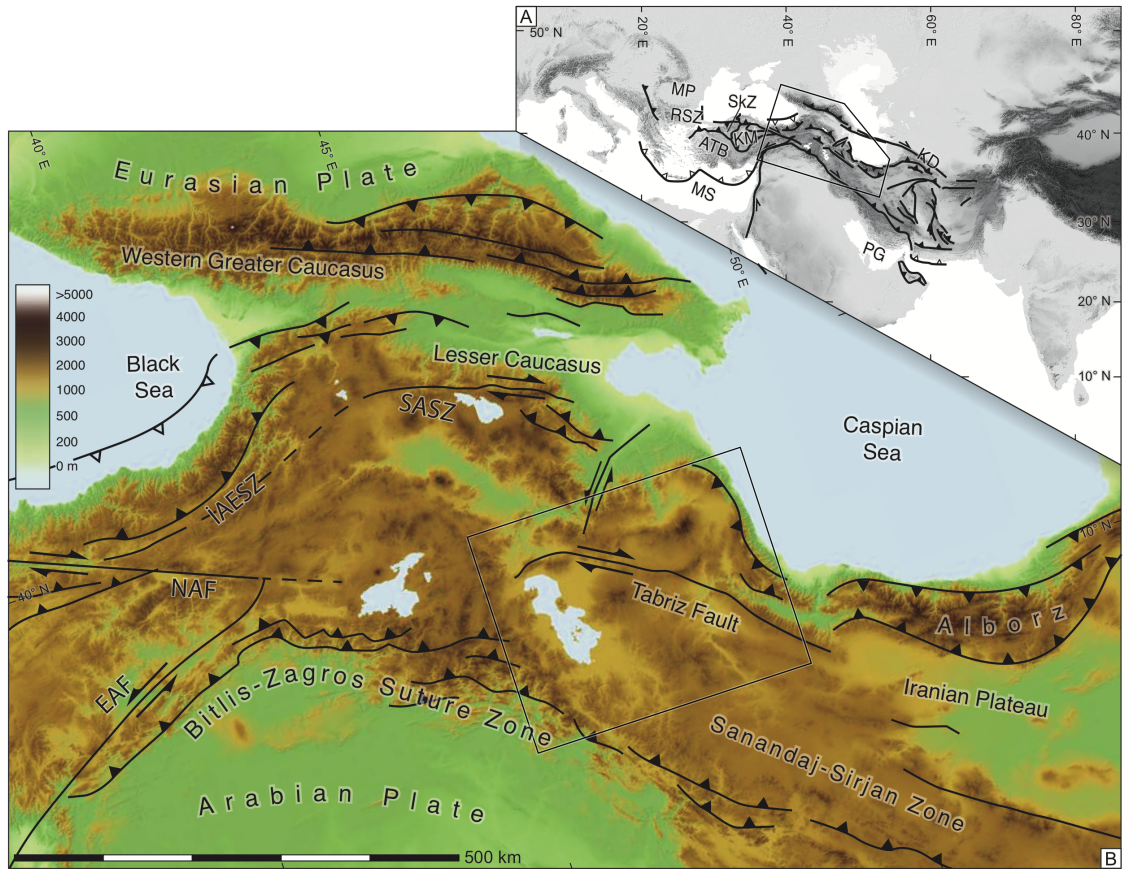


Figure A.2

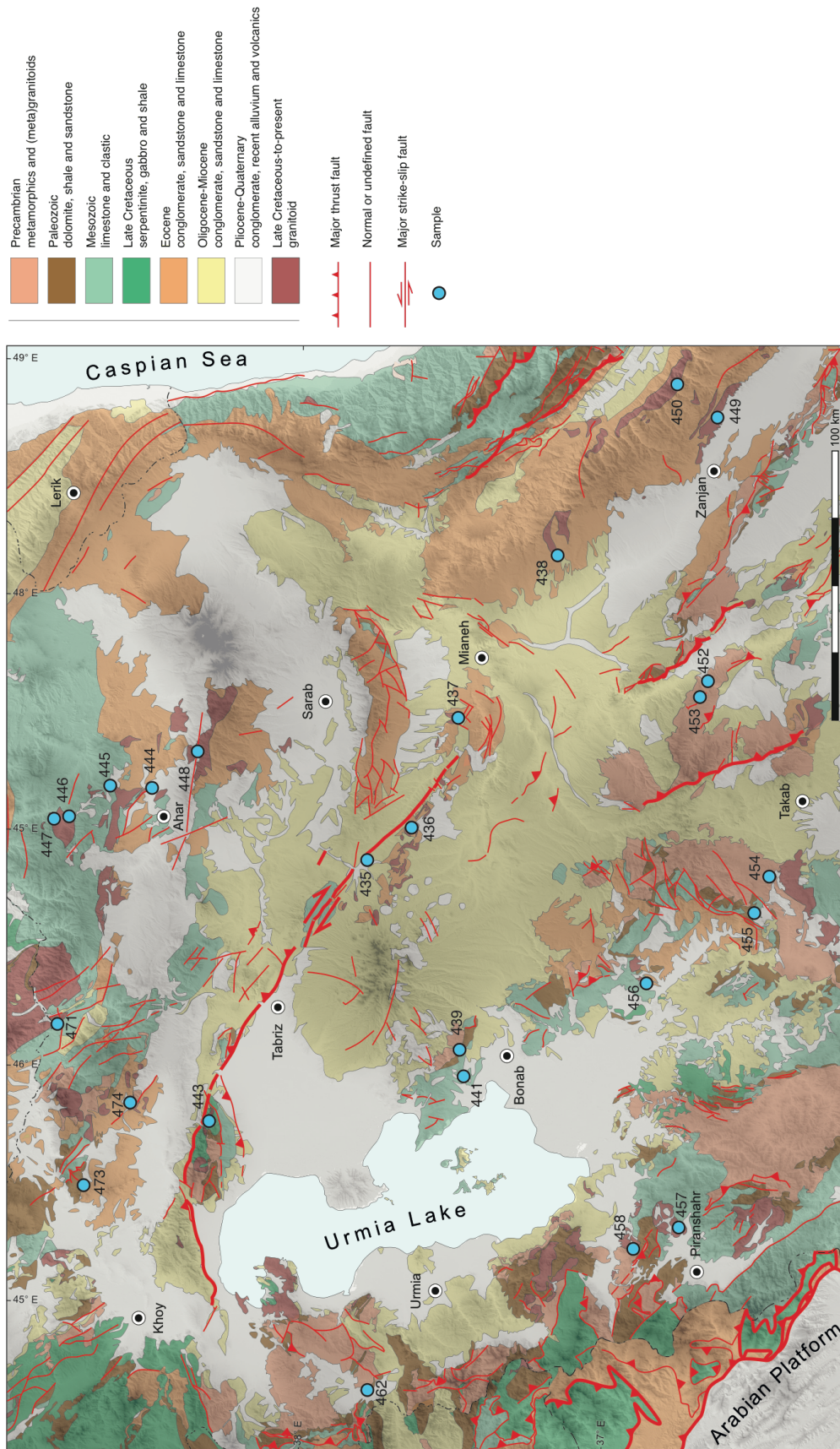


Figure A.3

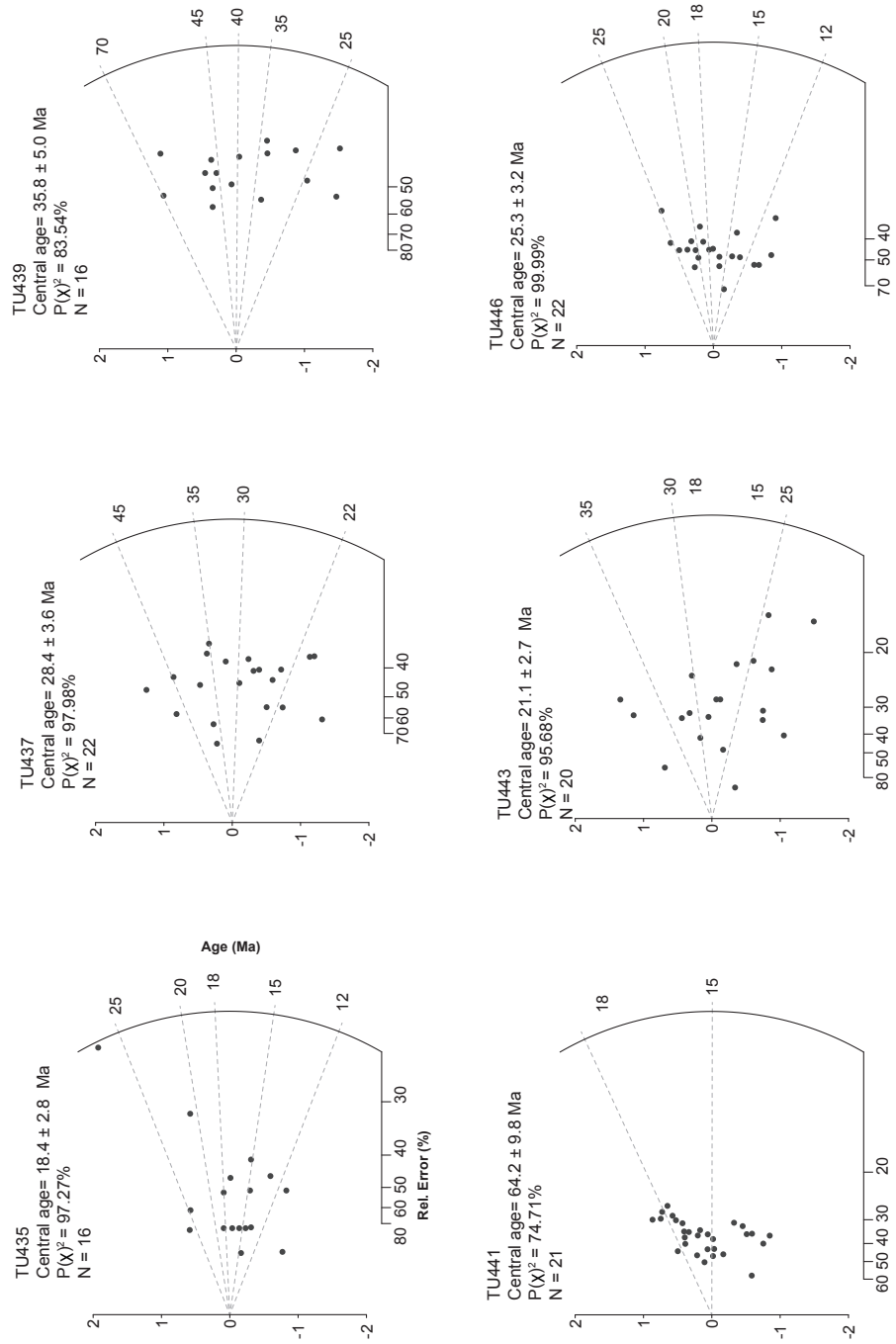


Figure A.4

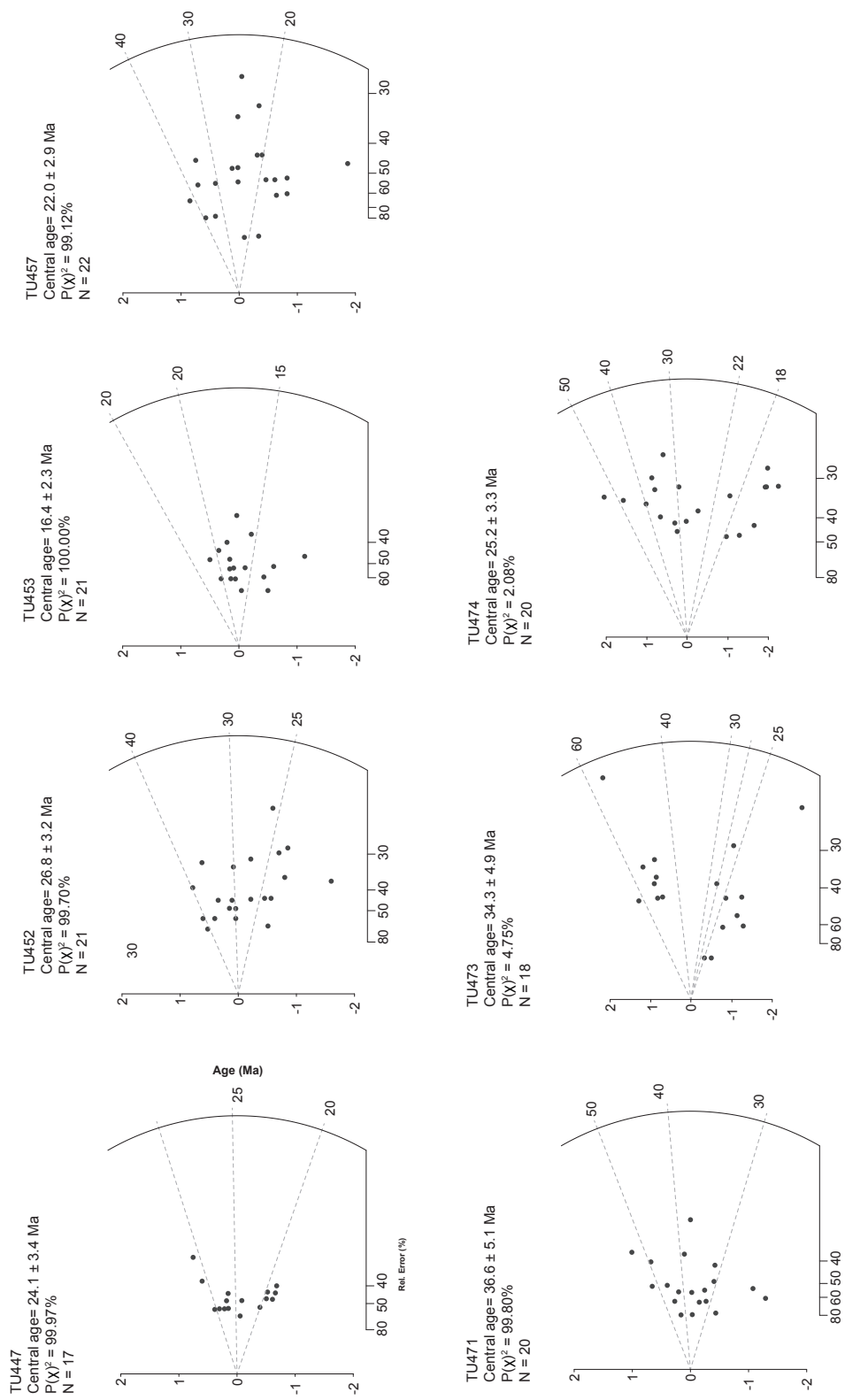




Figure A.5

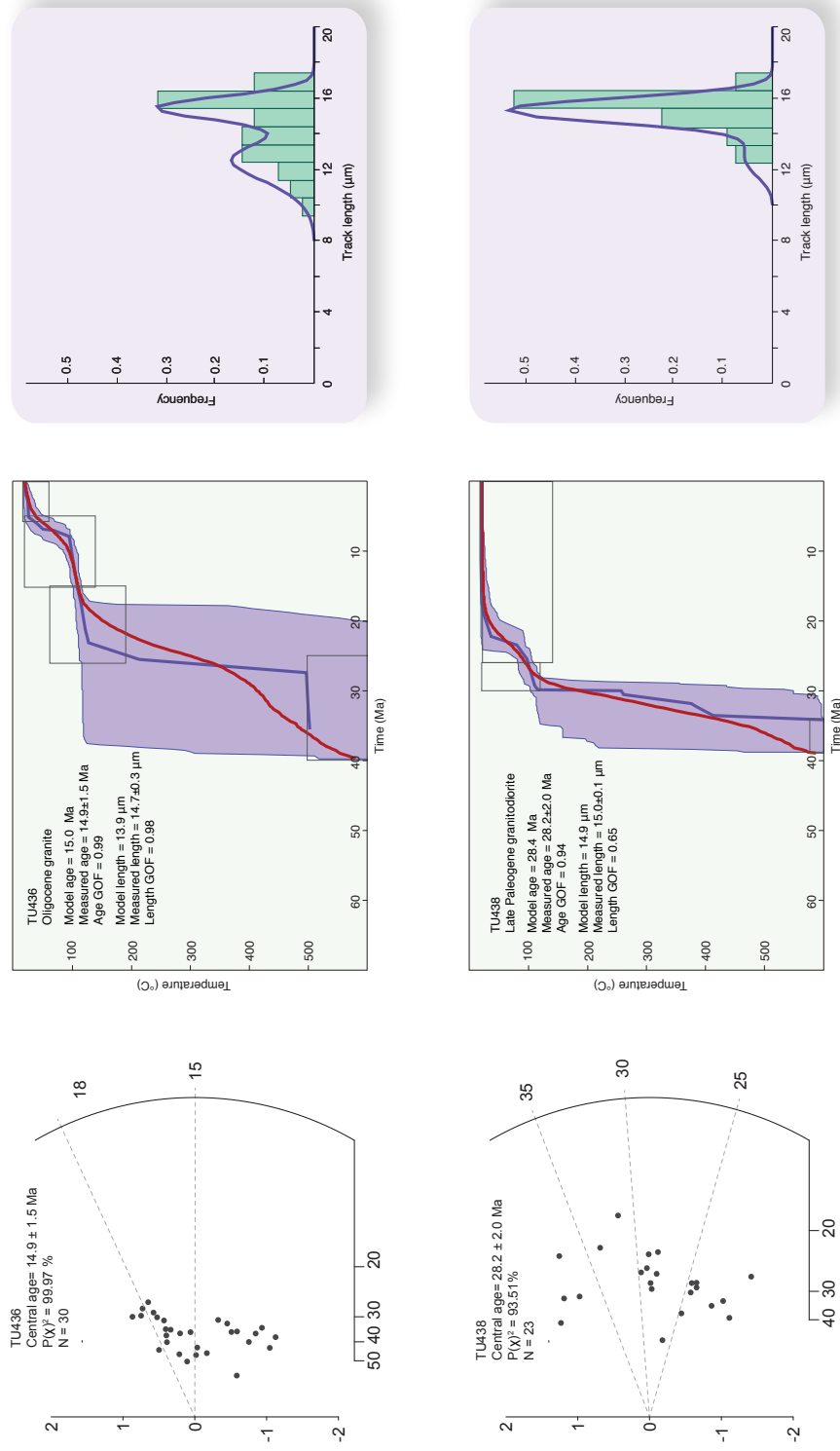


Figure A.6

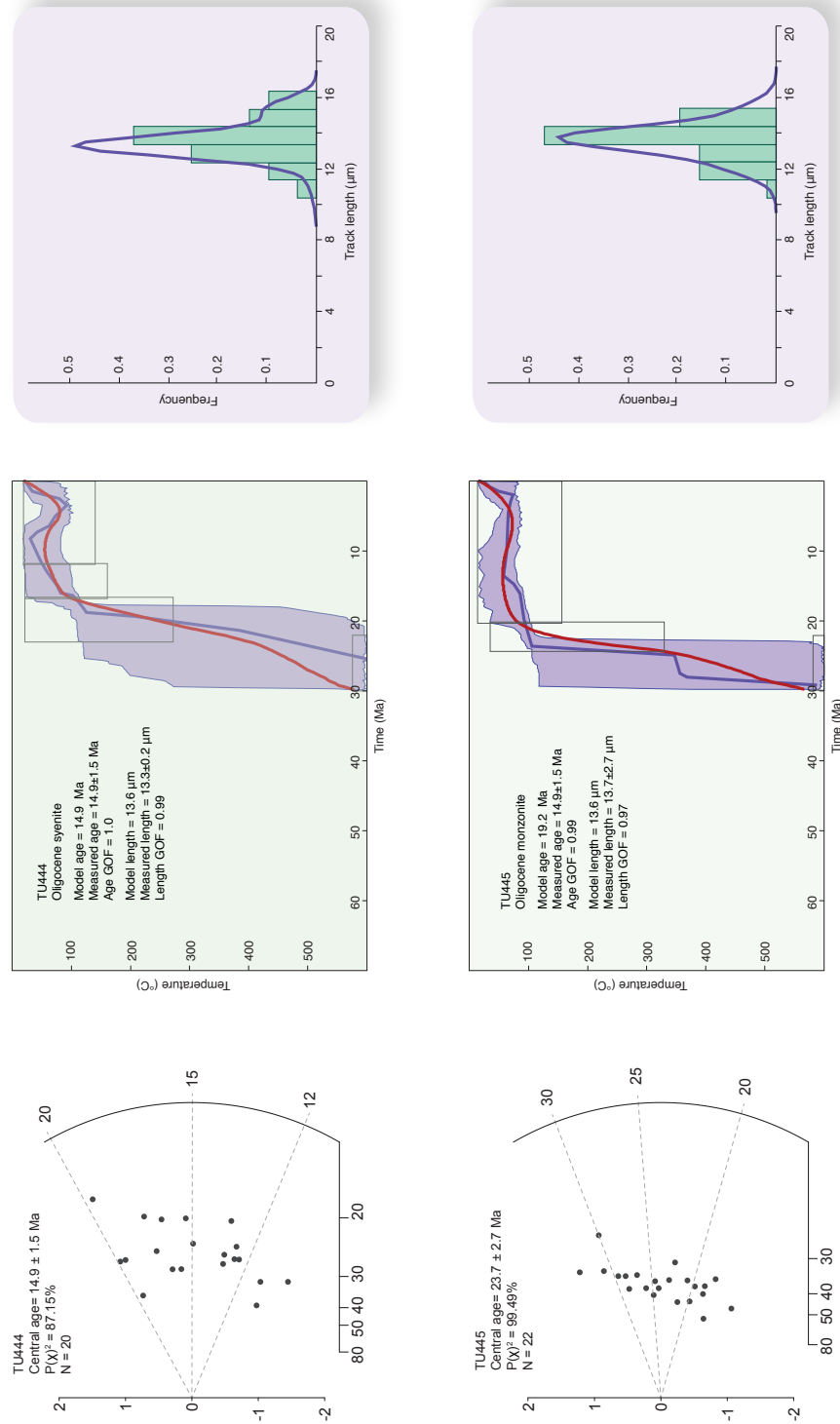


Figure A.7

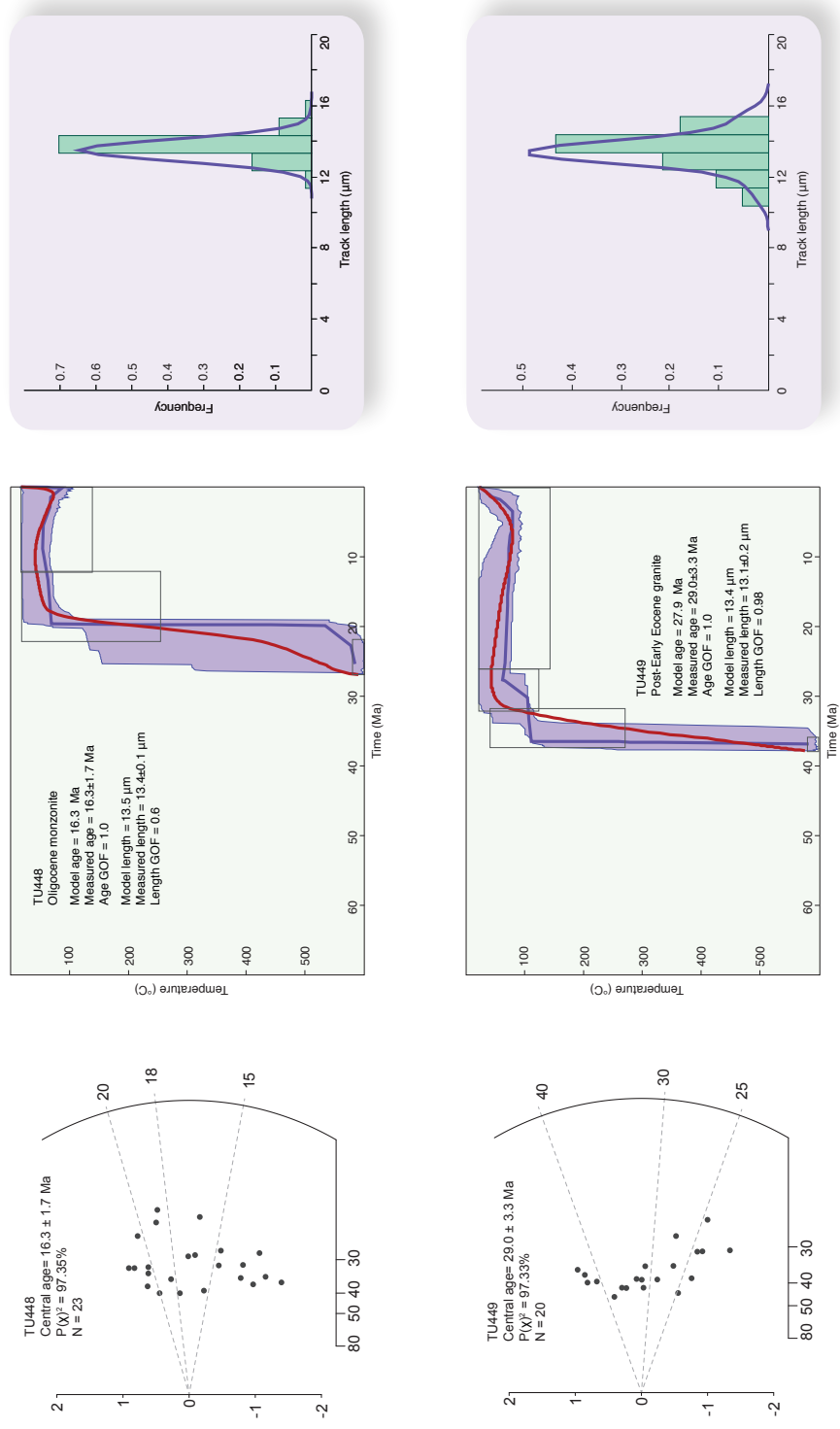


Figure A.8

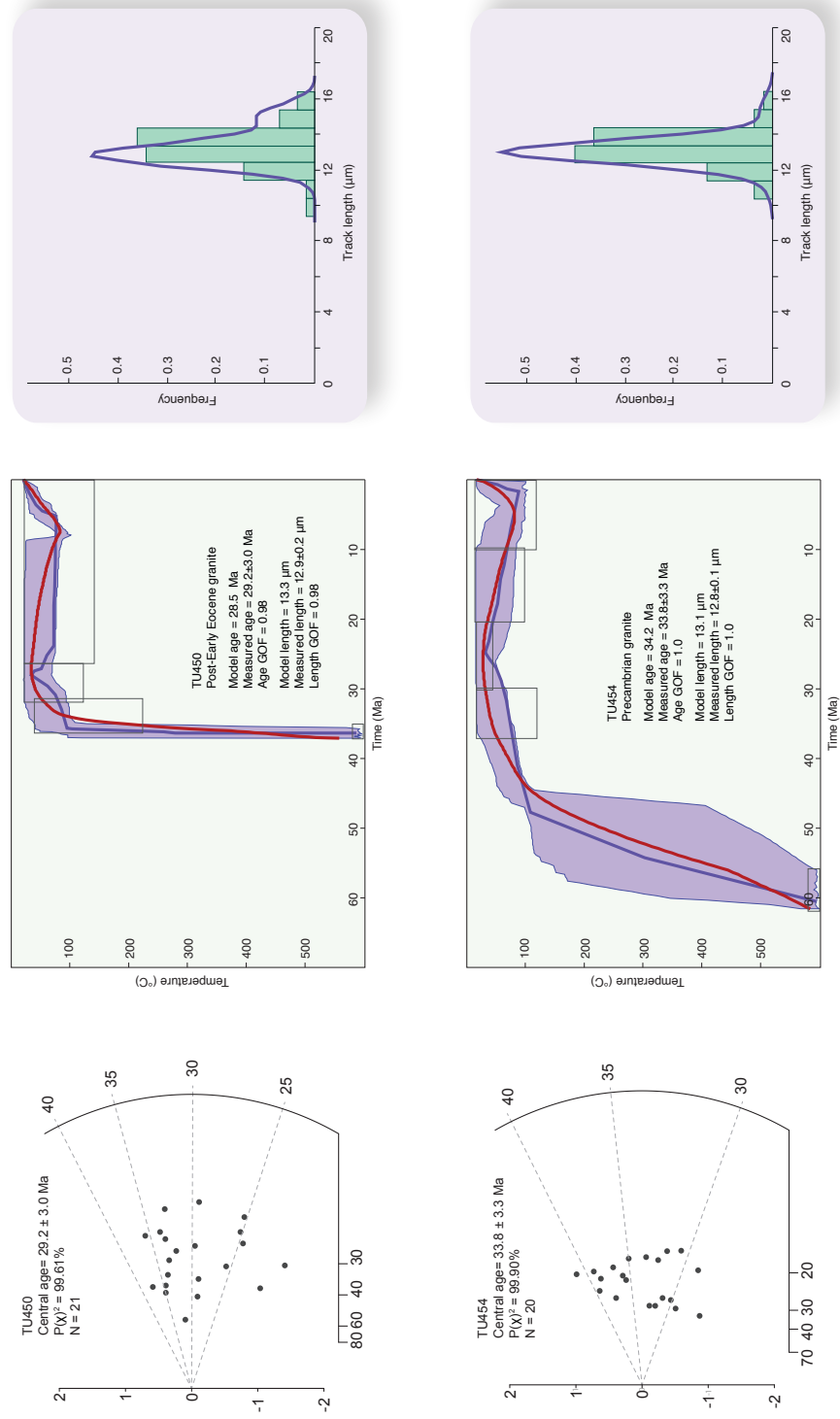


Figure A.9

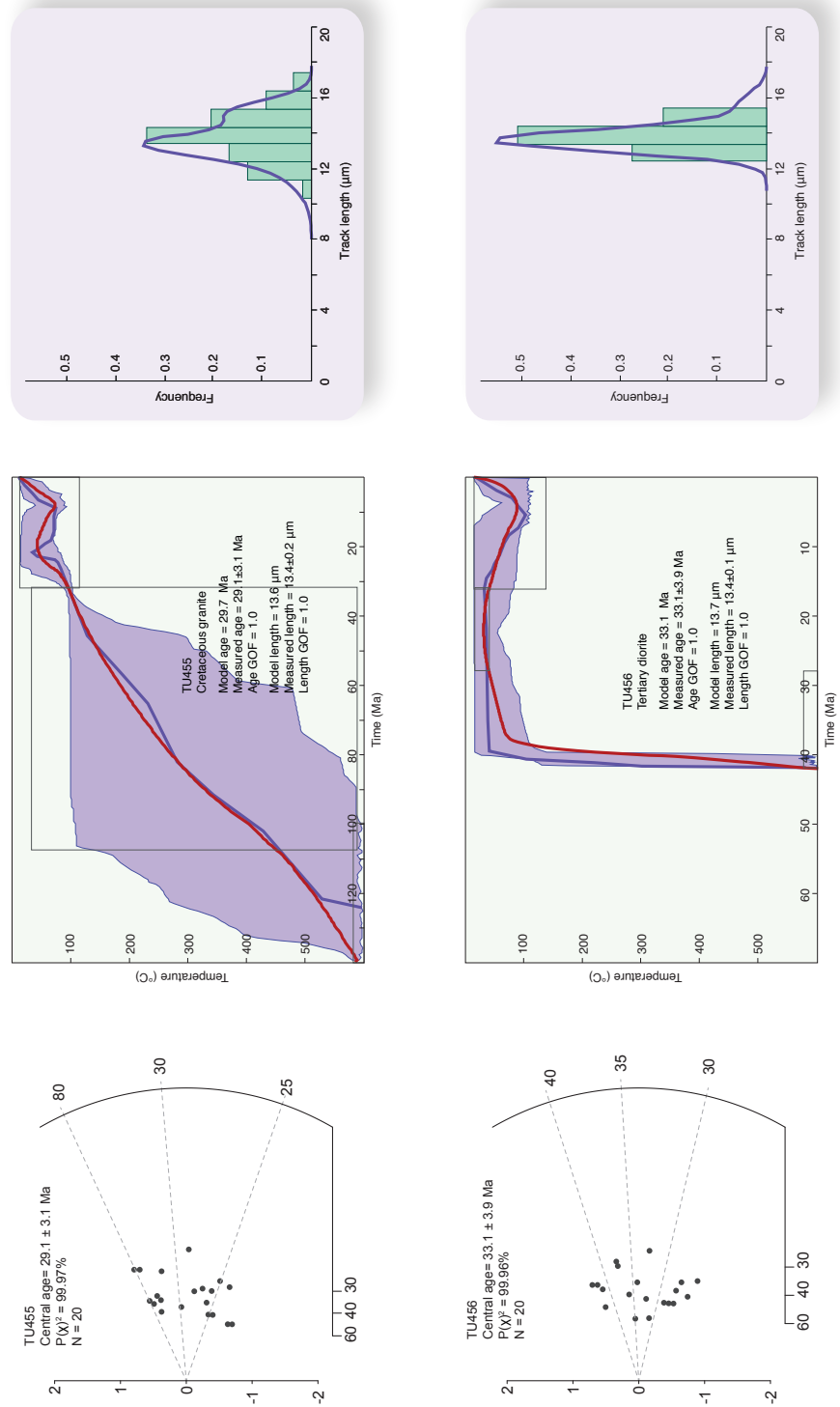


Figure A.10

